Constraining the nuclear matter equation of state from electromagnetic observables in finite nuclei

Dissertation

zur Erlangung des akademischen Grades
„Doktor der Naturwissenschaften“
am Fachbereich Physik, Mathematik und Informatik
der Johannes Gutenberg-Universität Mainz

Francesca Bonaiti
geboren am 23. August 1995 in Bergamo, Italien
Mainz, den 10. Mai 2024

Francesca Bonaiti
Institut für Kernphysik
Johannes-Gutenberg Universität Mainz
Johann-Joachim-Becher-Weg 45
55128 Mainz

D77 / Dissertation der Johannes Gutenberg-Universität Mainz

Datum der mündlichen Prüfung: 19 Juli 2024

Abstract

Understanding the nature of neutron stars, where matter reaches extremely high density conditions, is one of the most fascinating questions in nuclear astrophysics. The structure, dynamics and composition of these astrophysical objects are governed by the nuclear matter equation of state, which relates the pressure supporting the star against gravitational collapse to the huge range of densities present in its interior. Around the densities reached in the atomic nucleus, the nuclear matter equation of state can be investigated in laboratory experiments targeting nuclear electromagnetic properties, such as electric dipole polarizabilities and isoscalar monopole resonances. These observables, connected to parameters entering the nuclear matter equation of state, shed light also on the collective excitations of the nucleus at low energy.

Ab initio calculations, combining nuclear forces from chiral effective field theory with systematically improvable many-body methods, represent now the gold standard of nuclear structure computations in increasingly large systems. In this framework, computing electromagnetic observables involves additional challenges, as it requires the knowledge of both bound and continuum excited states of the nucleus. Such calculations have become possible in medium-mass nuclei thanks to the coupled-cluster (CC) formulation of the Lorentz integral transform (LIT) technique, known as LIT-CC method, limited thus far to doubly magic or semi-magic nuclei.

This thesis extends the reach of ab initio LIT-CC calculations of electromagnetic observables beyond closed-shell nuclei and towards the dripline. We show how the LIT-CC approach can be reformulated for nuclei in the vicinity of closed shells, focusing on two-particle-attached (2PA) systems, which are characterized by having two nucleons outside a closed-shell core. For most of this thesis, we focus on the electric dipole polarizability. We first test LIT-CC predictions on new experimental data for the closed-shell ^{40}Ca, serving as an additional benchmark for constraints on the nuclear matter equation of state from chiral forces. Next, we validate the newly developed LIT-CC method for 2PA nuclei, computing the non-energy-weighted dipole sum rule and the dipole polarizability of ^{16,24}O in both the closed-shell and the new frameworks, finding agreement between error bars. We analyse the evolution of the dipole polarizability along the oxygen and calcium isotopic chains, providing predictions for ^{24}O and ^{54,56}Ca, which will serve as motivation for future experimental studies at the dripline. We then present a study of the exotic halo nucleus ^{8}He, where we compare our predictions for the dipole polarizability with recent high-statistics data obtained at RIKEN, Japan by the SAMURAI collaboration. In the end, we move our attention to isoscalar monopole resonances, and extract a preliminary estimate of the incompressibility of symmetric nuclear matter.

Lay Summary

At the heart of one of the most intriguing questions in physics lies the study of neutron stars, among the densest form of matter which can be found in our Universe. These incredibly compact stellar remnants are born from the collapse of massive stars in supernova explosions. Their structure, composition and dynamics is dominated by the nuclear matter equation of state, which determines the pressure supporting the star in the extreme densities found in its interior. Through a combination of theoretical models, experimental data, and observations, scientists are piecing together the ingredients of the nuclear equation of state. In this thesis, we focus on a specific region within neutron stars, where matter reaches the typical density of atomic nuclei. By employing advanced computational techniques and mathematical tools, we study how protons and neutrons bind together in the atomic nucleus, and how the nucleus behaves when immersed in electromagnetic fields, unravelling properties of the nuclear equation of state in this regime.

List of Publications

The work presented in this thesis is based on published and unpublished material produced by the author Francesca Bonaiti. The following publications were produced during the PhD studies:

- [1] **F. Bonaiti**, S. Bacca, G. Hagen. *Ab-initio coupled-cluster calculations of ground and dipole excited states in* ^{8}He. Phys. Rev. C 105, 034313 (2022).

  I am the leading author for this publication. I implemented part of the code needed for the calculation of the dipole sum rules, and performed all the numerical calculations. I analysed the results presented and wrote the first draft of the manuscript.

- [2] B. Acharya, S. Bacca, **F. Bonaiti**, et al. *Uncertainty quantification in electromagnetic observables of nuclei.* Front. Phys. 10:1066035 (2023).

  This is a review on recent progress in calculations of electromagnetic observables in nuclei. I performed the new ^{8}He calculations and wrote the corresponding part of the manuscript.

- [3] D. Bazin, K. Becker, **F. Bonaiti**, et al. *Perspectives on few-body cluster structures in exotic nuclei.* Few-Body Syst. 64 (2023) 2, 25.

  This paper was written by the participants of the FRIB-TA Topical Program ”Few-Body Clusters in Exotic Nuclei and their Role in FRIB Experiments”, held at Michigan State University in August 2022. I took part in devising, shaping and writing the paragraphs regarding “Deformation” and “Clustering” of the piece “Emergence of Few-Body Effects in Exotic Nuclei”.

- [4] P. Capel, D. R. Phillips, A. Andis, M. Bagnarol, B. Behzadmoghaddam, **F. Bonaiti** et al. *Effective field theory analysis of the Coulomb breakup of the one-neutron halo nucleus* ^{19}C. Eur. Phys. J. A 59, 273 (2023).

  This paper is the product of the final project assigned during the TALENT School “Effective field theories in light nuclei: from structure to reactions”, held in August 2022 in Mainz, Germany.

- [5] R. W. Fearick, P. von Neumann-Cosel, S. Bacca, J. Birkhan, **F. Bonaiti** et al. *Electric dipole polarizability of* ^{40}Ca. Phys. Rev. Research 5, L022044 (2023).

  This is a project in collaboration with experimentalists and density functional theorists. I contributed in running and checking the coupled-cluster calculations of the dipole polarizability of ^{40}Ca, in writing the theory part of the manuscript and reviewing the paper before submission.

- [6] **F. Bonaiti** and S. Bacca. *Low-Energy Dipole Strength in* ^{8}He, Few-Body Syst. 65, 54 (2024).

  I am the leading author of this publication, part of the Special Issue of Few-Body Systems on “Advances on the Few-Body Problem in Physics - Selected and refereed papers from the 25th European Conference”, where I won the poster prize for the Best Presentation. I performed the ^{8}He calculations of this work, analysed the results presented and wrote the first draft of the manuscript.

- [7] **F. Bonaiti**, S. Bacca, G. Hagen, G. R. Jansen. *Electromagnetic observables of open-shell nuclei from coupled-cluster theory*, arXiv:2405.05608 [nucl-th], submitted to Physical Review C.

  I am the leading author of this publication, which presents an extension of the LIT-CC approach to nuclei in the vicinity of closed shells, focusing on two-particle-attached (2PA) systems. I devised this extension from a conceptual point of view, built from scratch the LIT-CC code for 2PA systems, employing the Nuclear Tensor Contraction Library (NTCL), performed all the calculations contained in this paper, analysed the results presented and wrote the first draft of the manuscript.

- [8] **F. Bonaiti**, S. Bacca, W. Jiang. *Nuclear incompressibility from isoscalar monopole resonances of medium-mass nuclei*, in preparation.

  For this project, I implemented the isoscalar monopole operator in the LIT-CC suite of codes, performed calculations of monopole sum rules and matter radii, and used those to extract an estimate of the incompressibility of symmetric nuclear matter.

Contents

List of Figures

List of Tables

List of Acronyms

1PA	One-particle-attached
1PA-EOM-CC	One-particle-attached equation-of-motion coupled-cluster
1PR	One-particle-removed
1PR-EOM-CC	One-particle-removed equation-of-motion coupled-cluster
2PA	Two-particle-attached
2PA-EOM-CC	Two-particle-attached equation-of-motion coupled-cluster
2PR	Two-particle-removed
2PR-EOM-CC	Two-particle-removed equation-of-motion coupled-cluster
2PA-LIT-CC	Two-particle-attached Lorentz integral transform coupled-cluster
3N(F)	Three-nucleon (force)
4N(F)	Four-nucleon (force)
CC	Coupled-cluster
CCSD	Coupled-cluster singles and doubles
CCSDT-1	Coupled-cluster singles, doubles and linear triples
COSM	Cluster orbital shell model
CREX	Calcium radius experiment
DOM	Dispersive optical model
EFT	Effective field theory
EDF	Energy density functional
EM	Electromagnetic or in the context of nuclear forces, Entem and Machleidt
EMPM	Equation-of-motion multiphonon approach
EOM	Equation of motion
EOM-CCSD	Equation-of-motion coupled-cluster singles and doubles
EOM-CCSDT-1	Equation-of-motion coupled-cluster singles, doubles and linear triples
EOS	Equation of state
GDR	Giant dipole resonance
HF	Hartree-Fock
HO	Harmonic oscillator
IMSRG	In-medium similarity renormalization group
ISGMR	Isoscalar giant monopole resonance
LEC	Low-energy constant

LIT	Lorentz integral transform
LIT-CC	Lorentz integral transform coupled-cluster
LO	Leading order
MESA	Mainz energy-recovering superconducting accelerator
MREX	Mainz radius experiment
NCSM	No-core shell model
N^{3}LO	Next-to-next-to-next-to-leading order
N^{2}LO or **NNLO**	Next-to-next-to-leading order
NICER	Neutron star interior composition explorer
NN	Nucleon-nucleon
NTCL	Nuclear tensor contraction library
PAV	Projection after variation
PDR	Pygmy dipole resonance
PGCM	Projected generator coordinate method
PNM	Pure neutron matter
PREX	Lead (^{208}Pb) radius experiment
PVES	Parity violating electron scattering
PWA	Partial wave analysis
RPA	Random phase approximation
QCD	Quantum chromodynamics
SCGF	Self consistent Green's function
SA-NCSM	Symmetry-adapted no-core shell model
SNM	Symmetric nuclear matter
SRG	Similarity renormalization group
TOV	Tolman-Oppenheimer-Volkoff (equations)

1 Introduction

How does matter behave at the most extreme densities in the Universe? This question, ranking among the most exciting challenges driving nuclear physics and astrophysics today [9], has propelled neutron stars at the center of interdisciplinary research efforts at the interface between these fields.

With black holes, neutron stars feature the densest form of matter in the Universe. They are compact astrophysical objects originating from the supernova explosion of stars with total mass above 8 solar masses [10]. Typically, they have a mass of more than 1.4 times the mass of our sun, $M_\odot$, compressed into a sphere with a radius varying between 10 and 14 km. Neutron stars emerge from the competition between gravity and the quantum mechanical pressure from its constituents (mostly neutrons, with small fractions of protons and electrons), preventing the collapse of the star into a black hole. The study of neutron stars is then intrinsically linked to investigations of the strong interaction between nucleons, involving typical distances of the order of 1 fm. Therefore, understanding the structure of neutron stars establishes a fascinating connection between physics domains separated by more than 15 orders of magnitude in length scale.

The first hypothesis regarding the existence of neutron stars dates back to the 1930s. At that time, Landau put forward the idea of compact stars similar to giant atomic nuclei [11]. The first written trace of such conjecture can be found in the 1933 proceedings of the American Physical Society by Baade and Zwicky who claimed: *With all reserve we advance the view that supernovae represent the transition from ordinary stars into neutron stars, which in their final stages consist of extremely closed packed neutrons* [12]. Later, in 1939, using Einstein's theory of general relativity, Tolman [13] and Oppenheimer and Volkoff [14] derived independently the equations governing the structure of neutron stars, the so-called Tolman-Oppenheimer-Volkoff (TOV) equations. A fundamental input of the TOV equations is the equation of state (EOS) of neutron stars, which determines the pressure supporting the star against gravity over the wide range of densities found in its interior. In their seminal paper [14], assuming that neutron star matter behaves as a non-interacting gas of neutrons, Oppenheimer and Volkoff deduced that a neutron star would collapse into a black hole once its mass surpassed around 0.7 $M_\odot$. However, experimental observations, starting with Jocelyn Bell's pioneering work [15], have challenged this prediction, with recent data reporting that this critical mass limit is at least 3 times higher [16]. This underlines the key role played by the nuclear interaction in shaping the equation of state of a neutron star. Heavier stars are in fact stabilized by the short-range repulsion between nucleons.

Different theoretical, experimental and observational techniques, in space- and Earth-based laboratories, can be used to constrain the equation of state of neutron star matter at progressively higher density (see Ref. [17] and references therein). The synergy between these different techniques culminated in the groundbreaking detection of the gravitational wave GW170817 [18], which sparked the "golden era" of multimessenger astronomy [19]. Attributed to a binary neutron star merger, such event encoded properties of nuclear matter and its equation of state through the tidal deformabilities of neutron stars during inspiral [20].

In this thesis, we will focus on constraining the EOS around the typical density reached in the interior of the atomic nucleus, the so-called saturation density, $n_0 \approx 0.16\ \mathrm{fm}^{-3}$. To have a concrete reference, this corresponds to 100 trillion times the density of water. In this regime, the EOS can be modeled as a uniform gas of nucleons, interacting solely via the strong force. This can be a good approximation for the conditions found in the outer core of a neutron star [17].

Around saturation density, the EOS can be probed through the study of properties of finite nuclei, such as the neutron skin, defined as the difference between the neutron and proton radii in the nucleus. Theoretical calculations found correlations between this observable and crucial parameters of the EOS [21], which can be exploited in the presence of precise experimental measurements of neutron skins in neutron-rich nuclei. The latter, however, are particularly challenging (see Ref. [22] for a recent review). As the neutron has no electric charge, the neutron distribution has been tested in the past via hadronic probes, which introduce systematic uncertainties in the analysis due to the modelling of the strong interaction. At the moment, parity violating elastic electron scattering (PVES), relying on the electroweak interaction, has emerged as the cleanest and least model-dependent technique [23]. In the last few years, it has been used to measure neutron skins in ^{48}Ca [24] and ^{208}Pb [25, 26]. The implications of these measurements on the EOS are still debated by the nuclear physics and astrophysics community [27–31].

Another interesting opportunity to constrain the EOS is offered by electromagnetic observables, which characterize the behaviour of the nucleus interacting with photons. In fact, the density dependence of the EOS can be investigated by slightly perturbing the nucleus from its ground state, as it happens with electromagnetic probes. As a consequence, correlations have been found between crucial parameters of the EOS and the electric dipole polarizability α_D [32], which measures the tendency of the nuclear charge distribution to deform in the presence of an external electromagnetic field. Other properties of the EOS, as the incompressibility of nuclear matter, can be constrained by systematic studies of collective excitations as isoscalar monopole resonances [33].

From the theory point of view, extensive studies of electromagnetic observables across the nuclear chart have been carried out mainly in the framework of energy density functional (EDF) theory, combined with the random phase approximation (RPA) and its refinements (see e.g. Refs. [34–36] and references therein). In this thesis, we instead focus our attention on the description of such observables within an ab initio framework.

Ref. [37] describes ab initio methods as *a systematically improvable approach for quantitatively describing nuclei using the finest resolution scale possible while maximizing its* *predictive capabilities*. At the energy scales probing the electromagnetic observables of interest, the best compromise between resolution and predictive power is reached by choosing protons and neutrons as the building blocks of the problem, and combining systematically improvable many-body solvers with chiral effective field theory (EFT) interactions, linking directly the nuclear force to the underlying theory of strong interactions, Quantum Chromodynamics. While being for a long time limited to light nuclei, ab initio methods have experienced an exponential increase of their reach in mass number, as illustrated by Figure 1.1.

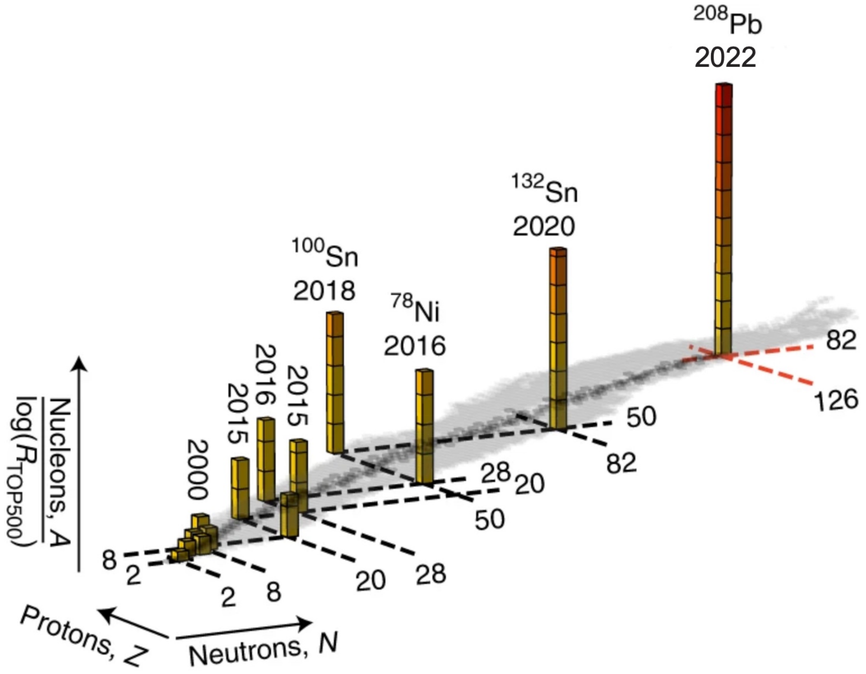

Figure 1.1: Progress in ab initio nuclear theory calculations. On the top of each bar, the year of the first ab initio calculation for the corresponding closed-shell nucleus is indicated. The height of each bar represents the mass number A divided by the logarithm of the total computational capability R_{TOP500} (measured in flops s^{-1} floating-point operations per second) from the TOP500 list [38]. This quantity would remain constant if advancements were only driven by a consistent exponential growth in computing power. However, the availability of many-body methods that scale polynomially in A has significantly expanded the reach of these calculations. Figure adapted from Ref. [30].

Figure 1.1 shows that ab initio nuclear theory has not only benefitted by advances in high-performance computing, but also by the availability of many-body methods allowing one to solve the many-body Schrödinger equation with controlled approximations, while scaling polynomially with mass number. Examples of such methods are Coupled-Cluster (CC) theory [39], In-Medium Similarity Renormalization Group (IMSRG) [40], Self Consistent Green's function (SCGF) [41] and many others (see Ref. [42] for a recent review on ab initio techniques).

Ab initio calculations of electromagnetic properties are way more difficult than for ground-state properties as the neutron skin, as they require the knowledge of all the bound and continuum states of the nucleus. Coupling CC theory with the Lorentz integral transform (LIT) technique [43], ensuring a proper treatment of continuum wavefunctions, has led to a new method, called LIT-CC [44, 45], which provided the first ab initio calculations of electric dipole polarizabilities in medium-mass nuclei [46]. First applications of this method focused on medium-mass nuclei as ^{48}Ca [47, 48], and unstable neutron-rich nuclei, as ^{68}Ni [49]. More recently, Ref. [30] has delivered the first ab initio prediction for the polarizability of ^{208}Pb, based on the IMSRG approach. Good agreement is found between available experimental data and ab initio predictions [5, 30, 48, 49], however limited thus far to closed-(sub)shell nuclei.

Together with these promising benchmarks with theory, the connection of electric dipole polarizability with the EOS is motivating experimental investigations in regions of the nuclear chart where it has not been explored yet. Open-shell calcium and nickel isotopes are the object of ongoing experimental campaign at iThemba Labs, South Africa and RCNP, Japan [50]. Moreover, with a future upgrade of FRIB, USA to 400 MeV/u, measurements of the dipole polarizability in very neutron-rich nuclei will become possible [51]. This could lead to unique opportunities to constrain the EOS from nuclei with an extreme neutron excess. These experimental endeavours motivate the core of the work presented in this thesis, which extends the reach of ab initio calculations of α_D within the LIT-CC method beyond closed-shell nuclei and towards the dripline.

This thesis is structured as follows. In Chapter 2, we will model the EOS of nuclear matter around saturation density and review the role of properties of finite nuclei, such as neutron skins, electric dipole polarizabilities and isoscalar monopole resonances, in constraining it. In the following Chapters, we will present the ingredients of our computations: nuclear forces grounded in chiral EFT (Chapter 3), coupled-cluster theory (Chapter 4) and the LIT-CC method (Chapter 5). Motivated by the experimental interest in open-shell nuclei, in Chapter 5 we extend the LIT-CC method to these systems. In particular, we focus on two-particle-attached nuclei, which can be obtained adding two nucleons to a closed-shell core. The conceptualization and implementation of this new method for open-shell nuclei constitute the novelty of this work [7]. These approaches are then employed in Chapter 6 to obtain the results of this thesis, focusing mainly on the electric dipole polarizability. Furthermore, as a proof of the potential of constraining the EOS from nuclear electromagnetic observables, we will also present a preliminary study of the incompressibility of nuclear matter from isoscalar monopole resonances. In Chapter 7, we conclude providing a brief summary and outlook of the work presented.

2 Neutron Stars and their Connection to Low-Energy Nuclear Physics

This Chapter is dedicated to an analysis of the connection between the physics of neutron stars and atomic nuclei, both governed by the nuclear matter EOS. After presenting the TOV equations, which describe the structure of neutron stars in general relativity, and sketching their internal structure, we model the nuclear matter EOS around saturation density. In the end, we focus our attention on EOS constraints from studies of nuclear structure and electromagnetic observables, and review the main developments in this direction. This Chapter is mostly based on Refs. [17, 35, 52].

2.1 Tolman-Oppenheimer-Volkoff equations

In general relativity, the structure of neutron stars is described by the Tolman-Oppenheimer-Volkoff (TOV) equations

$$\begin{aligned}
\frac{dP(r)}{dr} &= -\frac{Gm(r)}{r^2}\left(1+\frac{P(r)}{\rho(r)c^2}\right)\left(1+\frac{4\pi r^3 P(r)}{m(r)c^2}\right)\left(1-\frac{2Gm(r)}{rc^2}\right)^{-1}, \\
\frac{dm(r)}{dr} &= 4\pi r^2 \rho(r),
\end{aligned} \tag{2.1}$$

which characterize the behaviour of a spherically symmetric body of isotropic material in hydrostatic equilibrium. In Eq. (2.1), $P(r)$ is the pressure as a function of the radial coordinate r, $m(r)$ is the mass of the object contained within a given radius r, c is the speed of light and $\rho(r) = \varepsilon(r)/c^2$ is defined in terms of the energy density $\varepsilon(r)$.

As the TOV equations contain three unknown functions, $P(r)$, $\varepsilon(r)$ and $m(r)$, additional information in the form of an equation of state (EOS) $P = P(\varepsilon)$, relating the pressure to the density, needs to be supplied. At this point, the TOV equations are solved specifying the boundary conditions $P = P_c$ and $m = 0$ at the center of the star $r = 0$. The equations are then integrated from P_c to $P = 0$, corresponding to the pressure at the surface of the star. Once $P(r)$ and $m(r)$ are known, the radius R of the star is obtained from the condition $P(R) = 0$, while the mass M of the star corresponds to $M = m(R)$. Given the equation of state, the mass $M(P_c)$ and radius $R(P_c)$ can be computed for every value of the central pressure P_c, leading to the mass-radius relationship for neutron stars. Therefore, the TOV equations appear as an efficient map between the equation of state $P(\varepsilon)$ and the mass-radius relation $M(R)$. In this sense, they fully determine the structure of neutron stars.

As a qualitative example of the TOV mapping, in Figure 2.1 we show a modern set of representative equations of state and the corresponding mass-radius relations, taken from Ref. [52]. By using the TOV equations, the relatively monotonic growth of the pressure with the energy density translates into a steep increase of the mass of the neutron star in a limited range of values for radii. Lower values of the pressure at a fixed energy density identify soft equations of state, as for instance the solid green line in Figure 2.1. The latter yield smaller neutron star radii and support less heavier stars with respect to stiffer EOS (e.g., the solid blue line in Figure 2.1). The right panel of Figure 2.1 shows how the degree of softness/stiffness of the EOS determines a broad range of allowed maximum masses for a neutron star, enlarging also the uncertainty on the neutron star radius. In this regard, joint mass-radius measurements from the Neutron Star Interior Composition Explorer (NICER) (see, e.g., Ref. [54, 55]), as well as the detection of the gravitational wave GW170817 [18], associated to a binary neutron star merger, can provide an upper bound. As the TOV equations create a unique connection between the EOS and the mass-radius relation [56], they can be used to derive $M(R)$ based on our knowledge of the nuclear interaction and conversely, to infer information on the EOS, starting from astrophysical measurements [53, 57]. Constraining the EOS from both nuclear theory and neutron star observations is an active area of research (see, e.g., Refs. [28, 58–61] for recent works on the topic).

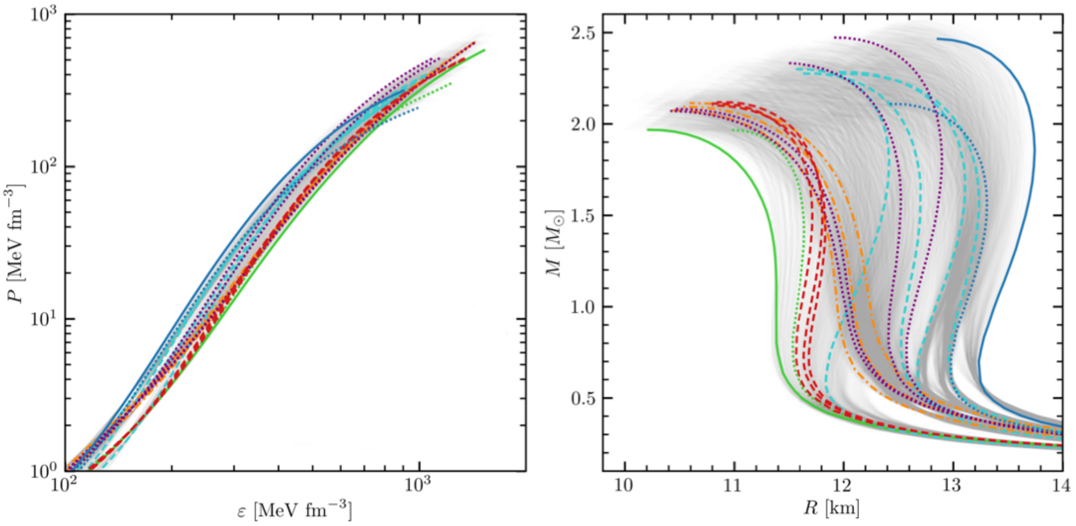

Figure 2.1: Left panel: set of representative equations of state $P(\varepsilon)$ (colored lines) obtained from microscopic nuclear matter calculations in Ref. [52]. Right panel: corresponding mass-radius relation derived via Eq. (2.1). The grey area represents the EOS compatible with constraints from nuclear theory and observations of Ref. [53]. Figure adapted from Ref. [52].

2.2 The structure of neutron stars

Our understanding of neutron stars relies on our ability to predict their behaviour over the huge range of density and pressures that can be found in their interior. In this Section, we give a brief description of the different density regions which can be found in a neutron star. They are schematically represented in Figure 2.2. The interested reader can find more details on the structure of neutron stars in, e.g., Ref. [17].

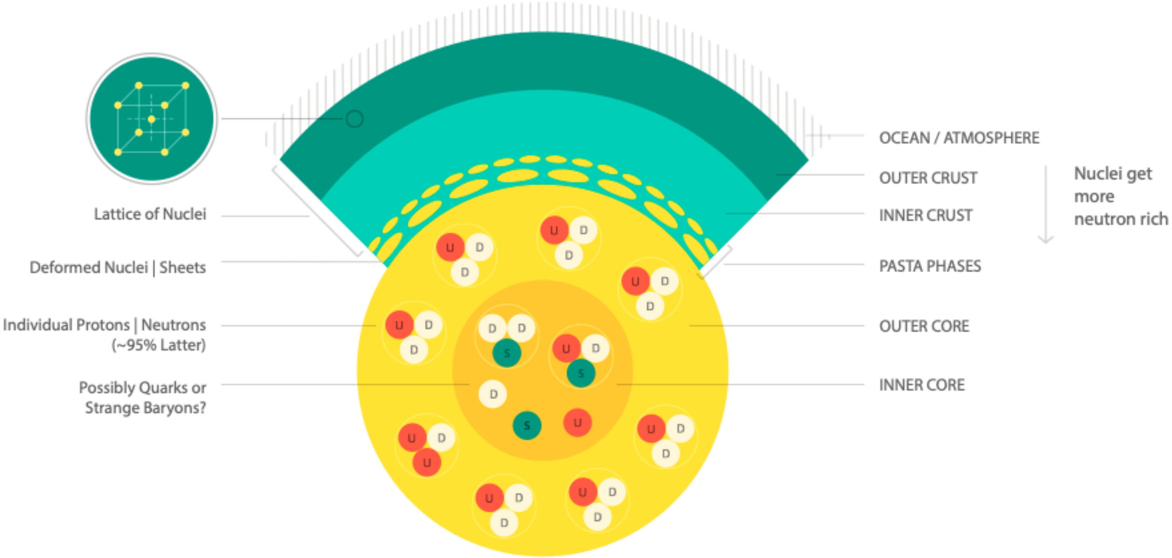

Figure 2.2: Schematical representation of the different layers composing the interior of a neutron star. Figure taken from Ref. [62].

The surface of a neutron star is characterized by a thin atmosphere, mainly composed by hydrogen and helium. Despite its relatively small thickness, the atmosphere plays a key role in astrophysical observations, as the thermal radiation emitted from this layer allows for measurements of chemical composition and other neutron star features [17].

In the outer crust, where the density ranges from 10^4 to 10^{11} $\mathrm{g/cm^3}$ [63], matter organizes itself into increasingly neutron-rich nuclei immersed in a uniform electron gas. The boundary between outer and inner crust is represented by the neutron drip density, around 4×10^{11} $\mathrm{g/cm^3}$, where atomic nuclei become unable to bind any more neutrons. In the inner crust region, the competition between the short-range strong interaction and the long-range Coulomb repulsion, a phenomenon called “Coulomb frustration”, is believed to drive the emergence of complex structures with different topologies, collectively dubbed as “nuclear pasta” phases [64].

The crust-core boundary is located at around half of nuclear saturation density $\rho_0 \approx 2.8\times10^{14}$ $\mathrm{g/cm^3}$ (or in terms of number density $n_0 \approx 0.16$ $\mathrm{fm^{-3}}$), where nuclei dissolve completely and the system is composed mostly by a uniform sea of neutrons, with small fractions of protons, electrons and muons in chemical equilibrium. Going towards the center of the star, at densities well above $2\rho_0$, more exotic forms of matter as hyperons or deconfined quarks are predicted to emerge [65].

2.3 Nuclear matter equation of state

We now focus on how to model the EOS of neutron stars at densities up to $1-2$ times saturation density, where constraints from nuclear physics can be obtained. As the temperature T in this regime is much lower with respect to typical nuclear energy scales, in the following we assume $T = 0$ K.

In these conditions, it is useful to work with nuclear matter. The latter represents an idealized uniform mixture of neutrons and protons, which interact exclusively through the strong force. Nuclear matter is characterized by an infinite mass number A and volume V, ensuring a finite total density $n = A/V$. The difference between the neutron and proton densities is given by the asymmetry parameter

$$\alpha = \frac{n_n - n_p}{n}, \tag{2.2}$$

where n_n is the neutron density, n_p the proton density and consequently $n = n_p + n_n$ is the total nucleon number density. For $\alpha = 1$, pure neutron matter (PNM) is obtained. In this case, both the energy per particle and pressure are positive, implying the absence of self-bound states for neutrons alone. In symmetric nuclear matter (SNM), instead, neutron and proton densities coincide ($\alpha = 0$). In SNM, an energy minimum emerges at the saturation density n_0. This implies the presence of a bound state, and results in vanishing pressure at this specific density. The energy per particle E/A as a function of density for SNM and PNM is shown in Figure 2.3.

The dependence of $E(n,\alpha)$ on α is usually parametrized as

$$\frac{E}{A}(n,\alpha) = \frac{E}{A}(n,0) + S(n)\alpha^2 + \mathscr{O}[\alpha^4], \tag{2.3}$$

where $\frac{E}{A}(n,0)$ is the EOS of symmetric nuclear matter, where $n_p = n_n$, and $S(n)$ is the so-called symmetry energy. Two comments are in order. First, odd powers of α do not occur due to isospin invariance of the nuclear interaction. Second, according to various nuclear many-body calculations (see Ref. [66] and references therein), retaining up to quadratic contributions in α in Eq. (2.3) represents a reliable approximation of the α dependence of E/A for $\alpha \in [0,1]$ and densities up to $2n_0$. One can then express the symmetry energy as the difference between the energy per nucleon of PNM and SNM

$$S(n) = \frac{E}{A}(n,1) - \frac{E}{A}(n,0). \tag{2.4}$$

In this picture, the symmetry energy is a measure of how the energy of the system is affected by replacing protons with neutrons.

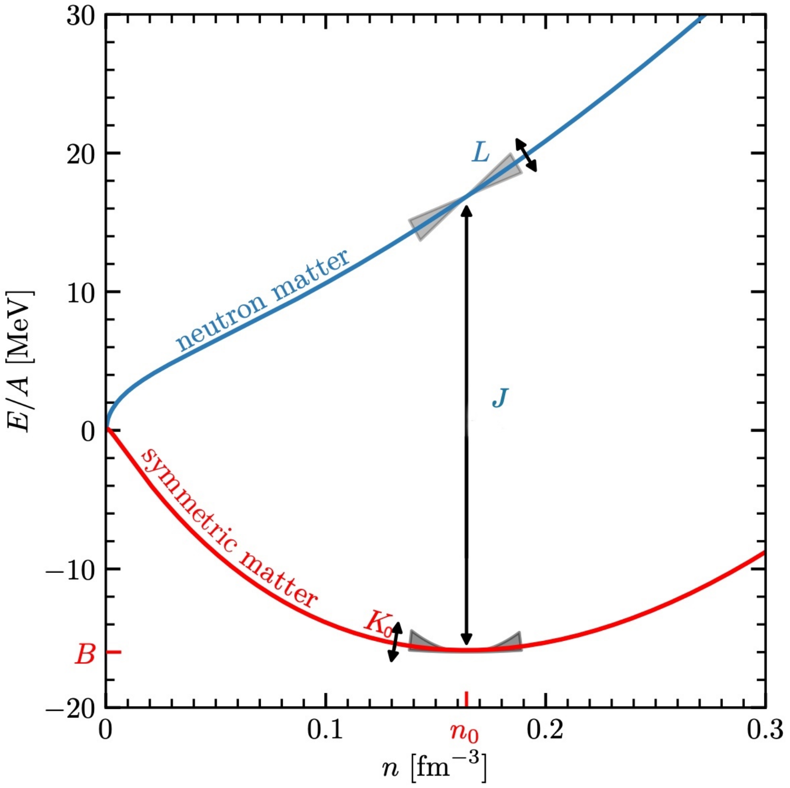

Figure 2.3: Equation of state of pure neutron matter (blue) and symmetric nuclear matter (red) as a function of density. The parameters defining the EOS at saturation density n_0, corresponding to the energy per nucleon of SNM at saturation B, incompressibility K_0, symmetry energy at saturation J and slope parameter L are also highlighted. Figure adapted from Ref. [52].

The EOS of symmetric nuclear matter can be expanded around n_0, yielding

$$\frac{E}{A}(n,0) = \frac{E}{A}(n_0,0) + \frac{1}{2}K_0\left(\frac{n-n_0}{3n_0}\right)^2 + \mathscr{O}(n-n_0)^3, \tag{2.5}$$

where $B = \frac{E}{A}(n_0,0)$ is the energy per nucleon of SNM at saturation. Introducing the pressure $P = n^2\frac{\partial E/A}{\partial n}$, it is possible to identify

$$K_0 = 9\frac{\partial P}{\partial n}\bigg|_{n_0,\alpha=0} = 9n_0^2\frac{\partial^2 E/A}{\partial n^2}\bigg|_{n_0,\alpha=0} \tag{2.6}$$

with the incompressibility of SNM. As shown in Figure 2.3, K_0 correspond to the curvature of the energy per particle of SNM. It measures the response of nuclear matter to compression.

Performing an expansion around n_0 also for the symmetry energy, we obtain

$$S(n) = J + L\frac{n-n_0}{3n_0} + \mathscr{O}(n-n_0)^2, \tag{2.7}$$

where $J = S(n_0)$ is the symmetry energy at saturation and L is the so-called slope parameter. We point out that since in SNM the pressure vanishes at saturation, the slope parameter L is proportional to the pressure of PNM at saturation density

$$L = 3n_0 \frac{\partial S}{\partial n}\bigg|_{n_0} = \frac{3}{n_0} P(n_0, \alpha = 1). \tag{2.8}$$

The slope parameter plays a key role in constraining the radius of neutron stars. In fact, a higher value of L implies a steeper PNM curve in Figure 2.3. This leads to a stiffer EOS, which translates into larger values of neutron star radii, as shown in Figure 2.1.

It is clear that the parameters B, K_0, J and L provide a detailed picture of the EOS around saturation density n_0. Accurate constraints for the values of $n_0 = 0.164(7)$ fm^{-3} itself and $B = -15.86(57)$ MeV have been obtained employing Skyrme energy density functionals (EDFs) fitted to properties of nuclei and nuclear matter and including an additional systematic uncertainty for B [67]. These ranges also agree with microscopic nuclear matter calculations [67–69] and with a very recent Bayesian mixture model analysis of multiple EDF predictions, yielding $n_0 = 0.157(10)$ fm^{-3} itself and $B = -15.97(40)$ MeV at 95% credibility level [70]. We will then focus on the symmetry energy parameters J and L and the incompressibility K_0, which determine the density dependence of the EOS at and around saturation density.

2.4 Constraints on the symmetry energy

The symmetry energy at saturation density J and the slope parameter L can be constrained investigating ground- and excited-state properties of nuclear systems, linking directly nuclear physics to astrophysics. We will now give an overview of the main research efforts undertaken in the recent years on both the theoretical and experimental side, focusing on two observables: the neutron skin thickness and the electric dipole polarizability.

2.4.1 Neutron skin thickness

The neutron skin thickness is defined as the difference between the point-neutron radius and the point-proton radius of a nucleus

$$R_{skin} = R_n - R_p. \tag{2.9}$$

The formation of neutron skins can be understood by looking at nuclear density distributions. In this regard, we can distinguish three main scenarios on the basis of the ratio between the number of neutrons N and the number of protons Z of the nucleus. The latter are schematically shown in Figure 2.4.

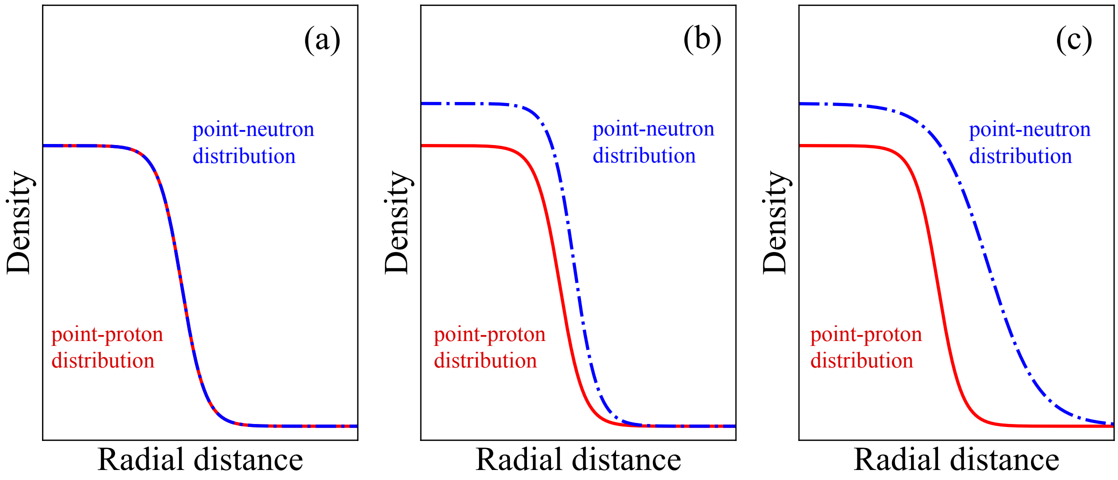

Figure 2.4: Schematic representation of point-proton (red) and point-neutron (blue) density distributions in three different N/Z scenarios: symmetric nuclei, with $N/Z \simeq 1$ [panel (a)], asymmetric nuclei ($N \gg Z$) with skin structure [panel (b)] and asymmetric nuclei with halo structure [panel (c)].

As shown in Figure 2.4 (a), if the nucleus is symmetric with respect to N and Z, the point-proton and point-neutron densities are expected to be similar. Increasing the N/Z ratio, instead, the excess neutrons tend to accumulate in the outer region of the nucleus, resulting in the formation of a neutron skin (see Figure 2.4 (b)). In some extreme cases, around the dripline, as illustrated in Figure 2.4 (c), the tail of the nuclear wavefunction is characterized by a slow exponential fall-off, leading to the emergence of halos. In the following we will focus on the scenario of panel (b).

The neutron skin of heavy, neutron-rich nuclei, and in particular of ^{208}Pb, has been analysed in a variety of theoretical frameworks. Energy density functional theory has been for a long time the only tool available to address the heavy mass region of the nuclear chart. However, in the last few years, thanks to advances in high performance computing and in many-body theory, ab initio calculations progressed exponentially in their reach in mass number [42]. These efforts culminated in a recent ab initio study on the neutron skin of ^{208}Pb [30]. In both EDF and ab initio approaches, the emergence of a strong correlation between the neutron skin of ^{208}Pb and the slope parameter L entering the symmetry energy has been found, as can be seen for example in Figure 2.5.

The sensitivity of this observable to L suggests that a precise experimental determination of the neutron skin of ^{208}Pb can be used to infer constraints on the density dependence of the symmetry energy. To this purpose, according to Eq. (2.9), knowledge of both the point-proton and point-neutron distributions is required.

However, while nuclear charge (and consequently, point-proton) densities can be measured in a clean way via, e.g., electron scattering, experimental data for neutron distribu-

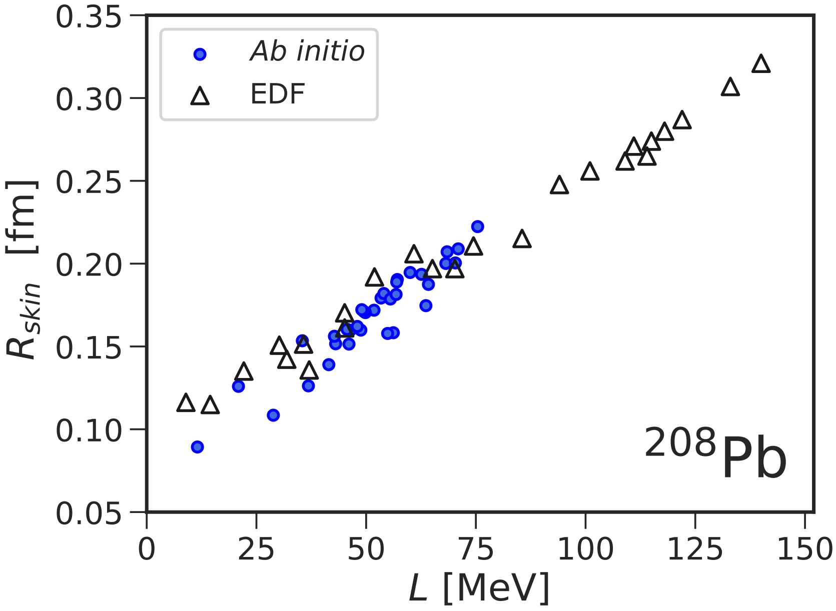

Figure 2.5: Slope parameter L as a function of the neutron skin thickness of ^{208}Pb, as obtained from the ab initio calculations of Ref. [30] and the relativistic and non-relativistic mean-field models of Ref. [21]. Figure adapted from Ref. [30], courtesy of Weiguang Jiang.

tions are extremely scarce even for stable nuclei. As neutrons are characterized by zero total electric charge, mainly strongly interacting particles (see, e.g., [71–73]) or exotic antiprotonic atoms [74] have been employed as probes of neutron distributions. While hadronic probes in some cases can achieve high statistics, and therefore small experimental errors, the analysis of these experiments is characterized by systematic uncertainties related to the treatment of the strong interaction.

On the other hand, parity violating elastic electron scattering (PVES), by relying exclusively on the electroweak interaction, minimizes the model dependence in the determination of the skin. PVES is based on the measurement of the parity-violating asymmetry A_{PV}, consisting in the difference between the cross sections of right-handed and left-handed electrons, which allows for the extraction of R_{skin} with minimal assumptions. More details can be found, e.g., in Refs. [22, 75]. However, PVES is at the moment only applicable on stable nuclei. In the last fifteen years, the Lead (Pb) Radius EXperiment (PREX) Collaboration at Jefferson Lab, USA has provided a first experimental determination of the neutron skin of ^{208}Pb (PREX-I, [25]), followed by a second experiment (PREX-II, [26]) where the accuracy was improved by approximately a factor of 2. The combination of the two measurements (from now on indicated only with PREX) implies $R_{skin} = 0.283 \pm 0.071$ fm^2 [26]. In calculations employing different families of EDFs, the neutron skin of ^{208}Pb comes out to be strongly correlated also with the skin of other neutron-rich nuclei, as ^{48}Ca [76]. This has motivated a recent PVES measurement of the neutron skin of ^{48}Ca, the so-called Calcium Radius EXperiment (CREX), yielding a much smaller value of R_{skin} in this nucleus with respect to ^{208}Pb: 0.121 ± 0.035 fm^2 [24].

The comparison between PVES results in ^{48}Ca and ^{208}Pb with previous neutron skin measurements, and their translation into symmetry energy constraints have attracted a lot of interest in the nuclear physics and astrophysics community. In Figure 2.6, we show the available experimental data on the neutron skin of ^{48}Ca and ^{208}Pb. The results of the ab initio calculations on ^{48}Ca from Hagen et al. [47] and Simonis et al. [77] and on ^{48}Ca and ^{208}Pb from Hu et al. [30], as well as those of a dispersive optical model (DOM) analysis of bound and scattering data [78, 79], are reported for comparison. For the neutron skin of ^{208}Pb, we also include EDF-based constraints given by the detection of the gravitational wave GW170817 [80] and the joint mass-radius NICER measurements [27], as well as the value inferred by Essick et al. [28], on the basis of neutron star observations and chiral effective field theory constraints.

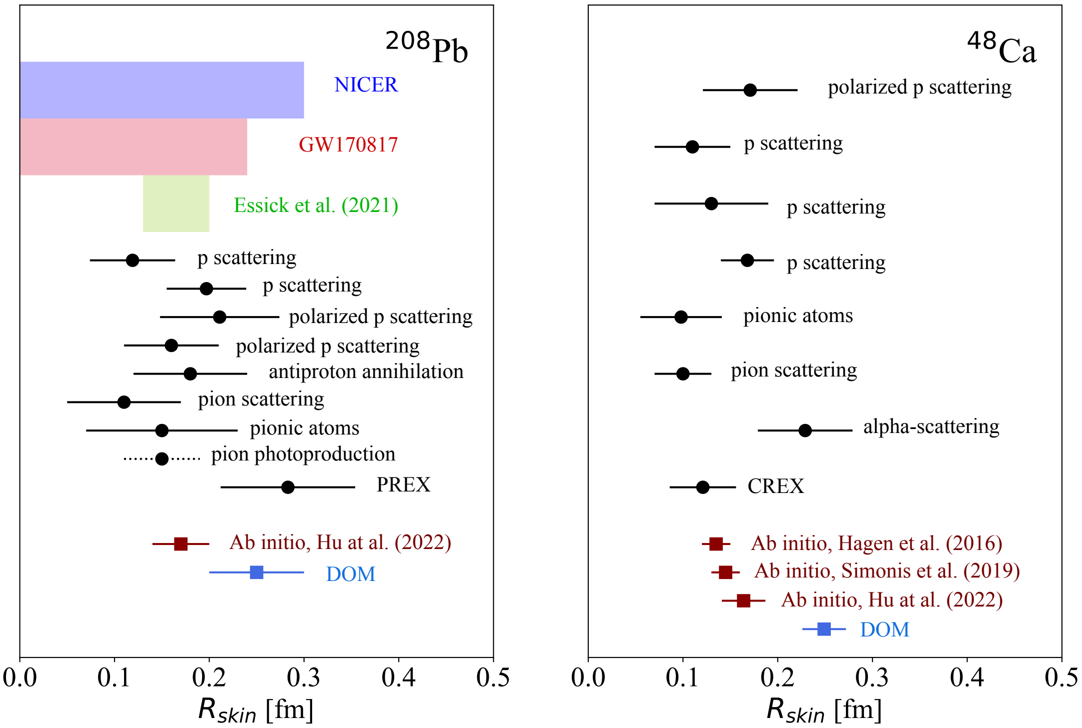

Figure 2.6: Experimental determinations of the neutron skin thickness of ^{208}Pb (left panel) and ^{48}Ca (right panel) in black, in comparison to ab initio [30,47,77] and dispersive optical model [78,79] calculations, in red and blue respectively. Experimental data are taken from Table 4 of Ref. [81] for ^{208}Pb and Table 5 of Ref. [81] for ^{48}Ca. See Ref. [81] and references therein for details on the experiments. The coherent pion photoproduction experiment of Ref. [82] is indicated with a dotted line, as Ref. [83] casts doubts on the sensitivity of this probe to the neutron distribution. For ^{208}Pb, constraints given by the detection of the gravitational wave GW170817 [80] and the joint mass-radius NICER measurements [27] are also reported, together with the value inferred by Essick et al. [28].

In the case of ^{48}Ca, the CREX measurement, on the small side with respect to the other experimental determinations, is in excellent agreement with ab initio calculations from Refs. [30,47,77], while the DOM analysis overshoots the data. Passing to ^{208}Pb, the PREX result is more than one standard deviation larger than the average of previous ^{208}Pb skin measurements [81]. There exist a mild tension (at the 1.5σ level) between PREX and the ab initio result of Ref. [30], yielding $0.139 < R_{skin} < 0.200$ fm. Also Essick et al. [28] favour slightly smaller values of R_{skin}. The DOM prediction, delivering instead high values for the skin, is in accordance with PREX. Also the upper bounds obtained from the NICER measurement and from GW180817 turn out to be consistent with PVES measurements.

Let us now consider the implications of these measurements on the EOS. The CREX experiment, suggesting a small R_{skin} in ^{48}Ca, favours a corresponding small value of the slope parameter L and a softer equation of state, while the PREX determination moves in the opposite direction, implying a stiffer EOS. In particular, when taken individually, PREX leads to $L = 106 \pm 37$ MeV [27], while CREX to $L = -5 \pm 40$ MeV [81].

In a recent review by Lattimer [81], two different strategies to reconcile the PREX and CREX constraints are considered. In the first case, a weighted average of all the measurements of R_{skin} in ^{48}Ca and ^{208}Pb is calculated. Subsequent comparison to theoretical models suggest a final constraint of 40 ± 8 MeV on the slope parameter. In the second case, the analysis is instead restricted only to the PREX and CREX results, obtaining a slope parameter of 50 ± 12 MeV. The two strategies considered in Ref. [81] lead also to constraints on the value of J, amounting to 30.8 ± 1.5 MeV in the first case and 32 ± 2 MeV in the second case.

The second strategy considered in Ref. [81] agrees with earlier microscopic nuclear matter calculations by Drischler et al. [84]. There, combining an accurate many-body framework, chiral effective field theory interactions and Bayesian techniques for uncertainty quantification, J and L were constrained to the 1-sigma intervals:

$$J = 31.70 \pm 1.11 \text{ MeV}, \quad L = 59.80 \pm 4.12 \text{ MeV}. \tag{2.10}$$

Later, employing Gaussian processes to constrain the EOS from observational data and nuclear matter calculations in chiral effective field theory, Essick et al. [28] reported larger ranges of J and L:

$$J = 33^{+2.0}_{-1.8} \text{ MeV}, \quad L = 53^{+14}_{-15} \text{ MeV}, \tag{2.11}$$

consistent with both Lattimer [81] and Drischler et al. [67]. Moreover, as shown in Figure 2.5, it is worth pointing out that ab initio predictions of the neutron skin of ^{48}Ca and ^{208}Pb in Hu et al. [30] are accompanied by estimates of nuclear matter parameters, obtained consistently within the same many-body method used for finite nuclei properties. There, Bayesian history matching was used to calibrate a new ensemble of “non-implausible” chiral EFT interactions. Via nuclear matter calculations, the latter led to the 68% credible intervals:

$$29.1 \leq J \leq 33.2 \text{ MeV}, \quad 38.3 \leq L \leq 68.5 \text{ MeV}. \tag{2.12}$$

This result agrees with both the ranges identified by Ref. [81], as well as being in accordance with Refs. [28, 84]. In Ref. [30], it is also observed that higher values of R_{skin} (and consequently of L), in agreement with PREX, can be obtained in their ab initio framework only at the cost of degrading the description of nucleon-nucleon scattering data at low energy.

With the goal of removing model assumptions in the analysis of the PREX and CREX experimental results, Refs. [29, 85] consider directly the parity-violating asymmetry A_{PV} in ^{48}Ca and ^{208}Pb instead of the corresponding R_{skin}. Within EDF theory, they showed that the PREX and CREX A_{PV} results cannot be simultaneously reproduced within one standard deviation by EDF models ensuring a good description of bulk properties of nuclei across the nuclear chart [29]. In Ref. [31], new functionals, accomodating constraints coming from PREX and CREX, are proposed. They yield stiff equations of state, which however fail to reproduce the mass-radius constraints provided by NICER.

The debate on the PREX and CREX experiments and their implications is still ongoing. In this regard, the planned Mainz Radius EXperiment (MREX) [75] at the Mainz Energy-recovering Superconducting Accelerator (MESA) under construction in Mainz, Germany will play a key role, as it is foreseen to further cut down the uncertainty budget on the PVES measurement of the skin of ^{208}Pb.

2.4.2 Electric dipole polarizability

One could also adopt a different strategy and look for other observables which provide information on the symmetry energy parameters. In thermodynamics, the equation of state of an ideal gas can be derived by investigating the behaviour of the system when performing slow variations of macroscopic quantities, as volume, pressure and temperature.

In analogy to that case, the density dependence of the EOS of nuclear matter, determined by J and L, can be investigated in experiments where nuclei are slightly perturbed from their ground state, for instance, by the presence of an external electromagnetic (EM) field. Electromagnetic probes represent a particularly convenient choice: the small value of the electromagnetic coupling constant α ensures the applicability of perturbation theory, allowing for a straightforward connection between theoretical calculations and experimental measurements.

From a quantum-mechanical point of view, the interaction of the nucleus with the EM field is modeled as the absorption of a real photon γ with momentum $\vec{q}$ and energy $\omega = |\vec{q}|$, producing a transition from the ground state of the system $|\Psi_0\rangle$ to a final state $|\Psi_\mu\rangle$. This process is schematically shown in Figure 2.7.

The information about all the possible final states that the nucleus can reach by interacting with γ are encoded in the so-called response function, defined as

$$R(\omega) = \sum_{\mu} \langle\Psi_0|\Theta^\dagger|\Psi_\mu\rangle \langle\Psi_\mu|\Theta|\Psi_0\rangle \, \delta(\omega - E_\mu + E_0), \tag{2.13}$$

where Θ is the electromagnetic operator and E_μ and E_0 are the energies of the ground state and final state μ, respectively. Eq. (2.13) is derived by calculating the differential cross

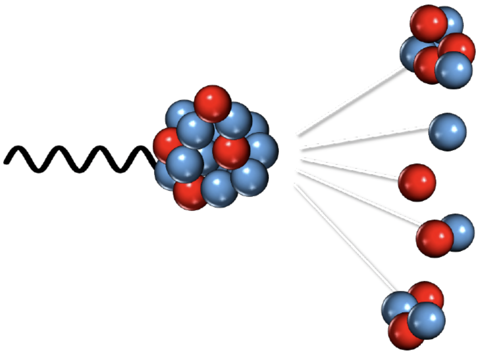

Figure 2.7: Schematic representation of the interaction between the nucleus and a photon. Figure taken from Ref. [86].

section of the process depicted in Figure 2.7, which depends on the transition matrix element of the interaction Hamiltonian

$$H_{int} = \int d\vec{x}\ \vec{A}(x)\cdot\vec{J}(x), \tag{2.14}$$

involving the photon field $\vec{A}(x)$ and the nuclear current $\vec{J}(x)$, with $x = (t, \vec{x})$. A complete derivation can be found in Ref. [86]. Here, we will focus on a particular class of EM transitions, driven by the electric dipole operator

$$\Theta = e\sqrt{\frac{4\pi}{3}}\sum_{i=1}^{A} r_i\, Y_{10}(\hat{r}_i)\left(\frac{1+\tau_i^z}{2}\right), \tag{2.15}$$

where e is the electric charge, $r_i = |\vec{R}_i - \vec{R}_{\mathrm{CM}}|$ is defined in terms of the difference between the position of the i-th nucleon $\vec{R}_i$ and the one of the center of mass $\vec{R}_{\mathrm{CM}}$, $Y_{10}(\hat{r}_i)$ is the spherical harmonics with rank 1 and projection 0 and τ_i^z is the isospin z-axis projection of the i-th nucleon.

The typical behaviour of electric dipole (or E1) response functions is illustrated in Figure 2.8. Low photon energies excite the nucleus to discrete excited bound states. When instead the energy of the photon overcomes the break-up threshold (i.e. the energy needed to remove a nucleon from the nucleus), the system populates continuum states. Here, the response is characterized by broad resonances: the pygmy dipole resonance, appearing in the presence of a large neutron excess, and the giant dipole resonance at higher energies. The latter are traditionally associated to collective excitations of the nucleus [87].

Also sum rules, defined as the energy moments of the response function distribution, provide substantial insight into the dynamics of a quantum system. Among them, the electric dipole polarizability α_D stands out as a noteworthy example. Classically, it corresponds to the proportionality constant characterizing the induced electric dipole moment $\vec{d}$ acquired by a charge distribution in an external electric field $\vec{E}$: $\vec{d} = \alpha_D\vec{E}$. In quantum mechanics,

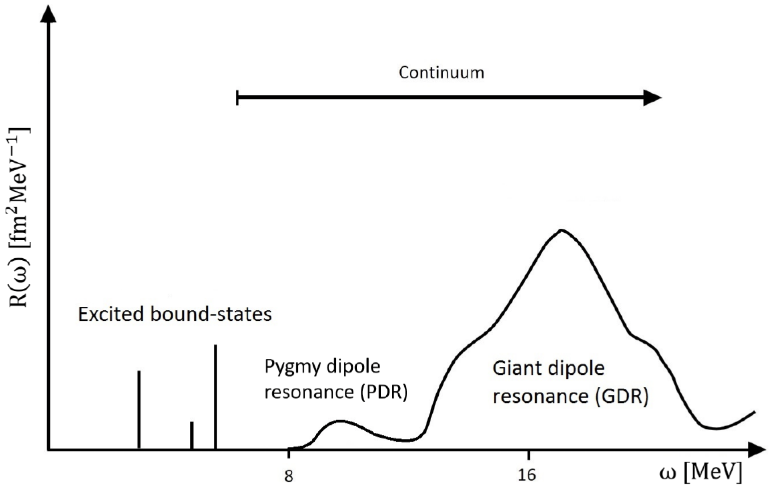

Figure 2.8: Schematic representation of the electric dipole response function of a nucleus. Figure taken from Ref. [86].

α_D is defined as an inverse energy-weighted sum rule of the dipole response function

$$\alpha_D = 2\alpha \int_0^\infty d\omega \frac{R(\omega)}{\omega}. \tag{2.16}$$

In the past, the dipole polarizability of stable nuclei has been extracted from measurements of photoabsorption cross sections [88], focusing in the region of the giant dipole resonance. In the last few years, proton inelastic scattering (p, p') at very forward angles [89] has been established as a solid experimental technique providing access to α_D with good resolution and over a wide excitation energy range (see, e.g., Refs. [5, 48, 90, 91]). Moreover, Coulomb excitation measurements in inverse kinematics made it possible to study α_D in unstable nuclei as ^{68}Ni [92] and ^{6,8}He [93, 94].

The interest around the electric dipole polarizability has risen since evidences of a correlation between α_D and the neutron skin R_{skin} have been observed. As in turn R_{skin} is correlated to the slope parameter L, a consequent correlation between α_D and L could be envisioned. The first steps in this direction have been made in the framework of energy density functional theory. In Ref. [95], a covariance analysis based on EDF calculations found evidences of a correlation between α_D and R_{skin} in the case of ^{208}Pb. The result of Ref. [95] was subsquently employed in Ref. [90] to infer the neutron skin of ^{208}Pb from a new measurement of α_D via inelastic proton scattering. The experimental value of α_D, equal to 20.1 ± 0.6 fm^3, was then translated into an R_{skin} estimate of $0.156^{+0.025}_{-0.021}$ fm. It is worth noticing that this result is almost 50% smaller than the PREX central value, but in agreement with the ab initio calculation of Ref. [30] and the value inferred by Ref. [28]. Later, in Ref. [76], it was pointed out that while the correlation between α_D and R_{skin} emerges in individual families of EDFs, the same linear dependence becomes less clean when combining a host of different EDF models.

A year later, on the basis of calculations of finite nuclei and EOS properties, employing different sets of relativistic and non-relativistic EDFs, Roca-Maza et al. [32] proved the presence of a correlation between the product of α_D and the symmetry energy at saturation J, $\alpha_D J$, and R_{skin} for ^{208}Pb. Via the product $\alpha_D J$, also the dipole polarizability could then be used to constrain L. The correlation between $\alpha_D J$ and L in ^{208}Pb found in Ref. [32] is represented in Figure 2.9. The latter features also more recent ab initio results from Ref. [30], which confirm the presence of a correlation between $\alpha_D J$ and L.

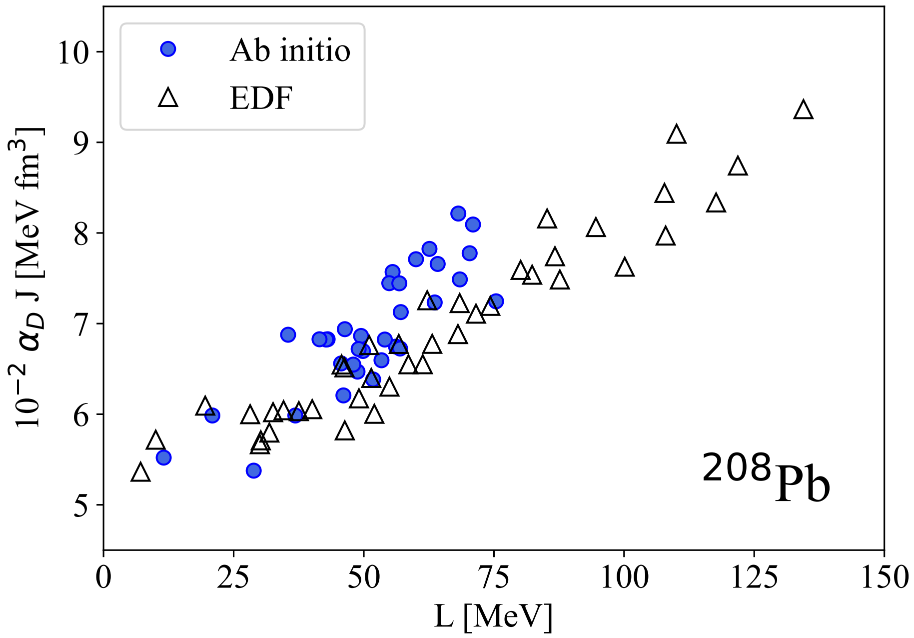

Figure 2.9: Correlation between the product $\alpha_D J$ between the electric dipole polarizability and the symmetry energy at saturation density and the slope parameter L, as described by the ab initio calculation of Ref. [30] and by the EDF calculations from Ref. [32].

In Ref. [32], the correlation between $\alpha_D J$ and R_{skin} is corroborated by a reference to the so-called droplet model [96]. The latter consists in a refinement of the liquid drop model, from which the well-known von Weizsäcker formula describing the evolution of the binding energy per nucleon as a function of the number of nucleons A is derived. Within the droplet model, α_D scales with A as [97]

$$\alpha_D^{\mathrm{DM}} \propto \frac{A\,\langle R_m^2\rangle}{48J}\left(1+\frac{5}{3}\frac{9J}{4Q}A^{-1/3}\right), \tag{2.17}$$

where $R_m = \langle R_m^2\rangle^{1/2}$ is the matter radius of the nucleus and Q is the surface stiffness coefficient, quantifying the resistance of neutrons against being separated by protons [96]. In Ref. [32], it is shown that Eq. (2.17) can be expressed in terms of the neutron skin thickness

R_{skin}^{DM} in the droplet model as

$$\alpha_D^{\mathrm{DM}} \propto \frac{A\,\langle R_m^2 \rangle}{48J}\left(1+\frac{5}{2}\frac{R_{skin}^{\mathrm{DM}}A}{R_m(N-Z)}\right), \tag{2.18}$$

which indicates that the product $\alpha_D J$, instead of α_D alone, correlates with R_{skin}, and therefore L. So an experimental value of α_D can be exploited to get a direct relation between J and L. In Ref. [32], combining the experimental determination of α_D in ^{208}Pb [90] with a realistic value of $J = 32 \pm 2$ MeV [98] led to $R_{skin}(^{208}\mathrm{Pb}) = 0.165 \pm 0.043$ fm^3 and $L = 43 \pm 26$ MeV. This value of R_{skin} is consistent with the estimate of Refs. [28, 90], as well as with the ab initio calculations of Ref. [30], while lying below the PREX result.

In Ref. [99], Roca-Maza et al. expand their previous analysis [32] including also new experimental data for the polarizability of ^{68}Ni [92] and ^{120}Sn [91]. Combining the experimental values of ^{208}Pb, ^{120}Sn and ^{68}Ni with microscopic calculations using different EDFs, they extracted the relations between J and L illustrated in Figure 2.10. The bands obtained by using the experimental data of ^{208}Pb, ^{120}Sn and ^{68}Ni in the $\alpha_D J - L$ correlation show a substantial overlap between each other. By considering only the EDFs reproducing experiment for all the three nuclei, the following ranges of J and L are deduced:

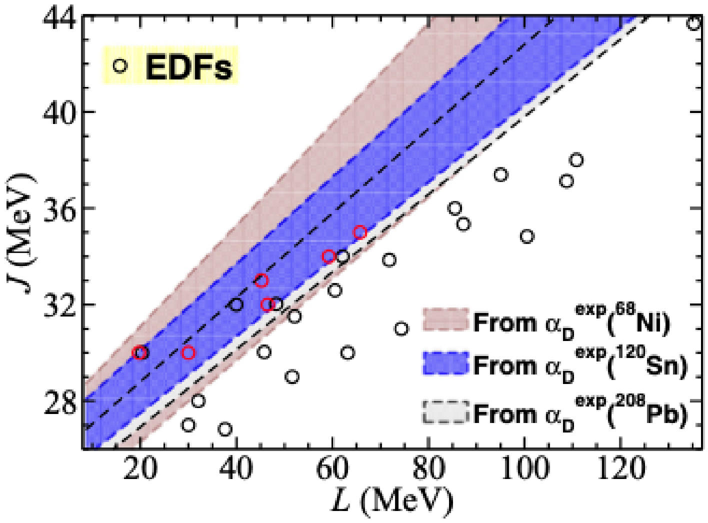

Figure 2.10: Correlation between the slope parameter and the symmetry energy at saturation density obtained from combining the experimental values of the polarizability of ^{208}Pb, ^{120}Sn and ^{68}Ni with EDF calculations. Red circles represent EDFs reproducing the experimental value for α_D for the three nuclei under consideration. Figure taken from Ref. [99].

$$30 \leq J \leq 35 \text{ MeV}, \qquad 20 \leq L \leq 66 \text{ MeV}. \tag{2.19}$$

These ranges are consistent with the constraints of Essick et al. [28] (Eq. (2.11)), as well as with the nuclear matter calculations of Drischler et al. [84] (Eq. (2.10)), and of Hu at al. [30] (Eq. (2.12)). Constraints coming from the polarizability are then indicating a slightly softer EOS with respect to PREX. By incorporating PREX information into the fitting of EDFs, Ref. [100] infers systematically higher values of α_D with respect to experiment. Also here, the debate is still open.

In parallel, in recent years, new developments in ab initio nuclear theory have made calculations of observables like α_D possible also in the medium-mass region of the nuclear chart. As mentioned in Chapter 1, computing α_D is far more arduous than in the case of R_{skin}. In fact, as shown in Eq. (2.16), α_D depends on the response function $R(\omega)$, which depends on both the bound and continuum nuclear spectra (see Eq. (2.13)). Combining the Lorentz Integral Transform (LIT) [43], a few-body technique allowing a correct treatment of continuum states, with the mild computational scaling of Coupled-Cluster (CC) theory [39] into the so-called LIT-CC method [44, 45] has enabled first ab initio calculations of α_D for medium-mass nuclei thus far closed-shell.

After testing the method on ^{4}He, ^{16}O and ^{22}O, obtaining good agreement with available data [46], LIT-CC calculations of the dipole polarizability of ^{48}Ca, obtained employing different chiral EFT models, accompanied the first ab initio estimate of the neutron skin of this nucleus [47]. In Ref. [48], these predictions for α_D were then compared to a new experimental determination, based on (p, p') measurements, and to EDF results. Later, augmenting the accuracy of the LIT-CC method, more precise estimates of α_D in ^{48}Ca were provided in Refs. [77, 101]. In Figure 2.11, we show the latest LIT-CC predictions of α_D for ^{48}Ca [77, 101], using different chiral forces [68, 102], in comparison to the experimental value of Ref. [48] and the ranges obtained using different EDF families in Refs. [76, 99]. The α_D result of Hagen et al. [47] is also reported.

In general, we observe an excellent agreement between ab initio predictions, EDF theory and experiment. Comparing the latest LIT-CC predictions with the corresponding result in Hagen et al. [47], we can appreciate how increasing the precision of the many-body method improves the overlap with experiment. These updated results also indicate a slightly smaller α_D with respect to EDF calculations. Ab initio predictions are able to reproduce well both the neutron skin from CREX and the polarizability of ^{48}Ca from Ref. [48], supporting the constraints on symmetry energy parameters given by the interactions used in these works. Via nuclear matter calculations, the nuclear force models used in Figure 2.11 suggest [47, 103][1]

$$27 \leq J \leq 33 \text{ MeV}, \quad 44 \leq L \leq 49 \text{ MeV}. \tag{2.20}$$

These ranges are in agreement with the ones obtained by Essick et al. [28] (Eq. (2.11)), Hu et al. [30] (Eq. (2.12)) and Lattimer [81]. Moreover, while the J constraint of Eq. (2.20) overlaps with the nuclear matter prediction of Drischler et al. [84] in Eq. (2.10), L turns out to be smaller than predicted by [84].

Later, the LIT-CC method was employed to tackle the unstable neutron-rich nucleus

---

[1] The slope parameter range has been updated with respect to Ref. [47] due to an error reported in nuclear matter calculations with the NNLO$_{\text{sat}}$ interaction [103]. The corresponding J range remains unaffected.

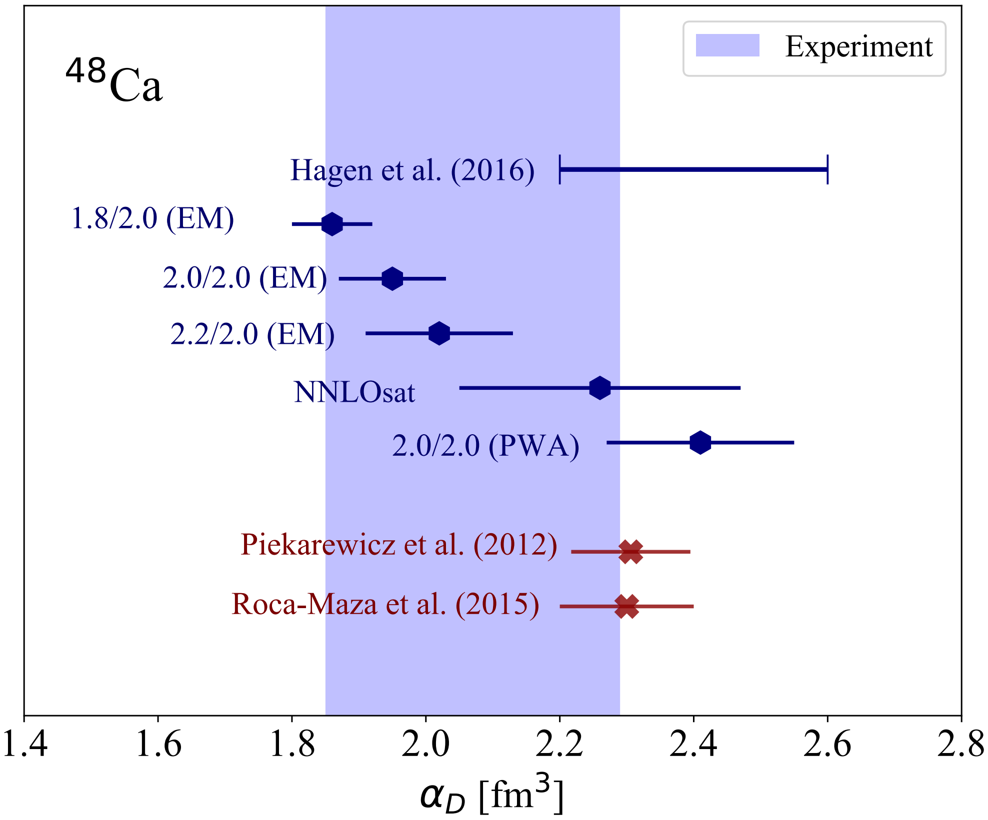

Figure 2.11: Experimental value of the dipole polarizability of ^{48}Ca [48] (blue band) in comparison with the LIT-CC predictions of Refs. [77, 101] obtained using the family of chiral interactions of Ref. [68] and the chiral force NNLO$_{\text{sat}}$ [102] (dark blue hexagons). Ranges obtained from different families of EDFs in Refs. [76, 99] (red cross marks) and the previous α_D result of Hagen et al. [47] are also included.

^{68}Ni [49]. In that work it was observed that predictions with different chiral forces describe a linear correlation between the dipole polarizability and the charge radius, which nicely overlaps with the experimental values of both observables. The CC calculations of Ref. [49] constrains the neutron skin of ^{68}Ni in the range $0.18-0.20$ fm, which is in agreement with the EDF analysis of Roca-Maza et al. [99].

More recently, the dipole polarizability of ^{208}Pb has been computed for the first time from an ab initio perspective, as shown in Figure 2.9. The non-implausible chiral interactions selected in Ref. [30] predict $\alpha_D = 22.6^{+2.6}_{-1.8}$ fm^3, which is in agreement with the experimental value of Ref. [90]. In this case, a different ab initio approach, the IMSRG [40], has been employed.

As mentioned in Chapter 1, together with these promising benchmarks with theory, the connection between α_D and the symmetry energy parameters is driving experimental investigations of this observable in regions of the nuclear chart where it has not been mapped yet [50, 51]. These experimental efforts motivate the work presented in this thesis, which extends the reach of ab initio calculations of α_D, as shown in Chapter 6.

2.5 Constraints on the incompressibility of nuclear matter from isoscalar monopole resonances

Electromagnetic observables are key also in the study of other ingredients of the nuclear EOS. Here, we focus on the incompressibility K_0, which determines the curvature of symmetric nuclear matter at saturation (see Eq. (2.6)). It has been shown that this parameter can be constrained by looking at isoscalar monopole (or E0) transitions in finite nuclei [33]. Such transitions are driven by the operator

$$\Theta = \frac{1}{2}\sum_{i=1}^{A} r_i^2, \tag{2.21}$$

where we use the notation of Eq. (2.15).

First measurements of isoscalar monopole responses in the 1970s [104] have shown that the E0 strength is typically dominated by a broad peak, known as isoscalar giant monopole resonance (ISGMR), interpreted as a nuclear ”breathing” mode. As an example, in Figure 2.12, we show the experimental isoscalar monopole strength of nuclei with $A \simeq 90$ from Ref. [105], where we see the emergence of the ISGMR between 15 and 20 MeV of excitation energy.

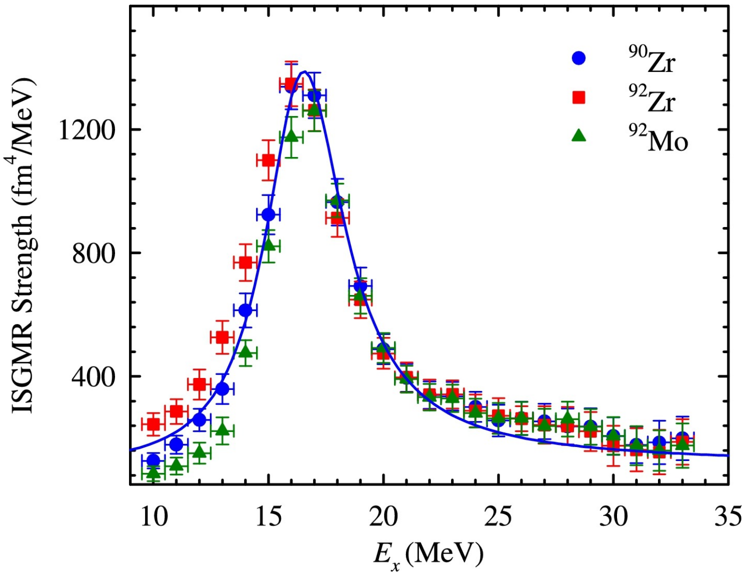

Figure 2.12: Experimental data for the isoscalar monopole response of ^{90,92}Zr and ^{92}Mo. The solid blue line is a Lorentzian fit for ^{90}Zr. Figure taken from Ref. [105].

In 1980, Blaizot [33] established a relation between the mean energy of the ISGMR,

E_{ISGMR} and the incompressibility of nuclear matter. According to Ref. [33], the incompressibility of a A-body nucleus can be defined as

$$K_A = \frac{M}{\hbar^2} \langle R_m^2 \rangle E_{\mathrm{ISGMR}}^2, \tag{2.22}$$

where M is the nucleon mass and R_m is the rms matter radius of the nucleus. In analogy to the case of the liquid drop formula for the binding energy per nucleon, we can perform a leptodermous expansion of K_A [33, 106]

$$K_A = K_{vol} + K_{surf} A^{-1/3} + K_{Coul} Z^2 A^{-4/3} + K_\tau \frac{(N-Z)^2}{A^2}, \tag{2.23}$$

where K_{vol}, K_{surf}, K_{Coul}, K_τ are the volume, surface, Coulomb and isospin coefficients, respectively. Taking the $A \to \infty$ limit of this formula suggests that the volume term K_{vol} can be interpreted as the incompressibility of nuclear matter K_0. Therefore, assuming $K_{vol} = K_0$, a sufficient number of experimental data or theoretical calculations of E_{ISGMR} can be fitted to Eq. (2.23), allowing for an extraction of K_0.

Calculating the mean energy E_{ISGMR} becomes then a crucial part of the game. In this regard, different strategies to estimate E_{ISGMR} can be adopted [107]. In fact, the mean energy E_{ISGMR} can be calculated as

$$E_{\mathrm{ISGMR}} = \frac{m_1}{m_0}, \tag{2.24}$$

or

$$E_{\mathrm{ISGMR}}^{(k)} = \sqrt{\frac{m_k}{m_{k-2}}}, \tag{2.25}$$

where m_k are energy moments of the monopole response

$$m_k = \int d\omega \omega^k R(\omega). \tag{2.26}$$

However, if the strength of the resonance is mostly concentrated in a narrow energy region (as in the cases that will be considered in this thesis), the different estimates of the mean energy give similar results [107]. Therefore in our calculations we choose to focus on the so-called constrained energy, which is defined putting $k = 1$ in Eq. (2.25)

$$E_{\mathrm{ISGMR}}^{(1)} \equiv E_{\mathrm{ISGMR}} = \sqrt{\frac{m_1}{m_{-1}}}. \tag{2.27}$$

At present, large uncertainties characterize the value of K_0 [35, 106]. In Shlomo et al. [108], the available experimental data on the ISGMR were compared to EDF calculations. By selecting the EDFs able to reproduce experimental values of E_{ISGMR}, the range 240 ± 20 MeV for the incompressibility of nuclear matter was identified. Later, Eq. (2.23) was employed explicitly by Stone et al. [107] to extract the incompressibility parameters from experimental determinations of E_{ISGMR}. The latter study reproduces the constraint of Shlomo et al. [108] applying the condition $c = K_{surf}/K_{vol} = -1$, which is compatible with most EDFs. However, if the value of c is allowed to vary, the analysis of Stone et al. [107] delivers a much higher estimate of K_0 with respect to Shlomo et al. [108], amounting to $250 < K_0 < 315$ MeV. In Hu et al. [30], CC nuclear matter calculations, based on a set of non-implausible chiral interactions, predict $242 \leq K_0 \leq 331$ MeV, in agreement with both the estimates of Refs. [107, 108].

Being derived within the liquid drop model, a very approximate description of the nucleus, Eq. (2.23) is to be taken with caution. It is anyway useful, within the same interaction model, to compare estimates of K_0 obtained from calculations in nuclear matter and finite nuclei [106]. Some very recent ab initio works, building on the symmetry-adapted no-core shell model (SA-NCSM) [109] and the projected generator coordinate method (PGCM) [110] are moving in this direction.

Motivated by the need of more precise constraints on K_0 and by the recent theoretical interest, we will focus on this problem at the end of Chapter 6.

3 Nuclear forces in Chiral Effective Field Theory

As shown in the previous Chapter, the study of finite nuclei and their electromagnetic properties gives rise to key scientific connections between physics phenomena at microscopic and macroscopic scales. To analyse such connections, in this thesis we seek for systematic predictions of electromagnetic observables across the nuclear chart within an ab initio framework. In an ab initio calculation, the nonrelativistic Schrödinger equation for A interacting nucleons is solved, starting from two ingredients: the interaction among the constituent protons and neutrons, and a suitable many-body solver. The latter provides virtually exact solutions or it comes with controlled approximations, allowing for a reliable estimate of theoretical uncertainties.

Here, we focus on the first ingredient of the ab initio recipe, concerning how to model the nuclear force. In this regard, one cannot ignore that nucleons are compound objects, made by quarks, fundamental particles with spin 1/2. Quantum Chromodynamics (QCD) is the fundamental theory describing their strong interactions, mediated by gluons [111]. At high energy, QCD is asymptotically free: its coupling constant approaches zero, making the theory perturbative in this regime [112, 113]. At low energy, instead, it rapidly increases, confining quarks into colorless objects, as mesons and baryons [114]. A direct derivation of nuclear forces from QCD is then hindered by the large value of the coupling constant at the low energies relevant for nuclear physics, making pertubation theory not applicable in this regime. Direct solutions of nuclear theory problems in QCD are anyway an active line of research. Lattice QCD calculations, for example, achieve this via a discretization of spacetime on a four-dimensional grid [115]. However, the predictive power of such approaches is currently restricted to single mesons, baryons and few-nucleon systems [116, 117] due to their huge computational cost.

The seminal work of Weinberg in the 1990s [118–120] suggested to employ a low-energy effective field theory for QCD in order to tame these problems. In the presence of a separation of scales, effective field theories give a detailed description of the low-energy/long-range physics while high-energy/short-range modes are suppressed. Information on the high-energy dynamics is carried by low-energy constants (LECs), which can be fitted to experimental data or deduced from a more fundamental theory. In Ref. [121], the different steps leading to a nuclear EFT are summarized as follows:

1. Identify the separation of scales at the basis of the EFT and the appropriate degrees of freedom for low-energy nuclear theory.

2. Consider the QCD Lagrangian and identify relevant symmetries of the theory.
3. Write the most general Lagrangian fulfilling those symmetries and possible symmetry breakings.
4. Define the relative importance of each contribution in a low-momentum expansion, applying a suitable organizational scheme ("power counting").
5. Calculate the Feynman diagrams of the theory up to the desired precision.

This procedure led to the development of nuclear interactions based on chiral EFT [121–123], a low-energy effective field theory for QCD, retaining the symmetries of the underlying theory. Today, chiral EFT represents the foundation of the most widely adopted family of nuclear Hamiltonians.

In this Chapter, we will mainly follow Refs. [121, 124]. As the work presented in this thesis does not concern the development of nuclear interactions, we will only outline the main aspects of the topic. In Section 3.1, we will elaborate on the separation of scales at the heart of effective field theories, and its application to nuclear physics. In Section 3.2, we will review the concept of chiral symmetry and its importance in the formulation of chiral effective Lagrangians. In Section 3.3 we will review the construction of chiral EFT interactions, and provide a description of the nuclear force models used to obtain the results of this thesis in Chapter 6.

3.1 Separation of scales

Effective field theories are based on the presence of a separation of scales, represented by an energy gap between a soft scale Q and an hard scale Λ, with $Q \ll \Lambda$. The soft scale is the typical energy scale of the physics phenomena that the EFT aims to describe, while the hard scale identifies the physics regimes not explicitly resolved by the theory. Once Q and Λ are defined, the EFT can be formulated in terms of an order-by-order expansion in Q/Λ, where contributions proportional to $(Q/\Lambda)^\nu$ enter at order ν.

A typical example of this approach concerns the derivation of the Coulomb potential generated by an extended charge distribution at large distances [125]. In this limit, the exact electrostatic potential, accessible only if the charge distribution is known, can be approximated by an expansion in different multipole orders (the well-known multipole expansion). Going to higher orders increase the precision of the expansion, which can be truncated once the desired accuracy is reached.

Let us now consider the case of low-energy nuclear physics. The hadron spectrum clearly shows a separation of scales between the mass of the pions, $M_\pi = 140$ MeV, and the mass of the next heavier mesons, ρ, with $M_\rho = 770$ MeV, and ω, with $M_\omega = 782$ MeV. We can then naturally identify the soft scale of the theory with Q of the order of M_π and the hard one with $\Lambda \approx M_\rho$. An EFT framework based on a low-momentum expansion in powers of Q/Λ is suitable to describe most nuclear phenomena, as their typical energy is much smaller than the mass difference between pions and ρ mesons. In chiral EFT, nucleons and pions are the relevant degrees of freedom. Other choices are possible, e.g., for phenomena below M_π scale, pionless EFT, with only nucleons as building blocks, can be considered (see Ref. [123] and references therein). In this work, we will only focus on applications of chiral EFT.

3.2 Chiral symmetry

Once the separation of scales and the effective degrees of freedom are identified, the symmetries of the underlying theory, QCD, relevant at the low energies involved in nuclear phenomena, need to be investigated. We begin by looking at the QCD Lagrangian, which in Einstein's notation is given by

$$\mathscr{L}_{QCD} = \bar{q}(i\gamma^\mu \mathscr{D}_\mu - \mathscr{M})q - \frac{1}{4}\mathscr{G}^a_{\mu\nu}\mathscr{G}^{\mu\nu}_a, \tag{3.1}$$

where q and $\bar{q}$ correspond to the quark fields, and $\mathscr{M}$ to the quark mass matrix. Moreover, we can write the covariant derivative as

$$\mathscr{D}_\mu = \partial_\mu - ig\frac{\lambda_a}{2}\mathscr{A}^a_\mu, \tag{3.2}$$

and the gluon field strength tensor as

$$\mathscr{G}^a_{\mu\nu} = \partial_\mu \mathscr{A}^a_\nu - \partial_\nu \mathscr{A}^a_\mu + g f_{abc}\mathscr{A}^b_\mu \mathscr{A}^c_\nu. \tag{3.3}$$

In the above equations g indicates the strong coupling constant and $\mathscr{A}^a_\mu$ the gluon fields. λ_a are the Gell-Mann matrices and f_{abc} the structure constants of the $SU(3)_{color}$ Lie algebra. The last term of Eq. (3.3) reveals one of the most interesting properties of QCD: being a gluon-gluon interaction vertex, it leads to gluon self-interactions in the Lagrangian.

The sum in Eq. (3.1) runs in general over all quark flavours u, d, s, c, b and t. As in the low-energy regime of QCD only up and down quarks are relevant, we restrict the sum to u and d in the following. Their masses, given by [126]

$$m_u \approx 2\,\text{MeV}, \quad m_d \approx 5\,\text{MeV}, \tag{3.4}$$

are negligible with respect to the typical energies of hadronic phenomena, of the order of 1 GeV. Therefore, it is instructive to consider the QCD Lagrangian of Eq. (3.1) in the limit $\mathscr{M} \approx 0$. By rewriting the quark fields in terms of right-handed and left-handed spinors

$$\begin{aligned} q_R &= \frac{1}{2}(1+\gamma_5)q, \\ q_L &= \frac{1}{2}(1-\gamma_5)q, \end{aligned} \tag{3.5}$$

the Lagrangian becomes

$$\mathscr{L}^0_{QCD} = \sum_{j=R,L} \bar{q}_j i\gamma^\mu \mathscr{D}_\mu q_j - \frac{1}{4}\mathscr{G}^a_{\mu\nu}\mathscr{G}^{\mu\nu}_a . \tag{3.6}$$

It is possible to show that $\mathscr{L}^0_{QCD}$ is invariant under a global unitary transformation of the spinors

$$\begin{aligned} q_R &= \begin{pmatrix} u_R \\ d_R \end{pmatrix} \rightarrow e^{-i\Theta^R_i \tau_i/2} \begin{pmatrix} u_R \\ d_R \end{pmatrix} , \\ q_L &= \begin{pmatrix} u_L \\ d_L \end{pmatrix} \rightarrow e^{-i\Theta^L_i \tau_i/2} \begin{pmatrix} u_L \\ d_L \end{pmatrix} , \end{aligned} \tag{3.7}$$

where τ_i $(i = 1,2,3)$ are Pauli spin matrices. The fact that under the transformation of Eq. (3.7) right- and left-handed quarks conserve their helicity and do not mix is at the core of chiral symmetry.

In QCD, chiral symmetry is both spontaneously and explicitly broken [127]. A symmetry is spontaneously broken if it is present in the Lagrangian but not in its ground state. An exact chiral symmetry in QCD would imply the appearance of degenerate parity doublets, i.e. states with identical quantum numbers and masses, but opposite parity. However, while the 1^+ ρ meson has a mass of around 770 MeV, the 1^- a_1 pseudovector meson is characterized by a much higher mass of around 1230 MeV, resulting from a spontaneously broken chiral symmetry. According to Goldstone's theorem, a spontaneously broken symmetry leads to the emergence of massless Goldstone bosons in the theory. However, chiral symmetry is also explicitly broken, as the mass term in Eq. (3.1) is not exactly 0. For this reason the Goldstone bosons of the theory acquire a mass, and they can be identified with pions. Their lighter mass with respect to the other hadrons can be traced back to the fact that pions reflect both the spontaneous and explicit breaking of chiral symmetry in QCD.

3.3 Building chiral effective field theory interactions

Considering nucleons and pions as effective degrees of freedom, we can now write the most general Lagrangian consistent with chiral symmetry, which represent the foundation of chiral EFT interactions. We obtain [118, 128, 129]

$$\mathscr{L}_{eff} = \mathscr{L}_{\pi\pi} + \mathscr{L}_{\pi N} + \mathscr{L}_{NN} + \ldots , \tag{3.8}$$

where the effective Lagrangian receives contributions from pion-pion ($\pi\pi$), pion-nucleon (πN) and nucleon-nucleon (NN) interactions. Higher-order terms account for interactions between more pionic and nucleonic fields.

Although Eq. (3.8) contains an infinite number of terms, and as a consequence an infinite number of Feynman diagrams should be calculated, employing an expansion of $\mathscr{L}_{eff}$

in terms of $(Q/\Lambda)^\nu$ allows us to systematically organize these terms according to their importance, ensuring that at each order ν a limited number of Feynman diagrams needs to be computed. Such a power-counting scheme allows to establish a hierarchy of nuclear forces, where the significance of each nucleon-nucleon, three-nucleon or many-nucleon contribution arising in the Q/Λ expansion can be easily identified. While the most relevant terms appear at low orders in ν, including higher orders increases the accuracy of the theory.

To determine the order ν of a Feynman diagram, naive dimensional analysis can be applied. In this framework, a nucleon propagator counts as Q^{-1}, a pion propagator as Q^{-2}, each derivative appearing in the Lagrangian is Q and each four-momentum integration Q^4 [121]. Applying some topological identities, one obtains the most frequently used power counting, that is Weinberg's power counting [118, 121]

$$\nu = -2 + 2A - 2C + 2L + \sum_i \Delta_i, \tag{3.9}$$

where A is the number of nucleons, C the number of separately connected pieces and L the number of loops of the diagram. The sum over i runs over all the vertices of the diagram, with Δ_i given by

$$\Delta_i = d_i + \frac{1}{2}n_i - 2, \tag{3.10}$$

where d_i is the number of derivatives or pion-mass insertions and n_i the number of nucleons at the i-th vertex. In this scheme the leading order is determined by $\nu = 0$. Discussions on the correct power counting choice for nuclear forces are ongoing, with some alternative approaches outlined in Refs. [121, 123, 130]. In all the chiral EFT interactions used in this thesis, Weinberg's power counting scheme is employed.

The diagrams contributing to chiral EFT up to order $\nu = 5$ are shown in Figure 3.1. Their analytical expressions can be found in Ref. [121] and references therein. Looking at Figure 3.1, we observe that the diagrammatic contributions to the nuclear force are characterized by two types of interaction vertices: contact interactions between nucleons and vertices denoting a pion-nucleon interaction. Contact interactions capture short-range effects in the nuclear interaction, while pion-nucleon vertices, instead, indicate one and multiple pion-exchange processes, which define the long- and medium-range behaviour of the nuclear force.

At leading order (LO), characterized by $\nu = 0$, one finds a contact term and a one-pion-exchange term. Although this is a rough approximation to the NN force, chiral EFT at LO is already able to capture important features of the deuteron system. For instance, the one-pion-exchange term contains the tensor force, which is essential to give a correct description of the deuteron's quadrupole moment. While all contributions to order $\nu = 1$ vanish due to parity and time-reversal symmetry, at next-to-leading order ($\nu = 2$ or NLO) two-pion-exchange terms, enriching the long- and intermediate-range description of the NN interaction, appear. At next-to-next-to-leading order ($\nu = 3$, N^{2}LO or NNLO) one finds the first contributions to the three-nucleon (3N) force, accounting for medium-range many-body effects. It is worth pointing out how the order-by-order expansion of chiral EFT leads

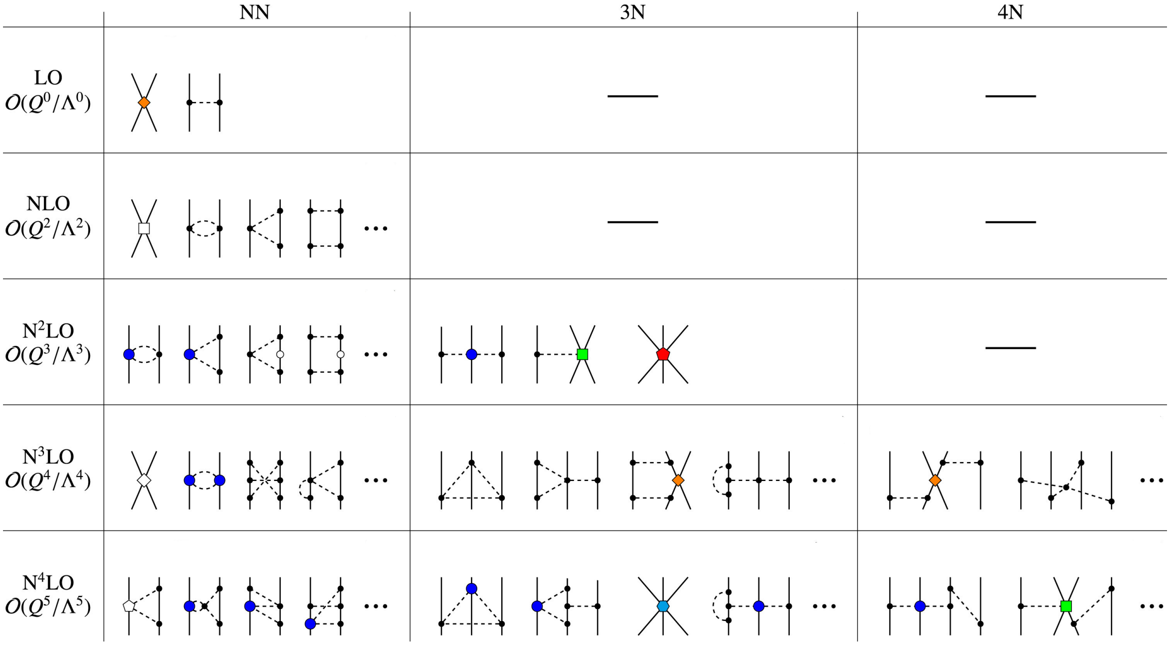

Figure 3.1: Diagrammatic contributions to the nuclear force in Δ-less chiral EFT up to N^4LO in the chiral expansion. NN, 3N and 4N diagrams are distiguished by column. Solid and dashed lines represent nucleons and pions, respectively. Markers (diamonds, squares, circles, pentagons, and hexagons) of different shape are associated to interaction vertices of different orders. White symbols denote LECs entering only the 2N force, while colored symbols appear also in the 3N interaction. Figure adapted from Ref. [124].

to a natural appearance of many-body forces in the theory. Moreover, such an expansion reproduces in a more rigorous framework the empirically known dominance of NN forces with respect to 3N forces. At next-to-next-to-next-to-leading order ($\nu = 4$ or N^3LO) even four-nucleon (4N) forces start to contribute. Currently, NN potentials up to N^4LO [131] and selected N^5LO terms [132] are available, while 3N forces up to N^3LO have been derived [124].

In Figure 3.1 white and colored markers correspond to interaction vertices appearing in the NN or 3N force, respectively, and they are characterized by different low-energy constants (LECs). Currently, LECs are fitted to experimental data, but in principle they should be determined starting from the underlying microscopic theory (see, e.g., Ref. [133] and references therein for recent work in this direction).

Chiral EFT can be reformulated considering the delta isobar Δ(1232) as an explicit degree of freedom of the theory [134–138]. By simply looking at energy scales, this appears to be a sensible choice. Exciting the nucleon to the delta requires $m_\Delta - m_N \approx 293$ MeV, an energy lying well below the hard scale Λ of chiral EFT. Taking explicitly the Δ isobar into account leads to the so-called Δ-full chiral EFT. On top of the diagrams of Figure 3.1, representing the "Δ-less" theory, additional contributions appear in Δ-full theory. They are reported in Figure 3.2. Although the addition of the Δ isobar does not modify the Q/Λ expansion at LO,

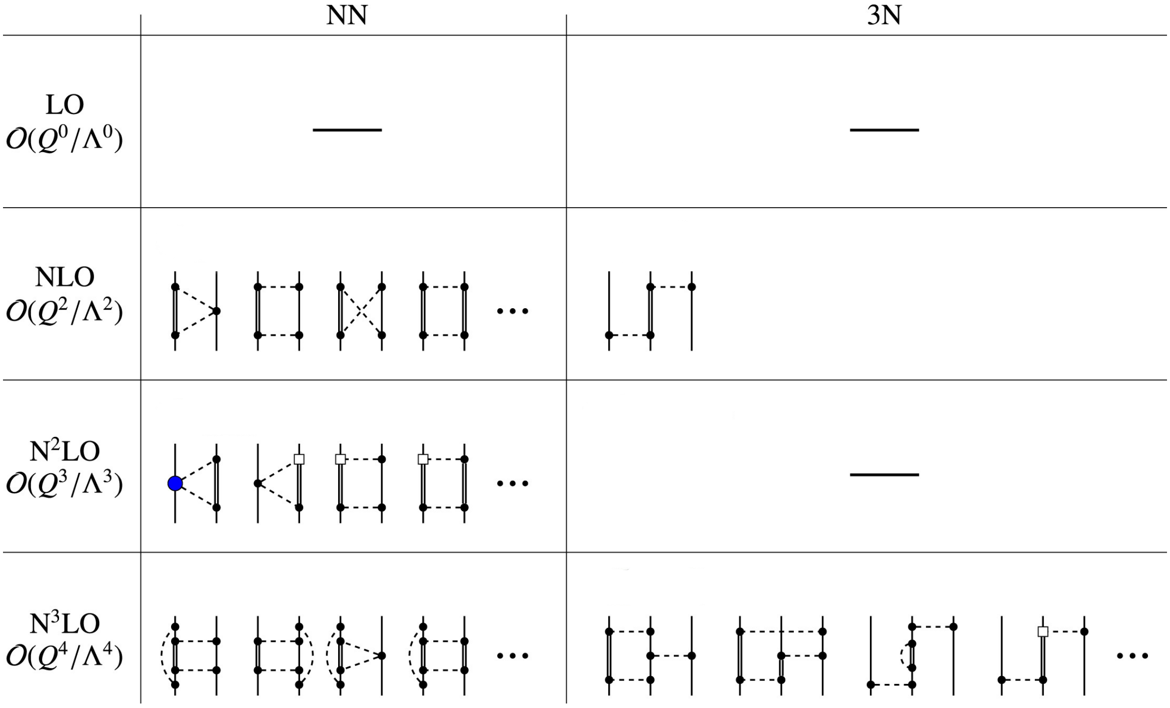

Figure 3.2: Same as Figure 3.1 but for the additional diagrammatic contributions to the nuclear force in Δ-full chiral EFT. Virtual excitations to the Δ isobar are represented by double solid lines. Figure adapted from Ref. [124].

3N forces emerge already at NLO in Δ-full theory. Including the Δ resonance as a degree of freedom in chiral EFT also leads to a reduction in the value of some LECs. The latter are characterized by unnaturally large values in Δ-less theory, reflecting implicit Δ excitation effects [121].

The inherent systematic improvability of chiral EFT, given by its order-by-order expansion, offers a significant benefit: it enables the calculation of nuclear observables with a desired level of precision, while also allowing for the estimation of uncertainties stemming from the neglected higher orders in the chiral expansion. Also electroweak currents can be derived order-by-order in chiral EFT, allowing for a consistent description of structure and electroweak interactions of nuclei within this framework (see Refs. [139, 140] for reviews on the topic).

This thesis is not focused on the development of nuclear forces from chiral EFT, but rather on the use of various families of chiral EFT interactions and on the analysis of the results obtained with these Hamiltonians for light and medium-mass nuclei. In fact, a broad range of nuclear force models from chiral EFT are currently available on the market. They differ between each other in many respects, summarized in the following:

1. The implicit or explicit inclusion of the Δ isobar.

2. The order at which 2N and 3N forces are considered. In this work, 4N forces, first appearing at N^{3}LO, are neglected as their contribution is expected to be small [141, 142].

3. The calculation of the Feynman diagrams contributing to the nuclear force is characterized by the presence of loops. The latter need to be regularized specifying a function, called a regulator, which suppresses the nuclear interaction above a certain momentum scale, called a cutoff [143]. Such a cutoff is usually of the order of the hard scale of chiral EFT. Nuclear interaction models from chiral EFT differ for the choice of regulator and cutoff value. In this work, we will use chiral EFT interactions employing a nonlocal regulator (see Refs. [144, 145] for details).

4. Low-energy constants in the interactions can be fitted considering different sets of experimental data. Traditionally, low-energy constants have been determined restricting the fit only to few-nucleon data (see, e.g., Ref. [121]), but recently, also information from medium-mass nuclei [102] or nuclear matter [138] has been included.

5. Similarity Renormalization Group (SRG) transformations [146] can be used to make the shape of the Hamiltonian more amenable to the application of many-body methods. As they are unitary, observables are kept unaltered as long as all other operator and wavefunctions are evolved accordingly.

We now briefly sketch the main features of the chiral EFT interactions employed in this thesis to obtain the results of Chapter 6.

- **1.8/2.0 (EM)** [68]. This is a Δ-less NN+3N interaction, based on the Entem and Machleidt (EM) NN interaction of Ref. [144], derived at N^3LO and SRG-evolved up to a scale $\lambda_{\mathrm{NN}} = 1.8~\mathrm{fm}^{-1}$, and on an unevolved 3N interaction at N^2LO with cutoff $\Lambda_{3\mathrm{N}} = 2.0~\mathrm{fm}^{-1}$. The LECs appearing in the short-range terms of the 3N force are fitted on the binding energy of ^{3}H and the matter radius of ^{4}He. For the LECs entering the 3N two-pion-exchange diagram, values consistent with Ref. [144] are used. The 1.8/2.0 (EM) interaction is known for being able to reproduce quite well the ground-state energies of nuclei up to $A \approx 100$ [147, 148], while underestimating radii [138].

- **2.0/2.0 (EM)** [68]. This interaction, developed in Ref. [68], is part of the same family of the 1.8/2.0 (EM) one. The only difference with respect to 1.8/2.0 (EM) lies in the value of the SRG-evolution scale λ_{NN}, which in this case corresponds to $2.0~\mathrm{fm}^{-1}$.

- **2.2/2.0 (EM)** [68]. This interaction differs from the previous two only for the SRG-evolution scale, equal to $\lambda_{\mathrm{NN}} = 2.2~\mathrm{fm}^{-1}$.

- **2.0/2.0 (PWA)** [68]. This interaction, of the same family as the ones listed above, differs from 2.0/2.0 (EM) for the LECs entering the 3N two-pion-exchange diagram. In this case, the NN phase shift analysis of Ref. [149] was employed in the fit.

- **NNLO$_{\mathrm{sat}}$** [102] This is a Δ-less interaction including NN and 3N forces up to NNLO in the chiral expansion, with a momentum cutoff of 450 MeV/c. In this case, the LECs have been optimized including in the fit binding energies and charge radii of medium-mass nuclei, as carbon and oxygen isotopes.

- **ΔNNLO$_{\mathrm{GO}}$** [138]. This is a Δ-full interaction model, developed in Ref. [138], incorporating NN and 3N forces up to NNLO, available with a softer cutoff of 394 MeV/c and a harder one of 450 MeV/c. Comparing the results of these two interactions we can appreciate the effects of the cutoff variation on many-body observables. The LECs of this family of interactions have been fixed considering properties of $A \leq 4$ nuclei and nuclear matter. This interaction model is also available at NLO with a cutoff of 450 MeV/c, making it possible to explore the effect of truncating the chiral EFT expansion.

4 Coupled-cluster theory

As explained in the previous Chapter, our goal is to employ chiral EFT interactions, grounded in QCD, to study nuclear response functions and electromagnetic observables in an ab initio framework. To this aim, one needs to solve the quantum many-body problem

$$H\,|\Psi\rangle = E\,|\Psi\rangle\,, \tag{4.1}$$

with H the nuclear Hamiltonian and E the energy of state $|\Psi\rangle$, for the nuclear ground state and all the possible final states induced by electromagnetic operators. In this Chapter, we will show how this can be achieved in a systematically improvable way within coupled-cluster theory.

Originally introduced in the realm of nuclear physics by Coester and Kümmel [150, 151] as an effective approach for addressing the strong nuclear correlations, coupled-cluster theory has been widely employed in quantum chemistry to describe properties of many-electron systems, as atoms and molecules (see [152, 153] and references therein). After few sporadic applications to nuclei [154, 155], in the last twenty years, the availability of SRG-evolved nuclear Hamiltonians, together with significant advancements in high performance computing infrastructures, led to a reinassance of coupled-cluster theory in nuclear physics [39]. Noteworthy coupled-cluster achievements in the field include the first ab initio calculation of the neutron skins of ^{48}Ca [47] and ^{208}Pb [30], mentioned in Chapter 2, and the solution of the longstanding experiment-theory discrepancy in β-decay rates [156]. Thanks to its polynomial computational scaling with increasing mass number A, coupled-cluster theory stands out as an ideal tool to study nuclear systems in the medium mass region of the nuclear chart and beyond.

After giving an overview of second quantization, we will show how coupled-cluster theory can be employed in solving the many-body Schrödinger equation for ground-state and excited-state properties of nuclei. We will also discuss the issues arising when open-shell nuclei are considered and show how they can be addressed in coupled-cluster theory. This Chapter is mainly based on Refs. [39, 86, 153].

4.1 Basic tools

4.1.1 Second quantization

In many-body theory, second quantization is a convenient formalism allowing for a simpler representation of the states of a many-body system, using a basis where each state is expressed in terms of the occupation number of some single-particle states. Although this framework is quite general, our focus will be on many-nucleon systems. Given a single-particle basis $\{|\phi_1\rangle, |\phi_2\rangle, \dots, |\phi_m\rangle\}$, we identify with n_i the number of particles occupying a state $|\phi_i\rangle$. At this point, we can create a new basis of vectors $|n_1, n_2, \dots, n_m\rangle$ labelled by the occupation numbers, where $\sum_i n_i = A$, with A the total number of particles. The space spanned by the occupation number basis takes the name of Fock space and it can be built as a direct sum of Hilbert spaces

$$\mathscr{F} = \mathscr{H}_0 \oplus \mathscr{H}_1 \oplus \mathscr{H}_2 \oplus \cdots \oplus \mathscr{H}_m, \tag{4.2}$$

where $|n_1\rangle \in \mathscr{H}_1$, $|n_1, n_2\rangle \in \mathscr{H}_2$, $|n_1, n_2, \dots, n_m\rangle \in \mathscr{H}_m$ and $|0\rangle \in \mathscr{H}_0$ is the physical vacuum state, where no particles exist and all n_i vanish. In this space, creation $a_i^\dagger$ and annihilation a_i operators with respect to the vacuum state $|0\rangle$ can be defined. One can compute every state belonging to the Fock space applying creation operators on the vacuum, as

$$|n_1, n_2, \dots, n_m\rangle = \left(a_1^\dagger\right)^{n_1} \left(a_2^\dagger\right)^{n_2} \dots \left(a_m^\dagger\right)^{n_m} |0\rangle. \tag{4.3}$$

Because nuclei are many-fermion systems, their wavefunction must be antisymmetric. In the first quantization formalism the many-body wavefunction corresponds to a Slater determinant, i.e. an antisymmetrized product of single-particle states

$$|\Phi\rangle = \mathscr{A}[|\phi_i\rangle |\phi_j\rangle \dots |\phi_k\rangle], \tag{4.4}$$

where $\mathscr{A}$ is an antisymmetrizing operator. In second quantization, instead, we can rewrite Eq. (4.4) as

$$|\Phi\rangle = |ij \dots k\rangle = a_i^\dagger a_j^\dagger \dots a_k^\dagger |0\rangle, \tag{4.5}$$

where $a_i^\dagger$ creates a particle in the single-particle state $|\phi_i\rangle$. Annihilation and creation operators satisfy the following anti-commutation relations

$$\begin{aligned} \{a_i^\dagger, a_j^\dagger\} &= 0, \\ \{a_i, a_j\} &= 0, \\ \{a_i^\dagger, a_j\} &= \delta_{ij}, \\ \{a_j, a_i^\dagger\} &= \delta_{ij}. \end{aligned} \tag{4.6}$$

These conditions can be deduced considering that $a_i |0\rangle = 0$ and $(a_i^\dagger a_i + a_i a_i^\dagger) |0\rangle = |0\rangle$, while for $i \neq j$ it holds $(a_i^\dagger a_j + a_j a_i^\dagger) |0\rangle = 0$.

In the second quantization formalism, it is possible to show that every operator of the theory can be expressed as strings of creation and annihilation operators. In particular we have that

$$F = \sum_{pq} \langle p|f|q\rangle \, a_p^\dagger a_q, \tag{4.7}$$

$$V = \frac{1}{2}\sum_{pqrs} \langle pq|v|rs\rangle \, a_p^\dagger a_q^\dagger a_s a_r = \frac{1}{4}\sum_{pqrs} \langle pq||rs\rangle \, a_p^\dagger a_q^\dagger a_s a_r, \tag{4.8}$$

$$W = \frac{1}{6}\sum_{pqrstu} \langle pqr|w|stu\rangle \, a_p^\dagger a_q^\dagger a_r^\dagger a_s a_t a_u = \frac{1}{36}\sum_{pqrstu} \langle pqr||stu\rangle \, a_p^\dagger a_q^\dagger a_r^\dagger a_s a_t a_u, \tag{4.9}$$

where F, V and W are one-body, two-body and three-body operators, characterized by one-body $\langle p|f|q\rangle$, two-body $\langle pq|v|rs\rangle$ and three-body matrix elements $\langle pqr|w|stu\rangle$, respectively. In the case of V, we indicated with $\langle pq||rs\rangle$ the antisymmetric matrix element $\langle pq||rs\rangle = \langle pq|v|rs\rangle - \langle pq|v|sr\rangle$. An analogous expression is used for the three-body operator W.

4.1.2 Wick's theorem

Wick's theorem is a fundamental tool to compute matrix elements in the formalism of second quantization. To understand its implications, we first need to introduce the concepts of normal product and contraction between operators.

1. The normal product $\mathscr{N}[\ldots]$ of a string of operators $ABC\ldots Z$ consists in reordering these operators in such a way that annihilation operators lie at the right of creation operators, with a phase that takes into account the total number of permutation required.

2. The contraction between two operators is defined as

$$\overbracket{AB} = AB - \mathscr{N}[AB]. \tag{4.10}$$

According to the time-independent Wick's theorem, a product of a string of creation and annhilation operators is equal to their normal product plus the sum of all possible normal product with contractions, i.e.,

$$ABC\ldots Z = \mathscr{N}[ABC\ldots Z] + \sum_{contr} \mathscr{N}[ABC\ldots Z]. \tag{4.11}$$

A proof of this theorem can be found in Ref. [153]. Let us consider an example for a string of three operators. On the basis of Wick's theorem, we can write

$$ABC = \mathscr{N}[ABC] + \mathscr{N}[\overbracket{AB}C] + \mathscr{N}[\overbracket{ABC}] + \mathscr{N}[A\overbracket{BC}], \tag{4.12}$$

where the normal product with contractions is given by

$$\mathscr{N}[A\overbracket{BC\ldots V}Z] = (-1)^P \overbracket{BV}\mathscr{N}[AC\ldots Z], \tag{4.13}$$

with P representing the number of permutation needed to move V next to B. As the vacuum expectation value of a normal-ordered product is zero, from Eq. (4.11) we have that the vacuum expectation value of any string of operators vanishes unless all operators are contracted in the last term.

4.1.3 Particle-hole formalism and normal-ordered operators

Instead of referring every many-body state to the physical vacuum $|0\rangle$ according to Eq. (4.3), a more convenient choice for nuclear physics and quantum chemistry applications is to begin with a different reference state, given by

$$|\Phi_0\rangle = |ijk\ldots\rangle\,, \tag{4.14}$$

which takes the name of Fermi vacuum. The indices $i,j,k,\ldots$ define the occupied single-particle states in the reference, identifying the so-called Fermi sea. Single-particle states below the Fermi sea are called hole states, while the other orbitals above the Fermi sea, labelled with the indices $a,b,c\ldots$, are called particle states. The indices $p,q,r,\ldots$ are used to identify particle and hole states alike. We can then build excited states by promoting particles from the region below the Fermi sea to the one above it

$$|\Phi^{abc\ldots}_{ijk\ldots}\rangle = a^\dagger_a a^\dagger_b a^\dagger_c \ldots a_k a_j a_i |\Phi_0\rangle\,. \tag{4.15}$$

A schematic representation of the reference state and of some excited states is given in Figure 4.1.

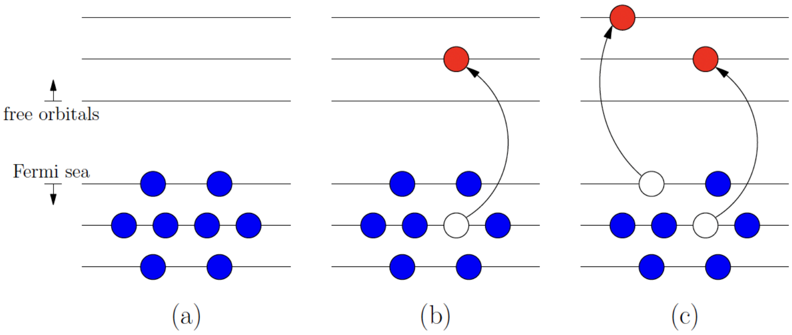

Figure 4.1: Schematic representation of the reference state and excited states in the particle-hole formalism. Occupied orbitals below the Fermi level are represented by blue circles, holes in the Fermi sea by white circles and excited occupied orbitals above the Fermi level by red circles. (a) is a representation of the reference $|\Phi_0\rangle$, (b) of a one-particle one-hole (1p-1h) state, obtained applying $a^\dagger_a a_i$ on $|\Phi_0\rangle$, (c) of a two-particle-two-hole (2p-2h) state, obtained applying $a^\dagger_a a^\dagger_b a_j a_i$ to $|\Phi_0\rangle$. Figure taken from Ref. [86].

Adopting the vacuum state of Eq. (4.14), we also need to redefine creation and annihilation operators with respect to the new reference. In this framework, $a^\dagger_a$ and a_i represent pseudo-creation operators: $a^\dagger_a$ generates a particle in the unoccupied orbitals above the Fermi surface, while a_i creates a hole in the occupied orbitals of the reference state. Similarly, $a^\dagger_i$ and a_a become pseudo-annihilation operators: $a^\dagger_i$ eliminates a hole in the reference, while a_a destroys a particle above the Fermi sea. The new reference state choice of Eq. (4.14), equipped with a corresponding redefinition of the creation and annihilation operators, identifies the so-called particle-hole formalism.

Also the definition of normal-ordered product entering Wick's theorem needs to be extended when $|\Phi_0\rangle$ is chosen as reference and pseudo-creation and pseudo-annihilation operators are introduced. In this case, a string of creation and annihilation operators is defined to be normal-ordered if all pseudo-creation operators ($a^\dagger_a$ and a_i) are found on the left of all pseudo-annihilation operators ($a^\dagger_i$ and a_a). With this definition, it is possible to show that Wick's theorem holds in the same form of Eq. (4.11), ensuring that expectation values on the Fermi vacuum vanish.

We now employ Wick's theorem and the anti-commutation relations of Eq. (4.6) to rewrite the F, V and W operators of Eqs. (4.7), (4.8), (4.9) in a normal-ordered format with respect to $|\Phi_0\rangle$. Let us start from the one-body operator F

$$\begin{aligned} F &= \sum_{pq} \langle p|f|q\rangle\, a^\dagger_p a_q \\ &= \sum_{pq} \langle p|f|q\rangle\, \mathscr{N}[a^\dagger_p a_q] + \sum_{pq} \langle p|f|q\rangle\, \wick{\c a^\dagger_p \c a_q} \\ &= \sum_{pq} \langle p|f|q\rangle\, \mathscr{N}[a^\dagger_p a_q] + \sum_{i} \langle i|f|i\rangle \\ &= F_N + \sum_i \langle i|f|i\rangle\,, \end{aligned} \tag{4.16}$$

where in the second sum the only non-zero contraction appears when the indices p and q correspond to hole states: $\wick{\c a^\dagger_i \c a_j} = \delta_{ij}$. We also indicate with F_N the normal-ordered part of the operator F. The expectation value of F on the Fermi vacuum will then be

$$\langle\Phi_0|F|\Phi_0\rangle = \langle\Phi_0|F_N|\Phi_0\rangle + \sum_i \langle i|f|i\rangle = \sum_i \langle i|f|i\rangle\,, \tag{4.17}$$

as the expectation value of normal-ordered operators vanish by construction. We can repeat the same reasoning also for the two-body operator V, obtaining

$$\begin{aligned} V = \frac{1}{2}\sum_{pqrs} \langle pq||rs\rangle\, \mathscr{N}[& a^\dagger_p a^\dagger_q a_s a_r + \wick{\c a^\dagger_p a^\dagger_q \c a_s a_r} + \wick{\c a^\dagger_p a^\dagger_q a_s \c a_r} \\ &+ \wick{a^\dagger_p \c a^\dagger_q \c a_s a_r} + \wick{a^\dagger_p \c a^\dagger_q a_s \c a_r} + \wick{\c1 a^\dagger_p \c2 a^\dagger_q \c1 a_s \c2 a_r} + \wick{\c1 a^\dagger_p \c2 a^\dagger_q \c2 a_s \c1 a_r}] \\ = \frac{1}{4}\sum_{pqrs} & \langle pq||rs\rangle\, \mathscr{N}[a^\dagger_p a^\dagger_q a_s a_r] + \sum_{ipq} \langle pi||qi\rangle\, \mathscr{N}[a^\dagger_p a_q] + \frac{1}{2}\sum_{ij} \langle ij||ij\rangle \\ = V^{2b}_N & + V^{1b}_N + \langle\Phi_0|V_N|\Phi_0\rangle\,. \end{aligned} \tag{4.18}$$

Here, V^{2b}_N is the normal-ordered two-body part of V and V^{1b}_N the normal-ordered one-body part.

Analogously, for the three-body operator W we find:

$$\begin{aligned} W &= \frac{1}{36}\sum_{pqrstu} \langle pqr||stu\rangle \mathcal{N}[a_p^\dagger a_q^\dagger a_r^\dagger a_s a_t a_u] + \frac{1}{4}\sum_{ipqrs} \langle ipq||irs\rangle \mathcal{N}[a_p^\dagger a_q^\dagger a_s a_r] \\ &\quad + \frac{1}{2}\sum_{ijpq} \langle ijp||ijq\rangle \mathcal{N}[a_p^\dagger a_q] + \frac{1}{6}\sum_{ijk} \langle ijk||ijk\rangle \\ &= W_N^{3b} + W_N^{2b} + W_N^{1b} + \langle \Phi_0|W_N|\Phi_0\rangle\,, \end{aligned} \tag{4.19}$$

where W_N^{3b}, W_N^{2b} and W_N^{1b} correspond to the normal-ordered three-body, two-body and one-body parts of the operator W, respectively.

In nuclear physics calculations, we usually deal with three-body Hamiltonians of the form $H = F + V + W$. Using Eqs. (4.16), (4.18), (4.19) and grouping the zero-, one-, two- and three-body normal-ordered terms, we can write the Hamiltonian as

$$\begin{aligned} H &= F + V + W \\ &= \langle \Phi_0|F+V+W|\Phi_0\rangle + (F_N + V_N^{1b} + W_N^{1b}) + (V_N^{2b} + W_N^{2b}) + W_N^{3b} \\ &= H_0 + H_N^{1b} + H_N^{2b} + H_N^{3b}\,. \end{aligned} \tag{4.20}$$

The normal-ordered Hamiltonian will then correspond to

$$H_N = H - H_0 = H_N^{1b} + H_N^{2b} + H_N^{3b}\,. \tag{4.21}$$

Using the normal-ordered Hamiltonian, the Schrödinger equation for a state $|\Psi_\mu\rangle$ becomes

$$H_N\,|\Psi_\mu\rangle = \Delta E_\mu\,|\Psi_\mu\rangle\,, \tag{4.22}$$

where $\Delta E_\mu = E_\mu - H_0 = E_\mu - \langle \Phi_0|H|\Phi_0\rangle$ is the so-called correlation energy, defined in terms of the uncorrelated energy H_0 of the reference state $|\Phi_0\rangle$. In this work, the results presented in Chapter 6 have been obtained starting from the harmonic oscillator single-particle basis and performing a Hartree-Fock calculation (see Refs. [157,158] for details). We select the resulting Slater determinant expanded on the Hartree-Fock basis as our reference state $|\Phi_0\rangle$. Therefore, the uncorrelated energy H_0 corresponds to the Hartree-Fock energy of the nucleus under consideration. The correlation energy ΔE_μ of the state $|\Psi_\mu\rangle$ is then computed employing an appropriate many-body method to solve Eq. (4.22).

Incorporating three-body forces in the nuclear Hamiltonian is essential for accurately describing nuclear observables. However, a complete treatment of three-nucleon interactions poses significant technical challenges, as it leads to more complex equations to handle and it requires the storage of numerous matrix elements. A cost-effective approach to partially simplify the inclusion of three-body effects in nuclear structure calculations is the so-called normal-ordered two-body approximation. The latter consists in omitting the pure three-body interaction $H_N^{3b} = W_N^{3b}$, and accounting for three-body forces by keeping the lower-rank W_N terms. While still requiring the storage of three-body matrix elements, the normal-ordered two-body approximation allows one to employ similar algorithms as the ones needed to handle two-body forces. We adopted such approximation in obtaining all the results presented in Chapter 6. In Refs. [159, 160], it has been shown that the effect of an explicit inclusion of H_N^{3b} in both light and medium-mass nuclei is safely negligible.

4.2 The exponential ansatz

Starting from Eq. (4.22), the Schrödinger equation for the ground state $|\Psi_0\rangle$ of an A-body nucleus can be written as

$$H_N\,|\Psi_0\rangle = \Delta E_0\,|\Psi_0\rangle\,. \tag{4.23}$$

where ΔE_0 is the ground-state correlation energy. To solve this equation, coupled-cluster theory relies on the so-called exponential ansatz

$$|\Psi_0\rangle = e^{T}\,|\Phi_0\rangle\,, \tag{4.24}$$

which connects the ground-state wavefunction to the reference state $|\Phi_0\rangle$ given by Eq. (4.14). The exponentiated operator T, also known as cluster operator, introduces correlations in the many-body ground state. It can be expanded according to the following expression

$$T = T_1 + T_2 + T_3 + \cdots + T_A = \sum_{n=1}^{A} T_n. \tag{4.25}$$

where T_n generates n-particle n-hole (np-nh) excitations on top of the reference $|\Phi_0\rangle$

$$T_n = \left(\frac{1}{n!}\right)^2 \sum_{ij\ldots ab\ldots} t_{ij\ldots}^{ab\ldots}\, a_a^\dagger a_b^\dagger \ldots a_j a_i. \tag{4.26}$$

The ground state is then fully determined once the so-called coupled-cluster amplitudes $t_{ij\ldots}^{ab\ldots}$ are found. Inserting Eq. (4.24) in Eq. (4.23) and multiplying by e^{-T} on the left, we obtain

$$e^{-T} H_N e^{T}\,|\Phi_0\rangle \equiv \overline{H}_N\,|\Phi_0\rangle = \Delta E_0\,|\Phi_0\rangle\,, \tag{4.27}$$

where we introduced the similarity-transformed Hamiltonian $\overline{H}_N = e^{-T} H_N e^{T}$. The expectation value of $\overline{H}_N$ on the reference state corresponds to the correlation energy

$$\Delta E_0 = \langle\Phi_0|\overline{H}_N|\Phi_0\rangle\,. \tag{4.28}$$

To determine ΔE_0, which depends on the similarity-transformed Hamiltonian, the coupled-cluster amplitudes need to be known. They can be computed by solving the so-called coupled-cluster equations, which result from projecting Eq. (4.27) on the np-nh excited states of the reference:

$$\langle \Phi_{ij\dots}^{ab\dots} | \overline{H}_N | \Phi_0 \rangle = \Delta E_0 \langle \Phi_{ij\dots}^{ab\dots} | \Phi_0 \rangle = 0. \tag{4.29}$$

It is worth pointing out that unlike the configuration interaction linear ansatz [161], the exponential ansatz of Eq. (4.24) ensures the size extensivity of the solution [162, 163], i.e. the correlation energy of the system exhibits a linear scaling with the number of particles in the limit of infinite size. This property is also relevant in studying finite nuclei for two reasons. First, it matches the saturation properties of the nuclear interaction. Second, it implies that the accuracy of the coupled-cluster ansatz remains constant with respect to the mass number of the system under study [164].

The similarity-transformed Hamiltonian is not Hermitian. For this reason, knowledge of both the left and right eigenstates is required to compute coupled-cluster expectation values. The right eigenstate coincides with the reference state, while the left one can be expressed in the form

$$\langle \Phi_{0,L} | = \langle \Phi_0 | (\mathbb{1} + \Lambda). \tag{4.30}$$

In analogy to the cluster operator T, also Λ can be written as a sum of np-nh de-excitation operators as

$$\Lambda = \Lambda_1 + \Lambda_2 + \cdots + \Lambda_A = \sum_{n=1}^{A} \Lambda_n, \tag{4.31}$$

with

$$\Lambda_n = \left(\frac{1}{n!}\right)^2 \sum_{ij\dots ab\dots} \lambda_{ab\dots}^{ij\dots} a_i^\dagger a_j^\dagger \dots a_b a_a. \tag{4.32}$$

The amplitudes $\lambda_{ab\dots}^{ij\dots}$ of the Λ operator can be found by solving the equations

$$0 = \langle \Phi_0 | \overline{H}_N | \Phi_{ij\dots}^{ab\dots} \rangle + \langle \Phi_0 | \Lambda \overline{H}_N | \Phi_{ij\dots}^{ab\dots} \rangle + \sum_{k<l<\dots c<d<\dots} \langle \Phi_0 | \overline{H}_N | \Phi_{kl\dots}^{cd\dots} \rangle \langle \Phi_{kl\dots}^{cd\dots} | \Lambda | \Phi_{ij\dots}^{ab\dots} \rangle . \tag{4.33}$$

Since the intermediate state $|\Phi_{kl\dots}^{cd\dots}\rangle$ represents a de-excitation with respect to the initial state $|\Phi_{ij\dots}^{ab\dots}\rangle$, the indices of $|\Phi_{kl\dots}^{cd\dots}\rangle$ are a subset of the indices of the initial state. A detailed derivation of Eq. (4.33) can be found in Ref. [86].

4.2.1 Computing the similarity-transformed Hamiltonian

Eqs. (4.27) and (4.33) highlight the pivotal role that the similarity-transformed Hamiltonian $\overline{H}_N$ plays in coupled-cluster theory. For this reason, in the following we will briefly sketch how it can be evaluated. We begin by applying the Baker-Campbell-Hausdorff formula [165], obtaining

$$\overline{H}_N = H_N + [H_N, T] + \frac{1}{2!}[[H_N, T], T] + \frac{1}{3!}[[[H_N, T], T], T] + \dots . \tag{4.34}$$

The similarity-transformed Hamiltonian thus corresponds to an infinite sum of nested commutators involving the normal-ordered Hamiltonian and the cluster operator T. Such commutators can be determined by employing the generalized Wick's theorem [153]. The latter focuses on a general product of creation and annihilation operators, where some of them are already in normal-ordered product form. The theorem states that such product equals to the overall normal product of all creation and annihilation operators plus the sum of all overall normal products with contractions. In the latter, pair of operators within the same original normal product are excluded. As an example, let us focus on the commutator $[H_N, T]$. In this case, the theorem leads to the following expression

$$[H_N, T] = H_N T - T H_N = \mathscr{N}[H_N T] + \wick{\c H_N \c T} - \mathscr{N}[T H_N] - \wick{\c T \c H_N}, \tag{4.35}$$

where in the $\wick{\c H_N \c T}$ and $\wick{\c T \c H_N}$ terms creation and annihilation operators are fully contracted (otherwise vacuum expectation values would be zero). We get $\mathscr{N}[H_N T] = \mathscr{N}[T H_N]$, as both H_N and T are characterized by an even number of creation and annihilation operators. Therefore, the commutator reduces to

$$[H_N, T] = \wick{\c H_N \c T} - \wick{\c T \c H_N}. \tag{4.36}$$

Considering the possible combinations of contractions involving pseudo-creation and pseudo-annihilation operators, only

$$\begin{aligned} \wick{\c a_i^\dagger \c a_j} &= \delta_{ij}, \\ \wick{\c a_a \c a_b^\dagger} &= \delta_{ab}, \end{aligned} \tag{4.37}$$

do not vanish. This has two consequences. First, as only particle creation operators $a_a^\dagger, a_b^\dagger, \dots$ and hole annihilation operators $a_i, a_j, \dots$ enter in T, contractions between T operators give zero. Second, the commutator receives non-zero contribution only from contractions between H_N and T where T lies on the right of H_N. These remarks lead to an important conclusion: the nested commutator expansion naturally terminates at a point determined by the shape of the Hamiltonian. When dealing with a two-body Hamiltonian, the expansion is truncated at fourfold nested commutators, while considering a three-body Hamiltonian, it is truncated at the level of sixfold nested commutators. For simplicity, we show the case of a two-body Hamiltonian, where we can rewrite Eq. (4.34) as

$$\overline{H}_N = H_N + \wick{\c H_N \c T} + \frac{1}{2!}\wick{\c1{\c2{H_N}} \c1 T \c2 T} + \frac{1}{3!}\wick{\c1{\c2{\c3{H_N}}} \c1 T \c2 T \c3 T} + \frac{1}{4!}\wick{\c1{\c2{\c3{\c4{H_N}}}} \c1 T \c2 T \c3 T \c4 T} = (H_N e^T)_C, \tag{4.38}$$

where the new notation $(H_N e^T)_C$ indicates that $\overline{H}_N$ contains only connected terms, that is terms in which each T operator is contracted with H_N.

4.2.2 Coupled-cluster approximations for ground-state calculations

If we are interested in the ground state properties of an A-body nucleus, the particle-hole expansion of both the cluster and Λ operators entering the similarity transformation corresponds to the sum of A terms. However, as Ap-Ah calculations are not feasible from a computational point of view, one resorts to truncations of Eqs. (4.26) and (4.32). The most frequently adopted approximation is coupled-cluster singles-and-doubles (CCSD), where we have

$$T = T_1 + T_2, \quad \Lambda = \Lambda_1 + \Lambda_2. \tag{4.39}$$

In this approximation, one needs to solve the coupled equations

$$\langle \Phi_i^a | H_N e^{T_1+T_2} | \Phi_0 \rangle_C = 0, \quad \langle \Phi_{ij}^{ab} | H_N e^{T_1+T_2} | \Phi_0 \rangle_C = 0. \tag{4.40}$$

to determine the T_1 and T_2 amplitudes of the cluster operator, and Eq. (4.33) at the corresponding order for the Λ_1 and Λ_2 amplitudes. The subscript C indicates that only connected contributions enter the equations. The CCSD approximation scheme typically accounts for the 90% of the correlation energy. Increased precision can be obtained by adding linear triples excitations via the so-called CCSDT-1 truncation [166]. In this case, the exponential in the similarity-transformation becomes

$$e^T \approx e^{T_1+T_2} + T_3. \tag{4.41}$$

In this approximation scheme, the T_1 equation will get an additional term $V_N T_3$, while the T_2 equation will include contributions from $F_N T_3$ and $V_N T_3$. An additional equation is also needed for the t_{ijk}^{abc} amplitudes of T_3, yielding

$$\langle \Phi_{ijk}^{abc} | \overline{H}_N | \Phi_0 \rangle = 0 \rightarrow 0 = \overline{F_N T}_3 + \overline{V_N T}_3 + \overline{V_N T}_2. \tag{4.42}$$

A corresponding approximation is adopted for the Λ operator

$$\Lambda = \Lambda_1 + \Lambda_2 + \Lambda_3 \tag{4.43}$$

in the left eigenvalue problem of Eq. (4.33). With the inclusion of triples excitations, around 98-99% of the correlation energy can be captured [167].

4.3 The equation-of-motion coupled-cluster method for excited states

While Eqs. (4.29) and (4.33) determine the structure of the nuclear ground state, we need an approach to compute arbitrary excited states of the Hamiltonian via the following equation

$$\overline{H}_N |\Psi_\mu\rangle = \Delta E_\mu |\Psi_\mu\rangle . \tag{4.44}$$

This can be achieved in the framework of the equation-of-motion coupled-cluster (EOM-CC) method [168]. In the EOM-CC approach, we assume that a general target state $|\Psi_\mu\rangle$ can be written as

$$|\Psi_\mu\rangle = R_\mu |\Psi_0\rangle = R_\mu e^T |\Phi_0\rangle . \tag{4.45}$$

Here R_μ is an EOM excitation operator that connects the ground state of the nucleus $|\Psi_0\rangle$ to the state $|\Psi_\mu\rangle$ under consideration. As $\overline{H}_N$ is non-Hermitian, also for excited states we need to differentiate between left and right eigenstates of the Hamiltonian. Therefore, a similar ansatz holds for the corresponding bra state

$$\langle\Psi_\mu| = \langle\Phi_0| L_\mu e^{-T}, \tag{4.46}$$

where L_μ is an EOM de-excitation operator. Inserting Eq. (4.45) in Eq. (4.44) and multiplying the resulting expression on the left by e^{-T} we get

$$H_N R_\mu e^T |\Phi_0\rangle = \Delta E_\mu R_\mu e^T |\Phi_0\rangle \Rightarrow \overline{H}_N R_\mu |\Phi_0\rangle = \Delta E_\mu R_\mu |\Phi_0\rangle , \tag{4.47}$$

where ΔE_μ is the energy of the target state with respect to the reference $|\Phi_0\rangle$. We observe that $[R_\mu, T] = 0$ as they are both excitation operators. Analogously for $\langle\Psi_\mu|$ it holds that

$$\langle\Phi_0| L_\mu e^{-T} H_N = \langle\Phi_0| L_\mu e^{-T} \Delta E_\mu \Rightarrow \langle\Phi_0| L_\mu \overline{H}_N = \langle\Phi_0| L_\mu \Delta E_\mu . \tag{4.48}$$

Eqs. (4.47) and (4.48) take the name of EOM-CC equations. Left and right eigenstates are bi-orthogonal, and as with proper normalization the following relation is valid

$$\langle\Phi_0|L_{\mu'} R_\mu|\Phi_0\rangle = \delta_{\mu'\mu}, \tag{4.49}$$

the completeness relation applies in the form of

$$\sum_\mu R_\mu |\Phi_0\rangle \langle\Phi_0| L_\mu = \mathbb{1}. \tag{4.50}$$

It is useful to notice that for $\mu = 0$ Eqs. (4.47) and (4.48) provide the right and left ground state of the system, respectively. Given Eqs. (4.24) and (4.30), we deduce that in this special case the EOM operators reduce to $R_0 = \mathbb{1}$ and $L_0 = (1 + \Lambda)$. When considering instead excited states of an A-body nucleus the EOM-CC operators R_μ and L_μ can be expanded as

$$R_\mu = r_{0,\mu} + \sum_{ai} r^a_{i,\mu} a^\dagger_a a_i + \frac{1}{4} \sum_{abij} r^{ab}_{ij,\mu} a^\dagger_a a^\dagger_b a_j a_i + \ldots , \tag{4.51}$$

and

$$L_\mu = l_{0,\mu} + \sum_{ai} l^i_{a,\mu} a^\dagger_i a_a + \frac{1}{4} \sum_{abij} l^{ij}_{ab,\mu} a^\dagger_i a^\dagger_j a_b a_a + \ldots , \tag{4.52}$$

where $r^{ab\dots}_{ij\dots,\mu}$ and $l^{ij\dots}_{ab\dots,\mu}$ are the amplitudes of the right and left EOM-CC operators, respectively. In order to determine $r^{ab\dots}_{ij\dots,\mu}$ and $l^{ij\dots}_{ab\dots,\mu}$, we can express the EOM-CC equations in a more convenient format. As an example, let us focus on the right Schrödinger equation, and consider the difference between Eq. (4.47) and Eq. (4.27) multiplied by R_μ. We obtain the following expression

$$[\overline{H}_N, R_\mu] \left|\Phi_0\right\rangle = \omega_\mu R_\mu \left|\Phi_0\right\rangle . \tag{4.53}$$

where $\omega_\mu = \Delta E_\mu - \Delta E_0$ is the excitation energy with respect to the ground state. The equation above can be rewritten as

$$(\overline{H}_N R_\mu)_C \left|\Phi_0\right\rangle = \omega_\mu R_\mu \left|\Phi_0\right\rangle , \tag{4.54}$$

as only connected terms survive in the commutator. In Eq. (4.54), we can recognise the form of an eigenvalue problem, where the amplitudes of R_μ are the components of the eigenstates and the excitation energies ω_μ are the eigenvalues. Solving the corresponding left eigenvalue problem allows to find the amplitudes of L_μ.

Due to computational limitations, also R_μ and L_μ need to be truncated in analogy to the T and Λ operators. The EOM-CCSD framework is defined by keeping only singles and doubles excitation terms in Eqs. (4.51) and (4.52). Adding also linear triples contributions lead to the EOM-CCSDT-1 approximation [169].

4.4 Coupled-cluster theory for open-shell nuclei

Understanding the different many-body treatment required by open-shell nuclei with respect to the case of closed-shell nuclei requires a premise on the relation between the symmetries of the system and the choice of the single-particle basis. In our derivation, we labelled single-particle states with the indices $a, b, \dots, i, j, \dots$, which collectively represent the set of quantum numbers specifying the given orbital. For the result presented in Chapter 6, we choose to work with an Hartree-Fock reference expanded on the single-particle harmonic oscillator (HO) basis. The latter depends on the HO frequency parameter $\hbar\Omega$, and it is truncated at a maximum number of major oscillator shells N_{max}. Taking into account also the spin and isospin quantum numbers, a single-particle orbital $|p\rangle$ is identified by

$$|p\rangle = |n_p, (l_p, s_p) j_p m_p\rangle \otimes |\tau_p, \tau_p^z\rangle , \tag{4.55}$$

where n_p is the radial quantum number, and l_p and $s_p = 1/2$ are the orbital angular momentum and spin. The sum of l_p and s_p gives the total angular momentum j_p with projection m_p, while τ_p and τ_p^z correspond to the isospin and its z-axis projection, respectively. Eq. (4.55) is employed in the so-called m-scheme formulation of coupled-cluster theory, where m_p is considered explicitly in the single-particle states and in the calculation of matrix elements as a good quantum number.

For closed (sub-)shell nuclei, characterized by $J^\pi = 0^+$, the set of quantum numbers characterizing $|p\rangle$ can be simplified. In this case, in fact, the Hamiltonian and the T and Λ operators (and as a consequence, also the similarity-transformed Hamiltonian) are scalar under rotations. This makes it possible to adopt an angular-momentum-coupled formalism where the dependence of $|p\rangle$ on m_p in the calculation of matrix elements can be removed and $|p\rangle$ reduces to

$$|p\rangle = |n_p,(l_p,s_p)j_p\rangle \otimes |\tau_p,\tau_p^z\rangle\,. \tag{4.56}$$

The angular-momentum-coupled formulation of coupled-cluster theory is known with the name of j-scheme coupled-cluster or spherical coupled-cluster. Despite limiting the number of accessible nuclei, the j-scheme formulation, reducing the computational cost of the method [39], has extended dramatically its reach in mass number [30, 170, 171].

In the case of open-shell nuclei, while the nuclear Hamiltonian remains invariant under rotations, the coupled-cluster reference state breaks rotational symmetry, as it does not have a well defined total angular momentum [172]. In this case, one has to resort to the use of the m-scheme formulation, and once the desired state has been calculated, rotational symmetry needs to be restored via angular momentum projection techniques [173]. Coupled-cluster calculations of ground-state properties and rotational spectra of open-shell nuclei are now possible starting from axially symmetric reference states [174] and including angular momentum projection, which however comes at a considerably heavier computational cost with respect to bare m-scheme coupled-cluster [175, 176].

There is a way to tackle selected open-shell nuclei in coupled-cluster theory without breaking rotational symmetry in the reference state, allowing us to avoid the computationally demanding angular momentum projection step required by m-scheme calculations. The EOM-CC approach, in fact, can also be applied to describe nuclei in the vicinity of closed shells, characterized by having $A\pm 1,2$ valence nucleons with respect to the doubly-magic or semi-magic A-body neighbour [39]. Since ongoing experimental campaigns measuring electromagnetic observables as the dipole polarizability are focusing on such nuclei, we choose to follow this path and leave the development of a framework to calculate response functions in m-scheme coupled-cluster to future work.

4.4.1 Equation-of-motion coupled-cluster for nuclei in the vicinity of closed shells

In the EOM-CC approach, states of $A\pm k$ nuclei are modeled as excited states of the A-body closed-shell neighbour. The form of the wavefunction in this case is given by

$$|\Psi_\mu^{A\pm k}\rangle = R_\mu^{A\pm k}|\Psi_0^{(A)}\rangle = R_\mu^{A\pm k}e^T|\Phi_0\rangle\,, \tag{4.57}$$

with an analogous expression on the bra side

$$\langle\Psi_\mu^{A\pm k}| = \langle\Phi_0|L_\mu^{A\pm k}e^{-T}. \tag{4.58}$$

Here, $R_\mu^{A\pm k}$ ($L_\mu^{A\pm k}$) is a (de-)excitation operator which involves the net creation (annihilation) of k nucleons, starting from the coupled-cluster wavefunction of the neighbouring closed-shell system. In Eqs. (4.57) and (4.58) our starting point $|\Phi_0\rangle$ is the reference state of the closed-shell core calculated with a mass shift $A^* = A \pm k$ in the Hamiltonian. Here, A^* is the mass number of the nucleus that we want to describe and $k = 1,2$. This guarantees that the correct kinetic energy of the center of mass is employed when computing properties of $A^* = A \pm k$ nuclei.

For $k = 1$, the operators

$$R_\mu^{A+1} = \sum_a r_\mu^a a_a^\dagger + \frac{1}{2}\sum_{abi} r_{i,\mu}^{ab} a_a^\dagger a_b^\dagger a_i + \dots, \tag{4.59}$$

$$L_\mu^{A+1} = \sum_a l_{a,\mu} a_a + \frac{1}{2}\sum_{abi} l_{i,\mu}^{ab} a_i^\dagger a_b a_a + \dots, \tag{4.60}$$

and

$$R_\mu^{A-1} = \sum_i r_{i,\mu} a_i + \frac{1}{2}\sum_{ija} r_{ij,\mu}^{a} a_a^\dagger a_j a_i + \dots, \tag{4.61}$$

$$L_\mu^{A-1} = \sum_i l_\mu^i a_i^\dagger + \frac{1}{2}\sum_{ija} l_{a,\mu}^{ij} a_i^\dagger a_j^\dagger a_a + \dots, \tag{4.62}$$

represent the foundation of the particle-attached equation-of-motion coupled-cluster (PA-EOM-CC) [177] and the particle-removed equation-of-motion coupled-cluster (PR-EOM-CC) [178] respectively. Implemented for the first time in quantum chemistry, these methods have found applications also in nuclear physics [179].

In Ref. [180], Jansen and coauthors introduced the 2PA-EOM-CC and 2PR-EOM-CC method for nuclei with two-particle-attached and two-particle-removed from a closed-shell nucleus. A spherical implementation of the 2PA-EOM-CC approach is presented in Ref. [181]. For $A^* = A+2$, the right and left EOM operators are given by

$$R_\mu^{A+2} = \frac{1}{2}\sum_{ab} r_\mu^{ab} a_a^\dagger a_b^\dagger + \frac{1}{6}\sum_{abci} r_{i,\mu}^{abc} a_a^\dagger a_b^\dagger a_c^\dagger a_i + \dots, \tag{4.63}$$

and

$$L_\mu^{A+2} = \frac{1}{2}\sum_{ab} l_{ab,\mu} a_a a_b + \frac{1}{6}\sum_{abci} l_{abc,\mu}^{i} a_i^\dagger a_c a_b a_a + \dots, \tag{4.64}$$

while for $A^* = A-2$ we get

$$R_\mu^{A-2} = \frac{1}{2}\sum_{ij} r_{ij,\mu} a_i a_j + \frac{1}{6}\sum_{ijka} r_{ijk,\mu}^{a} a_a^\dagger a_k a_j a_i + \dots, \tag{4.65}$$

and

$$L_\mu^{A-2} = \frac{1}{2}\sum_{ij} l_\mu^{ij} a_i^\dagger a_j^\dagger + \frac{1}{6}\sum_{ijka} l_{a,\mu}^{ijk} a_i^\dagger a_j^\dagger a_k^\dagger a_a + \dots. \tag{4.66}$$

The right EOM-CC equations

$$(\overline{H}_N R_\mu^{A\pm k})_C |\Phi_0\rangle = \omega_\mu R_\mu^{A\pm k} |\Phi_0\rangle \,, \tag{4.67}$$

and their left counterpart hold also when the EOM-CC approach is used to describe open-shell nuclei. In this case the energy difference ω_μ is given by $\Delta E_\mu - \Delta E_0^*$, where ΔE_0^* is the CC ground-state energy of the closed-shell core with respect to the reference $|\Phi_0\rangle$.

Let us focus on the 2PA-EOM-CC approach. The use of excitation operators that do not conserve the number of particles implies a different expansion in terms of particle-hole excitations with respect to the particle-number conserving case. While the terms of the many-body expansion of the cluster operator and particle-number conserving EOM involve the excitation of the same number of particles and holes, the 2PA-EOM-CC (de-)excitation operator R_μ (L_μ) is characterized by a 2p-0h term, a 3p-1h term and in general up to a (A+2)p-Ah term. The results in Chapter 6 have been obtained employing two different truncations for the 2PA-EOM-CC method. The latter can be distinguished on the basis of the number of particle-hole excitation kept in the operator. The 2PA-EOM-CC method in the 2p-0h approximation is given by keeping only the first term in the expansions of Eqs. (4.63) and (4.64), while adding also the second term leads to the 3p-1h approximation. In j-scheme formulation, the 2PA-EOM-CC approach truncated at the 3p-1h level has a significant computational cost. Depending on the nucleus and on the state under study, the size of the matrix in Eq. (4.67) can overcome 10^8 [181]. For this reason, the implementation of the 4p-2h approximation framework [182] is beyond the scope of this work.

4.5 Diagrammatic representation

Solving the coupled-cluster equations (4.29) and the EOM-CC equations for both excited states (4.54) and open-shell systems (4.67) requires the calculation of matrix elements of operators on many-body states. The most convenient way to carry out this endeavour is to adopt a diagrammatic representation of the operators and many-body states involved. This leads to more compact results, which can be more easily implemented numerically. The interested reader can find a detailed coverage of this subject in Ref. [153], while here we will only sketch the main practical aspects of diagrammatic techniques.

In diagrammatic notation, we represent a generic many-body state with upward and downward directed lines specifying the orbitals which differ from those in the reference state $|\Phi_0\rangle$. In particular, upward lines are associated to particle states and downward lines to hole states. As an example, using this convention, ket and bra 1p-1h determinants are graphically represented as

$|\Phi_i^a\rangle =$

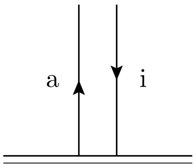

and

$\langle\Phi_i^a| =$

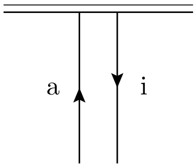

. (4.68)

As no excitations are present in the reference state, we conventionally represent it as empty space. Also operators can be expressed in a diagrammatic form. For a normal-ordered one-body operator we have

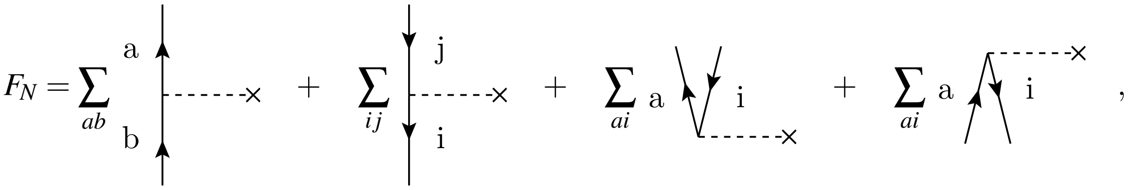

(4.69)

with a dashed line ending with a cross mark representing the action of the operator. These diagrams corresponds to the four contributions that are obtained when replacing explicit particle a, b and hole i, j indices to the generic p, q ones in the sum of Eq. (4.16). Explicitly, they are given by

$$\begin{aligned} F_N = &\sum_{ab} \langle a|f|b\rangle \mathcal{N}[a_a^\dagger a_b] + \sum_{ij} \langle i|f|j\rangle \mathcal{N}[a_i^\dagger a_j] \\ &+ \sum_{ai} \langle a|f|i\rangle \mathcal{N}[a_a^\dagger a_j] + \sum_{ai} \langle i|f|a\rangle \mathcal{N}[a_i^\dagger a_a]. \end{aligned} \tag{4.70}$$

A term-by-term comparison between algebraic and diagrammatic expressions shows that creation and annihilation operators are represented as outgoing and incoming lines with respect to the operator dashed line, respectively. In a similar way, we can picture the two-body part of a normal-ordered two-body operator in the following way

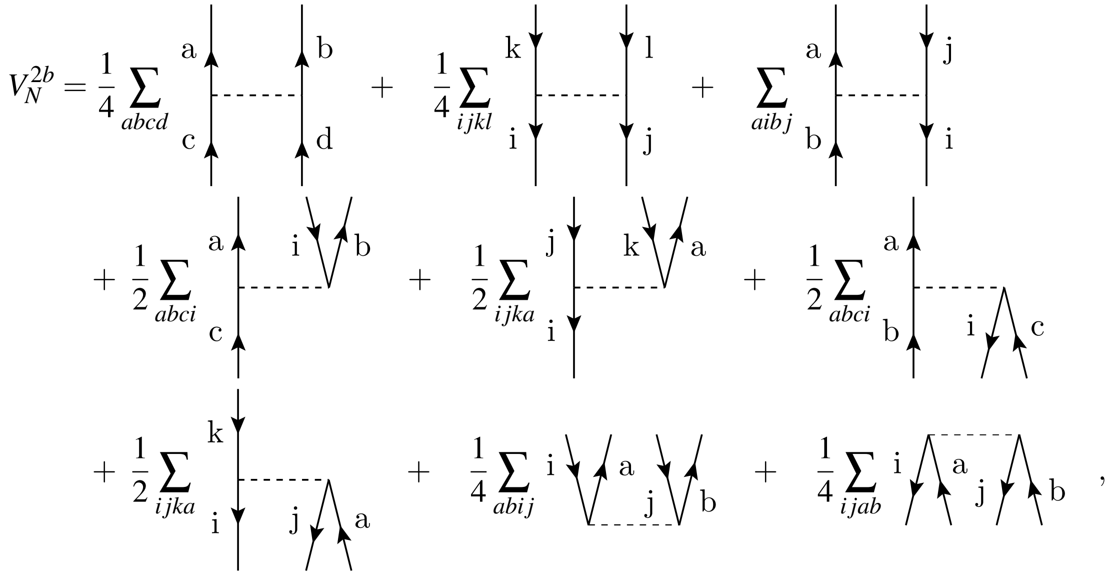

(4.71)

where there is a one-to-one correspondence with the explicit algebraic form

$$\begin{aligned} V_N^{2b} = {} & \frac{1}{4}\sum_{abcd}\langle ab||cd\rangle\,\mathcal{N}[a_a^\dagger a_b^\dagger a_d a_c] + \frac{1}{4}\sum_{ijkl}\langle ij||kl\rangle\,\mathcal{N}[a_i^\dagger a_j^\dagger a_k a_l] \\ & + \sum_{ijab}\langle ai||bj\rangle\,\mathcal{N}[a_a^\dagger a_i^\dagger a_j a_b] + \sum_{abci}\langle ab||ci\rangle\,\mathcal{N}[a_a^\dagger a_b^\dagger a_i a_c] \\ & + \frac{1}{2}\sum_{ijka}\langle ia||jk\rangle\,\mathcal{N}[a_i^\dagger a_a^\dagger a_k a_j] + \frac{1}{2}\sum_{aibc}\langle ai||bc\rangle\,\mathcal{N}[a_a^\dagger a_i^\dagger a_c a_b] \\ & + \frac{1}{2}\sum_{ijka}\langle ij||ka\rangle\,\mathcal{N}[a_i^\dagger a_j^\dagger a_a a_k] + \frac{1}{2}\sum_{abij}\langle ab||ij\rangle\,\mathcal{N}[a_a^\dagger a_b^\dagger a_j a_i] \\ & + \frac{1}{4}\sum_{ijab}\langle ij||ab\rangle\,\mathcal{N}[a_i^\dagger a_j^\dagger a_a a_k]. \end{aligned} \tag{4.72}$$

The presence of numerical factors in the equation above indicates how many equivalent ways of writing each diagram (up to a phase) exist by permuting the lines leaving or entering the left and right vertices.

To simplify the diagrammatic representation, we use the convention that each line without an explicit letter label is summed over all particle or hole indices. Moreover, we remove numerical factors from our graphical rendering. A set of rules reported in Appendix 1 allows to retrieve the correct numerical factors when evaluating full diagrams. We also choose to insert arrows only where necessary. The particle/hole nature of the lines without arrows can be chosen arbitrarily, making sure that lines linked to the same vertex correspond to particle/hole pairs, or it can be deduced from the context. In this simplified form we can picture one-body and two-body operators as

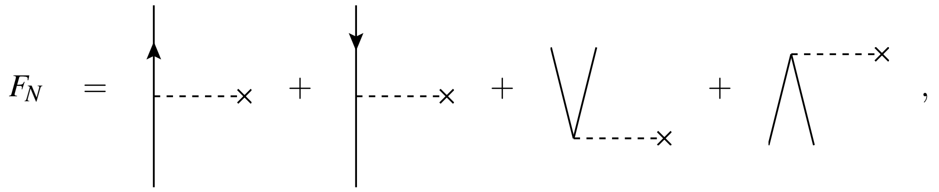

(4.73)

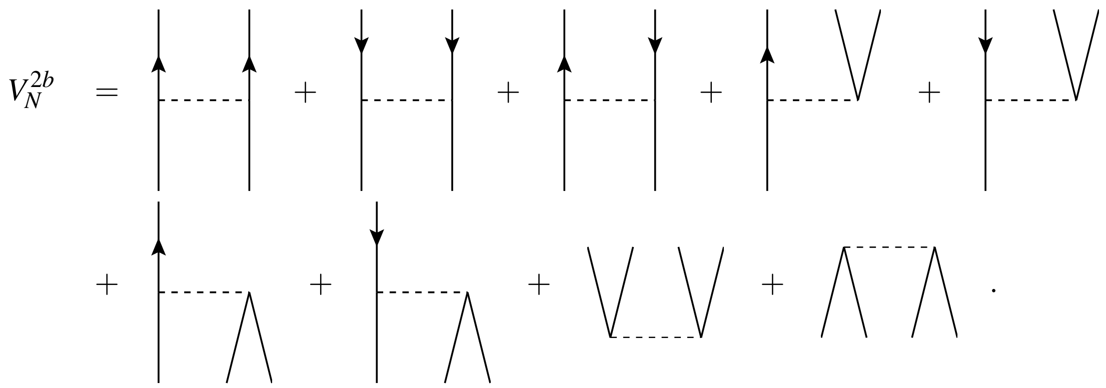

(4.74)

Also the cluster operator T can be expressed in graphical form. In particular, T_1, T_2 and T_3

can be pictured as

$T_1 =$ 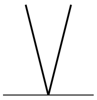 , $T_2 =$ 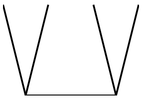 , $T_3 =$ 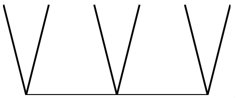 , (4.75)

As T includes only pseudo-creation operator strings, generating excited states of the reference, lines below the horizontal bar are absent. The contrary is valid for their de-excitation counterparts Λ_1, Λ_2 and Λ_3, which are denoted by:

$\Lambda_1 =$ 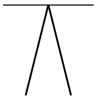 , $\Lambda_2 =$ 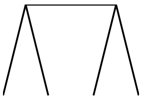 , $\Lambda_3 =$ 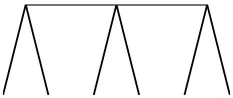 . (4.76)

The EOM-CC operators for excited states R and L can be diagrammatically represented as T and Λ, respectively. We can find a diagrammatic representation also for the mass-number-changing EOM-CC operators. Focusing on the 2PA-EOM-CC case, the 2p-0h and 3p-1h terms of the R^{A+2} and L^{A+2} operators can be graphically represented as

$R^{A+2}_{2\text{p}-0\text{h}} =$ 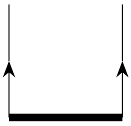 , $R^{A+2}_{3\text{p}-1\text{h}} =$ 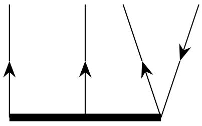 , (4.77)

$L^{A+2}_{2\text{p}-0\text{h}} =$ 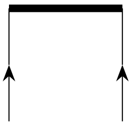 , $L^{A+2}_{3\text{p}-1\text{h}} =$ 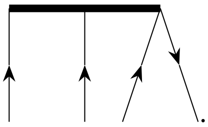 . (4.78)

5 Coupling the Lorentz Integral Transform technique with Coupled-Cluster theory

The coupled-cluster framework described in the previous Chapter allows us to handle the quantum many-body problem for ground- and bound excited-state properties of nuclei at closed shells and in their vicinity. However, this is not sufficient to calculate the nuclear response function. As shown in Chapter 2, the latter is defined as

$$R(\omega) = \sum_{\mu} \langle\Psi_0|\Theta^{\dagger}|\Psi_\mu\rangle\, \langle\Psi_\mu|\Theta|\Psi_0\rangle\, \delta(\omega - E_\mu + E_0), \tag{5.1}$$

where with the index μ we label all the possible final state in the nuclear spectrum, and Θ is a transition operator, e.g., the electric dipole operator. Calculating $R(\omega)$ requires the solution of the so-called "continuum problem". The sum over μ in the above equation, in fact, corresponds to both a sum over discrete excited states and an integral over continuum eigenstates of the Hamiltonian.

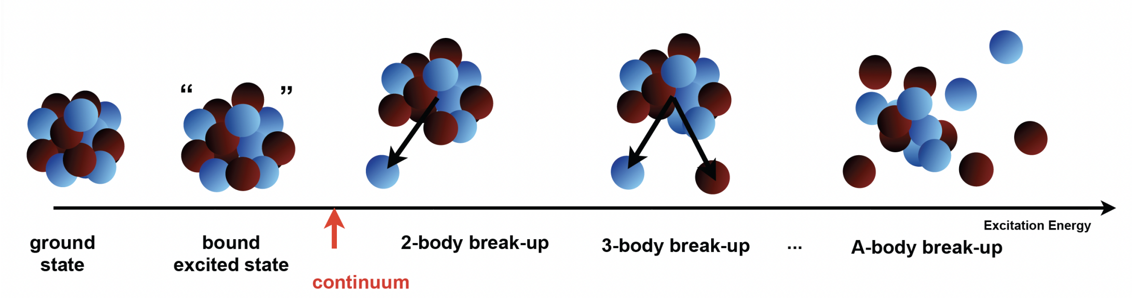

Figure 5.1: Graphical representation of the spectrum of the nucleus. Below the nucleon emission threshold, the system can be excited to excited bound states. Above the nucleon emission threshold, we enter the continuum spectrum. The latter is characterized by different fragmentation channels opening up by progressively increasing the excitation energy. Typically, the two-body break-up channel appears first, then the three-body channel and so on, up to the A-body break-up channel. Figure taken from Ref. [86].

While the calculation of bound excited states can be easily achieved, e.g., using the EOM-CC technique presented in Section 4.3, the description of continuum state wavefunctions represents a formidable task. They in fact contain information on all the possible break-up modes of the nucleus induced by an external probe at a given energy, as well as on the relative motion of the fragments, as graphically shown in Figure 5.1.

In this Chapter we will show how the continuum problem can be circumvented thanks to the use of the Lorentz integral transform (LIT) technique [43]. After reviewing its main aspects, we will illustrate how it can be merged with the coupled-cluster approach in the LIT-CC method for electromagnetic observables of nuclei at closed shells and in their vicinity. We will in particular focus on the extension of the LIT-CC capabilities to two-particle-attached (2PA) systems, characterized by having two valence neutrons outside a closed (sub)shell. This Chapter is mainly based on Refs. [7, 43–45, 86]. We point out that the derivation and implementation of the 2PA-LIT-CC method [7] are part of the original work of this thesis.

5.1 The Lorentz integral transform technique

Let us first show how the determination of an integral transform $\Phi(\sigma)$ of $R(\omega)$ implies a remarkable reduction in the amount of calculations required to determine the nuclear continuum spectrum. While $R(\omega)$ in Eq. (5.1) depends on the ground state $|\Psi_0\rangle$ and all the discrete and continuum excited states $|\Psi_\mu\rangle$, it is possible to prove that the integral transform $\Phi(\sigma)$ can be written as a ground-state expectation value. Such transform is defined by

$$\Phi(\sigma) = \int K(\sigma,\omega) R(\omega) d\omega, \tag{5.2}$$

where $K(\sigma,\omega)$ is a smooth kernel depending on the integration variable, which coincides with the energy ω, and on a parameter σ, in general complex. Substituting Eq. (5.2) in Eq. (5.1) we obtain

$$\begin{aligned}
\Phi(\sigma) &= \int d\omega\, K(\sigma,\omega) \sum_\mu \langle\Psi_0|\Theta^\dagger|\Psi_\mu\rangle \langle\Psi_\mu|\Theta|\Psi_0\rangle\, \delta(\omega - E_\mu + E_0) \\
&= \sum_\mu \langle\Psi_0|\Theta^\dagger|\Psi_\mu\rangle\, K(\sigma, E_\mu - E_0)\, \langle\Psi_\mu|\Theta|\Psi_0\rangle \\
&= \sum_\mu \langle\Psi_0|\Theta^\dagger|\hat{K}(\sigma, H - E_0)|\Psi_\mu\rangle \langle\Psi_\mu|\Theta|\Psi_0\rangle \\
&= \langle\Psi_0|\Theta^\dagger \hat{K}(\sigma, H - E_0)\Theta|\Psi_0\rangle\,,
\end{aligned} \tag{5.3}$$

where we employed the completeness of the Hamiltonian eigenstates

$$\sum_\mu |\Psi_\mu\rangle \langle\Psi_\mu| = \mathbb{1}. \tag{5.4}$$

Therefore, resorting to a transform of $R(\omega)$ we have reduced the continuum problem to the calculation of a ground-state expectation value, as shown in the last step of the derivation of Eq. (5.3). At this point, the only missing piece is the explicit form of the kernel, for which the Lorentzian function has been successfully used in the past. In this case, $K(\sigma, \omega)$ is defined as

$$K(\sigma, \omega) = \frac{\mathrm{Im}(\sigma)}{\pi} \frac{1}{(\omega - \sigma)^*(\omega - \sigma)} = \frac{\sigma_I}{\pi} \frac{1}{(\omega - \sigma_R)^2 + \sigma_I^2}, \tag{5.5}$$

with $\sigma = \sigma_R + i\sigma_I$, where σ_R is the centroid of the Lorentzian and σ_I its half width, as shown in Figure 5.2.

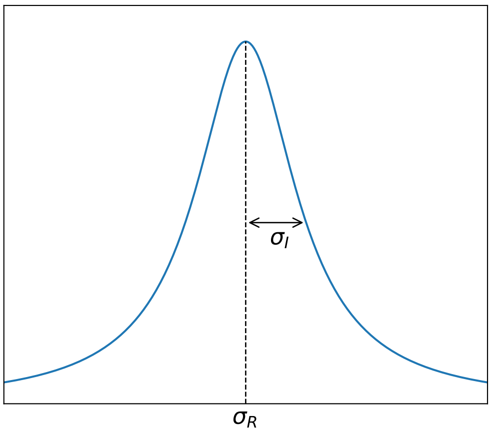

Figure 5.2: Lorentzian function centered in σ_R, with half width at half maximum given by σ_I.

Inserting Eq. (5.5) in Eq. (5.3), the so-called Lorentz integral transform (LIT) of the response function can be written as

$$\begin{aligned} L(\sigma_R, \sigma_I) &= \frac{\sigma_I}{\pi} \int d\omega \, \frac{R(\omega)}{(\omega - \sigma_R)^2 + \sigma_I^2} \\ &= \frac{\sigma_I}{\pi} \langle \Psi_0 | \Theta^\dagger \frac{1}{(H - E_0 - \sigma_R)^2 + \sigma_I^2} \Theta | \Psi_0 \rangle \\ &= \frac{\sigma_I}{\pi} \langle \Psi_0 | \Theta^\dagger \frac{1}{(H - E_0 - \sigma_R + i\sigma_I)(H - E_0 - \sigma_R - i\sigma_I)} \Theta | \Psi_0 \rangle \,. \end{aligned} \tag{5.6}$$

Using the auxiliary states $|\tilde{\Psi}'\rangle$ and $|\tilde{\Psi}\rangle$, defined as

$$\langle \tilde{\Psi}' | = \langle \Psi_0 | \, \Theta^\dagger \frac{1}{(H - E_0 - \sigma_R + i\sigma_I)}, \tag{5.7}$$

and

$$|\tilde{\Psi}\rangle = \frac{1}{(H - E_0 - \sigma_R - i\sigma_I)} \Theta \, |\Psi_0\rangle \,, \tag{5.8}$$

the LIT assumes the form

$$L(\sigma_R,\sigma_I)=\frac{\sigma_I}{\pi}\langle\tilde{\Psi}'|\tilde{\Psi}\rangle\,. \tag{5.9}$$

Therefore, the problem of calculating the sum over all the possible final states has been translated in computing for each value of σ_I and σ_R the auxiliary states $\langle\tilde{\Psi}'|$ and $|\tilde{\Psi}\rangle$, which are solutions of the following inhomogeneous Schrödinger-like equations

$$\langle\tilde{\Psi}'|\,(H-E_0-\sigma_R+i\sigma_I)=\langle\Psi_0|\,\Theta^\dagger, \tag{5.10}$$

$$(H-E_0-\sigma_R-i\sigma_I)\,|\tilde{\Psi}\rangle=\Theta\,|\Psi_0\rangle\,. \tag{5.11}$$

Two comments are in order. First, it is worth observing that although the auxiliary states $\langle\tilde{\Psi}'|$ and $|\tilde{\Psi}\rangle$ are solution of Eqs. (5.10) and (5.11), they do not correspond to physical eigenstates of the Hamiltonian, and they have to be interpreted just as convenient mathematical tools. Second, the source term of Eqs. (5.10) and (5.11) depends on the ground state, which is exponentially damped at $r\to\infty$. As a consequence, $|\tilde{\Psi}'\rangle$ and $|\tilde{\Psi}\rangle$ are localised functions and the solution of Eqs. (5.10) and (5.11) can be determined using bound-state type methods. This allows us to avoid imposing complicated continuous boundary conditions on the asymptotic behaviour of the eigenstates of H at large distances, as it should be done in the calculation of $|\Psi_\mu\rangle$ in Eq. (5.1). If $\Theta^\dagger=\Theta$, the LIT corresponds to the norm of $|\tilde{\Psi}\rangle$. Once $L(\sigma_R,\sigma_I)$ has been computed, $R(\omega)$ can be obtained via a numerical inversion procedure (see Refs. [183, 184] for details).

The LIT method has been originally introduced in the few-body sector [185, 186], and it has been benchmarked in this regime with exact continuum calculations employing Faddeev techniques [187, 188]. Reviews of LIT applications to few-body photoabsorption and electron scattering problems can be found in Refs. [43, 189].

5.2 The Lorentz integral transform - coupled-cluster method

In Refs. [44, 45], the LIT method has been combined with CC theory, leading to the so-called LIT-CC method. Thanks to the favourable computational scaling of CC theory with mass number, this approach has played a crucial role in extending ab initio calculations of electromagnetic observables, as dipole polarizabilities [5,46,49,77] and lepton-nucleus scattering cross sections [190, 191], to the medium-mass region of the nuclear chart. Previously limited to closed-(sub)shell nuclei, it can now also be applied to two-particle attached (2PA) systems, characterized by having two nucleons in addition to a closed-(sub)shell core [7]. The LIT-CC method for 2PA nuclei is the main outcome of this thesis.

Here we will first show how the response function of Eq. (5.1) can be rewritten in the CC formalism for nuclei at closed shells and in their vicinity. We will then derive the LIT equations in both cases and illustrate how to solve them via the Lanczos algorithm.

5.2.1 The similarity transformed response function

Let us now rewrite the response function of Eq. (5.1) in the coupled-cluster formalism. We first introduce the reference state $|\Phi_0\rangle$ and perform normal ordering of the transition operator Θ with respect to $|\Phi_0\rangle$, obtaining $\Theta_N = \Theta - \langle\Phi_0|\Theta|\Phi_0\rangle$. The response then takes the form

$$R(\omega) = \sum_\mu \langle\Psi_0|\Theta_N^\dagger|\Psi_\mu\rangle\,\langle\Psi_\mu|\Theta_N|\Psi_0\rangle\,\delta(\omega - \Delta E_\mu + \Delta E_0), \tag{5.12}$$

where $\Delta E_\mu = E_\mu - H_0$ and $\Delta E_0 = E_0 - H_0$ are the correlation energies with respect to the reference energy H_0 of the excited state μ and the ground state of the nucleus under study, respectively. As explained in Section 4.1.3, since in CC theory we work with normal-ordered Hamiltonians all energies are expressed as energy differences with respect to the uncorrelated reference.

Let us first consider the case of closed-shell nuclei. Employing the exponential ansatz of Eq. (4.24) and the EOM-CC representation of Eqs. (4.45) and (4.46) for right and left excited states, respectively, we get

$$\begin{aligned} R(\omega) &= \sum_\mu \langle\Phi_0|(\mathbb{1}+\Lambda)e^{-T}\Theta_N^\dagger e^T R_\mu|\Phi_0\rangle\,\langle\Phi_0|L_\mu e^{-T}\Theta_N e^T|\Phi_0\rangle\,\delta(\omega - \Delta E_\mu + \Delta E_0) \\ &= \sum_\mu \langle\Phi_0|(\mathbb{1}+\Lambda)\overline{\Theta}^\dagger R_\mu|\Phi_0\rangle\,\langle\Phi_0|L_\mu\overline{\Theta}|\Phi_0\rangle\,\delta(\omega - \omega_\mu), \end{aligned} \tag{5.13}$$

where

$$\overline{\Theta} = e^{-T}\Theta_N e^T \tag{5.14}$$

is the similarity-transformed transition operator, and $\omega_\mu = \Delta E_\mu - \Delta E_0$ is the excitation energy of the state $|\Psi_\mu\rangle$ with respect to the ground state.

The possibility of using the EOM-CC ansatz for open-shell nuclei suggests a straightforward way to extend the LIT-CC method to nuclei in the vicinity of closed shells, characterized by $\pm 1,2$ nucleons with respect to the A-body closed-shell neighbour. Here the starting point $|\Phi_0\rangle$ is the reference state of the closed-shell core calculated with a mass shift $A \pm k$ in the Hamiltonian, where k can be 1 or 2. Using the EOM-CC ansatz of Eqs. (4.57) and (4.58) for the right and left excited states, we obtain

$$R(\omega) = \sum_\mu \langle\Phi_0|L_0^{A\pm k}\overline{\Theta}^\dagger R_\mu^{A\pm k}|\Phi_0\rangle\,\langle\Phi_0|L_\mu^{A\pm k}\overline{\Theta}R_0^{A\pm k}|\Phi_0\rangle\,\delta(\omega - \omega_\mu + \omega_0), \tag{5.15}$$

where we indicate with $R_0^{A\pm k}$ ($L_0^{A\pm k}$) and the EOM excitation (de-excitation) operator associated with the ground state of the $A \pm k$ nucleus. Moreover, we denoted with ω_0 and ω_μ the excitation energies of the ground state and the μ excited states with respect to ΔE_0^*, which is the CC ground-state energy of the A-body closed-shell reference calculated with a mass shift $A \pm k$. In this work, we will in particular focus on the treatment of $A+2$ systems.

5.2.2 The LIT-CC equations for closed-shell nuclei

Let us now calculate the LIT focusing on the case of closed (sub-)shell nuclei. Using Eq. (5.13) for the similarity-transformed response in this case we get

$$\begin{aligned}
L(\sigma_R,\sigma_I) &= \frac{\sigma_I}{\pi}\int d\omega \frac{1}{(\omega-\sigma_R)^2+\sigma_I^2}\sum_\mu \langle\Phi_0|(\mathbb{1}+\Lambda)\overline{\Theta}^\dagger R_\mu|\Phi_0\rangle\,\langle\Phi_0|L_\mu\overline{\Theta}|\Phi_0\rangle\,\delta(\omega-\omega_\mu) \\
&= \frac{\sigma_I}{\pi}\sum_\mu \langle\Phi_0|(\mathbb{1}+\Lambda)\overline{\Theta}^\dagger R_\mu|\Phi_0\rangle\,\langle\Phi_0|L_\mu\overline{\Theta}|\Phi_0\rangle\,\frac{1}{(\Delta E_\mu-\Delta E_0-\sigma_R)^2+\sigma_I^2} \\
&= \frac{\sigma_I}{\pi}\sum_\mu \langle\Phi_0|(\mathbb{1}+\Lambda)\overline{\Theta}^\dagger(\Delta E_\mu-\Delta E_0-\sigma_R+i\sigma_I)^{-1}R_\mu|\Phi_0\rangle \\
&\quad\times\langle\Phi_0|L_\mu(\Delta E_\mu-\Delta E_0-\sigma_R-i\sigma_I)^{-1}\overline{\Theta}|\Phi_0\rangle \\
&= \frac{\sigma_I}{\pi}\sum_\mu \langle\Phi_0|(\mathbb{1}+\Lambda)\overline{\Theta}^\dagger(\overline{H}-\Delta E_0-\sigma_R+i\sigma_I)^{-1}R_\mu|\Phi_0\rangle \\
&\quad\times\langle\Phi_0|L_\mu(\overline{H}-\Delta E_0-\sigma_R-i\sigma_I)^{-1}\overline{\Theta}|\Phi_0\rangle \\
&= \frac{\sigma_I}{\pi}\langle\Phi_0|(\mathbb{1}+\Lambda)\overline{\Theta}^\dagger(\overline{H}-\Delta E_0-\sigma_R+i\sigma_I)^{-1}(\overline{H}-\Delta E_0-\sigma_R-i\sigma_I)^{-1}\overline{\Theta}|\Phi_0\rangle\,.
\end{aligned} \tag{5.16}$$

To obtain the above result we followed a procedure similar to Eq. (5.3), where we employed the EOM-CC equations for left and right excited states (Eqs. (4.48) and (4.47), respectively), and Eq. (4.50) for their completeness relation. We dropped for convenience the subscript N in $\overline{H}_N$. Defining the complex variable $z=\Delta E_0+\sigma_R+i\sigma_I$, we can rewrite Eq. (5.16) as

$$L(z)=\frac{\sigma_I}{\pi}\langle\Phi_0|(\mathbb{1}+\Lambda)\overline{\Theta}^\dagger(\overline{H}-z^*)^{-1}(\overline{H}-z)^{-1}\overline{\Theta}|\Phi_0\rangle\,. \tag{5.17}$$

Using the equality

$$\frac{1}{(\overline{H}-z^*)(\overline{H}-z)}=-\frac{i}{2\sigma_i}\left[\frac{1}{\overline{H}-z}-\frac{1}{\overline{H}-z^*}\right], \tag{5.18}$$

and introducing the auxiliary states

$$\begin{aligned}
|\Psi_R(z^*)\rangle &= (\overline{H}-z^*)^{-1}\overline{\Theta}\,|\Phi_0\rangle\,, \\
|\Psi_R(z)\rangle &= (\overline{H}-z)^{-1}\overline{\Theta}\,|\Phi_0\rangle\,,
\end{aligned} \tag{5.19}$$

we obtain

$$L(z)=-\frac{i}{2\pi}\Big[\langle\Phi_0|(\mathbb{1}+\Lambda)\overline{\Theta}^\dagger|\Psi_R(z)\rangle-\langle\Phi_0|(\mathbb{1}+\Lambda)\overline{\Theta}^\dagger|\Psi_R(z^*)\rangle\Big]\,. \tag{5.20}$$

Therefore, our calculation of the LIT depends entirely on the auxiliary states $|\Psi_R(z^*)\rangle$, $|\Psi_R(z)\rangle$. We can assume that the latter are determined by the action of an excitation operator on top of the reference state, in analogy to the EOM-CC ansatz of Section 4.3, as

$$\begin{aligned} |\Psi_R(z)\rangle &= \mathscr{R}(z)\,|\Phi_0\rangle\,, \\ |\Psi_R(z^*)\rangle &= \mathscr{R}(z^*)\,|\Phi_0\rangle\,, \end{aligned} \tag{5.21}$$

with

$$\mathscr{R}(z) = r_0(z) + \sum_{ai} r_i^a(z) a_a^\dagger a_i + \frac{1}{4}\sum_{abij} r_{ij}^{ab}(z) a_a^\dagger a_b^\dagger a_j a_i + \dots\,, \tag{5.22}$$

$$\mathscr{R}(z^*) = r_0(z^*) + \sum_{ai} r_i^a(z^*) a_a^\dagger a_i + \frac{1}{4}\sum_{abij} r_{ij}^{ab}(z^*) a_a^\dagger a_b^\dagger a_j a_i + \dots\,. \tag{5.23}$$

The amplitudes of the $\mathscr{R}$ operators of Eq. (5.22) and (5.23) are obtained solving

$$\begin{aligned} (\overline{H} - z)\mathscr{R}(z)\,|\Phi_0\rangle &= \overline{\Theta}\,|\Phi_0\rangle\,, \\ (\overline{H} - z^*)\mathscr{R}(z^*)\,|\Phi_0\rangle &= \overline{\Theta}\,|\Phi_0\rangle\,, \end{aligned} \tag{5.24}$$

which we will refer to as the LIT-CC equations for closed-shell systems. We notice that the equations in (5.24) correspond to EOM-CC equations with a source term, and they represents the coupled-cluster equivalent of Eqs. (5.10) and (5.11).

5.2.3 The LIT-CC equations for nuclei in the vicinity of closed shells

The calculation of the LIT for nuclei in the vicinity of closed (sub-)shells follows an analogous reasoning with respect to the previous Section. In this case, our starting point is Eq. (5.15). Focusing on the case of 2PA nuclei, the LIT can be rewritten as

$$\begin{aligned} L_{A+2}(\sigma_R,\sigma_I) &= \frac{\sigma_I}{\pi}\int d\omega \frac{1}{(\omega-\sigma_R)^2+\sigma_I^2} \\ &\quad \times \sum_\mu \langle\Phi_0|L_0^{A+2}\overline{\Theta^\dagger} R_\mu^{A+2}|\Phi_0\rangle\,\langle\Phi_0|L_\mu^{A+2}\overline{\Theta} R_0^{A+2}|\Phi_0\rangle\,\delta(\omega-\omega_\mu+\omega_0) \\ &= \frac{\sigma_I}{\pi}\sum_\mu \langle\Phi_0|L_0^{A+2}\overline{\Theta}^\dagger R_\mu^{A+2}|\Phi_0\rangle\,\langle\Phi_0|L_\mu^{A+2}\overline{\Theta} R_0^{A+2}|\Phi_0\rangle\,\frac{1}{(\Delta E_\mu-\Delta E_0-\sigma_R)^2+\sigma_I^2} \\ &= \frac{\sigma_I}{\pi}\sum_\mu \langle\Phi_0|L_0^{A+2}\overline{\Theta}^\dagger(\overline{H}-\Delta E_0-\sigma_R+i\sigma_I)^{-1}R_\mu^{A+2}|\Phi_0\rangle \\ &\quad \times \langle\Phi_0|L_\mu^{A+2}(\overline{H}-\Delta E_0-\sigma_R-i\sigma_I)^{-1}\overline{\Theta} R_0^{A+2}|\Phi_0\rangle \\ &= \frac{\sigma_I}{\pi}\,\langle\Phi_0|L_0^{A+2}\overline{\Theta^\dagger}(\overline{H}-\Delta E_0-\sigma_R+i\sigma_I)^{-1}(\overline{H}-\Delta E_0-\sigma_R-i\sigma_I)^{-1}\overline{\Theta} R_0^{A+2}|\Phi_0\rangle\,. \end{aligned} \tag{5.25}$$

Also in this case, using the completeness of the Hamiltonian eigenstates, we can express the LIT as an expectation value on the reference state. Introducing the variable $z = \Delta E_0 + \sigma +$

$i\sigma_I$, we can express the LIT in the form

$$L_{A+2}(z) = \frac{\sigma_I}{\pi} \langle\Phi_0|L_0^{A+2}\overline{\Theta}^\dagger(\overline{H}-z^*)^{-1}(\overline{H}-z)^{-1}\overline{\Theta}R_0^{A+2}|\Phi_0\rangle\,. \tag{5.26}$$

Using Eq. (5.18) and introducing the auxiliary states

$$\begin{aligned} |\Psi_R^{A+2}(z^*)\rangle &= (\overline{H}-z^*)^{-1}\overline{\Theta}R_0^{A+2}\,|\Phi_0\rangle\,, \\ |\Psi_R^{A+2}(z)\rangle &= (\overline{H}-z)^{-1}\overline{\Theta}R_0^{A+2}\,|\Phi_0\rangle\,, \end{aligned} \tag{5.27}$$

we obtain

$$L_{A+2}(z) = -\frac{i}{2\pi}\left[\langle\Phi_0|L_0^{A+2}\overline{\Theta}^\dagger|\Psi_R^{A+2}(z)\rangle - \langle\Phi_0|L_0^{A+2}\overline{\Theta}^\dagger|\Psi_R^{A+2}(z^*)\rangle\right]. \tag{5.28}$$

We observe that the form of $|\Psi_R^{A+2}(z)\rangle$ and $|\Psi_R^{A+2}(z^*)\rangle$ in Eq. (5.27) becomes more involved, as the additional application of the R_0^{A+2} operator is needed to produce a 2PA state. For closed-shell nuclei, this simply reduces to the identity.

In analogy to the closed-shell case, we can find a suitable excitation operator building the auxiliary states of the open-shell nucleus starting from the closed-shell reference. In the 2PA case, such an operator must involve a net creation of 2 nucleons. The ansatz then becomes

$$\begin{aligned} |\Psi_R^{A+2}(z)\rangle &= \mathscr{R}^{A+2}(z)\,|\Phi_0\rangle = \left(\frac{1}{2}\sum_{ab} r^{ab}(z)a_a^\dagger a_b^\dagger + \frac{1}{6}\sum_{abci} r_i^{abc}(z)a_a^\dagger a_b^\dagger a_c^\dagger a_i + \dots\right)|\Phi_0\rangle\,, \\ |\Psi_R^{A+2}(z^*)\rangle &= \mathscr{R}^{A+2}(z^*)\,|\Phi_0\rangle = \left(\frac{1}{2}\sum_{ab} r^{ab}(z^*)a_a^\dagger a_b^\dagger + \frac{1}{6}\sum_{abci} r_i^{abc}(z^*)a_a^\dagger a_b^\dagger a_c^\dagger a_i + \dots\right)|\Phi_0\rangle\,. \end{aligned} \tag{5.29}$$

The 2PA amplitudes of Eq. (5.29) are determined by solving

$$\begin{aligned} (\overline{H}-z)\mathscr{R}^{A+2}(z)\,|\Phi_0\rangle &= \overline{\Theta}R_0^{A+2}\,|\Phi_0\rangle\,, \\ (\overline{H}-z^*)\mathscr{R}^{A+2}(z^*)\,|\Phi_0\rangle &= \overline{\Theta}R_0^{A+2}\,|\Phi_0\rangle\,, \end{aligned} \tag{5.30}$$

which take the name of 2PA-LIT-CC equations. They resemble the 2PA-EOM-CC equation in (4.67), with the addition of a source term.

Two comments are in order. First, the two main differences between the 2PA-LIT-CC approach and the standard closed-shell technique lie in the form of the $\mathscr{R}^{A+2}(z)$ and $\mathscr{R}^{A+2}(z^*)$ operators, corresponding to mass-number-changing EOM excitation operators in the 2PA case, and in the source term, involving a product between $\overline{\Theta}$ and a 2PA operator for 2PA nuclei. Second, changing accordingly the shape of such operators, the same ansatz can be applied to write the LIT-CC equations not only for nuclei with $A^* = A+2$, but in general for open-shell systems with $A^* = A \pm k$, with $k = 1,2$.

The new approach developed in this thesis for 2PA nuclei takes the name of 2PA-LIT-CC method.

5.2.4 Non-symmetric Lanczos algorithm

To obtain the LIT, we should solve for every value of z and z^* Eqs. (5.24) and (5.30) for closed-shell and 2PA nuclei, respectively. This is not necessary if we rewrite the LIT in matrix form and apply the Lanczos algorithm. Let us focus first on the closed-shell case. Starting from Eq. (5.17), we can write

$$\begin{aligned} L(z) &= -\frac{i}{2\pi}\langle\Phi_0|(\mathbb{1}+\Lambda)\overline{\Theta^\dagger}\left(\frac{1}{\overline{H}-z}-\frac{1}{\overline{H}-z^*}\right)\overline{\Theta}|\Phi_0\rangle \\ &= -\frac{i}{2\pi}\mathbf{S}^L\left[(\mathbf{M}-z)^{-1}-(\mathbf{M}-z^*)^{-1}\right]\mathbf{S}^R, \end{aligned} \tag{5.31}$$

where the matrix elements $M_{\alpha,\alpha'}$ of $\mathbf{M}$ and the components S^R_α and S^L_α of the row and column vectors $\mathbf{S}^L$ and $\mathbf{S}^R$ are given by

$$M_{\alpha,\alpha'} = \langle\Phi_{\alpha'}|\overline{H}|\Phi_\alpha\rangle\,, \tag{5.32}$$

$$S^R_\alpha = \langle\Phi_\alpha|\overline{\Theta}|\Phi_0\rangle\,, \tag{5.33}$$

$$S^L_\alpha = \langle\Phi_0|(\mathbb{1}+\Lambda)\overline{\Theta^\dagger}|\Phi_\alpha\rangle\,, \tag{5.34}$$

and the indices α,α' run over the basis of np-nh states, namely

$$|\Phi_0\rangle\,,|\Phi_i^a\rangle = a_a^\dagger a_i^\dagger\,|\Phi_0\rangle\,,|\Phi_{ij}^{ab}\rangle = a_a^\dagger a_b^\dagger a_j a_i\,|\Phi_0\rangle\,,\dots\;. \tag{5.35}$$

We point out that the product between $\mathbf{S}^L$ and $\mathbf{S}^R$ corresponds to

$$\mathbf{S}^L\mathbf{S}^R = \langle\Phi_0|(\mathbb{1}+\Lambda)\overline{\Theta^\dagger}\overline{\Theta}|\Phi_0\rangle\,. \tag{5.36}$$

Also in the 2PA case, starting from Eq. (5.26) we can express the LIT in matrix notation, obtaining

$$\begin{aligned} L_{A+2}(z) &= -\frac{i}{2\pi}\langle\Phi_0|L_0^{A+2}\overline{\Theta^\dagger}\left(\frac{1}{\overline{H}-z}-\frac{1}{\overline{H}-z^*}\right)\overline{\Theta}R_0^{A+2}|\Phi_0\rangle \\ &= -\frac{i}{2\pi}\mathbf{S}^L_{2\mathrm{PA}}\left[(\mathbf{M}-z)^{-1}-(\mathbf{M}-z^*)^{-1}\right]\mathbf{S}^R_{2\mathrm{PA}}. \end{aligned} \tag{5.37}$$

In the above equation, the matrix $\mathbf{M}$ as well as the vectors $\mathbf{S}^R_{2\mathrm{PA}}$ and $\mathbf{S}^L_{2\mathrm{PA}}$ are expanded on the set of states involving a net creation of two nucleons on top of the closed-shell reference

$$|\Phi_{ab}\rangle = a_a^\dagger a_b^\dagger\,|\Phi_0\rangle\,,|\Phi_i^{abc}\rangle = a_a^\dagger a_b^\dagger a_c^\dagger a_i\,|\Phi_0\rangle\,,\dots\;. \tag{5.38}$$

It is worth recalling here that the reference state used in 2PA calculations includes a mass shift $A^* = A+2$ in the Hamiltonian. Using the indices α,α' to design the set of states in Eq. (5.38), we obtain

$$M_{\alpha,\alpha'} = \langle\Phi_{\alpha'}|\overline{H}|\Phi_\alpha\rangle\,, \tag{5.39}$$

$$S^R_{2\mathrm{PA},\alpha} = \langle \Phi_\alpha | \overline{\Theta} R_0^{A+2} | \Phi_0 \rangle \,, \tag{5.40}$$

$$S^L_{2\mathrm{PA},\alpha} = \langle \Phi_0 | L_0^{A+2} \overline{\Theta^\dagger} | \Phi_\alpha \rangle \,. \tag{5.41}$$

Since the similarity-transformed Hamiltonian is non-Hermitian, we employ the complex-symmetric variant of the Lanczos algorithm [192]. Given a $n \times n$ non-symmetric matrix A, the latter allows to define a right and left set of orthonormal states, known as the left and right Lanczos bases, in which A assumes a tridiagonal form, i.e., it can be represented as

$$A = \begin{pmatrix} a_0 & b_1 & 0 & 0 & 0 & \dots & 0 \\ b_1 & a_1 & b_2 & 0 & 0 & \dots & 0 \\ 0 & b_2 & a_2 & b_3 & 0 & \dots & 0 \\ 0 & 0 & b_3 & a_3 & b_4 & \dots & 0 \\ \dots & \dots & \dots & \dots & \dots & \dots & 0 \\ \dots & \dots & \dots & \dots & \dots & \dots & b_{m-1} \\ 0 & 0 & 0 & 0 & 0 & \dots & a_m \end{pmatrix}, \tag{5.42}$$

where $m < n$. To achieve this, as a first step, two pivot vectors $\mathbf{w}_0$ and $\mathbf{v}_0$ are chosen, such that $\mathbf{w}_0\mathbf{v}_0 = 1$. We also set $\mathbf{w}_{-1} = \mathbf{v}_{-1} = 0$ and $b_0 = 0$. Then for each $i = 0, \dots, m \leq n-1$, we can calculate the matrix elements of the triadiagonal matrix corresponding to A via

$$a_i = \mathbf{w}_i A \mathbf{v}_i, \tag{5.43}$$

$$\mathbf{p}_i = A\mathbf{v}_i - a_i\mathbf{v}_i - b_i\mathbf{v}_{i-1}, \tag{5.44}$$

$$\mathbf{s}_i = \mathbf{w}_i A - a_i\mathbf{w}_i - b_i\mathbf{w}_{i-1}, \tag{5.45}$$

$$b_{i+1} = \sqrt{\mathbf{s}_i\mathbf{p}_i}, \tag{5.46}$$

$$\mathbf{v}_{i+1} = \frac{\mathbf{p}_i}{b_{i+1}}, \qquad \mathbf{w}_{i+1} = \frac{\mathbf{s}_i}{b_{i+1}}. \tag{5.47}$$

Despite being relatively straightforward, the Lanczos algorithm is often affected by numerical instability. In fact increasing the number of iterations a loss of orthogonality in the Lanczos vectors $\mathbf{w}_i$ and $\mathbf{v}_i$ could occur. For this reason, our implementation is accompanied by an additional two-sided Gram-Schmidt orthogonalization step.

In the closed-shell LIT-CC approach, we define the right and left Lanczos pivots as

$$\mathbf{v}_0 = \mathbf{S}^R / \sqrt{\mathbf{S}^L\mathbf{S}^R}, \tag{5.48}$$

$$\mathbf{w}_0 = \mathbf{S}^L / \sqrt{\mathbf{S}^L\mathbf{S}^R}, \tag{5.49}$$

while in the 2PA-LIT-CC framework, they are given by

$$\mathbf{v}_0^{2\mathrm{PA}} = \mathbf{S}^R_{2\mathrm{PA}} / \sqrt{\mathbf{S}^L_{2\mathrm{PA}}\mathbf{S}^R_{2\mathrm{PA}}}, \tag{5.50}$$

$$\mathbf{w}_0^{2\mathrm{PA}} = \mathbf{S}^L_{2\mathrm{PA}} / \sqrt{\mathbf{S}^L_{2\mathrm{PA}}\mathbf{S}^R_{2\mathrm{PA}}}. \tag{5.51}$$

As the introduction of the 2PA-LIT-CC method represents the novelty of this thesis, we will now focus how the Lanczos algorithm simplifies the calculation of the LIT in the 2PA case. A detailed treatment of the application of the Lanczos algorithm in the closed-shell LIT-CC approach can be found in Refs. [45, 86].

Applying the complex-symmetric Lanczos algorithm outlined above, the matrix $(\mathbf{M}-z)$ can be expressed in the following form

$$(\mathbf{M}-z)=\begin{pmatrix} a_0-z & b_1 & 0 & 0 & 0 & \dots & 0 \\ b_1 & a_1-z & b_2 & 0 & 0 & \dots & 0 \\ 0 & b_2 & a_2-z & b_3 & 0 & \dots & 0 \\ 0 & 0 & b_3 & a_3-z & b_4 & \dots & 0 \\ \dots & \dots & \dots & \dots & \dots & \dots & 0 \\ \dots & \dots & \dots & \dots & \dots & \dots & b_{m-1} \\ 0 & 0 & 0 & 0 & 0 & \dots & a_m-z \end{pmatrix} \tag{5.52}$$

with $z=\Delta E_0+\sigma_R+i\sigma_I$. An analogous expression can be obtained for $(\mathbf{M}-z^*)$. Using Eqs. (5.50), (5.51) and the tridiagonal representation of $(\mathbf{M}-z)$ and $(\mathbf{M}-z^*)$, we can rewrite Eq. (5.37) as

$$L_{A+2}(z)=-\frac{i}{2\pi}\left(\mathbf{S}^L_{2\mathrm{PA}}\mathbf{S}^R_{2\mathrm{PA}}\right)\mathbf{w}_0^{2\mathrm{PA}}\left[(\mathbf{M}-z)^{-1}-(\mathbf{M}-z^*)^{-1}\right]\mathbf{v}_0^{2\mathrm{PA}}, \tag{5.53}$$

with

$$\mathbf{S}^L_{2\mathrm{PA}}\mathbf{S}^R_{2\mathrm{PA}}=\langle\Phi_0|L_0^{A+2}\overline{\Theta^\dagger}\overline{\Theta}R_0^{A+2}|\Phi_0\rangle\,. \tag{5.54}$$

From the definition of the identity, we obtain:

$$\begin{aligned} (\mathbf{M}-z)(\mathbf{M}-z)^{-1}=\mathbb{1}\rightarrow\sum_k(\mathbf{M}-z)_{ik}\{(\mathbf{M}-z^*)^{-1}\}_{kj}=\delta_{ij}, \\ (\mathbf{M}-z^*)(\mathbf{M}-z^*)^{-1}=\mathbb{1}\rightarrow\sum_k(\mathbf{M}-z^*)_{ik}\{(\mathbf{M}-z^*)^{-1}\}_{kj}=\delta_{ij}. \end{aligned} \tag{5.55}$$

Setting $j=0$ and introducing the vectors

$$x_k(z)=\{(\mathbf{M}-z)^{-1}\}_{k0},\quad x_k(z^*)=\{(\mathbf{M}-z^*)^{-1}\}_{k0}, \tag{5.56}$$

we can rewrite the equalities in (5.55) in the form of two linear systems

$$\begin{aligned} \sum_k(\mathbf{M}-z)_{ik}x_k(z)=\delta_{i0}, \\ \sum_k(\mathbf{M}-z^*)_{ik}x_k(z^*)=\delta_{i0}. \end{aligned} \tag{5.57}$$

Observing that $x_0(z)$ corresponds to $\mathbf{w}_0^{2\mathrm{PA}}(\mathbf{M}-z)^{-1}\mathbf{v}_0^{2\mathrm{PA}}$ and $x_0(z^*)$ to $\mathbf{w}_0^{2\mathrm{PA}}(\mathbf{M}-z^*)^{-1}\mathbf{v}_0^{2\mathrm{PA}}$, Eq. (5.53) becomes

$$L_{A+2}(z) = -\frac{i}{2\pi}\left(\mathbf{S}^{L}_{\text{2PA}}\mathbf{S}^{R}_{\text{2PA}}\right)\left[x_0(z) - x_0(z^*)\right]. \tag{5.58}$$

The evaluation of the LIT then reduces to computing $x_0(z)$ and $x_0(z^*)$. The latter correspond to the solution of the linear systems in (5.57), and they can be found by applying Cramer's rule. Given a linear system $A\mathbf{x} = \mathbf{b}$, the components of the vector $\mathbf{x}$ are determined by

$$x_i = \frac{\det\left[(A)_i\right]}{\det\left[A\right]}, \tag{5.59}$$

where $(A)_i$ is the matrix obtained by replacing the i-th column of A with the column vector $\mathbf{b}$. In our case, focusing on $x_0(z)$, this translates to

$$x_0(z) = \frac{\det\left[(\mathbf{M}-z)_0\right]}{\det\left[(\mathbf{M}-z)\right]} = \frac{\det\left[P\right]}{(a_0-z)\det\left[P\right] - b_1\det\left[P_0\right]} = \frac{1}{(a_0-z) - b_1\frac{\det[P_0]}{\det[P]}}, \tag{5.60}$$

where

$$P = \begin{pmatrix} a_1-z & b_2 & 0 & \dots \\ b_2 & a_2-z & b_3 & \dots \\ 0 & b_3 & a_3-z & \dots \\ \dots & \dots & \dots & \dots \end{pmatrix}, \quad P_0 = \begin{pmatrix} b_1 & b_2 & 0 & \dots \\ 0 & a_2-z & b_3 & \dots \\ 0 & b_3 & a_3-z & \dots \\ \dots & \dots & \dots & \dots \end{pmatrix}. \tag{5.61}$$

In turn, we obtain

$$\frac{\det\left[P_0\right]}{\det\left[P\right]} = \frac{b_1\det\left[Q\right]}{(a_1-z)\det\left[Q\right] - b_2\det\left[Q_0\right]} = \frac{b_1}{(a_1-z) - b_2\frac{\det[Q_0]}{\det[Q]}}, \tag{5.62}$$

where

$$Q = \begin{pmatrix} a_2-z & b_3 & 0 & \dots \\ b_3 & a_3-z & b_4 & \dots \\ 0 & b_4 & a_4-z & \dots \\ \dots & \dots & \dots & \dots \end{pmatrix}, \quad Q_0 = \begin{pmatrix} b_2 & b_3 & 0 & \dots \\ 0 & a_3-z & b_4 & \dots \\ 0 & b_4 & a_4-z & \dots \\ \dots & \dots & \dots & \dots \end{pmatrix}. \tag{5.63}$$

Eqs. (5.60) and (5.62) show that each determinant ratio occurring in $x_0(z)$ is characterized by the same structure. Generalizing this to the full size n of $(\mathbf{M}-z)$, we get

$$x_0(z) = \frac{1}{(a_0-z) - \frac{b_1^2}{(a_1-z) - \frac{b_1^2}{(a_2-z) - \frac{b_3^2}{(a_3-z) - \dots}}}}, \tag{5.64}$$

and analogously for $x_0(z^*)$

$$x_0(z^*) = \frac{1}{(a_0 - z^*) - \frac{b_1^2}{(a_1 - z^*) - \frac{b_1^2}{(a_2 - z^*) - \frac{b_3^2}{(a_3 - z^*) - \dots}}}}. \tag{5.65}$$

Therefore, the LIT of Eq. (5.58) correspond to a difference of continued fractions of Lanczos coefficients

$$L_{A+2}(z) = -\frac{i}{2\pi} \left(\mathbf{S}^L_{2\mathrm{PA}} \mathbf{S}^R_{2\mathrm{PA}}\right) \left[\frac{1}{a_0 - z + \frac{b_1^2}{a_1 - z + \frac{b_2^2}{a_2 - z + b_3^2 \dots}}} - \frac{1}{a_0 - z^* + \frac{b_1^2}{a_1 - z^* + \frac{b_2^2}{a_2 - z^* + b_3^2 \dots}}} \right]. \tag{5.66}$$

The use of the Lanczos algorithm makes the calculation of the LIT very efficient. In fact, the LIT for different values of σ_R and σ_I can be computed by performing the tridiagonalization of the $\mathbf{M}$ matrices only once. The knowledge of the Lanczos coefficients allows to vary the LIT parameters trivially, while calculating the LIT via Eq. (5.28) requires to solve the LIT-CC equations as many times as all the possible combinations of σ_R and σ_I values.

5.3 Moments of the response function

Starting from the LIT, one can easily obtain an estimate of the electromagnetic sum rules, i.e., the moments of the response function interpreted as a distribution function. Knowing all the moments is equivalent to knowing the distribution itself. However, it is sometimes easier to compute just a few moments of a distribution rather than the full distribution, and yet obtain substantial insights into the dynamics of a quantum system.

As mentioned in Chapter 2, the moments (or sum rules) of the response function are defined as[1]

$$m_n = \int d\omega\, \omega^n R(\omega), \tag{5.67}$$

where n is an integer. Because in the limit $\sigma_I \to 0$ the Lorentzian kernel becomes a delta function, we have that

$$L(\sigma_R, \sigma_I \to 0) = \int d\omega\, R(\omega) \delta(\omega - \sigma_R) = R(\sigma_R), \tag{5.68}$$

i.e., the moments can be computed from the LIT as

$$m_n = \lim_{\sigma_I \to 0} \int d\sigma_R\, \sigma_R^n L(\sigma_R, \sigma_I). \tag{5.69}$$

---

[1] For moments of the response, the integration range in excitation energy corresponds to $[0, \infty]$ unless otherwise specified.

In this limit, the LIT takes the form of a discretized response function, given by smeared δ-peaks. While the latter does not properly account for the continuum, the use of Eq. (5.69) has been proved to be equivalent to the integration of $R(\omega)$ obtained from the inversion [46]. This gives us the advantage of avoiding this additional step, which can contribute substantially to the numerical uncertainty budget.

Let us consider here specific sum rules which will be analysed in the rest of this work.

- **Non-energy-weighted sum rule.** The non-energy-weighted sum rule or m_0 sum rule, defined as
$$m_0 = \int d\omega\, R(\omega) = \lim_{\sigma_I \to 0} \int d\sigma_R\, L(\sigma_R, \sigma_I), \tag{5.70}$$
correspond to the total strength of the response function. This quantity can also be calculated as a ground-state expectation value. In fact, it corresponds to the product $\mathbf{S}^L\mathbf{S}^R$ of Eq. (5.36) in closed-shell LIT-CC and to $\mathbf{S}^L_{2\mathrm{PA}}\mathbf{S}^R_{2\mathrm{PA}}$, defined in Eq. (5.54), in the 2PA framework. Comparing such products with the corresponding result for m_0 from Eq. (5.70) represents a good consistency check. In Chapter 6, we will use m_0 as a benchmark observable for our numerical implementation of the 2PA-LIT-CC method.

- **Inverse energy-weighted sum rule.** The inverse energy-weighted sum rule or m_{-1} is particularly sensitive to the low-energy states in the response function. Focusing on electric dipole transitions, the electric dipole polarizability is related to the inverse energy-weighted dipole sum rule by
$$\alpha_D = 2\alpha m_{-1} = 2\alpha \lim_{\sigma_I \to 0} \int d\sigma_R\, \frac{L(\sigma_R, \sigma_I)}{\sigma_R}. \tag{5.71}$$
Calculations of α_D for closed-shell and 2PA nuclei will represent the main core of Chapter 6.

- **Energy-weighted sum rule.** The energy-weighted sum rule or m_1 is defined as
$$m_1 = \int d\omega\, \omega\, R(\omega) = \lim_{\sigma_I \to 0} \int d\sigma_R\, \sigma_R\, L(\sigma_R, \sigma_I). \tag{5.72}$$
The energy-weighted sum rule can be used to estimate the position of giant resonances. In particular, as mentioned in Chapter 2, the mean energy E_{ISGMR} of the isoscalar giant monopole resonance (ISGMR) can be evaluated as the ratio
$$E_{\mathrm{ISGMR}} = \sqrt{\frac{m_1}{m_{-1}}} \tag{5.73}$$
between the energy-weighted and inverse energy-weighted isoscalar monopole sum rules. In Chapter 6, we will use this to estimate the incompressibility K_A of a A-body nucleus. Considering instead electric dipole excitations, the m_1 dipole sum rule can be connected to the photoabsoption cross section $\sigma_\gamma(\omega)$. In the so-called unretarded

dipole approximation, valid at low energy, $\sigma_\gamma(\omega)$ can be written solely in terms of the dipole response function as

$$\sigma_\gamma(\omega) = 4\pi^2 \alpha \omega R(\omega). \tag{5.74}$$

An extensive proof of Eq. (5.74) can be found in Ref. [86]. Combining Eq. (5.74) with Eq. (5.72), we get that m_1 is proportional to the integral of the photoabsorption cross section

$$m_1 = \frac{1}{4\pi^2\alpha} \int d\omega \, \sigma_\gamma(\omega). \tag{5.75}$$

In Chapter 6, we will calculate the energy-weighted dipole sum rule m_1 in selected cases to analyse the high-energy part of the dipole-excited spectrum, in comparison to α_D, which is instead more sensitive to low-lying states.

A comment on the integration range employed in Eqs. (5.70), (5.71) and (5.72) is in order. We point out that the integral in Eq. (5.69) runs over the excitation energy of the nucleus with respect to its ground state. While in the closed-shell case, the ground-state energy of the nucleus is by construction the EOM-CC reference energy, in the 2PA-EOM-CC framework the latter corresponds to the CC ground-state energy ΔE_0^* of the closed-shell core. This means that in the 2PA case the LIT in Eq. (5.69) needs to be calculated starting from $\omega_0 = \Delta E_0 - \Delta E_0^*$. In this way, the integration variable correctly corresponds to the excitation energy with respect to the ground state of the 2PA nucleus.

5.4 Coupled-cluster diagrams for the 2PA-LIT-CC method

In this Section we will analyse the different stages of a 2PA-LIT-CC calculation and derive the corresponding diagrammatic contributions. Evaluating the LIT for a 2PA nucleus requires three preliminary steps:

(i) Hartree-Fock computation of the reference state $|\Phi_0\rangle$. For 2PA systems, $|\Phi_0\rangle$ is the reference state of the A-body closed-shell neighbour, calculated with a $A+2$ mass shift in the Hamiltonian.

(ii) Determination of the coupled-cluster ground state of the closed-shell reference, fixing the mass number to $A+2$, as in the previous step. To this aim, in this work we adopt the CCSD approximation.

(iii) Calculation of the left and right ground state of the 2PA nucleus, employing the 2PA-EOM-CC method. We choose to truncate the many-body expansion of the R^{A+2} and L^{A+2} operators of Eqs. (4.63) and (4.64) at the 3p-1h level.

At this point, to compute the LIT with Eq. (5.66), two ingredients are needed, which are listed below.

1. The Lanczos pivots $\mathbf{S}_R^{\text{2PA}}$ and $\mathbf{S}_L^{\text{2PA}}$. This entails the evaluation of matrix elements of the product between the similarity-transformed operator and the 2PA-EOM-CC ground state operators R_0^{A+2} and L_0^{A+2}, respectively.

2. The Lanczos coefficients obtained from the tridiagonalization of the matrix $(\mathbf{M}-z)$ of Eq. (5.37) via the complex-symmetric Lanczos algorithm. As $(\mathbf{M}-z)$ and the similarity transformed Hamiltonian differ only by a diagonal term, this is equivalent to consider the tridiagonalization of $\overline{H}$. The core of the Lanczos algorithm is then the repeated matrix-vector product between $\overline{H}$ and the right and left Lanczos vectors, expanded on the 2PA basis.

In the following, we provide the derivation of the diagrammatic contributions to the matrix elements involved in Step 1 and 2. We employ the 3p-1h approximation scheme in evaluating both the Lanczos pivots and the matrix elements contributing to the matrix-vector product.

5.4.1 Right and left Lanczos pivots

Here we focus on the treatment of the right and left Lanczos pivots. For convenience, we recall here the expression of their components

$$S^R_{\text{2PA},\alpha} = \langle \Phi_\alpha | \overline{\Theta} R_0^{A+2} | \Phi_0 \rangle \,, \quad S^L_{\text{2PA},\alpha} = \langle \Phi_0 | L_0^{A+2} \overline{\Theta^\dagger} | \Phi_\alpha \rangle \,, \tag{5.76}$$

expanded on the set of states of Eq. (5.38).

In this work, we will consider applications of the 2PA-LIT-CC method to electric dipole transitions. For the bare dipole operator, defined in Eq. (2.15), we have $\Theta = \Theta^\dagger$. In diagrammatic notation, its normal-ordered form can be represented as

$$\Theta_N \quad =$$

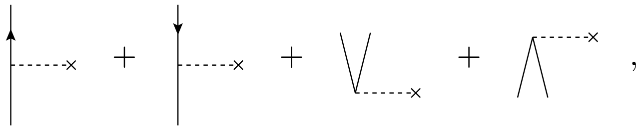

(5.77)

where the action of Θ is represented by a dashed line ended by a cross. Consistently with the closed-shell CCSD ground state, we consider only up to doubles contributions to the similarity transformed operator. This is equivalent to calculate the connected product

$$\overline{\Theta} = (\Theta_N e^{T_1+T_2})_C = \left[\Theta_N \left(1 + T_1 + T_2 + \frac{1}{2} T_1^2 + T_1 T_2 \right) \right]_C . \tag{5.78}$$

Powers of T exceeding 2 are dropped, since we can connect at most two excitation operators with a one-body operator as the dipole. Moreover, we do not consider the term $\propto T_2^2$, as a triple contribution would be obtained when contracting it with Θ_N. The diagrams contributing to $\overline{\Theta}$ at the CCSD level have been derived in Ref. [86]. Using the graphical notation for Θ_N and T, they correspond to

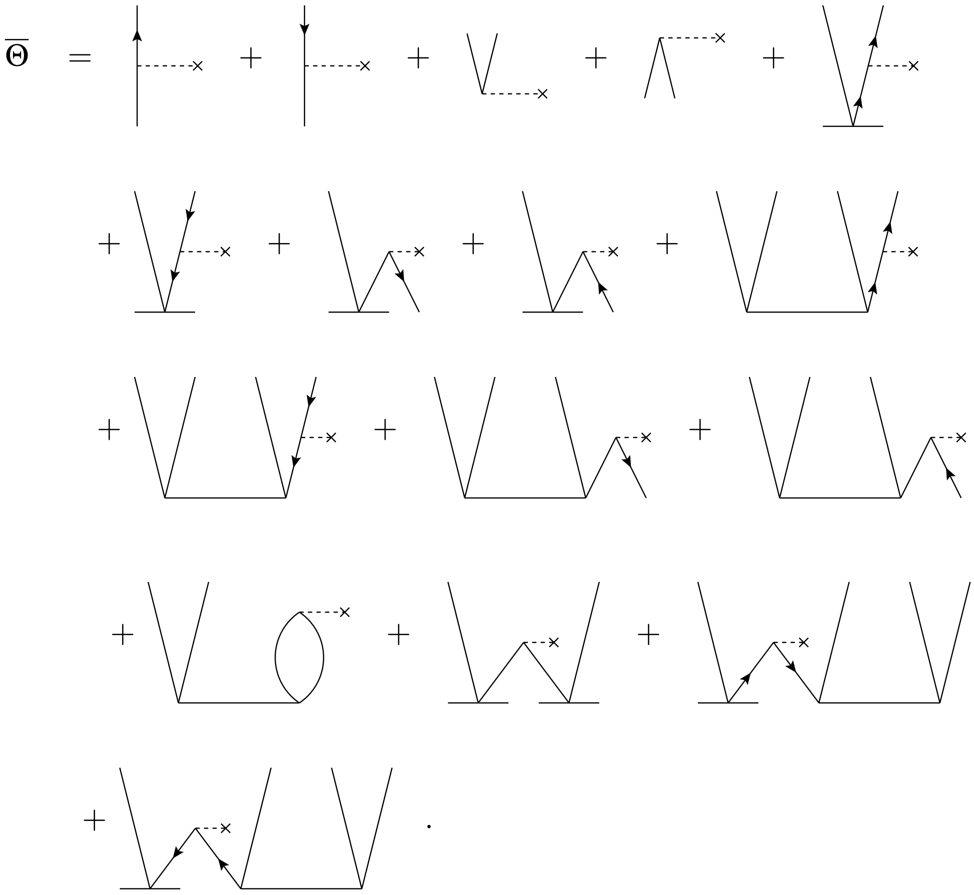

(5.79)

To reduce the complexity of the calculation it is useful to group the diagrams in Eq. (5.79) into "effective diagrams". The action of the effective operator is represented by a curly line ended by a cross. The latter are reported below alongside with their algebraic expressions, derived using the rules in Appendix 1.

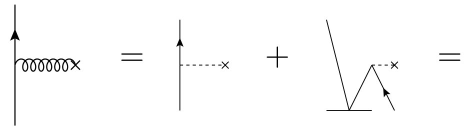

$$\langle a|\Theta|b\rangle - \sum_i \langle a|t_1|i\rangle\langle i|\Theta|b\rangle, \tag{5.80}$$

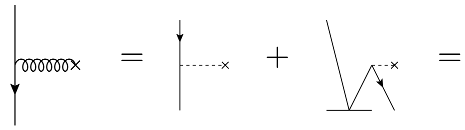

$$\langle j|\Theta|i\rangle + \sum_a \langle a|t_1|i\rangle\langle j|\Theta|a\rangle, \tag{5.81}$$

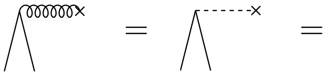

$$\langle i|\Theta|a\rangle, \tag{5.82}$$

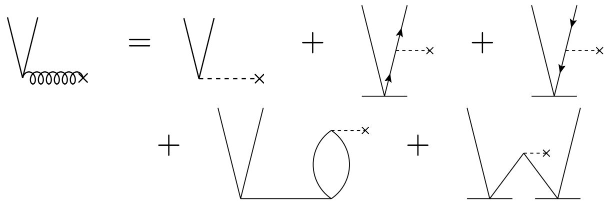

$$= \langle a|\Theta|i\rangle + \sum_b \langle b|t_1|i\rangle\langle a|\Theta|b\rangle - \sum_j \langle a|t_1|j\rangle\langle j|\Theta|i\rangle$$
$$+ \sum_{jb} \langle ab|t_2|ij\rangle\langle j|\Theta|b\rangle - \sum_{jb} \langle a|t_1|j\rangle\langle b|t_1|i\rangle\langle j|\Theta|b\rangle,$$

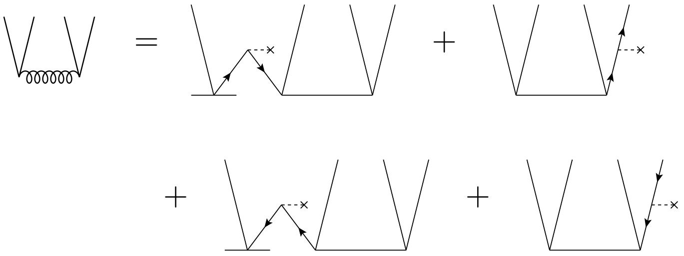

$$= -P(ij)\sum_{kc} \langle c|t_1|i\rangle\langle ab|t_2|kj\rangle\langle k|\Theta|c\rangle + P(ab)\sum_c \langle ac|t_2|ij\rangle\langle b|\Theta|c\rangle$$
$$-P(ab)\sum_{kc} \langle a|t_1|k\rangle\langle cb|t_2|ij\rangle\langle k|\Theta|c\rangle - P(ij)\sum_k \langle ab|t_2|ik\rangle\langle k|\Theta|j\rangle, \tag{5.83}$$

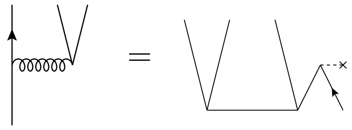

$$= -\sum_j \langle ab|t_2|ij\rangle\langle j|\Theta|c\rangle, \tag{5.84}$$

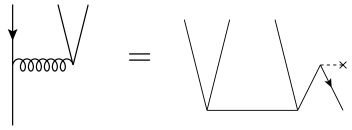

$$= \sum_b \langle ab|t_2|ij\rangle\langle k|\Theta|b\rangle. \tag{5.85}$$

In the equations above, the bra-ket notation for the T amplitudes was employed as

$$t_i^a = \langle a|t_1|i\rangle, \quad t_{ij}^{ab} = \langle ab|t_2|ij\rangle. \tag{5.86}$$

Moreover, some diagrams need to be supplemented with a permutation operator

$$P(ab) = \mathbb{1} - P_{a,b}, \tag{5.87}$$

which is needed to obtain antisymmetric amplitudes. It is worth to point out that the similarity transformation has led from a bare one-body operator to a transformed two-body operator. In fact, two-body vertices appear in the effective diagrams of Eqs. (5.83), (5.84) and (5.85).

At this point, we can identify the diagrammatic contributions to $\mathbf{S}^R_{\mathrm{2PA}}$ and $\mathbf{S}^L_{\mathrm{2PA}}$ combining the effective diagrams of $\overline{\Theta}$ with the ones representing the amplitudes of R_0^{A+2} and L_0^{A+2}, respectively. Also in this case, the algebraic expression associated with the diagrams presented is obtained using the rules of Appendix 1. The derivation and numerical implementation of the $\mathbf{S}^R_{\mathrm{2PA}}$ and $\mathbf{S}^L_{\mathrm{2PA}}$ diagrams constitutes original work of this thesis.

Let us start from $\mathbf{S}^R_{\mathrm{2PA}}$. Recalling the representation of the 2p-0h and 3p-1h terms of the 2PA excitation operator from Eq. (4.77)

$$R^{A+2}_{2\mathrm{p}-0\mathrm{h}} =$$

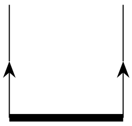

$$, \quad R^{A+2}_{3\mathrm{p}-1\mathrm{h}} =$$

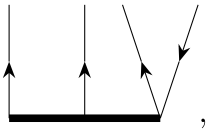

$$, \qquad (5.88)$$

the right Lanczos pivot in the 3p-1h approximation scheme is determined by

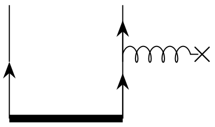

$$= P(ab)\sum_e \langle b|\overline{\Theta}|e\rangle \, \langle ae|R^{A+2}|0\rangle \,, \qquad (5.89)$$

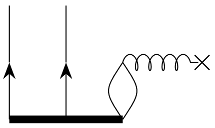

$$= \sum_n \langle n|\overline{\Theta}|e\rangle \, \langle abe|R^{A+2}|n\rangle \,, \qquad (5.90)$$

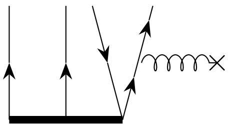

$$= P(ab,c) \, \langle c|\overline{\Theta}|e\rangle \, \langle abe|R^{A+2}|i\rangle \,, \qquad (5.91)$$

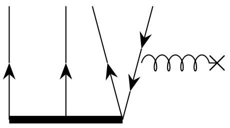

$$= -\sum_n \langle n|\overline{\Theta}|i\rangle \, \langle abc|R^{A+2}|n\rangle \,, \qquad (5.92)$$

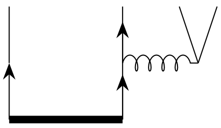

$$= P(a,bc)\sum_e \langle bc|\overline{\Theta}|ei\rangle \, \langle ae|R^{A+2}|0\rangle \,, \qquad (5.93)$$

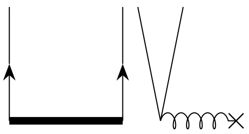

$$= P(ab,c) \, \langle c|\overline{\Theta}|i\rangle \, \langle ab|R^{A+2}|0\rangle \,. \qquad (5.94)$$

We obtain in total six diagrams, of which two contribute at the 2p-0h level, and four at the 3p-1h level. The bra-ket notation for the amplitudes of the 2PA excitation operator is employed as

$$r^{ab} = \langle ab|R^{A+2}|0\rangle\,, \qquad r_i^{abc} = \langle abc|R^{A+2}|i\rangle\,. \tag{5.95}$$

Moreover, in some of the above diagrams a three-body permutation operator appears. Its explicit form is $P(ab,c) = \mathbb{1} - P_{a,c} - P_{b,c}$.

Let us continue with $\mathbf{S}^L_{\mathrm{2PA}}$. Given the graphical notation for the left 2PA amplitudes

$$L^{A+2}_{\mathrm{2p-0h}} =$$

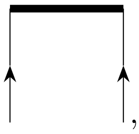

$$, \qquad L^{A+2}_{\mathrm{3p-1h}} =$$

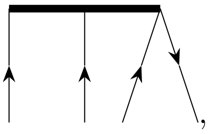

$$, \tag{5.96}$$

the diagrams contributing to the left Lanczos pivots at the 3p-1h level are

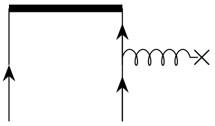

$$= \quad P(ab)\sum_e \langle e|\overline{\Theta^\dagger}|b\rangle\,\langle 0|L^{A+2}|ae\rangle\,, \tag{5.97}$$

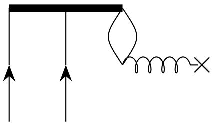

$$= \quad \sum_{en} \langle e|\overline{\Theta^\dagger}|n\rangle\,\langle n|L^{A+2}|abe\rangle\,, \tag{5.98}$$

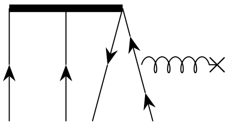

$$= \quad P(ab,c)\sum_e \langle e|\overline{\Theta^\dagger}|c\rangle\,\langle i|L^{A+2}|abe\rangle\,, \tag{5.99}$$

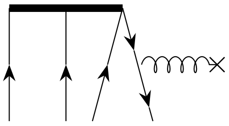

$$= \quad -\sum_n \langle i|\overline{\Theta^\dagger}|n\rangle\,\langle n|L^{A+2}|abc\rangle\,, \tag{5.100}$$

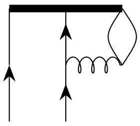

$$= \quad \frac{1}{2}P(ab)\sum_{efn} \langle ef|\overline{\Theta^\dagger}|bn\rangle\,\langle n|L^{A+2}|aef\rangle\,, \tag{5.101}$$

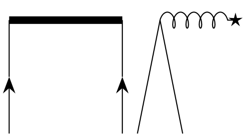

$$= \quad P(ab,c)\,\langle i|\overline{\Theta^\dagger}|c\rangle\,\langle 0|L^{A+2}|ab\rangle\,. \tag{5.102}$$

Also in this case, we used the bra-ket notation for the amplitudes of the left 2PA operator as

$$l_{ab} = \langle 0|L^{A+2}|ab\rangle\,, \qquad l^i_{abc} = \langle i|L^{A+2}|abc\rangle\,. \tag{5.103}$$

Similarly to the right Lanczos pivot, also the left pivot is determined by six diagrams. However, as a difference with respect to the right pivot, we get three contributions at both the 2p-0h and 3p-1h level. In fact, in both $\mathbf{S}_R^{\text{2PA}}$ and $\mathbf{S}_L^{\text{2PA}}$, there is only one diagram which comes from combining the amplitudes of the EOM operators with the two-body part of $\overline{\Theta}$. Such diagram contributes at the 3p-1h level in $\mathbf{S}_R^{\text{2PA}}$ and at the 2p-0h level in $\mathbf{S}_L^{\text{2PA}}$.

Moreover, we observe that the only two-body diagram of $\overline{\Theta}$ entering in $\mathbf{S}_R^{\text{2PA}}$ and $\mathbf{S}_L^{\text{2PA}}$ is given by Eq. (5.84). The two-body diagram of Eq. (5.83), which as shown in Ref. [86] completely determines the right Lanczos pivot of Eq. (5.48) in the closed-shell case, starts to contribute at 4p-2h level in the 2PA expansion.

5.4.2 Right and left matrix-vector product

Once the Lanczos pivots are determined, we can apply the Lanczos algorithm to $\overline{H}$ to obtain the Lanczos coefficients in Eq. (5.66). Here, we focus on the diagrammatic contributions to the matrix-vector products of Eqs. (5.44) and (5.45) between $\overline{H}$ and the right and left Lanczos vectors, respectively. We start by expanding the Lanczos vectors $\mathbf{w}_i$ and $\mathbf{v}_i$ on the set of states of Eq. (5.38) including up to 3p-1h excitations. The matrix-vector product is then obtained calculating matrix elements of the form

$$\langle \Phi^{ab} | (\overline{H} R^{A+2})_C | \Phi_0 \rangle \,, \tag{5.104}$$

$$\langle \Phi_i^{abc} | (\overline{H} R^{A+2})_C | \Phi_0 \rangle \,, \tag{5.105}$$

and their left counterparts. In analogy to the case of the Lanczos pivots, the diagrammatic contributions to the matrix-vector product can be obtained by combining the diagrams of $\overline{H}$ with the ones of the R^{A+2} and L^{A+2} amplitudes.

Let us start from the graphical representation of $\overline{H}$. Also in this case, we can define effective diagrams, in analogy to the case of $\overline{\Theta}$. Pointing to Ref. [153] for a complete derivation, we get:

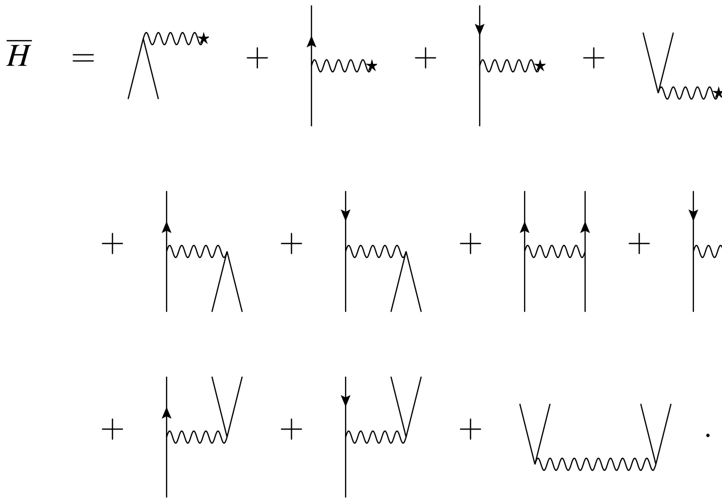

(5.106)

where the action of the Hamiltonian is pictured with a wiggly line and a star. At this point, contracting the diagrams of Eq. (5.106) with the ones of the right 2PA amplitudes, shown in

Eq. (4.77), we obtain the graphical contributions to the right matrix-vector product

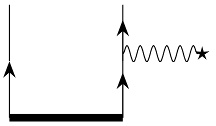

$$= P(ab)\sum_{e}\langle b|\overline{H}|e\rangle\,\langle ae|R^{A+2}|0\rangle\,, \tag{5.107}$$

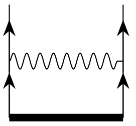

$$= \frac{1}{2}\sum_{ef}\langle ab|\overline{H}|ef\rangle\,\langle ef|R^{A+2}|0\rangle\,, \tag{5.108}$$

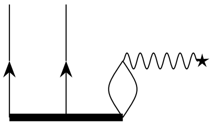

$$= \sum_{ne}\langle n|\overline{H}|e\rangle\,\langle abe|R^{A+2}|n\rangle\,, \tag{5.109}$$

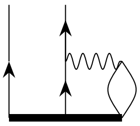

$$= \frac{1}{2}P(ab)\sum_{efn}\langle bn|\overline{H}|ef\rangle\,\langle aef|R^{A+2}|n\rangle\,, \tag{5.110}$$

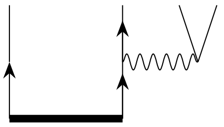

$$= P(a,bc)\sum_{e}\langle bc|\overline{H}|ei\rangle\,\langle ae|R^{A+2}|0\rangle\,, \tag{5.111}$$

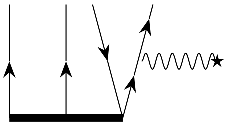

$$= P(ab,c)\sum_{e}\langle c|\overline{H}|e\rangle\,\langle abe|R^{A+2}|i\rangle\,, \tag{5.112}$$

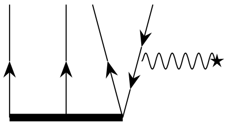

$$= -\sum_{n}\langle n|\overline{H}|i\rangle\,\langle abc|R^{A+2}|n\rangle\,, \tag{5.113}$$

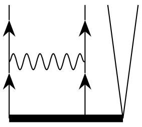

$$= \frac{1}{2}P(ab,c)\sum_{ef}\langle ab|\overline{H}|ef\rangle\,\langle efc|R^{A+2}|i\rangle\,, \tag{5.114}$$

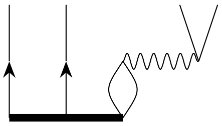

$$= P(ab,c)\sum_{ne}\langle nc|\overline{H}|ei\rangle\,\langle abe|R^{A+2}|n\rangle\,. \tag{5.115}$$

Similarly, the diagrammatic contributions to the left matrix-vector product are given by

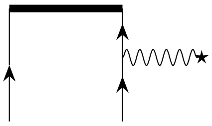

$$= \quad P(ab)\sum_{e}\langle e|\overline{H}|b\rangle\,\langle 0|L^{A+2}|ae\rangle\,, \tag{5.116}$$

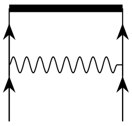

$$= \quad \frac{1}{2}\sum_{ef}\langle ef|\overline{H}|ab\rangle\,\langle 0|L^{A+2}|ef\rangle\,, \tag{5.117}$$

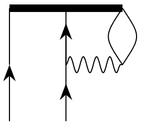

$$= \quad \frac{1}{2}P(ab)\sum_{efn}\langle ef|\overline{H}|bn\rangle\,\langle n|L^{A+2}|aef\rangle\,, \tag{5.118}$$

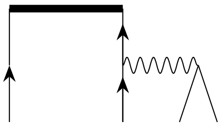

$$= \quad P(a,bc)\sum_{e}\langle ei|\overline{H}|bc\rangle\,\langle 0|L^{A+2}|ae\rangle\,, \tag{5.119}$$

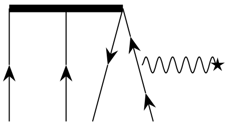

$$= \quad P(ab,c)\sum_{e}\langle e|\overline{H}|c\rangle\,\langle i|L^{A+2}|abe\rangle\,, \tag{5.120}$$

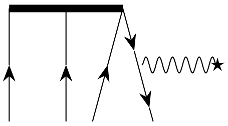

$$= \quad -\sum_{n}\langle i|\overline{H}|n\rangle\,\langle i|L^{A+2}|abc\rangle\,, \tag{5.121}$$

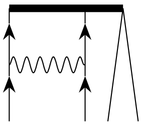

$$= \quad \frac{1}{2}P(ab,c)\sum_{ef}\langle ef|\overline{H}|ab\rangle\,\langle i|L^{A+2}|efc\rangle\,, \tag{5.122}$$

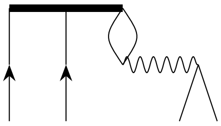

$$= \quad P(ab,c)\sum_{en}\langle ei|\overline{H}|nc\rangle\,\langle n|L^{A+2}|abe\rangle\,, \tag{5.123}$$

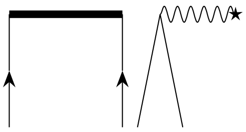

$$= \quad P(ab,c)\,\langle i|\overline{H}|c\rangle\,\langle 0|L^{A+2}|ab\rangle\,. \tag{5.124}$$

The algebraic expressions presented here are derived employing the diagrammatic rules of Appendix 1.

We observe that the diagrams contributing to the left and right matrix vector product are the upside-down version of one another, except for two cases. In the left matrix-vector product, the flipped version of the right diagram of Eq. (5.109) is not present, while a disconnected diagram (Eq. (5.124)), absent in the right matrix-vector product, appears in the left one. The reason for this lies the fact that the following contribution to $\overline{H}$ vanishes as it is the diagrammatic representation of the CCSD T_1 equations

$$= \quad \langle\Phi_i^a|\overline{H}|\Phi_0\rangle \quad = \quad 0. \tag{5.125}$$

In this derivation, we neglect the three-body terms induced by the similarity transformation in $\overline{H}$, which produce two diagrammatic contributions to the matrix-vector produce at 3p-1h level. A detailed derivation of such terms can be found in Refs. [180,181]. According to our calculations, their effect is less than 1%.

We point out that the matrix-vector product diagrams illustrated above are the same diagrams solving the 2PA-EOM-CC eigenvalue problem of Eq. (4.67) and its left companion, and they have been derived in Refs. [180, 181]. We have reported them here to give a complete overview of the 2PA-LIT-CC method.

As explained in Section 4.4, the advantage of using EOM-based approaches to calculate properties of nuclei in the vicinity of closed shells is given by the possibility of working in a j-scheme formulation [180, 181]. The latter drastically reduces memory requirements with respect to its m-scheme counterpart, without the need of resorting to symmetry restoration procedures. As the algebraic expressions reported in this Section for $\overline{\Theta}$, the Lanczos pivots and the matrix-vector product are written in a m-scheme basis, it is necessary to perform angular momentum coupling in order to obtain the corresponding formulas in a j-scheme basis. The details of this procedure, based on the use of the Wigner-Eckart theorem [193], are illustrated in Appendix 2.

Developing a spherical formulation of the 2PA-LIT-CC method has represented an important part of the work presented in this thesis. In the case of the diagrams contributing to the matrix-vector product, the j-scheme expressions have been published in Refs. [180, 181]. As a learning tool, they have been re-derived prior to numerical implementation. The use of a different convention in the Wigner-Eckart theorem with respect to Ref. [86] has required a new calculation of the j-scheme contributions to $\overline{\Theta}$. The j-scheme expressions corresponding to the left and right Lanczos pivot diagrams have been derived for the first time during the work of this thesis, and they are reported in Appendix 3.

After all the j-scheme expressions have been obtained, the next step of the work of this thesis has been to implement and test all the diagrams shown in this Section (the contributions to $\overline{\Theta}$, the Lanczos pivots and the matrix-vector product) as well as the complex-symmetric Lanczos algorithm in the framework of the Nuclear Tensor Contraction Library (NTCL) [194], authored by Gustav R. Jansen, staff scientist at Oak Ridge National Laboratory, USA. This library provides a unique tensor contraction interface compatible with multiple hardware architectures, and it allows us to use more efficiently the computational resources of ORNL's top-tier supercomputers. With the use of NTCL, the 2PA-LIT-CC code was developed from scratch during the work of this thesis, in a completely independent way with respect to the closed-shell LIT-CC and 2PA-EOM-CC programs. The 2PA-LIT-CC code is an original outcome of the work of this thesis.

6 Results

In the previous Chapters, we built the computational framework allowing us to explore electromagnetic observables which strongly correlate with parameters entering the nuclear matter EOS, as electric dipole polarizabilities and isoscalar monopole resonances. Our goal is to analyse the connection between microscopic and macroscopic physics scales on the basis of ab initio calculations in finite nuclei, employing chiral EFT interactions rooted in QCD. Such an analysis cannot be separated from the necessity to deliver reliable theoretical uncertainties for our predictions. In this regard, the systematic improvability of ab initio methods constitutes an inherent advantage. Therefore, we begin this Chapter by discussing our strategy for uncertainty quantification, based on Refs. [2,77].

We continue with an overview of the results of this thesis, focusing first on the electric dipole polarizability α_D. Following Ref. [5], we show a comparison between our LIT-CC predictions, experimental data and energy density functional theory for the electric dipole polarizability of ^{40}Ca. Next, leveraging the computational achievement of Ref. [7], we illustrate how the development of the 2PA-LIT-CC method extended the reach of our α_D calculations to open-shell nuclei. We then push our α_D calculations to the most exotic nucleus on Earth, ^{8}He [1,2,6]. In the end, we move our attention to the analysis of isoscalar monopole resonances in medium-mass nuclei, with the goal of extracting constraints on the incompressibility of symmetric nuclear matter [8].

6.1 Uncertainty quantification

We can distinguish two main contributions to the theoretical uncertainty σ^2_{th} associated with ab initio predictions

$$\sigma^2_{\text{th}} = \sigma^2_{\text{method}} + \sigma^2_{\text{model}}, \tag{6.1}$$

where σ^2_{method} accounts for the uncertainties coming from approximations introduced in the various stages of a many-body calculation, and σ^2_{model} encodes the uncertainty associated with the choice of the input Hamiltonian.

Let us now consider the treatment of the method error in LIT-CC calculations. In this case, the latter is determined by two sources: the residual dependence on model space parameters σ_{conv} and the effect of the truncations applied to the coupled-cluster expansions $\sigma_{\text{many-body}}$.

Our coupled-cluster calculations start from an Hartree-Fock reference state (see Refs. [157, 158] for details), expanded on single-particle HO eigenstates, characterized by specific values of radial quantum number n, orbital angular momentum l and HO frequency $\hbar\Omega$. Convergence is controlled by the number of major HO shells included in the calculation. In closed-shell LIT-CC calculations, we are able to reach up to 15 major HO shells, corresponding to a maximum model space size $N_{max} = 2n + l = 14$, with $l \leq 10$. In the current implementation of the 2PA-LIT-CC method, a maximum model space size of $N_{max} = 12$ for the Hartree-Fock basis is available. For both LIT-CC approaches, the uncertainty related to convergence σ_{conv} is estimated by considering the residual dependence on $\hbar\Omega$ at the largest N_{max} under study.

We point out that 3N forces matrix elements come with an additional energy cut of $E_{3,max} = 16$ (in units of $\hbar\Omega$), where $E_{3,max} = \varepsilon_p + \varepsilon_q + \varepsilon_r$ corresponds to the energy of the three-body state $|pqr\rangle$. For the light and medium-mass nuclei under study in this thesis, fixing $E_{3,max} = 16$ is sufficient to obtain converged results [86, 195].

Let us now analyse the effect of the many-body truncation. To this aim, we need to consider the different approximation schemes characterizing the closed-shell and 2PA-LIT-CC methods. In the case of the closed-shell LIT-CC approach, approximations enter in the T and Λ operators involved in the ground-state calculation and in the R_μ and L_μ operators of Eqs. (4.51) and (4.52) involved in the EOM calculation. For both the ground state and the excited states, a specific truncation has to be chosen, either CCSD or CCSDT-1 (in short, D or T-1, which is the notation we will adopt in the following). Therefore, two expansion schemes need to be indicated. The resulting CC approximations are listed in Table 6.1.

Table 6.1: List of labels used to identify the CC truncation for the ground state (left of '/') and the excited states (right of '/') in the closed-shell LIT-CC approach.

Ground state	Excited states	Truncation scheme
D	D	D/D
T-1	D	T-1/D
T-1	T-1	T-1/T-1

For light nuclei as ^{8}He, it is possible to perform calculations in the T-1/T-1 scheme, including triples in both the ground-state and EOM calculation. However, as the inclusion of triples in the EOM calculation is computationally demanding, for nuclei with $A > 10$ we adopt the T-1/D approximation, where triples are added only in the ground-state. Triples are anyway expected to give a small contribution at the EOM level in the medium-mass region [101]. An empirical way of estimating the contribution of many-body errors to an observable $\mathscr{O}$ is given by [2, 77]

$$\sigma_{\text{many-body}} = \frac{|\mathscr{O}^{D/D} - \mathscr{O}^{T-1/D}|}{2}, \tag{6.2}$$

which is the strategy applied throughout this Chapter. If the T-1/T-1 result is available, half of the difference between the D/D and T-1/T-1 values is used.

Let us now discuss our strategy to estimate $\sigma_{\text{many-body}}$ for the 2PA-LIT-CC approach. In this case, we first have to solve for the CC ground state of the closed-shell reference. To this aim, in this thesis we retain up to doubles correlations in the cluster operator, leaving a study of the effect of triples at this stage to future work. Then, in order to study properties of 2PA nuclei, we have to resort to truncations of the R_μ^{A+2} and L_μ^{A+2} operators of Eqs. (4.63) and (4.64) in both the ground-state and excited-state calculations. Keeping only the first term in the sum of Eqs. (4.63) and (4.64) leads to the 2p-0h approximation, while adding also the second term defines the 3p-1h approximation. The latter is expected to be accurate for states with a dominant 2PA structure [181]. States of more complex structure would require the inclusion of 4p-2h or higher order correlations. The approximation schemes used in the 2PA-LIT-CC calculations of this thesis are summarized in Table 6.2.

Table 6.2: List of labels used to identify the CC truncation for the ground state (left of '/') and the excited states (right of '/') in the 2PA-LIT-CC approach.

Ground state	Excited states	Truncation scheme
2p-0h	3p-1h	2p-0h/3p-1h
3p-1h	3p-1h	3p-1h/3p-1h

As in this work we are interested in observables such as the dipole polarizability, we choose to retain at least 3p-1h correlations in the excited-state 2PA operators. We will then estimate the many-body truncation uncertainty as half of the difference between the two approximation schemes of Table 6.2, in analogy to the closed-shell case, as

$$\sigma_{\text{many-body}} = \frac{|\mathscr{O}^{3\text{p}-1\text{h}/3\text{p}-1\text{h}} - \mathscr{O}^{2\text{p}-0\text{h}/3\text{p}-1\text{h}}|}{2}. \tag{6.3}$$

It is worth pointing out that in both the closed-shell and 2PA cases, the calculation of the similarity transformed operator $\overline{\Theta}$ involve an additional truncation. In all the results presented in this Chapter, $\overline{\Theta}$ is truncated at the D level, as shown in Eq. (5.78). In Ref. [101], it has been proved that the inclusion of triples in $\overline{\Theta}$ has negligible effects.

When results for ground-state properties are shown, only the truncation of the T and Λ (R^{A+2} and L^{A+2}) operators counts towards $\sigma_{\text{many-body}}$ for closed-shell (2PA) nuclei. In analogy to the previous case, we estimate it taking half of the difference between the T-1 (3p-1h) and D (2p-0h) outcomes for closed-shell (2PA) nuclei.

Once σ_{conv} and $\sigma_{\text{many-body}}$ are determined, we can compute the overall method error by summing them in quadrature as

$$\sigma^2_{\text{method}} = \sigma^2_{\text{conv}} + \sigma^2_{\text{many-body}}. \tag{6.4}$$

We point out that the method error cannot be interpreted statistically, because it is systematic in nature.

Let us now consider the model error σ^2_{model}. Throughout this work, we use interactions from chiral EFT, introduced in Chapter 3, including both NN and 3N forces. The different chiral forces available on the market can be distinguished mainly on the basis of the chosen degrees of freedom, the fitting procedure and the orders included in the chiral expansion. Variations in results obtained with different Hamiltonians allow us to assess these effects on the observables under study. This is the strategy mostly adopted in this thesis to estimate σ^2_{model}. In selected cases, we also analyse the chiral EFT truncation uncertainty by focusing on a specific chiral force and performing calculations at different orders. We observe that a more refined estimate for the chiral EFT truncation uncertainty can be obtained by employing modern Bayesian statistical tools [196, 197], which also allow for a statistical interpretation of the model error. We leave a Bayesian analysis of our results for future work.

6.2 Electric dipole polarizability of ^{40}Ca

As shown in Section 2.4.2, the correlation of the electric dipole polarizability with the symmetry energy parameters of the nuclear EOS has made it the object of intense experimental investigation. Experimental determinations of α_D for ^{48}Ca [48] and ^{68}Ni [49] and their comparison with theory led to an improved understanding of the neutron and proton distributions in nuclei, as well as their difference encoded in the neutron skin thickness. Here, we consider a comparison between closed-shell LIT-CC predictions, experimental data and energy density functional (EDF) theory results for ^{40}Ca, published in Ref. [5]. This comparison serves as a further test of the LIT-CC and EDF approaches as well as of the constraints on the nuclear EOS imposed by the chiral EFT interactions and energy density functionals employed in this work.

The inelastic proton scattering cross section on ^{40}Ca at very forward angles has been measured with an incident proton energy of 295 MeV at RCNP, Japan. Starting from $^{40}\text{Ca}(p,p')$ data, the photoabsorption cross section has been extracted for excitation energies ranging between 10 and 25 MeV. The new data have been matched with old photoabsorption data from Ref. [88, 198], allowing for a description of the photoabsorption cross section up to 60 MeV of excitation energy. Figure 6.1 shows the experimental result for the photoabsorption cross section, together with the running sum of the dipole polarizability.

The photoabsorption cross section, presented in the upper panel of Figure 6.1, is dominated by the giant dipole resonance peak at around 20 MeV. As shown in the lower panel of Figure 6.1, integrating the photoabsorption cross section up to 25 MeV, experimentalists obtained $\alpha_D = 1.60(14)$ fm^3. Considering the data at higher excitation energy up to 60 MeV, where the polarizability saturates, they were able to provide a final experimental value of $1.92(17)$ fm^3. We observe that the low-energy data up to 25 MeV, which include the contribution of the giant dipole resonance, determine more than 80% of the final experimental result for α_D.

In the lower panel of Figure 6.1, the experimental α_D is compared to coupled-cluster predictions obtained with the NNLO$_{\text{sat}}$ interaction [102]. We observe an excellent agreement between theory and experiment. Both D/D and T-1/D results, corresponding to the open and full black circles respectively, are reported. Their error bars account for the method uncertainty σ_{method}, stemming from the residual dependence on convergence parameters and the many-body truncation, according to the strategy illustrated in Section 6.1. To analyse

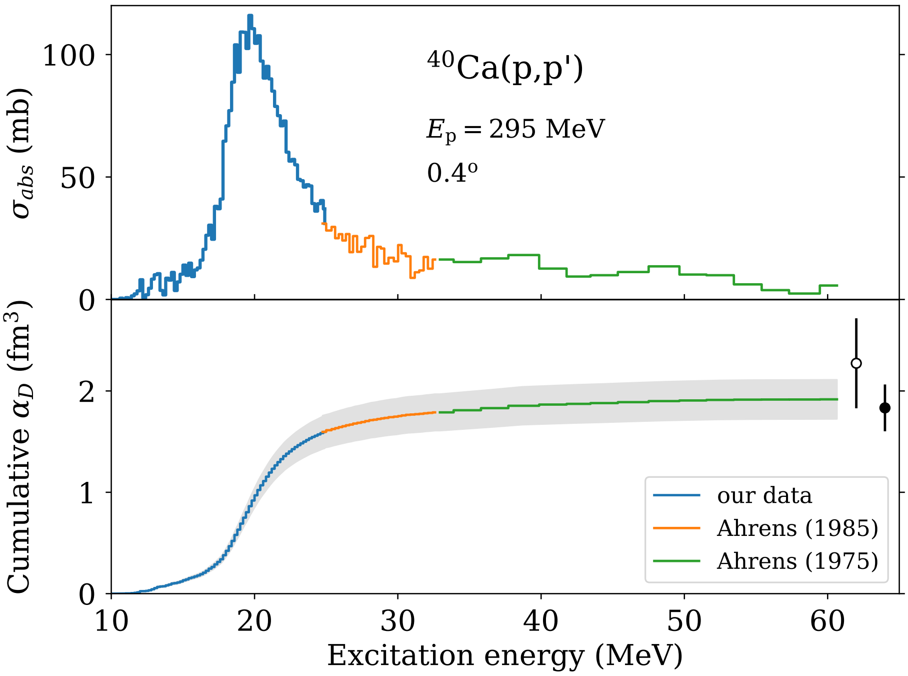

Figure 6.1: Upper panel: photoabsorption cross section derived at a scattering angle of 0.40°. Lower panel: electric dipole polarizability α_D derived from the photoabsorption cross sections. The blue curve shows the new data of Ref. [5], while the orange and green curves show the extrapolation to higher energies using the data of Refs. [88, 198]. The open (full) black circles are the CC results for the NNLO$_{\text{sat}}$ interaction including up to doubles (triples) contributions in the CC expansion for the ground state. Figure taken from Ref. [5].

the convergence of our results we varied the oscillator frequency in the range $\hbar\Omega = 12-16$ MeV at the maximum model space size employed ($N_{max} = 14$). As for the many-body truncation, a reduction of 20% in the central value is observed when including triples in the ground state. This effect was already observed in similar studies focusing on ^{48}Ca [48] and ^{68}Ni [49].

To assess the uncertainty associated with the Hamiltonian model, we also performed CC calculations with the family of interactions of Ref. [68], including SRG-evolved NN forces up to N^{3}LO and 3N forces at NNLO. More details on this family of interactions were given in Section 3.3. In the upper panel of Figure 6.2, we explore the correlation between the electric dipole polarizability in ^{40}Ca and ^{48}Ca as given by theory. The experimental value for ^{48}Ca is taken from Ref. [48], while the corresponding theoretical predictions can be found in Ref. [77].

The upper panel of Figure 6.2 shows the CC results including triples contributions. The theoretical uncertainties for the different Hamiltonians account for σ_{method}, calculated as detailed in Section 6.1. Also for the family of interactions of Ref. [68], we find that the inclusion of triples reduces the value of α_D by an amount varying between 10%–20% for the different force models. While the EM and PWA interactions are not simultaneously

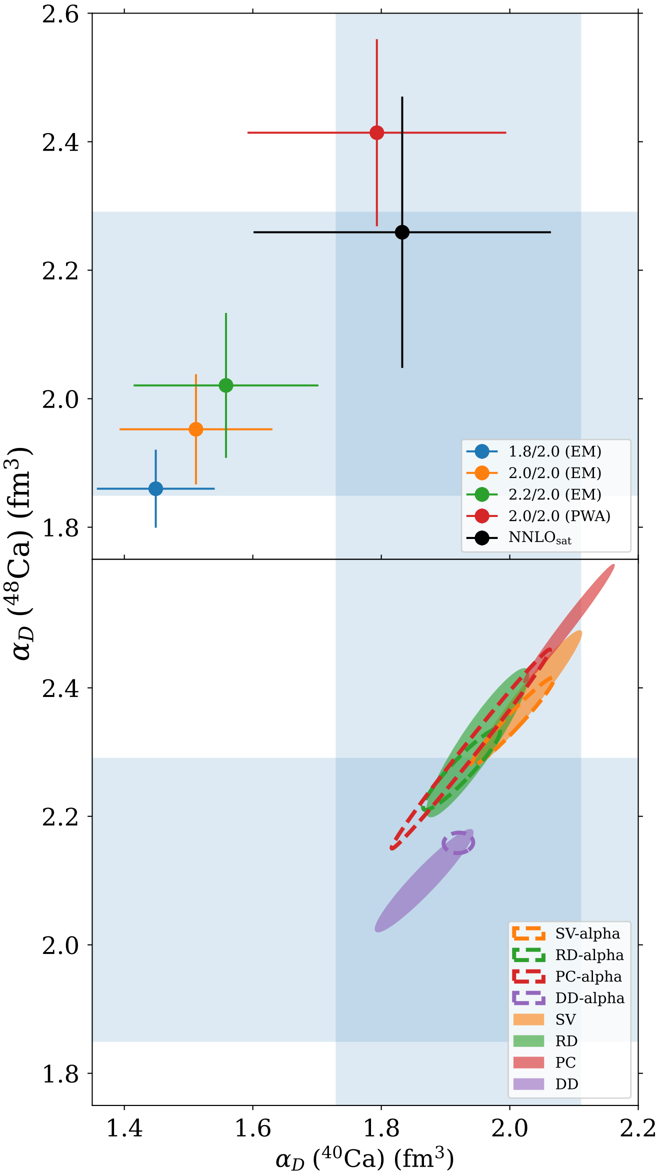

Figure 6.2: Comparison of the experimental dipole polarizabilites of ^{40}Ca and ^{48}Ca [48] shown as blue bands with CC calculations with different interactions, including triples contributions (upper panel) and EDF calculations with different energy density functionals (lower panel). Figure taken from Ref. [5].

compatible with both ^{40}Ca and ^{48}Ca experimental data, the set of employed interactions shows an approximately linear dependence between the two quantities, overlapping with both experimental results. The NNLO$_{\text{sat}}$ interaction is able to reproduce simultaneosly the experimental value of α_D for both ^{40}Ca and ^{48}Ca.

The lower panel of Figure 6.2 shows EDF results obtained with different energy density functionals. The functionals denoted with "*-alpha" include the dipole polarizability of ^{208}Pb in the fit. Further details on the employed EDFs can be found in Ref. [5]. We observe that the addition of $\alpha_D(^{208}\text{Pb})$ improves the agreement with experiment for both ^{40,48}Ca. It is remarkable to observe a similar linear correlation between the polarizabilities of ^{40,48}Ca emerging from both ab initio and EDF theoretical approaches. Similar correlations between the polarizabilities of heavier nuclei (^{208}Pb, ^{120}Sn and ^{68}Ni) were observed in the context of the EDF calculations of Ref. [99].

On the basis of the general accordance between the experimental data on ^{40,48}Ca, EDF and ab initio results, we can analyse the constraints on the symmetry energy parameters J and L obtained from the chiral EFT interactions and EDFs employed in Ref. [5].

In Figure 6.3, constraints on J and L derived from chiral EFT interactions[1] and EDFs of this work are compared with some of the works we presented in Chapter 2: the results of the nuclear matter calculations of Drischler et al. [84] and Hu et al. [30], the values inferred by Essick et al. [28] and the ranges from the global analysis of Ref. [81] by Lattimer. As for the latter result, two ranges (1 and 2) of J and L are obtained. As explained in Section 2.4.1, range 1 is based on a weighted average of neutron skin measurements in ^{48}Ca and ^{208}Pb, including CREX and PREX, while range 2 considers only PREX and CREX in the analysis.

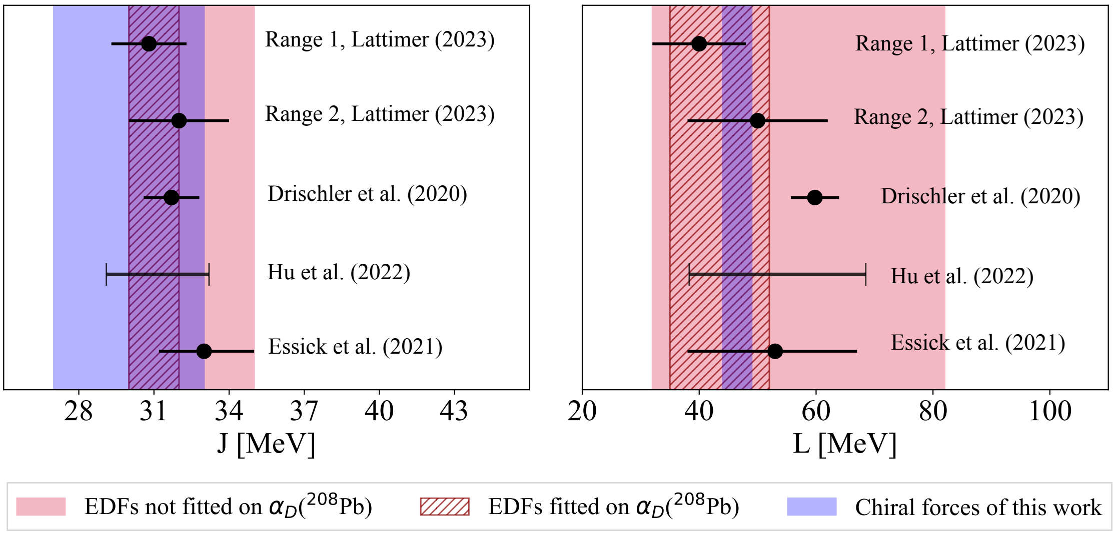

Figure 6.3: Constraints on the symmetry energy J (left panel) and slope parameter L (right panel) obtained starting from the chiral forces and EDFs employed in this work [5], compared with the two ranges of the global analysis of Lattimer [81], the values inferred by Essick et al. [28] and the nuclear matter calculations of Drischler et al. [84] and Hu et al. [30]. See text for details.

Let us start from analysing the constraints the symmetry energy at saturation density J. We observe a nice overlap between the predictions of the chiral forces and EDFs of our work, the nuclear matter calculations of Drischler et al. [67] and Hu et al. [30], and

---

[1] With respect to the ranges reported in Ref. [5], taken from [47], the constraints on L have been updated due an error reported in nuclear matter calculations with the NNLO$_{\text{sat}}$ interaction [103]. Constraints on J remain unaffected.

the constraint of Essick et al. [28] combining nuclear matter calculations with neutron star observations. A good agreement is also obtained with the global analysis of Lattimer [81]. Figure 6.3 suggests that J is well constrained at around 32 MeV. As shown in Figure 2.9, α_D is correlated to L via the product $\alpha_D J$. Therefore, a well defined range of J, as it emerges from Figure 6.3, would allow for a safer extraction of a corresponding range of L via the dipole polarizability.

Let us now consider the constraints on L. We observe a good agreement between the ranges of Lattimer [81] and the constraints obtained from chiral EFT interactions, also in the case of NNLO_{sat}, which provides a good description of α_D for both ^{40,48}Ca and gives $L = 45$ MeV. In the case of EDF theory, the range of values of L predicted by the functionals employed in Ref. [5] narrows considerably when considering the EDFs fitted to the polarizability of ^{208}Pb. The L constraints from Essick et al. [28] and Hu et al. [30] encompass both the EFT and EDF ranges, while Drischler et al. [84] favour slightly higher values of L.

Our work [5] supports on the one hand the robustness of current theoretical approaches in the description of the dipole polarizability for ^{40,48}Ca and on the other hand, it corroborates the constraints on J and L provided by the chiral EFT interactions and energy density functionals employed.

6.3 Extending the reach of our calculations to open-shell nuclei: 2PA-LIT-CC results

As shown in Ref. [5], the systematic comparison of coupled-cluster predictions of the dipole polarizability with experiment has identified the LIT-CC method as a successful tool to describe this observable in closed-(sub)shell systems.

Motivated by the recent experimental interest towards open-shell nuclei, in this thesis we move the first steps towards the ambitious goal of extending the LIT-CC method to open-shell nuclei, focusing on two-particle-attached (2PA) systems, which can be obtained adding two nucleons to a closed-(sub)shell core. In Chapter 5 we presented a derivation of the LIT-CC equations for 2PA systems, named 2PA-LIT-CC equations, and we showed how they can be solved employing the Lanczos algorithm. In the following, after providing a benchmark of the newly developed 2PA-LIT-CC approach, we examine the evolution of the dipole polarizability along the oxygen and calcium isotopic chains.

All the results have been obtained using the $\Delta\text{NNLO}_{\text{GO}}(394)$ interaction [138], and they represent the accomplishments of Ref. [7].

6.3.1 Validating the new method

We test the 2PA-LIT-CC approach considering nuclei which are both closed-(sub)shell and two-particle-attached with respect to a neighbouring closed-(sub)shell system. In these special cases, in fact, we can perform calculations with both the 2PA-LIT-CC method and the established closed-shell LIT-CC, allowing us to gauge the accuracy of the 2PA approximation. We focus in particular on two oxygen isotopes: ^{16}O, which can be computed starting from a ^{14}O reference, and ^{24}O, which is 2PA with respect to ^{22}O.

For ^{16,24}O, we examine the non-energy-weighted dipole sum rule m_0 and the electric dipole polarizability α_D. Given the same nuclear interaction, we expect the closed-shell and 2PA LIT-CC results for ^{16,24}O to be compatible within error bars, calculated as defined in Section 6.1.

Non-energy-weighted dipole sum rule

Let us concentrate first on the results for the non-energy-weighted sum rule m_0. This observable can be calculated in two ways: as an integral of $R(\omega)$ according to Eq. (5.70) and as a ground-state expectation value according to Eqs. (5.36) and (5.54) in the closed-shell and 2PA case, respectively. We verified that in our 2PA calculations both approaches lead to the same results.

We choose to present here the results obtained by calculating m_0 as a ground-state expectation value. In this way, we are able to assess the effect of using two independent many-body expansions (closed-shell and 2PA) in the calculation of the Lanczos pivots. For instance, different effective diagrams of the similarity-transformed operator are involved in the closed-shell and 2PA Lanczos pivots. In Section 5.4, we observed that the two-body effective diagram of Eq. (5.83), which fully determines the right Lanczos pivot of Eq. (5.48) in the closed-shell framework, contributes only starting at the 4p-2h level in the 2PA expansion.

In the rest of this paragraph, we specify only the many-body truncation adopted to describe the ground state: D or T-1 in the closed-shell case, and 3p-1h or 2p-0h in the 2PA case. In this regard, it is relevant to notice that starting from a 2p-0h ground state, the left and right Lanczos pivots become in general 3p-1h vectors, due to the presence of the diagram of Eq. (5.102) in $\mathbf{S}_L^{2PA}$ and of the ones of Eqs. (5.93) and (5.94) in $\mathbf{S}_R^{2PA}$.

In Figs. 6.4 and 6.5, we consider the convergence pattern of m_0 as a function of $\hbar\Omega$ for different values of N_{max} in ^{16}O and ^{24}O, respectively. For both nuclei, we show D and T-1 closed-shell results, as well as 2PA results in the 3p-1h and 2p-0h approximations. In all cases, we vary N_{max} between 8 and 12, and span a range of $\hbar\Omega$ values between 8 and 16 MeV. We report m_0 predictions in the closed-shell and 2PA frameworks for both nuclei in Table 6.3.

Let us start from the case of ^{16}O. In all the closed-shell and 2PA approximation schemes considered, m_0 is very well converged at $N_{max} = 12$. Focusing on the closed-shell results, we are able to identify the optimal frequency leading to a faster convergence with the crossing point of the different N_{max} curves, at $\hbar\Omega = 12$ MeV for D and $\hbar\Omega = 14$ MeV for T-1. The addition of triples lowers the value of m_0 of 1.5% with respect to the D result. In the 2PA calculations, the optimal frequency is located at $\hbar\Omega = 12$ MeV in the 3p-1h approximation and at $\hbar\Omega = 10$ MeV in the 2p-0h one. The effect of the many-body truncation is much larger in the 2PA case: the 2p-0h result is around 20% higher with respect to the 3p-1h

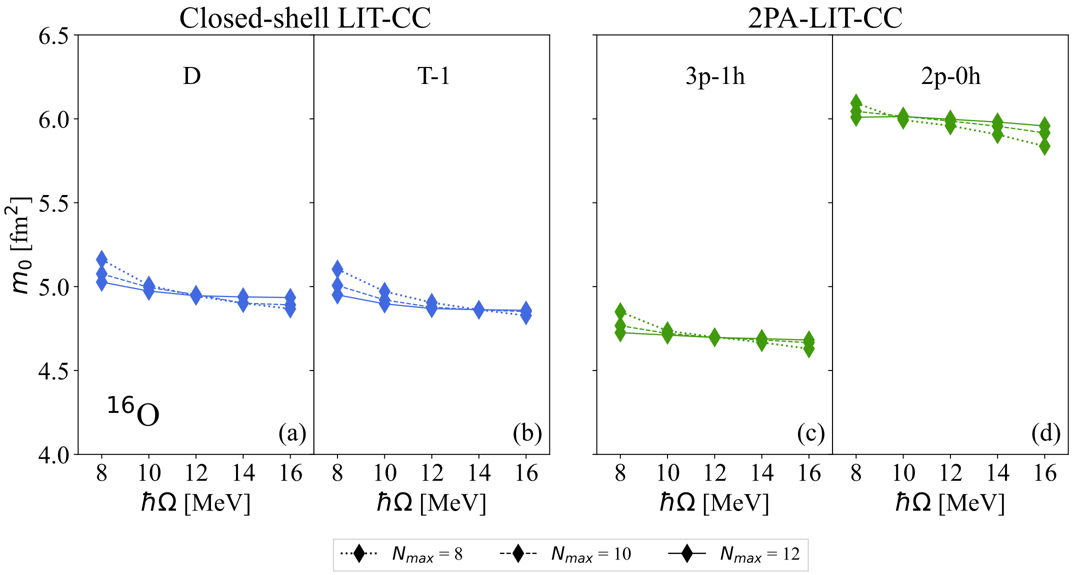

Figure 6.4: ^{16}O results for m_0 from the closed-shell D and T-1 approximations [panels (a) and (b), respectively] and the 2PA 3p-1h/3p-1h and 2p-0h/3p-1h approximations [panels (c) and (d), respectively]. Each panel shows m_0 as a function of $\hbar\Omega$ for different model space sizes.

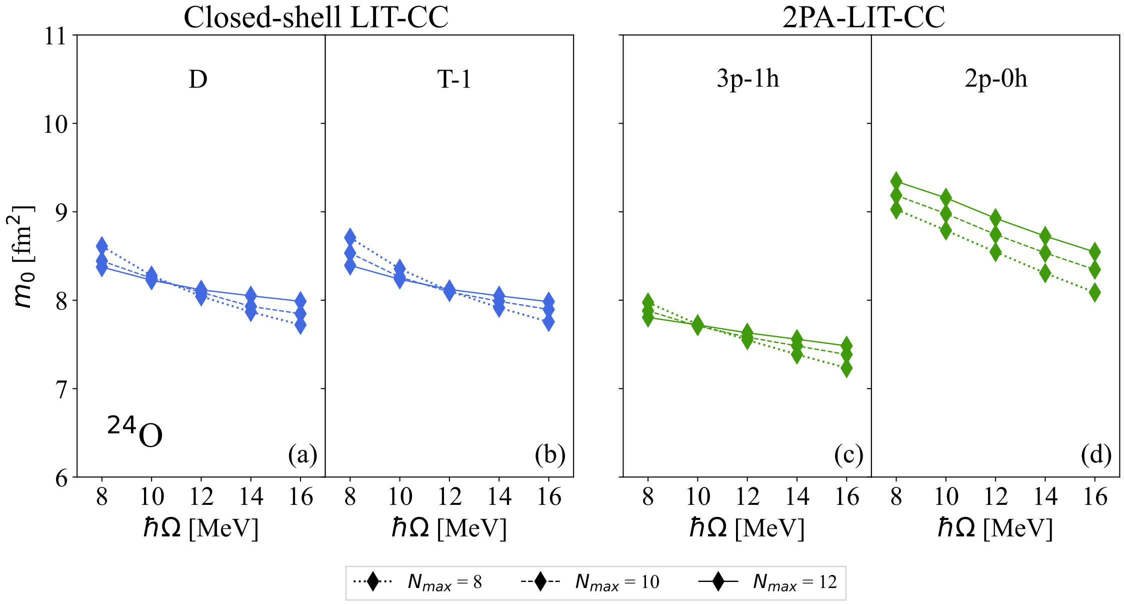

Figure 6.5: ^{24}O results for m_0 from the closed-shell D and T-1 approximations [panels (a) and (b), respectively] and the 2PA 3p-1h/3p-1h and 2p-0h/3p-1h approximations [panels (c) and (d), respectively]. Each panel shows m_0 as a function of $\hbar\Omega$ for different model space sizes.

result. Considering that the difference between the best closed-shell and 2PA approximation schemes (namely, T-1 and 3p-1h) is around 5%, the closed-shell and 2PA results are consistent, as can be seen in Table 6.3.

Table 6.3: Predictions for the non-energy-weighted sum rule m_0 in fm^2 of ^{16,24}O in the closed-shell T-1 and 2PA 3p-1h approximations obtained with the ΔNNLO$_{\rm GO}$(394) interaction. The theoretical uncertainty has been obtained as detailed in Section 6.1.

Nucleus	T-1	3p-1h
^{16}O	4.86(4)	4.7(7)
^{24}O	8.12(10)	7.7(8)

Let us now analyse the case of ^{24}O. The convergence patterns of Figure 6.5 for this nucleus show a larger residual dependence on the HO basis parameters in comparison to ^{16}O. This is a consequence of the more extended size characterizing the neutron-rich ^{24}O with respect to ^{16}O. Nevertheless, an optimal frequency can be found in most of the approximation schemes considered. Starting from the closed-shell calculations, the optimal frequency varies from $\hbar\Omega = 10$ MeV for D to $\hbar\Omega = 12$ MeV for T-1. Also for ^{24}O, the D value of m_0 at the optimal frequency is slightly higher than the T-1 one, with the difference between the two being less than 2%. Turning to the 2PA results, while it is possible to identify an optimal frequency of $\hbar\Omega = 10$ MeV for the 3p-1h approximation, the 2p-0h values are characterized by a slower convergence. Since the difference between numerical values for $N_{max} = 10$ and $N_{max} = 12$ reduces when going towards smaller values of $\hbar\Omega$, we can employ $\hbar\Omega = 8$ MeV as reference frequency for the uncertainty estimate. We can then say that the value of m_0 in the 2p-0h scheme is around 20% larger than the 3p-1h one. Since the T-1 and 3p-1h values differ by 5%, as in the ^{16}O case, the results obtained with the closed-shell and 2PA frameworks turn out to be compatible within error bars.

Electric dipole polarizability

Let us now analyse the results for the electric dipole polarizability of ^{16,24}O in the closed-shell and 2PA frameworks. This observable brings to light the effects of using a different coupled-cluster expansion not only in the ground state but also in the dipole-excited states. As a consequence, starting from this paragraph, we indicate the many-body truncation adopted in both the ground- and excited-state computation.

According to Eq. (5.71), the dipole polarizability is calculated starting from the inverse energy-weighted integral of the LIT, in the limit of vanishing Lorentzian width σ_I. The $\sigma_I \to 0$ limit of Eq. (5.71) converges quite quickly in both closed-shell and 2PA calculations. Lowering progressively the value of σ_I, we found that α_D is fully converged for $\sigma_I = 10^{-4}$ MeV. Fixing $\sigma_I = 0.01$ MeV, variations with respect to the converged result are already of the order of 0.001%. As it is proportional to the inverse energy-weighted sum rule m_{-1}, α_D shows a rapid convergence also with respect to the excitation energy, saturating at around 100 MeV.

It is also useful to look at the convergence of α_D with respect to the number of Lanczos coefficients included in the calculation of the LIT according to Eq. (5.66). Such an analysis

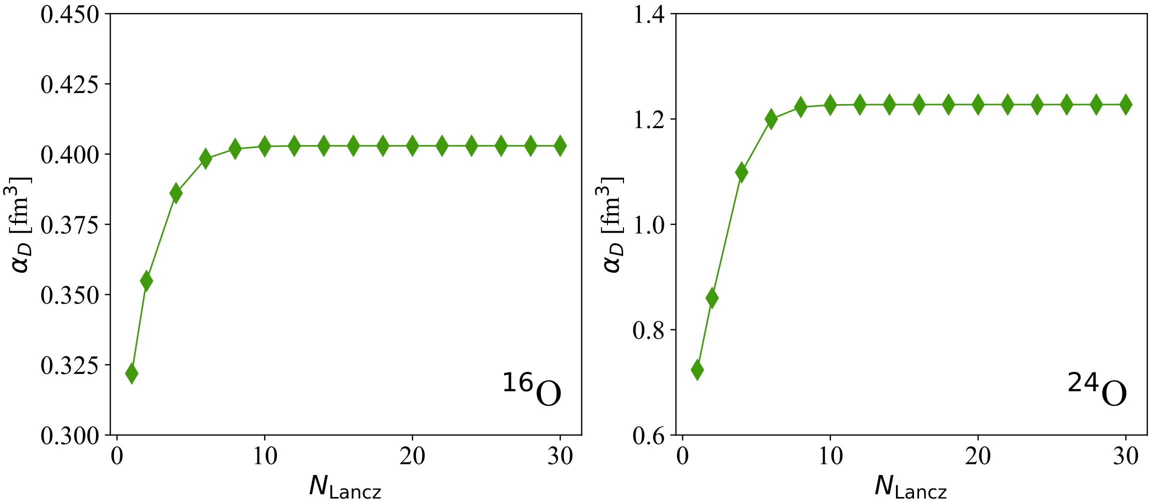

Figure 6.6: Left (right) panel: Dipole polarizability of ^{16}O (^{24}O) in the 3p-1h/3p-1h approximation as a function of the number of Lanczos coefficients N_{Lancz} used to calculate the LIT according to Eq. (5.66).

has already been carried out for closed-shell nuclei in Ref. [86]. We focus here on the case of 2PA-LIT-CC computations. In Figure 6.6, we present the dipole polarizability of the benchmark nuclei ^{16,24}O, calculated with the 2PA-LIT-CC method, as a function of the number of Lanczos coefficients N_{Lancz} included in Eq. (5.66) to determine the LIT.

For both ^{16,24}O, 20 Lanczos coefficients turn out to be sufficient for convergence. Already with $N_{\text{Lancz}} = 10$, differences from the fully converged result lie below 0.001%. This behaviour has been observed also in heavier nuclei, and it reflects the fact that being α_D an inverse energy-weighted sum rule, it depends only on the first few dipole-excited states of the spectrum, characterised by a faster convergence in the Lanczos algorithm.

In analogy to the case of m_0, Figs. 6.7 and 6.8 illustrate the dependence on $\hbar\Omega$ of both closed-shell and 2PA results at different levels of approximation varying N_{max} between 8 and 12. Closed-shell and 2PA predictions for α_D of ^{16,24}O can be found in Table 6.4.

Table 6.4: Predictions for the dipole polarizability α_D in fm^3 of ^{16,24}O in the closed-shell T-1/D and 2PA 3p-1h/3p-1h approximations obtained with the ΔNNLO$_{\text{GO}}$(394) interaction. The theoretical uncertainty has been obtained as detailed in Section 6.1.

Nucleus	T-1/D	3p-1h/3p-1h
^{16}O	0.54(4)	0.40(16)
^{24}O	1.32(6)	1.22(16)

In all the closed-shell and 2PA approximations under study, α_D for ^{16}O converges quite quickly at an optimal frequency of $\hbar\Omega = 12$ MeV. Considering the different closed-shell and 2PA truncations available, the α_D results share some commonalities with the behaviour

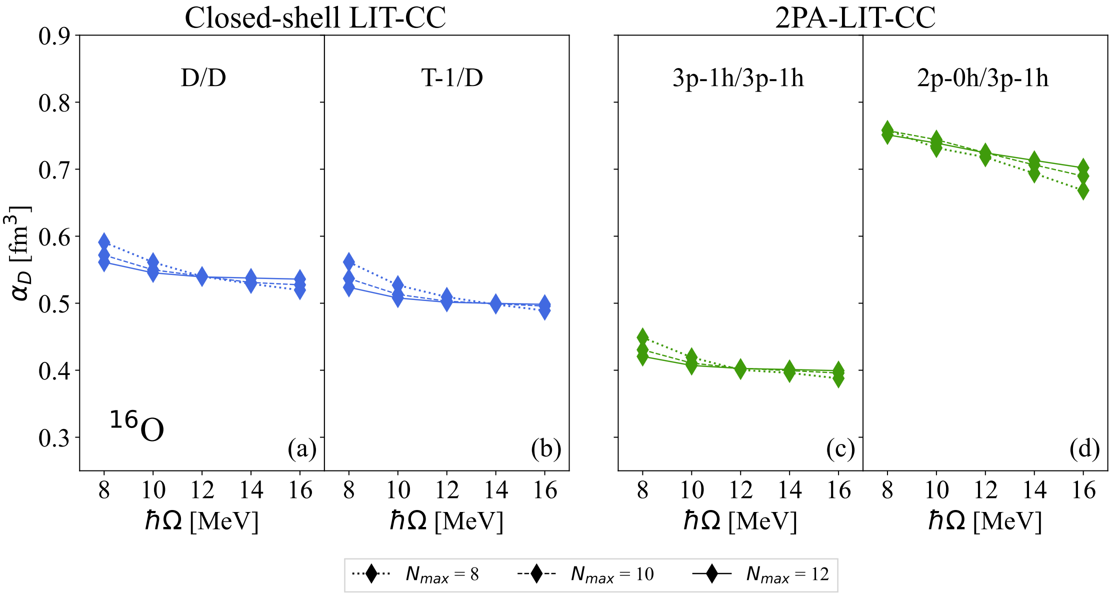

Figure 6.7: ^{16}O results for α_D from the closed-shell D/D and T-1/D approximations [panels (a) and (b), respectively] and the 2PA 3p-1h/3p-1h and 2p-0h/3p-1h approximations [panels (c) and (d), respectively]. Each panel shows α_D as a function of $\hbar\Omega$ for different model space sizes.

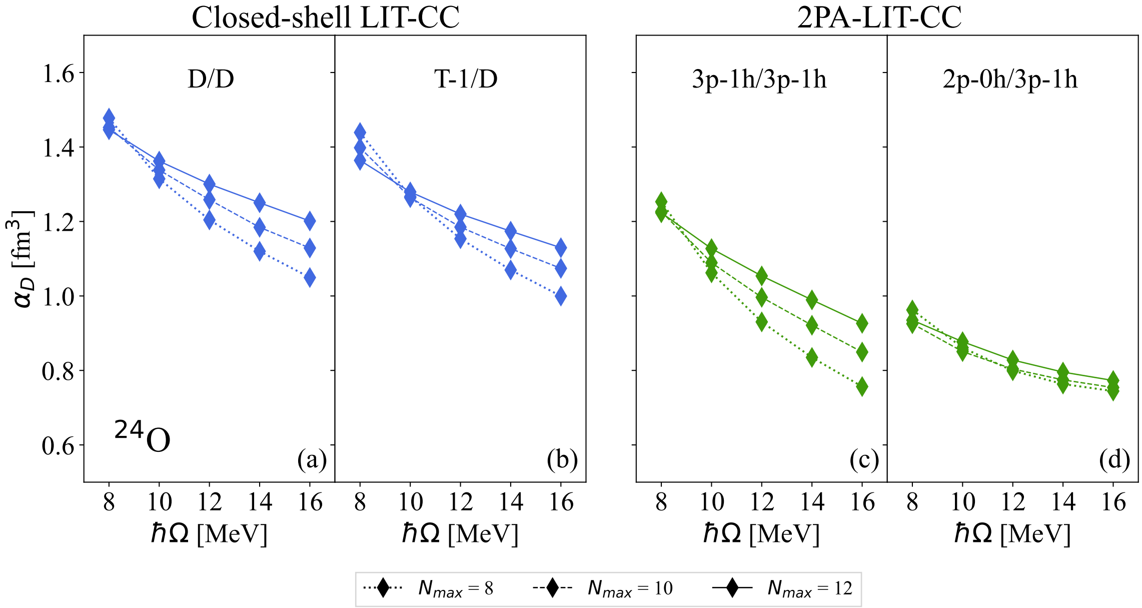

Figure 6.8: ^{24}O results for α_D from the closed-shell D/D and T-1/D approximations [panels (a) and (b), respectively] and the 2PA 3p-1h/3p-1h and 2p-0h/3p-1h approximations [panels (c) and (d), respectively]. Each panel shows α_D as a function of $\hbar\Omega$ for different model space sizes.

observed in the case of m_0. First, the T-1/D value for α_D is lower than the D/D one, of around 7%. As mentioned in Section 6.2, the reduction of α_D when triples are included has been already observed in the case of ^{16}O employing the NNLO$_{\text{sat}}$ interaction [101], and it is a feature shared by various medium-mass nuclei [5, 49, 77]. Second, as for the 2PA results, the 3p-1h/3p-1h approximation reduces the value of α_D with respect to the 2p-0h/3p-1h scheme of around 40%. The resulting large error bar then covers the difference between the T-1/D and 3p-1h/3p-1h optimal frequency values, which amounts to 20% (see Table 6.4).

In the case of ^{24}O, for all the approximation schemes considered the optimal frequency moves towards lower values of $\hbar\Omega$, ranging between 8 and 10 MeV. In analogy to the m_0 results, the larger spatial extension of ^{24}O leads to a more significant residual dependence on $\hbar\Omega$ with respect to the case of ^{16}O. The spread of the different N_{max} curves as a function of $\hbar\Omega$ appears to be similar among the different approximation schemes, except for the 2p-0h/3p-1h case, showing a more compressed pattern. Let us now consider the behaviour of α_D when going from the less accurate to the more accurate many-body framework for both closed-shell and 2PA calculations. In the closed-shell calculations, triples reduce α_D of around 7%, the same amount observed for ^{16}O. In the 2PA case, improving the precision of the calculation from 2p-0h/3p-1h to 3p-1h/3p-1h increases α_D, bringing it closer to the T-1/D value. The difference between the T-1/D and 3p-1h/3p-1h results amounts to 15%. Combining the many-body truncation and convergence contributions, the closed-shell and 2PA results are in agreement, as shown in Table 6.4.

It is interesting to analyse how the difference between the closed-shell and 2PA results for the polarizability originates as a function of the upper integration limit of the LIT in Eq. (5.71). To this aim, starting from Eq. (5.71), it is useful to define the α_D running sum, given by

$$\alpha_D(\varepsilon) = 2\alpha \lim_{\sigma_I \to 0} \int_0^{\varepsilon} d\sigma \, \frac{L(\sigma_R, \sigma_I)}{\sigma_R}. \tag{6.5}$$

This quantity allows one to identify the excitation energy regions where α_D receives the largest contributions. In Figure 6.9, the upper left (right) panel shows the LIT for $\Gamma = 0.01$ MeV for ^{16}O (^{24}O) in the closed-shell and 2PA frameworks. These curves have been obtained adopting the T-1/D approximation in the closed-shell case and the 3p-1h/3p-1h one in the 2PA case. In the lower left (right) panel, the corresponding running sum $\alpha_D(\varepsilon)$ is illustrated.

We observe that below 20 MeV of excitation energy, the low-lying states characterizing the LIT in the closed-shell and 2PA approaches are giving similar contributions to the polarizability of ^{16,24}O. However, at higher excitation energies, corresponding to the region of the giant dipole resonance (GDR), the 2PA result systematically underestimate the closed-shell one in both nuclei, leading in the end to a lower value for α_D. The origin of this behaviour becomes clear when looking at the LIT: in both ^{16,24}O the states corresponding to the GDR are shifted towards higher energies. This effect is more pronounced for ^{16}O, where the states characterized by the highest strength in the LIT appear close to 40 MeV, while in ^{24}O they are located at around 30 MeV.

To understand the reason of this behaviour, we introduce a tool to gauge the quality of the 3p-1h/3p-1h approximation in describing specific nuclear states. In Refs. [180, 181], the

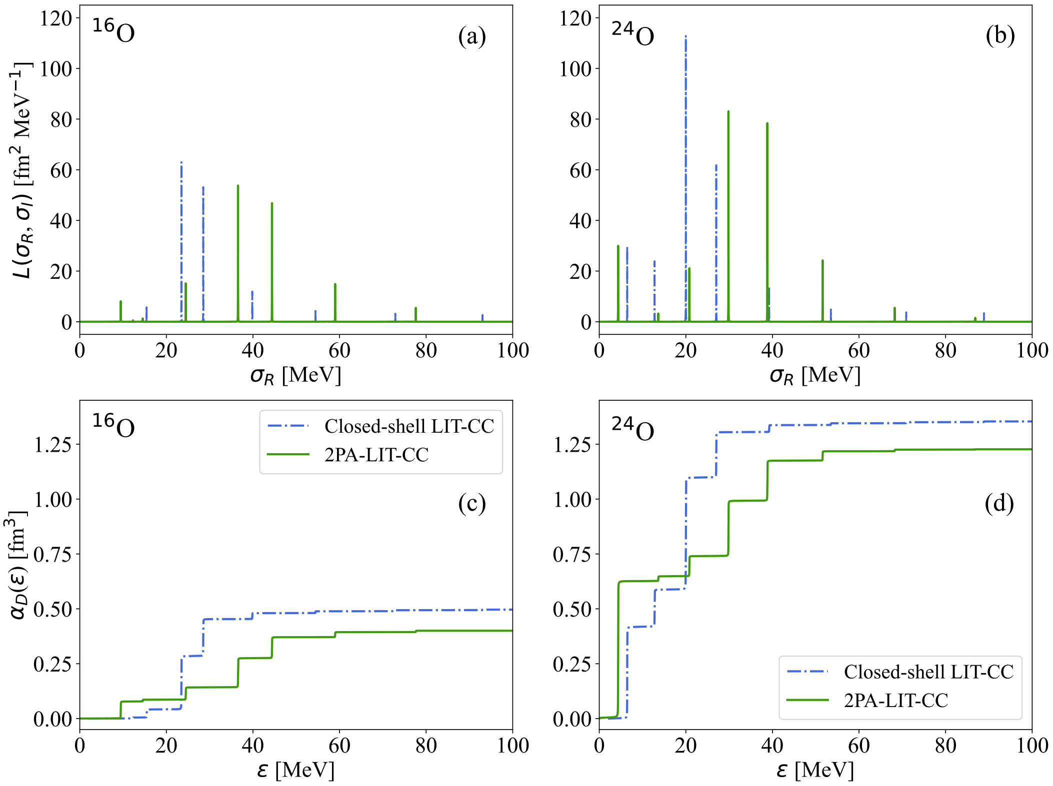

Figure 6.9: Panels (a) and (b): closed-shell and 2PA LIT with $\Gamma = 0.01$ MeV as a function of excitation energy for the ^{16}O and ^{24}O nuclei, respectively. Panels (c) and (d): corresponding α_D running sums as a function of the upper integration limit for the ^{16}O and ^{24}O nuclei, respectively. The results shown for ^{16}O (^{24}O) have been obtained with $N_{max} = 12$ and $\hbar\Omega = 12$ MeV ($\hbar\Omega = 8$ MeV) in the closed-shell T-1/D and the 2PA 3p-1h/3p-1h approximations.

partial 2p-0h and 3p-1h norms of the wavefunction have been identified as possible markers of missing higher order correlations in the 2PA expansion. It is worth to revise this here. Given the 2p-0h and 3p-1h amplitudes of a 2PA state with angular momentum J, the partial norms are defined as

$$\begin{aligned} n(\text{2p0h}) &= \frac{1}{2}\sum_{ab}(2J+1)(r^{ab})^2, \\ n(\text{3p1h}) &= \frac{1}{6}\sum_{abci}\sum_{J_{ab},J_{abc}}(2J_{abc}+1)(r_i^{abc})^2, \end{aligned} \tag{6.6}$$

where $n(\text{2p0h}) + n(\text{3p1h}) = 1$. $n(\text{2p0h})$ and $n(\text{3p1h})$ allow one to quantify the wavefunction's share in 2p-0h and 3p-1h configurations. As a rule of thumb, a 2p-0h partial norm of around 0.9 indicates an accurate description of the nuclear state of interest within a 3p-1h truncation of the 2PA expansion. A lower 2p-0h norm could point towards the need of including 4p-2h or higher correlations.

The calculation of the dipole polarizability is affected by the quality of the ground state and of the excited states that we can access via the Lanczos algorithm, as explained in Section 5.2.4. For both ^{16,24}O we computed the partial norm $n(\text{2p0h})$ for these states. In Table 6.5, we report the values of $n(\text{2p0h})$ for the ground state and the first dipole-excited state appearing in the LIT. Being α_D an inverse energy-weighted sum rule, the latter has a significant impact on this observable. For instance, in the 2PA case such state covers around $1/4$ of the total value of the polarizability for ^{16}O and almost $1/2$ for ^{24}O.

Table 6.5: Partial norms $n(\text{2p0h})$ of the ground state and first dipole-excited state of ^{16,24}O in the 2PA framework.

Nucleus	Ground state	First 1^- state
^{16}O	0.84	0.73
^{24}O	0.90	0.88

The results of Table 6.5 suggest that while for ^{24}O both the ground state and the first 1^- state, characterized by $n(\text{2p0h}) \approx 0.9$, appear to have a dominant 2PA structure, for ^{16}O the 3p-1h/3p-1h approximation turns out to be less accurate. Moreover, it is worth pointing out that considering the dipole-excited states at energies above 20 MeV, and in particular the GDR region, $n(\text{2p0h})$ quickly decreases for both nuclei, falling well below 50%. This could indicate the need of including higher order correlations for a more precise description of the GDR.

6.3.2 Electric dipole polarizability along the oxygen isotopic chain

Equipped with the closed-shell and 2PA-LIT-CC approaches, we can now explore how the dipole polarizability evolves along the oxygen isotopic chain. In addition to ^{16}O and ^{24}O, which can be addressed with both methods, we can consider ^{14}O and ^{22}O in the closed-shell framework and ^{18}O as a 2PA nucleus with respect to ^{16}O. We choose to adopt the T-1/D approximation for the closed-shell calculations and the 3p-1h/3p-1h approximation for the 2PA ones. In Figure 6.10, we show our results in comparison to available experimental data and theoretical predictions.

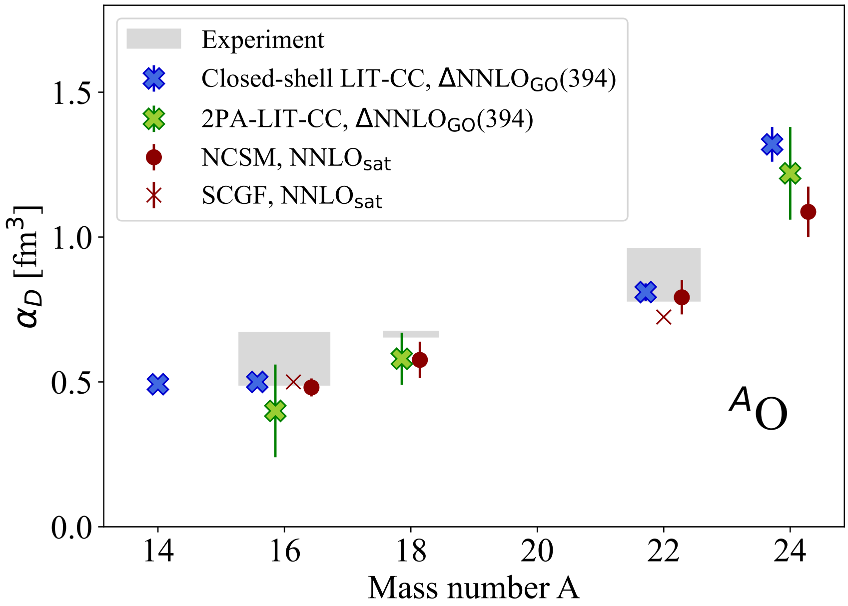

Figure 6.10: Predictions for the electric dipole polarizability of ^{14,16,18,22,24}O obtained either with closed-shell LIT-CC in the T-1/D approximation or with the 2PA-LIT-CC approach in the 3p-1h/3p-1h approximation in comparison with available experimental data for ^{16}O [88], ^{18}O [199], ^{22}O [200]. The data of Refs. [199, 200] are supplemented by theory at high excitation energy (see text for details). Ab initio results for ^{16,18,22,24}O from the NCSM approach [201, 202] and for ^{16,22}O from the SCGF method [203] are also included.

First of all, it is worth pointing out the significant increase of the polarizability obtained by moving from the valley of stability to more neutron-rich systems. Starting from ^{14}O and going towards ^{24}O, the polarizability becomes more than twice as large.

The uncertainty bands on our results are determined according to the recipe of Section 6.1. For the closed-shell results, the many-body and convergence contribution to the theoretical error are comparable, leading to a total uncertainty which varies from 3% to 5% going from ^{14}O to the more neutron-rich ^{24}O. For the 2PA results, the many-body uncertainty is dominant. While for ^{18}O and ^{24}O it amounts to 15 and 13% of the central value, respectively, for ^{16}O it grows up to 40%. The larger uncertainty in the case of ^{16}O could reflect the lower level of accuracy of the 3p-1h/3p-1h approximation for this nucleus, as shown in Table 6.5. Figure 6.10 makes the consistency between the LIT-CC and 2PA-LIT-CC results visually apparent for our benchmark ^{16}O and ^{24}O nuclei.

We find an excellent agreement between our theory and the available experimental data. The experimental values for α_D are obtained by integrating the data of Ref. [88] for ^{16}O, Ref. [199] for ^{18}O and Ref. [200] for ^{22}O. While for ^{16}O data are available up to an excitation energy of 100 MeV, which is sufficient for the integral of Eq. (5.71) to saturate, the maximum excitation energy reached by data is 40 MeV for ^{18}O and 18 MeV for ^{22}O. To obtain a final estimate of α_D for these two nuclei, we calculate $\alpha_D(\omega > 40\ \text{MeV})$ for ^{18}O and $\alpha_D(\omega > 18\ \text{MeV})$ for ^{22}O and add these values to the corresponding experimental result. In the case of ^{18}O, integration of the experimental data give $\alpha_D(\omega < 40\ \text{MeV}) = 0.58\ \text{fm}^3$, while on the theory side, we obtain $\alpha_D(\omega > 40\ \text{MeV}) = 0.090(14)\ \text{fm}^3$. Adding up the two values, we obtain a final determination of $\alpha_D = 0.670(14)\ \text{fm}^3$. We point out that the experimental data of Ref. [199] are reported without corresponding uncertainties, and that the error bar in this case accounts only for the theory uncertainty. For ^{22}O, the experimental data at low energy yield $\alpha_D(\omega < 18\ \text{MeV}) = 0.24(6)\ \text{fm}^3$, while $\alpha_D(\omega > 18\ \text{MeV}) = 0.63(3)$ fm^3. We then determine an upper and lower bound for α_D by adding up the corresponding upper and lower bounds of the theoretical and experimental values, respectively. This yields $0.78 < \alpha_D < 0.96\ \text{fm}^3$.

In Figure 6.10, we also reported α_D predictions for ^{16,18,22,24}O in the NCSM approach [201, 202] and for ^{16,22}O in the SCGF approach [203]. In both NCSM and SCGF calculations, the NNLO$_{\text{sat}}$ interaction was employed. NCSM predictions for ^{16,18,22}O agree well with CC values and with data. In particular, we highlight that the excellent accordance between the NCSM result for ^{18}O and our 2PA prediction provides an additional benchmark for the newly developed 2PA-LIT-CC method. The SCGF prediction for ^{16}O is consistent with our results and with experiment, while their value is slighly lower than the T-1/D one for ^{22}O.

Being at the dripline, ^{24}O represents an interesting physics case. With a polarizability of 1.087(87) fm^3, NCSM calculations underestimate this observable with respect to the T-1/D result of 1.32(6) fm^3, while being consistent with the 2PA value of 1.22(16) fm^3. To our knowledge, no experimental data are available for ^{24}O. However, the large spread of the predictions obtained with different ab initio methods and nuclear interaction models motivates an experimental investigation of the dipole strength of this nucleus.

6.3.3 Electric dipole polarizability along the calcium isotopic chain

Going towards heavier systems, we can address the evolution of the dipole polarizability along the calcium isotopic chain. In this case the polarizability of ^{36,40,48,52}Ca can be tackled with the usual closed-shell LIT-CC, while we can provide predictions of α_D for ^{38,42,50,56}Ca with the 2PA-LIT-CC approach. Both LIT-CC frameworks can be used to calculate α_D for ^{54}Ca, which serves as a benchmark nucleus in this isotopic chain. As in the previous Section, we adopt the T-1/D approximation for the closed-shell calculations, while we truncate the 2PA expansion at the 3p-1h/3p-1h level. The results are shown in Figure 6.11 in comparison to available experimental data.

We observe that predictions for the polarizability of 2PA nuclei appear to be smaller than the ones obtained for their closed-shell neighbours. The theoretical uncertainty of the

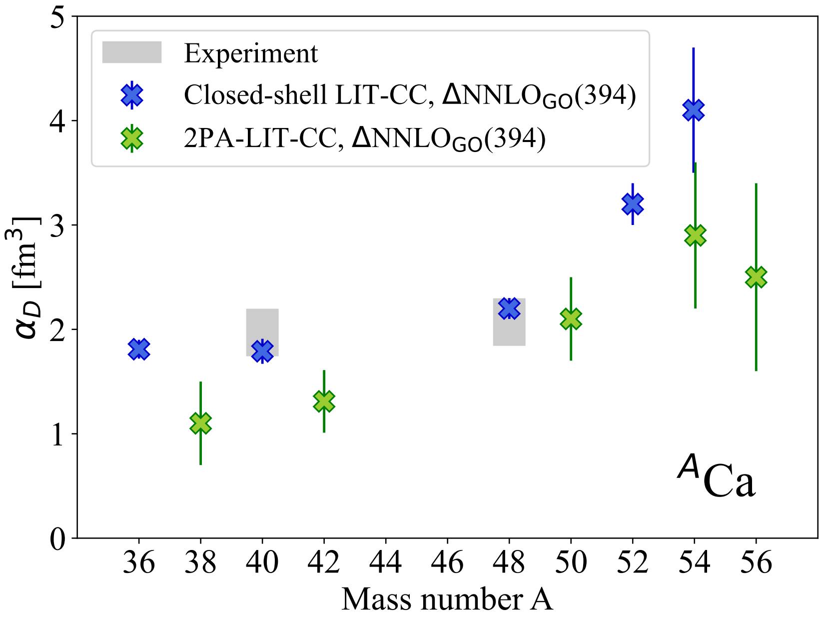

Figure 6.11: Predictions for the electric dipole polarizability of ^{36,38,40,42,48,50,52,54,56}Ca obtained either with closed-shell LIT-CC in the T-1/D approximation or with the 2PA-LIT-CC approach in the 3p-1h/3p-1h approximation. Experimental values of α_D for ^{40}Ca [5] and ^{48}Ca [48] are also reported for comparison.

closed-shell results, mainly determined by the many-body truncation, varies between 5% and 7% of the corresponding central value. It increases up to 15% only for the neutron-rich ^{54}Ca, where we notice a larger residual dependence on the convergence parameters. Also in the case of the 2PA calculations, the effect of truncating the many-body expansion dominates the theoretical error. Depending on the nucleus, the uncertainty ranges between 24% and 36% of the central value. This result is also affected by the slower convergence characterizing α_D for ^{50,54,56}Ca in the 2p-0h/3p-1h scheme, considered to evaluate the many-body truncation error. A further refinement of our 2PA results could come by including triples in the coupled-cluster reference calculation. We leave this analysis to future work.

It is useful to focus on the case of ^{54}Ca, where we can compare the two CC frameworks. While being compatible with the closed-shell outcome within error bars, the 2PA calculation leads to a smaller central value of α_D for ^{54}Ca. The reason of this behaviour lies in the shape of the LIT, where the GDR appears at higher excitation energies in the 2PA result with respect to the closed-shell one, as shown in Figure 6.12.

We have already observed a similar shift of the GDR towards higher energies for ^{16,24}O (see Figure 6.9). To understand this systematic effect, also in the case of ^{54}Ca we analysed the partial norm n(2p0h) for the ground state and the dipole-excited states, finding a situation similar to the case of ^{24}O. While the ground state and first 1^- state have a good 2PA-dominated structure, with $n(\text{2p0h}) \approx 0.9$ in both cases, n(2p0h) becomes rapidly much

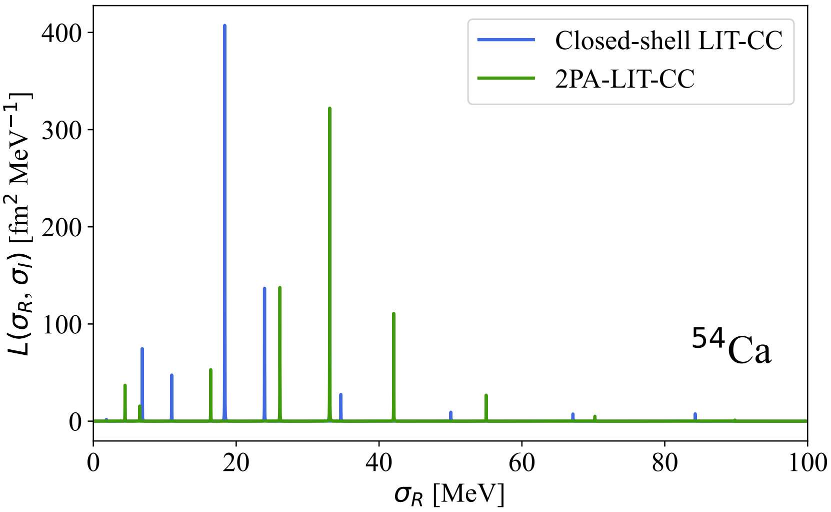

Figure 6.12: LIT with $\Gamma = 0.01$ MeV in the closed-shell and 2PA-LIT-CC approaches for ^{54}Ca as a function of excitation energy. These curves have been obtained with $N_{max} = 12$ and $\hbar\Omega = 8$ MeV. In the closed-shell case, the T-1/D approximation has been used, while for the 2PA case the 3p-1h/3p-1h result is shown.

smaller than $n(3\text{p}1\text{h})$ for the dipole-excited states in the GDR region, suggesting the need of higher-order correlations in this energy range.

Starting from ^{36}Ca all the way up to ^{54}Ca, our predictions for closed-shell and 2PA nuclei show an increase of the dipole polarizability with the number of neutrons, as observed for oxygen isotopes, but when going from ^{54}Ca to ^{56}Ca. In fact, the central value of α_D for ^{56}Ca is slightly lower than the one of ^{54}Ca in the 2PA framework, even though uncertainties increase in this region. This would make an experimental investigation of α_D in these neutron-rich nuclei particularly interesting.

To our knowledge, experimental data in this isotopic chain are available only for ^{40,48}Ca [5, 48]. As already mentioned in Section 6.2, the family of interactions from Ref. [68] and NNLO$_{\text{sat}}$ were employed in those works, but we observe here a good agreement also between the theoretical prediction obtained using ΔNNLO$_{\text{GO}}$(394) and experiment. Inelastic proton scattering data for ^{42}Ca from iThemba Labs, currently under analysis [50], could soon provide an experimental benchmark for our 2PA prediction.

6.4 Ground and dipole-excited states of ^{8}He

In the previous Section, we showed that combining the closed-shell and 2PA-LIT-CC approaches we can get a deeper understanding of the physics of α_D in the medium-mass region of the nuclear chart. In parallel to these efforts, during this thesis we have also extended our investigations to light-neutron rich nuclei at the dripline. Here, the nuclear force gives rise to intriguing phenomena, such as the emergence of halo structures, with weakly-bound nucleons orbiting a compact core at a distance. Halo nuclei are characterized by small separation energies and extended matter radii, which do not follow the typical $A^{1/3}$ scaling found in the valley of stability.

Among halo systems, ^{8}He represents an interesting case study. It has the most extreme neutron-to-proton ratio ($N/Z = 3$) in the nuclear chart and up to now, it is the only known four-neutron halo. This unique configuration has been leveraged in a recent groundbreaking experiment, performed at RIKEN, where a ^{8}He knockout reaction at large momentum transfer led to the observation of a correlated four-neutron state [204]. While from the theory point of view the existence of a bound tetraneutron is disputed (see, e.g., Ref. [205] and references therein), new experiments have either been made [206] or they are being planned for [207]. The debate around the interpretation of the RIKEN $4n$ signal has triggered new investigations of the neutron halo distribution and the possible correlations among the loosely-bound neutrons in ^{8}He [208, 209].

In halo nuclei, the extended size of the neutron cloud is often mentioned together with a strong enhancement of the electric dipole response at low excitation energies. Revealed by early measurements with radioactive ion beams [210], this so-called “soft E1 excitation” ranks among the main features identifying halo nuclei [211]. However, the presence of a soft dipole mode in ^{8}He is still a controversial issue from both the experimental and theoretical point of view.

Coulomb excitation [212] and nuclear fragmentation [213] experiments first supported the existence of a 1^- resonance at an excitation energy of around 4 MeV in the spectrum of ^{8}He. Later, (t, p) transfer reaction data [214] confirmed the presence of low-lying dipole strength, but at a lower energy of 3 MeV. In contrast, the Coulomb excitation experiment of Ref. [215] attributed a relatively small fraction of the total energy-weighted dipole sum rule (less than 3%) to a potential soft dipole mode. Also, a measurement of breakup of ^{8}He on carbon [216] found the spin-parity assignment of the excited state at 4 MeV to 1^- highly uncertain. These results were validated by a recent inelastic proton scattering experiment [217], where the measured angular distribution was found to be incompatible with a low-lying dipole resonance. Very recently, high-statistics Coulomb excitation data obtained at RIKEN by the SAMURAI collaboration [94] have indicated the presence of low-lying strength between 3 and 4 MeV, in agreement with Refs. [212–214].

From the theory point of view, our recent work, published in Ref. [1], was the first to tackle dipole excited-state properties of ^{8}He in the framework of ab initio LIT-CC calculations based on chiral EFT interactions. Together with the growing experimental interest, our effort has driven subsequent theoretical analysis within the random-phase approximation (RPA) in EDF theory [218], the cluster orbital shell model (COSM) [219, 220] and the equation-of-motion multiphonon approach (EMPM) [221].

In this Section, we summarise the results obtained on ^{8}He during the work of this thesis, drawing from Refs. [1, 2, 6]. We start our journey by testing our control on ground-state properties of ^{8}He, as its charge radius R_{ch}, and compare our predictions to available experimental data. We then analyse the dipole-excited spectrum, looking at the discretized dipole response function, and provide LIT-CC predictions for the dipole polarizability, comparing them to the results of the theoretical approaches mentioned above. We also explore the correlation of α_D with the point-neutron radius R_n, highlighting the sensitivity of the low-energy dipole strength to the extent of the point-neutron distribution in this exotic nucleus. We conclude by presenting a comparison between our LIT-CC predictions for the dipole polarizability and the high-precision RIKEN experimental data of Ref. [94].

In this Section, we calculate ^{8}He as a closed-shell nucleus. To assess the Hamiltonian dependence of our results, we use four chiral EFT interactions: 1.8/2.0 (EM), NNLO$_{\mathrm{sat}}$, ΔNNLO$_{\mathrm{GO}}$(450) and ΔNNLO$_{\mathrm{GO}}$(394). Among them, the latter two are Δ-full interactions, and they differ for the cutoff value, given by 450 MeV/c for the first and 394 MeV/c for the second. Moreover, the 1.8/2.0 (EM) interaction includes also NN force terms at N^{3}LO, while the other chiral force models are truncated at NNLO. More details on these interactions can be found in Section 3.3. The convergence of the observables considered in this Section has been examined increasing the model space size N_{max} from 10 to 14, and varying the $\hbar\Omega$ frequency between 12 and 16 MeV. In selected cases, calculations with $\hbar\Omega = 10$ MeV have been possible for the 1.8/2.0 (EM) and ΔNNLO$_{\mathrm{GO}}$(394) interactions.

6.4.1 Charge radius

In this paragraph we begin our investigation of the structure of ^{8}He by calculating its charge radius R_{ch}. To this aim, we first compute the point-proton radius $R_p = \sqrt{\langle R_p^2 \rangle}$, where the mean-square point-proton radius operator is defined as

$$R_p^2 = \frac{1}{Z} \sum_{i=1}^{A} r_i^2 \left(\frac{1+\tau_i^z}{2} \right). \tag{6.7}$$

Here, we use the same notation as Eq. (2.15). Figure 6.13 shows the convergence pattern of R_p with respect to the HO basis parameters for the four chiral EFT interactions under analysis, in the D and T-1 truncation schemes.

For all interactions, we can identify an optimal frequency leading to faster convergence. In particular, for NNLO$_{\mathrm{sat}}$ and ΔNNLO$_{\mathrm{GO}}$(450) the optimal frequency is $\hbar\Omega = 14$ MeV, while for ΔNNLO$_{\mathrm{GO}}$(394) and 1.8/2.0 (EM), the optimal frequency is 12 MeV. Focusing on the CC outcomes for the ΔNNLO$_{\mathrm{GO}}$(450) and ΔNNLO$_{\mathrm{GO}}$(394) interactions, we observe that the cutoff difference affects the $\hbar\Omega$ dependence of the results, leading to a faster convergence when the cutoff is lower. At the optimal frequency, the difference between the R_p values for D and T-1 varies between 1% and 1.5% for the different interactions.

Starting from R_p, we then compute the charge radius using

$$\langle R_{ch}^2 \rangle = \langle R_p^2 \rangle + r_p^2 + \frac{N}{Z} r_n^2 + \frac{3}{4M_p^2} + r_{so}^2\,, \tag{6.8}$$

where $r_p = 0.8414(19)$ fm [222] is the proton charge radius, $r_n^2 = -0.106^{+0.007}_{-0.005}$ fm^2 [223] is the neutron charge radius, $3/(4M_p^2) = 0.033$ fm^2 is the Darwin-Foldy term [224] and r_{so}^2 is

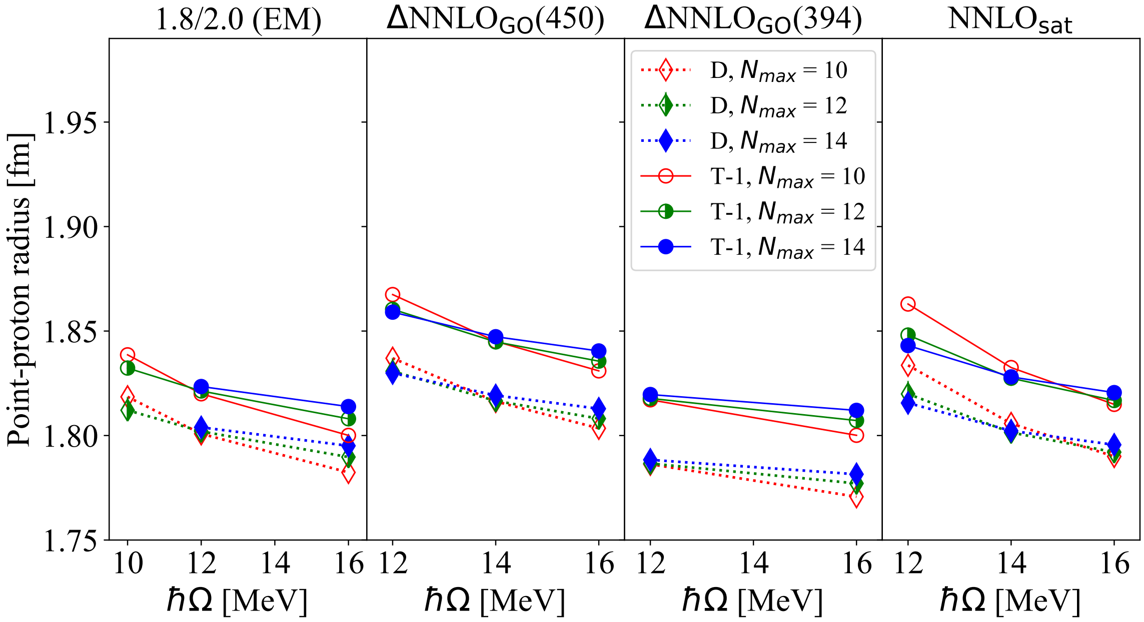

Figure 6.13: Convergence pattern of the point-proton radius of ^{8}He with respect to $\hbar\Omega$ for various N_{max} for the four Hamiltonians in the D and T-1 truncation schemes. Figure adapted from Ref. [1] and complemented with 1.8/2.0 (EM) results.

the spin-orbit correction [225].

In Ref. [225] it has been pointed out that r^2_{so} could give a remarkable contribution to the charge radius of halo nuclei. Therefore, we have consistently calculated this correction in CC theory. Our results are reported in Table 6.6, in comparison to previous theoretical estimates. The prediction of Ref. [225] is based on a shell model calculation, while in Ref. [226] the Gamow shell model is employed. In this framework, the CC approach allows us to account for many-body correlations, leading to a significant improvement with respect to previous calculations of this quantity. Taking the NNLO$_{\text{sat}}$ result as an example, the magnitude of r^2_{so} is reduced of about 10% with respect to Ref. [226], and of approximately

Table 6.6: Theoretical predictions for the spin-orbit correction to the charge radius of ^{8}He in fm^2 for the four different interactions in comparison to previous theoretical results. Uncertainties are calculated as detailed in Section 6.1.

Interaction	r^2_{so}
1.8/2.0 (EM)	-0.123(10)
ΔNNLO$_{\text{GO}}$(450)	-0.134(9)
ΔNNLO$_{\text{GO}}$(394)	-0.141(6)
NNLO$_{\text{sat}}$	-0.143(6)
Ref. [225]	-0.17
Ref. [226]	-0.158

15% with respect to the shell model estimate.

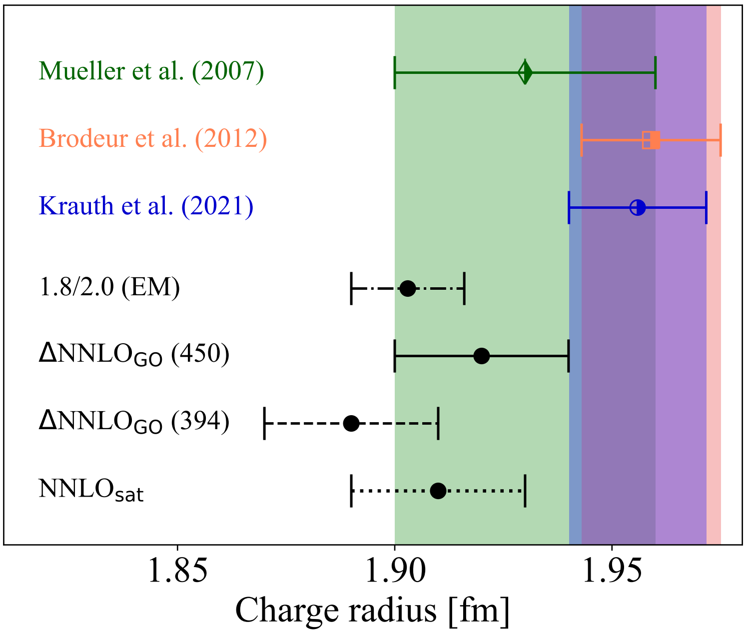

Figure 6.14: Comparison between the coupled-cluster theoretical values for the charge radius of ^{8}He using the four different Hamiltonians and the experimental results of Mueller et al. [227], Brodeur et al. [228] and Krauth et al. [229]. Figure adapted from Ref. [1] and complemented with 1.8/2.0 (EM) results.

The final results for the charge radius of ^{8}He are illustrated in Figure 6.14 in comparison to three experimental determinations. The charge radius of ^{8}He can be experimentally obtained from a measurement of the isotope shift, namely the frequency difference $\delta\nu_{\mathrm{A,A'}}$ between ^{8}He and the reference isotope ^{4}He, in the same atomic transition. The frequency shift is related to the difference $\delta\left\langle R^2_{ch}\right\rangle_{\mathrm{A,A'}}$ in the charge radius between ^{8}He and ^{4}He by

$$\delta\nu_{\mathrm{A,A'}} = \delta^{Mass}_{\mathrm{A,A'}} + K_{FS}\delta\left\langle R^2_{ch}\right\rangle_{\mathrm{A,A'}}\,, \tag{6.9}$$

where the mass shift $\delta^{Mass}_{\mathrm{A,A'}}$ and the field shift constant K_{FS} are obtained from precise atomic theory calculations. The first determination of the charge radius of ^{8}He using this method stems from Ref. [227], where the radius of ^{4}He measured from electron scattering was used as a reference. Later, Ref. [228] provided an improved estimate of the mass and field shift parameters, based on precise nuclear mass measurements. More recently, Ref. [229] achieved the first determination of the ^{4}He charge radius from muonic atoms, which, improving the reference, slightly modified R_{ch} for ^{8}He.

In general, we find that our theoretical results overlap with the area spanned by the three experimental determinations, as seen in Figure 6.14. The ΔNNLO$_{\mathrm{GO}}$(450) interaction leads to the largest charge radius, equal to 1.92(2) fm, which agrees best with Ref. [227]. Moreover, the distance between the upper end of the ΔNNLO$_{\mathrm{GO}}$(450) error bar and the lower end of the one of the most recent experimental determination [229] amounts to only 10^{-4}

fm. Comparing this to the scale of the values involved, we can still claim a good agreement between these two results.

6.4.2 Discretized response function and dipole polarizability

We now turn to the dipole-excited states in ^{8}He by first looking at the discretized response function. In our framework, this quantity can be simply calculated taking the limit of the LIT for $\sigma_I \to 0$, as shown in Eq. (5.68). Figure 6.15 shows the T-1/T-1 discretized response function obtained with the different chiral forces under analysis.

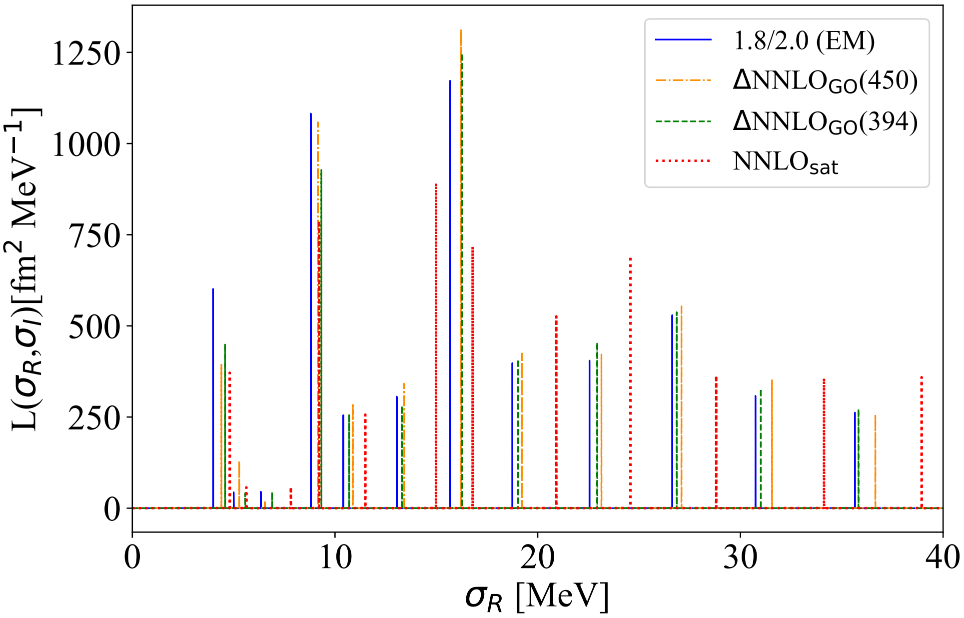

Figure 6.15: LIT of ^{8}He with $\sigma_I = 10^{-4}$ MeV in the T-1/T-1 framework for the four different Hamiltonians. Figure taken from Ref. [6].

For all the potentials, the LIT is characterized by low-energy peaks emerging at around 5 MeV. For the 1.8/2.0 (EM) interaction, the latter appear at slightly lower energies than predicted by the other chiral EFT interactions. This corroborates the consistency of our coupled-cluster predictions with the experiments of Ref. [212–214], and the recent RIKEN measurement [94], where low-lying strength has been detected between 3 and 4 MeV.

On the theory side, our findings agree with the COSM [219, 220] and EMPM [221] theoretical calculations, which predict the presence of a soft dipole resonance. On the other hand, the RPA calculation of Ref. [218] disfavours such scenario, attributing it to spurious center-of-mass contaminations.

Moving towards higher excitation energies, the large number of states that we observe for all the potentials employed correspond to the giant dipole resonance. Starting from the discretized response function and employing Eq. (5.71), we can study the dipole polarizability

α_D. In Figure 6.16, we show the convergence pattern of α_D with respect to $\hbar\Omega$ for the four Hamiltonians under analysis, in the D/D and T-1/T-1 truncation schemes.

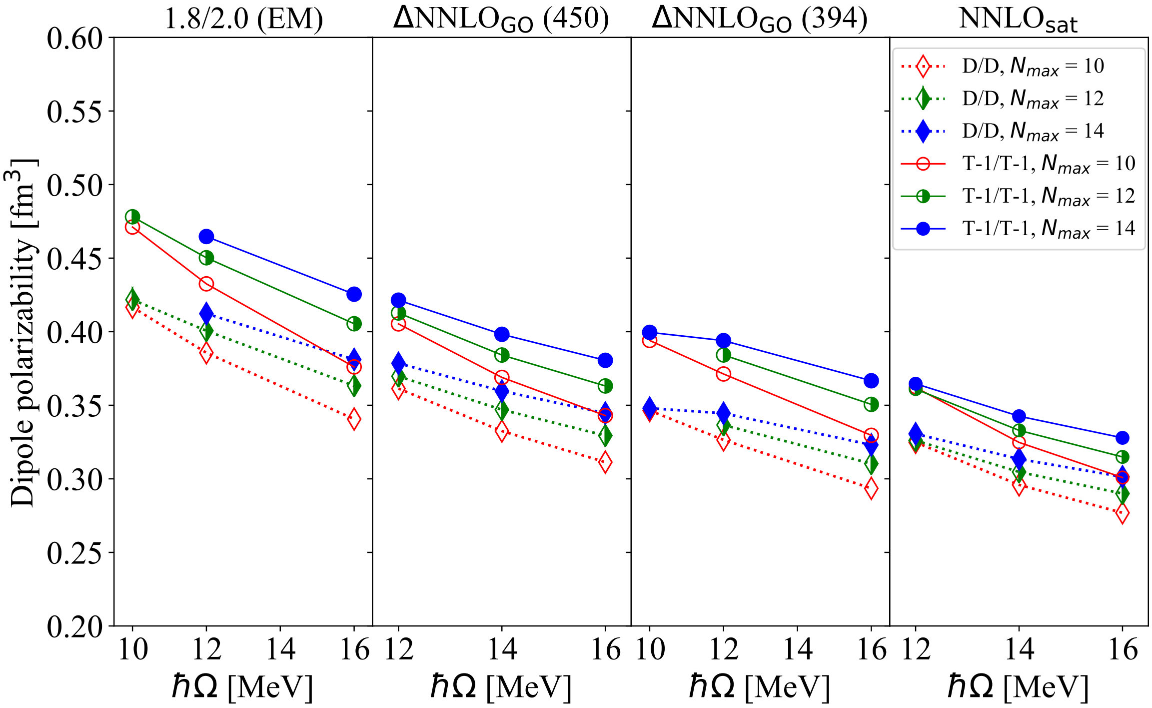

Figure 6.16: Convergence pattern of the dipole polarizability of ^{8}He with respect to $\hbar\Omega$ for various N_{max} for the four Hamiltonians, in the D/D and T-1/T-1 truncation schemes. Figure adapted from Ref. [1] and complemented with 1.8/2.0 (EM) results.

For all four interactions we observe a quite pronounced dependence of the results on the CC truncation and model space parameters. Variations with respect to N_{max} tend to reduce in correspondence to small values of the HO frequency. This slow convergence of the polarizability, reflecting the slow convergence of low-lying dipole states, might be due to the loosely bound halo neutrons in ^{8}He, which determine a more extended wavefunction.

Triples corrections give a non-negligible contribution to α_D both in the ground and excited state part of the CC calculation. For the different interactions, the inclusion of triples just in the ground state (T-1/D truncation, not shown in Figure 6.16) leads to an increase of α_D between 3% and 5% with respect to the D/D scheme result. In the T-1/T-1 approximation, where triples are present in both the ground- and excited-state computation, we achieve an overall 10% enhancement of the polarizability compared to the D/D framework. This deviates from what has been observed in the medium-mass region of the nuclear chart, where the inclusion of triples leads to a reduction of α_D [5, 48, 49].

Our predictions for the dipole polarizability are reported in Table 6.7, where RPA [218] and EMPM [221] results are also included for comparison. As the Coulomb excitation data from RIKEN are available only up to 15 MeV, we dedicate Section 6.4.4 to a detailed comparison between experimental and theoretical α_D running sums.

Table 6.7: Theoretical predictions for the dipole polarizability of ^{8}He in fm^3 with the T-1/T-1 approximation for the four chiral EFT interactions under analysis. RPA predictions based on three relativistic mean-field (RMF) energy density functionals [218] and the EMPM result [221], obtained with the NNLO$_{\text{sat}}$ interaction, are also reported. Uncertainties are calculated as detailed in Section 6.1.

Interaction	α_D
1.8/2.0 (EM)	0.48(3)
ΔNNLO$_{\text{GO}}$(450)	0.42(3)
ΔNNLO$_{\text{GO}}$(394)	0.40(3)
NNLO$_{\text{sat}}$	0.37(3)
RPA, RMF016	0.262
RPA, RMF022	0.242
RPA, RMF028	0.220
EMPM, NNLO$_{\text{sat}}$	0.206

Looking at Table 6.7, we notice that while α_D values from RPA [218] and EMPM [221] range between 0.20 and 0.26 fm^3, CC predictions are appreciably larger, with a theoretical uncertainty varying between 6% and 8% of the central value for the different interactions.

According to our calculations, α_D in ^{8}He turns out to be more than five times larger than the one of ^{4}He. Combining the photoabsorption cross section data of Refs. [230–232], the latter amounts to 0.074(9) fm^3, which is compatible with the results of Ref. [46]. This difference is driven by the fact that soft dipole modes, such as those shown in Figure 6.15 at about 5 MeV, are not seen in ^{4}He [45, 46].

Moreover, it is worth to point out the significant model dependence shown by our CC results for the polarizability of ^{8}He. The NNLO$_{\text{sat}}$ and ΔNNLO$_{\text{GO}}$(394) interactions, which performs well in reproducing the dipole polarizability in the medium-mass region, as shown in Sections 6.2 and 6.3, yield the lowest values for α_D in ^{8}He. The 1.8/2.0 (EM) interaction delivers instead the largest prediction, which is more than 20% higher than the NNLO$_{\text{sat}}$ result. This is a consequence of the location of the low-lying dipole strength in ^{8}He, which appears at slightly lower energies in the 1.8/2.0 (EM) case with respect to the other interactions, as shown in Figure 6.15.

To get further insight on the model uncertainty of our calculation, we can also study how predictions of α_D vary on the basis of the order of the chiral EFT expansion of the potential. We performed this analysis in the case of the Δ-full interaction model, for which also the NLO order is available [138]. In Figure 6.17, we show the $\hbar\Omega$ convergence pattern of α_D for the ΔNLO$_{\text{GO}}$(450) and ΔNNLO$_{\text{GO}}$(450) potentials at the highest value of N_{max} available ($N_{max} = 14$), indicating with bands the contribution of the coupled-cluster truncation uncertainty. For comparison, we also present results for the energy-weighted dipole sum rule, calculated employing Eq. (5.72).

In the case of the dipole polarizability, the theoretical error receives substantial contri-

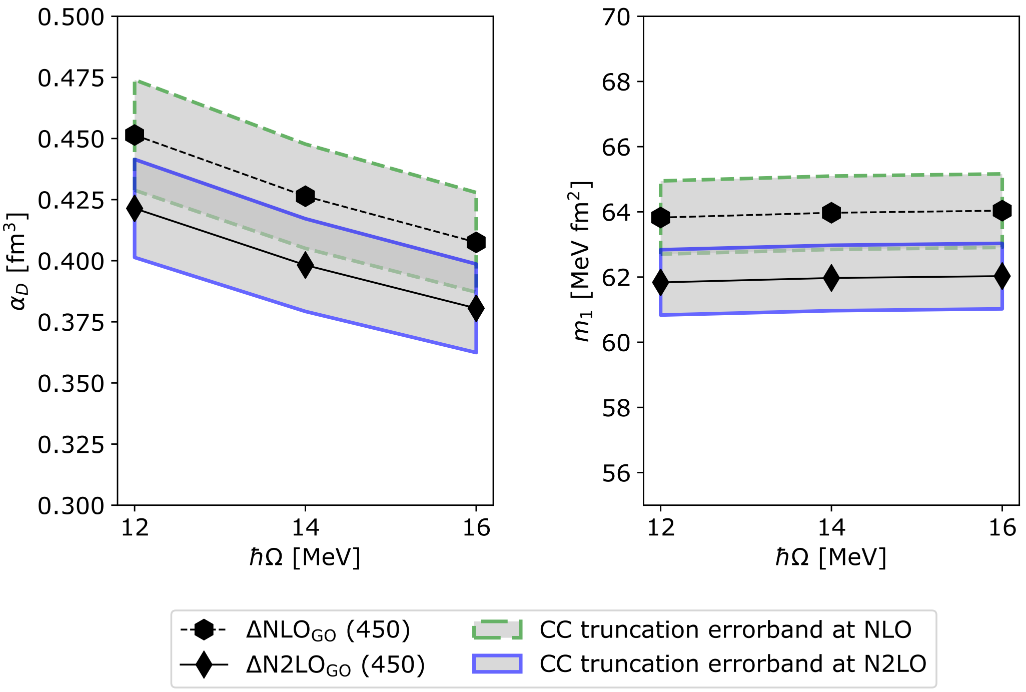

Figure 6.17: The $\hbar\Omega$ convergence pattern of α_D and m_1 for ^{8}He calculated with ΔNLO$_{\mathrm{GO}}(450)$ and ΔNNLO$_{\mathrm{GO}}(450)$ at fixed $N_{max} = 14$. The green and blue bands indicate the CC truncation uncertainty. The black points are the results obtained including triples in both the ground- and excited-state computations. Figure taken from Ref. [2].

butions from both the many-body method and the residual dependence on the CC convergence parameter. ΔNLO$_{\mathrm{GO}}(450)$ predicts a slightly larger polarizability with respect to ΔNNLO$_{\mathrm{GO}}(450)$. Taking into account the σ_{method} uncertainty, the two results agree within errobars.

The situation changes when turning to the energy-weighted sum rule. Here the overall uncertainty is dominated by the coupled-cluster truncation and it is estimated to be below 2%. Also in this case ΔNLO$_{\mathrm{GO}}(450)$ leads to a larger value for m_1. However, due to the smooth convergence of this observable, the difference between the two chiral orders, amounting to 3%, can be better appreciated than in the case of the polarizability.

A more sophisticated analysis of the EFT truncation uncertainty based on Bayesian statistics [196, 197] would require more chiral orders at our disposal. Therefore, for the moment we provide an estimate of σ_{model} in this case by exhibiting the spread of the results obtained using different chiral forces, as done in Table 6.7. It is anyway reassuring to see that in the case of the Δ-full interaction model the NLO and NNLO error bands overlap.

6.4.3 Point-neutron radius and correlation with the polarizability

To assess our understanding of the halo structure of ^{8}He and its impact on low-energy dipole excitations, we calculate the point-neutron radius R_n with the previously employed set of four Hamiltonians and investigate its correlation with the dipole polarizability. In analogy to the case of the point-proton radius, R_n is calculated as $\sqrt{\langle R_n^2 \rangle}$, where the mean-square point-neutron operator corresponds to

$$R_n^2 = \frac{1}{N} \sum_{i=1}^{A} r_i^2 \left(\frac{1 - \tau_i^z}{2} \right). \tag{6.10}$$

Here, the same notation as Eq. (2.15) is employed. Figure 6.18 shows CC predictions for α_D as a function of R_n, in comparison to three experimental determinations of R_n [233–235] and the theoretical estimates obtained by the RPA-EDF[2] [218] and EMPM [221] approaches. Experimental determinations of R_n have been obtained on the basis of interaction cross section measurements in inverse kinematics on carbon [233] and hydrogen targets [234, 235], respectively. A Glauber analysis of the experimental data allows for the extraction of the nuclear matter radius R_m, which in combination with the point-proton radius R_p can be employed to estimate R_n according to the relation $\langle R_m^2 \rangle = (Z \langle R_p^2 \rangle + N \langle R_n^2 \rangle)/A$.

We find that our theoretical predictions for R_n are in excellent agreement with all three experimental determinations. We estimated our theoretical uncertainty following the procedure outlined in Section 6.1. The residual dependence on convergence parameters and the truncation of the many-body CC expansion lead to a combined error band varying between 1 and 2% for the different interactions. The EMPM value for R_n is also in good accordance with experiment, while EDF results overestimate the data.

Looking at our predictions for different chiral forces, we notice the presence of a correlation between α_D and R_n, which emerges also from the RPA-EDF calculations of Ref. [218]. This reflects a link between the low-lying dipole strength, which mainly determines α_D, and an excitation of the weakly-bound excess neutrons. We can arrive to similar conclusions also for neutron-rich nuclei in the medium-mass region, as ^{48}Ca [77] and ^{68}Ni [49]. In fact, Refs. [49, 77] highlight the presence of a correlation between α_D and the point-proton radius R_p for these two nuclei. At the same time, the authors also observed that increasing values of R_p were associated to a corresponding rise in R_n, leading as a consequence to the emergence of a correlation between α_D and R_n.

6.4.4 Comparison of α_D with the RIKEN experimental data

In this Section, we compare our theoretical predictions with the data of Ref. [94], recently obtained at RIKEN by the SAMURAI collaboration. A Coulomb excitation experiment in inverse kinematics, combined with the detection of both the two-neutron and four-neutron

---

[2] Here, the combined notation "RPA-EDF" for the calculations of Ref. [218] indicates that R_n, being a ground-state property, is computed in EDF theory, while α_D requires to couple the RPA with EDF theory.

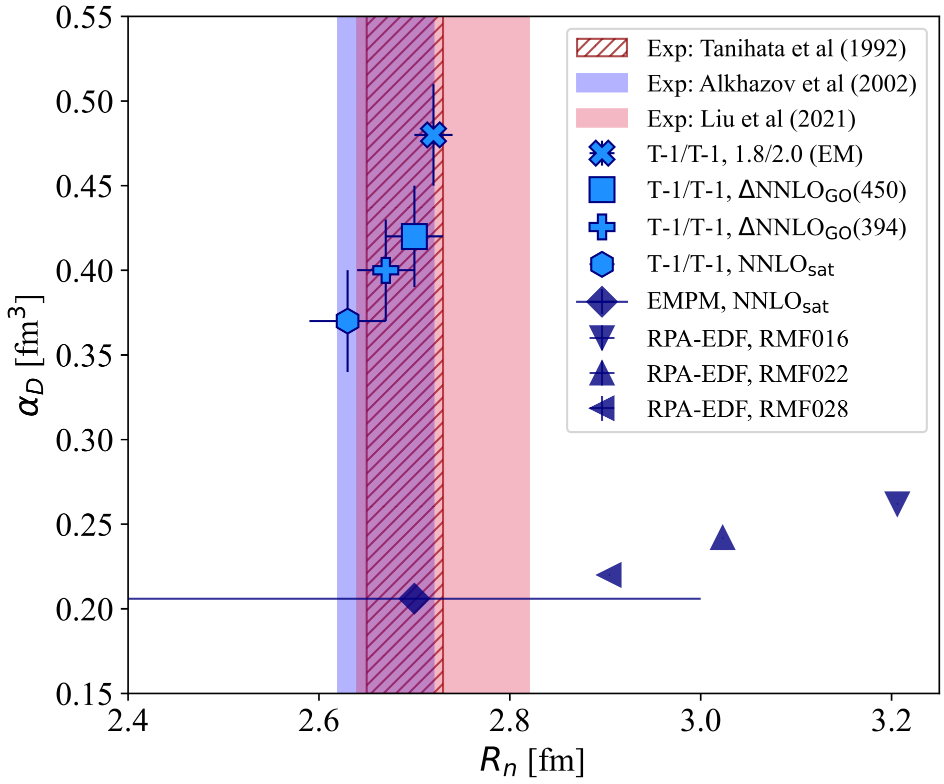

Figure 6.18: Electric dipole polarizability of ^{8}He as a function of the corresponding point-neutron radius for the four Hamiltonians under study. CC predictions for R_n (α_D) have been obtained with the T-1 (T-1/T-1) approximation. Comparison with the experimental determinations of Ref. [233–235] as well as with the RPA-EDF [218] and EMPM [221] results is shown. Figure adapted from Ref. [6].

decay channels, enabled for the first time the extraction of the complete dipole strength distribution of ^{8}He and of its dipole polarizability up to 15 MeV of excitation energy.

In Figure 6.19, we compare the experimental data for α_D with our theoretical running sums, calculated according to Eq. (6.5) for the previously employed set of chiral EFT interactions. The green and purple bands of Figure 6.19 encompass the results obtained with the different chiral EFT interactions in the T-1/T-1 and D/D truncation schemes, respectively. Each band is enlarged by the uncertainty contribution stemming from the residual dependence on the HO basis parameters.

We observe a striking discrepancy between theory and experiment. Although the addition of triples brings more strength to α_D and moves the theoretical running sums towards slightly lower energies, at 15 MeV the T-1/T-1 band reaches only 50% of the corresponding experimental value. We point out that while the first excited states contributing to α_D are located at around $4-5$ MeV, depending on the interaction, as seen also in Figure 6.15,

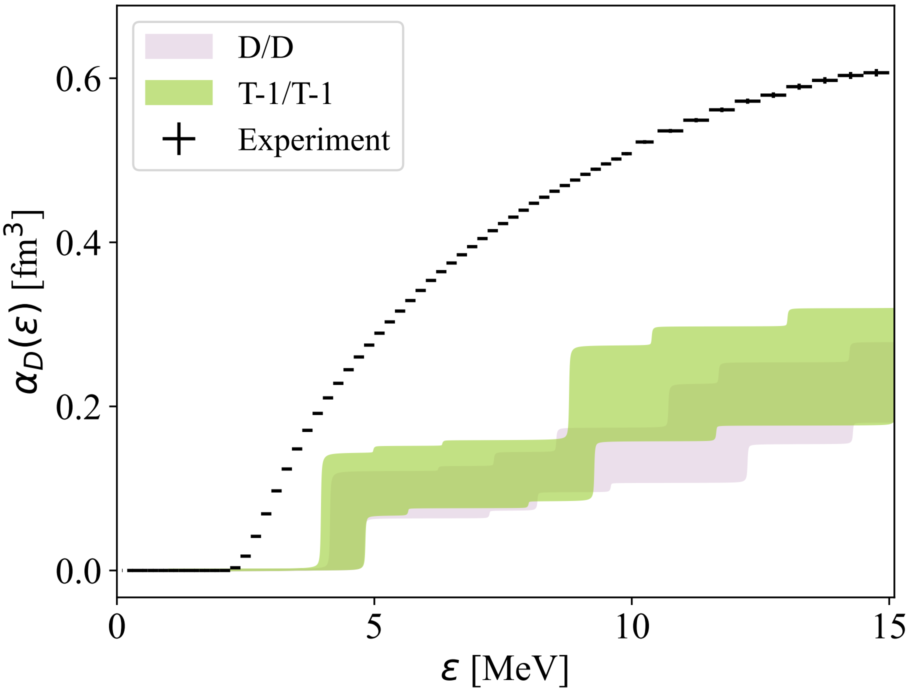

Figure 6.19: Running sum for the dipole polarizability of ^{8}He calculated with the four Hamiltonians in comparison with the experimental data of Ref. [94]. Both T-1/T-1 and D/D running sums are reported. The green (purple) band spans the area covered by the running sums of the different interactions in the T-1/T-1 (D/D) truncation scheme, and accounts also for the uncertainty coming from convergence. See text for details.

the experimental dipole strength distribution peaks at lower energies, at 3.3 MeV [94]. Being an inverse-energy-weighted sum rule of the response, α_D is particularly sensitive to the position of low-lying states.

In Figure 6.20, we focus on the result given by the 1.8/2.0 (EM) interaction, yielding the highest prediction for α_D, and we shift the running sum aligning the first excited state in the spectrum to the experimental low-energy peak. For this chiral force, such a shift amounts to 0.7 MeV. The filled (hatched) band correspond to the T-1/T-1 result obtained employing the theoretical (experimental) threshold, enlarged by the contribution of the method uncertainty σ_{method}. Moving the theoretical running sum to the experimental threshold improves the situation. The shifted result now reproduces the experimental data at low energy, below 5 MeV, Moreover, the overall discrepancy is reduced from 50% to 30% when integrating up to 15 MeV. Still, a significant gap between theory and experiment remains.

In this regard, it is useful to analyse how the discrepancy originates also at lower values of the excitation energy. In Table 6.8, we report a numerical comparison between the experimental value of α_D and our T-1/T-1 calculation with the 1.8/2.0 (EM) interaction, integrated up to 5, 10 and 15 MeV. We also include the results obtained including the energy shift.

Table 6.8 clearly shows that without energy shift, theory is losing around half of the strength over all the integration range up to 15 MeV. Focusing instead on the shifted result,

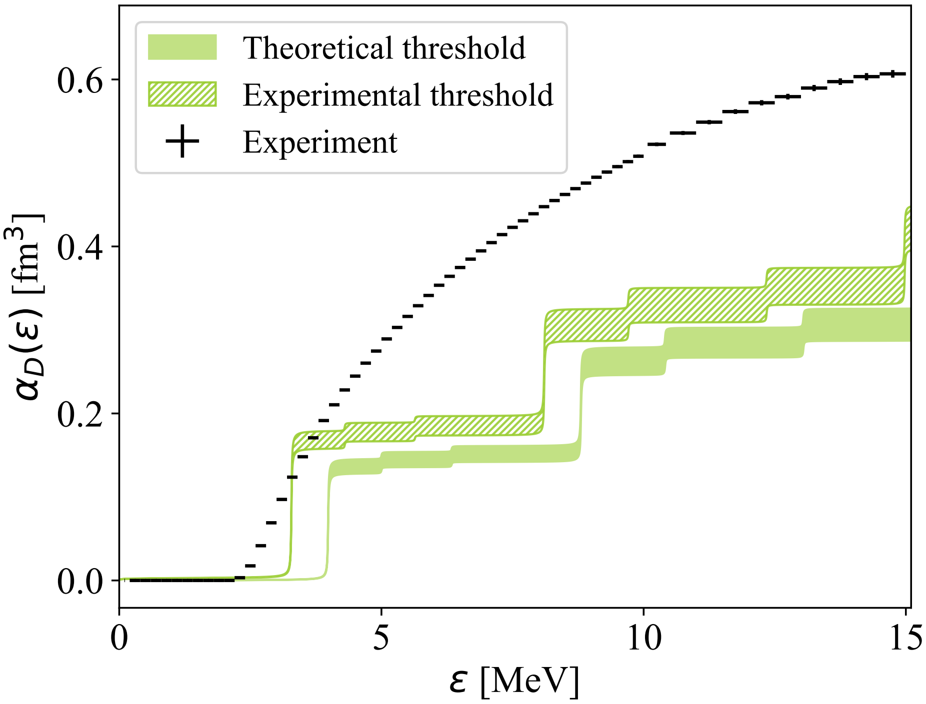

Figure 6.20: T-1/T-1 running sum for the dipole polarizability of ^{8}He calculated with the chiral EFT interaction 1.8/2.0 (EM) in comparison to the experimental data of Ref. [94]. The hatched running sum has been shifted to the experimental threshold. The band accounts for the method uncertainty σ_{method}, calculated according to Section 6.1.

Table 6.8: Theoretical and experimental [94] values of the dipole polarizability in fm^3, integrated up to an excitation energy of 5, 10 and 15 MeV. The theoretical values have been obtained with the 1.8/2.0 (EM) interaction in the T-1/T-1 approximation scheme.

Max excitation energy	$\alpha_{D,\text{exp}}$	$\alpha_{D,\text{th}}$	$\alpha_{D,\text{th}}^{\text{shifted}}$
5 MeV	0.27(1)	0.14(3)	0.18(3)
10 MeV	0.51(1)	0.26(3)	0.33(3)
15 MeV	0.61(2)	0.31(3)	0.42(3)

we observe that while the theoretical α_D grows of the same amount of the experimental one between 10 and 15 MeV (≈ 0.1 fm^3), the increase in α_D is only 60% of the experimental one between 5 and 10 MeV (0.15 fm^3 instead of 0.24 fm^3). Assuming the experiment is detecting the correct threshold for the dipole-excited spectrum, the core of the discrepancy turns out to be missing strength in the theoretical response at around $5-10$ MeV. Similar conclusions can be drawn by considering the α_D predictions obtained with the other chiral EFT interactions employed in Figure 6.19.

The fact that the 5 – 10 MeV region is driving the gap between theory and experiment is supported also by looking at the energy-weighted dipole sum rule m_1, calculated from the discretized response applying Eq. (5.72). While α_D is sensitive to the low-lying strength, m_1 is mostly affected by the high-energy states emerging in the spectrum. In Figure 6.21, we show theoretical m_1 running sums, with and without energy shift, in comparison to the experimental data of Ref. [94]. The bands of Figure 6.21 enclose the T-1/T-1 results obtained with the whole set of chiral EFT interactions, enlarged by the contribution of the method uncertainty σ_{method}.

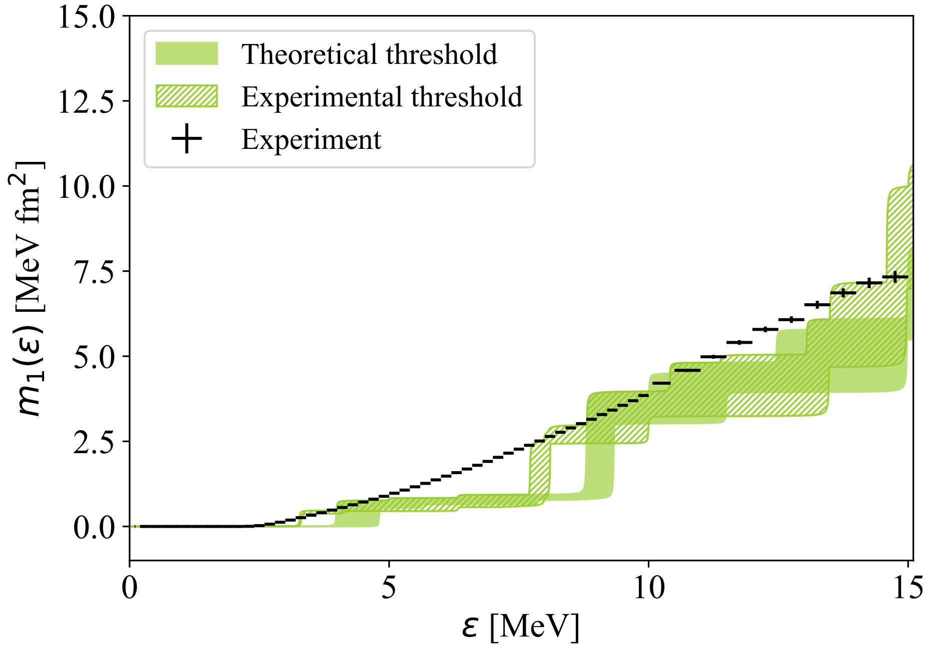

Figure 6.21: Running sum for the energy-weighted sum rule of ^{8}He calculated the four Hamiltonians in comparison to the experimental data of Ref. [94]. The hatched running sum has been shifted to the experimental threshold. Bands span the area covered by the running sums of the different interactions in the T-1/T-1 truncation scheme, and account for the σ_{method} uncertainty, calculated according to Section 6.1.

Figure 6.21 shows a good agreement between theory and experiment, especially between 10 and 15 MeV. The effect of the energy shift, impacting the low-energy part of the spectrum, is less evident for an observable like m_1, which is mostly affected by the high-energy states. However, also in this case we observe missing strength in the theoretical running sum at around 5 – 10 MeV, as in the case of the polarizability.

What could be the reason for missing strength in this energy region? This question has been food for thoughts during the work of this thesis. We report below some personal views on the possible deficiencies in our understanding of the polarizability of this exotic halo nucleus.

- **Missing higher-order CC correlations.** The most accurate α_D calculations presented in this Section have been performed in the T-1/T-1 approximation, where linear triples correlations are included in both the ground-state and excited-state computations. With the 1.8/2.0 (EM) interaction, we obtained additional results in the T-3/T-3 truncation scheme, which represent a more precise approximation of the full CCSDT framework (see Ref. [236] for details). The value of α_D obtained with the T-3/T-3 truncation scheme turns out to be only 2% higher than the T-1/T-1 outcome, well within the many-body truncation uncertainty of our prediction. Although it is reassuring to see the small effect of subleading triples, the fact that T-1/T-1 and T-3/T-3 results are almost identical gives us no information on the possible impact of higher order correlations, as 4p-4h. In an intuitive picture of ^{8}He, made of an α core surrounded by a four-neutron halo, α-clustering and the simultaneous excitation of the valence neutrons, which can be resolved starting from the 4p-4h level [39, 237], may have an impact on a continuum observable as the polarizability. This hypothesis is also supported by the fact that the region of missing strength between 5 and 10 MeV corresponds to where the four-neutron decay channel starts to contribute to the experimental response of Ref. [94]. Currently, 4p-4h calculations are not available. However, a more concrete evidence of the effect of higher-order correlations could be deduced by comparing CC results with virtually exact NCSM calculations of this observable.

- **Deficiencies in the nuclear Hamiltonian.** In Table 6.7, the significant model dependence of the polarizability of ^{8}He jumps immediately to the eye. In our CC predictions, the central values of α_D for the different interactions range from 0.37 fm^3 to 0.48 fm^3, corresponding to a 30% variation. It is also interesting to notice that such a difference reduces to around 15% when narrowing the field to NNLO interactions. The chiral force 1.8/2.0 (EM), in fact, contains also NN interaction terms at N^{3}LO, which may play a role in this case. Among the set of interactions employed in this Section, it is also the one contributing the most to α_D between 5 and 10 MeV of excitation energy. However, as explained in Section 3.3, the chiral order is only one of the aspects characterizing the nuclear interaction models on the market. Also the choice of degrees of freedom and the fitting strategy count. In this regard, following the line of previous works as Ref. [238], it would be interesting to perform a global sensitivity analysis of α_D in ^{8}He to identify which low-energy constants in the interaction are driving the substantial model dependence shown by this observable.

- **Deformation effects.** Recently, both theoretical and experimental works [217, 239] have claimed that ^{8}He could be soft towards being deformed in its ground state. According to the SA-NCSM calculation of Ref. [239], the ground state of this nucleus appears to be determined by the interplay of two shapes opposite in nature, one prolate and one oblate (corresponding to a positive and a negative value of quadrupole moment, respectively). The already mentioned proton inelastic scattering experiment of Ref. [217], aimed at measuring the first excited state in the ^{8}He spectrum, yielded a differential cross section compatible with a large deformation parameter. The static correlations associated with deformation are not accurately captured in our CC approach, where ^{8}He is treated as a spherical closed-shell nucleus. However, as already mentioned in Section 4.4, it is now possible to perform CC calculations starting from an axially symmetric reference state, and project the result on the correct value of total angular momentum via a symmetry restoration procedure. With the aim of looking for deformation signatures in CC, we first focused on the preliminary Hartree-Fock step in our calculations. We considered different axially-symmetric reference states, obtained constraining the HF calculation to a specific value of quadrupole moment Q, with and without angular momentum projection after variation (PAV) [175]. The evolution of the ground-state energy as a function of Q with and without PAV is illustrated in Figure 6.22. These calculations have been performed with the ΔNNLO$_{\text{GO}}$(394) interaction, fixing $N_{max} = 8$ and $\hbar\Omega = 16$ MeV. While the minimum of the ground-state energy occurs at vanishing Q in the unprojected calculation, the addition of projection leads to the appearance of two minima with $Q \neq 0$, one with oblate and one with prolate nature, in agreement with the SA-NCSM calculation of Ref. [239]. We then used the prolate and oblate references in two distinct CC calculations with angular momentum projection, which

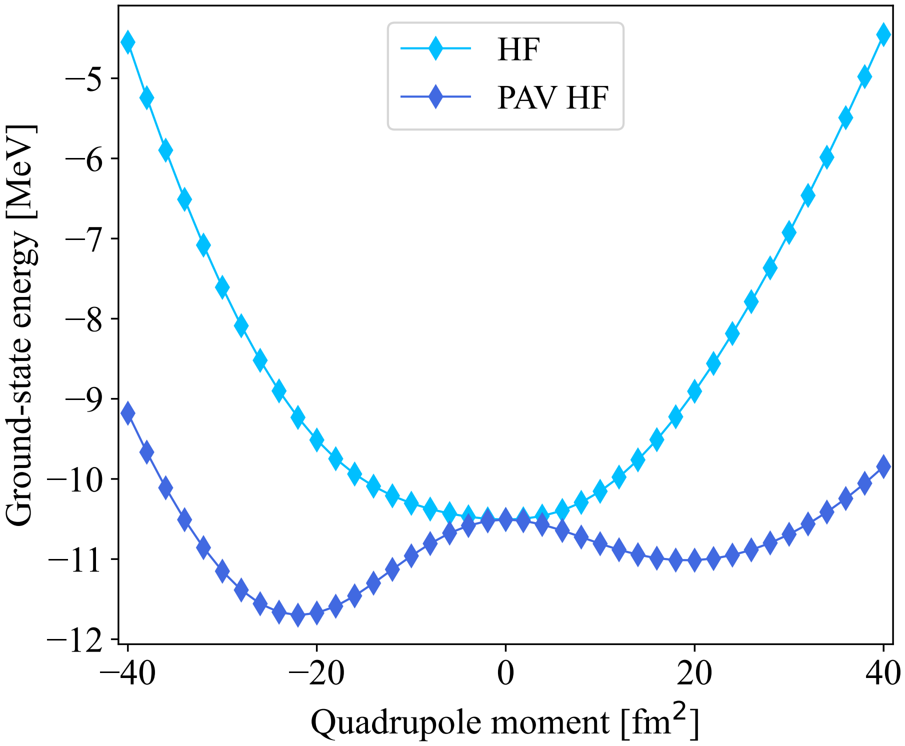

Figure 6.22: Hartree-Fock ground-state energy of ^{8}He, calculated with the ΔNNLO$_{\text{GO}}$(394) interaction, as a function of quadrupole moment with and without angular momentum projection. Such calculations have been performed with $N_{max} = 8$ and $\hbar\Omega = 16$ MeV.

confirmed the presence of a prolate and a oblate minimum in the CC ground-state energy, respectively. Therefore, our preliminary calculations are hinting towards ^{8}He being deformed, a contingency which may impact also α_D. Nevertheless, since an unambiguous claim of deformation typically comes from the observation of rotational bands emerging in the spectrum, together with a study of $B(E2)$ electromagnetic transitions, as we argued in Ref. [3], more theoretical and experimental investigation is needed.

- **Interpretation of experimental data.** The roots of the discrepancy seen in Figure 6.19 could also lie on the experimental side. On the basis of the behaviour observed in one-neutron halo nuclei [240], the analysis of Ref. [94] has been performed excluding the possible presence of higher multipolarity contributions to the Coulomb excitation data. However, the virtual photon spectra shown in Ref. [94] are characterized by a number of E2 photons around an order of magnitude larger than the one of E1 photons at the experimental beam energy. Moreover, considering the presence of a low-lying 2^+ state in the spectrum of ^{8}He, as observed in Ref. [217], a higher number of E2 photons is likely to lead to an enhancement of the E2 component in the measured electromagnetic excitation strength. To obtain a clear identification of the E1 contribution, we plan to propose a measurement of the E1 response of ^{8}He through inelastic proton scattering at forward angles in inverse kinematics at the Facility for Rare Isotope Beams (FRIB), USA. In such an experiment, in fact, the various multipolarity contributions to the spectra can be distinguished via a Multipole Decomposition Analysis [89]. The measurement of the angular distributions for a wide range of excitation energy (0 to 25 MeV) would take advantage of the Active Target Time Projection Chamber at FRIB [241], enabling the measurement of the E1 response in inverse kinematics. The proposal will be written in collaboration with Dr. Yassid Ayyad, researcher in experimental nuclear physics at the University of Santiago de Compostela.

6.5 Nuclear incompressibility from monopole resonances

We now move on to consider a different electromagnetic observable, the isoscalar monopole resonance. As explained in Section 2.5, the centroid energy of the resonance is connected to the incompressibility of a finite A-body nucleus as

$$K_A = \frac{M}{\hbar^2} \langle R_m^2 \rangle E_{\mathrm{ISGMR}}^2, \tag{6.11}$$

where M is the nucleon mass, R_m is the rms matter radius of the nucleus and E_{ISGMR} is a mean isoscalar monopole resonance energy. The latter is estimated

$$E_{\mathrm{ISGMR}} = \sqrt{\frac{m_1}{m_{-1}}}. \tag{6.12}$$

where moments of the response are key ingredients. Here, we present calculations of K_A for the closed-shell nuclei ^{16}O, ^{40}Ca and ^{56}Ni, employing the ΔNNLO$_{\rm GO}$(394) interaction. To this aim, we implemented the isoscalar monopole operator in the closed-shell LIT-CC framework [3]. The isoscalar monopole moments entering Eq. (6.12) can then be calculated according to Eq. (5.69). We analyse the convergence of the moments and of the matter radius by performing calculations at the maximum model space size available ($N_{max} = 14$), varying $\hbar\Omega$ between 12 and 16 MeV. All the results presented have been obtained adopting the D approximation in both ground- and excited-state computations.

In Figure 6.23, the discretized monopole responses of ^{16}O, ^{40}Ca and ^{56}Ni are shown. For all nuclei, the isoscalar monopole resonance is located between 20 and 30 MeV of excitation energy. With ^{40}Ca and ^{56}Ni, we observe a shift of the peaks characterized by the highest strength towards slightly lower energies with respect to ^{16}O. This behaviour is reflected in the corresponding value of $E_{\rm ISGMR}$, determined by the ratio of isoscalar monopole sum rules. In Table 6.9, we report for all nuclei our results for the matter radius R_m, the mean energy $E_{\rm ISGMR}$ and the corresponding incompressibility K_A, in comparison to available experimental data for R_m and $E_{\rm ISGMR}$.

Table 6.9: RMS matter radius in fm, mean ISGMR energy in MeV and incompressibility in MeV of ^{16}O, ^{40}Ca and ^{56}Ni obtained with the ΔNNLO$_{\rm GO}$(394) interaction in comparison to available experimental data for R_m and $E_{\rm ISGMR}$. For ^{16}O, ^{40}Ca and ^{56}Ni, experimental values of R_m are taken from Refs. [242–244] and the ones of $E_{\rm ISGMR}$ from Refs. [245–247], respectively. See text for details about theoretical uncertainties.

Nucleus	$R_{m,\rm th}$	$R_{m,\rm exp}$	$E_{\rm ISGMR,th}$	$E_{\rm ISGMR,exp}$	$K_{A,\rm th}$
^{16}O	2.53(5)	2.554(20)	23.2(3)	19.63(38)	83(5)
^{40}Ca	3.33(7)	3.38(7)	21.6(1.1)	17.29(12)	125(14)
^{56}Ni	3.57(7)	$3.74^{+0.03}_{-0.06}$	22.1(1.1)	19.3(5)	150(16)

The theoretical uncertainties reported in Table 6.9 are determined by convergence and by the effect of truncating the CC expansion. For all nuclei, the residual dependence on the model space parameters is quite small, lying below 0.1% and 1% for R_m and $E_{\rm ISGMR}$, respectively. On the basis of our expertise in coupled-cluster calculations of radii and dipole sum rules, we can tentatively assign a many-body truncation uncertainty of 2% for radii, 10% for the inverse-energy-weighted sum rule m_{-1} and 2% for the energy-weighted sum rule m_1 entering $E_{\rm ISGMR}$. This results in an overall error band on K_A ranging from 6% to 11% for the different nuclei.

CC calculations of R_m are in excellent agreement with experiment for ^{16}O and ^{40}Ca, while slightly underpredicting this quantity for ^{56}Ni. Furthermore, we observe that for all nuclei

---

[3] For the moment, we ignored the center-of-mass contribution to Eq. (2.21) in the implementation, as center-of-mass effects should be milder for medium-mass nuclei as the ones under study.

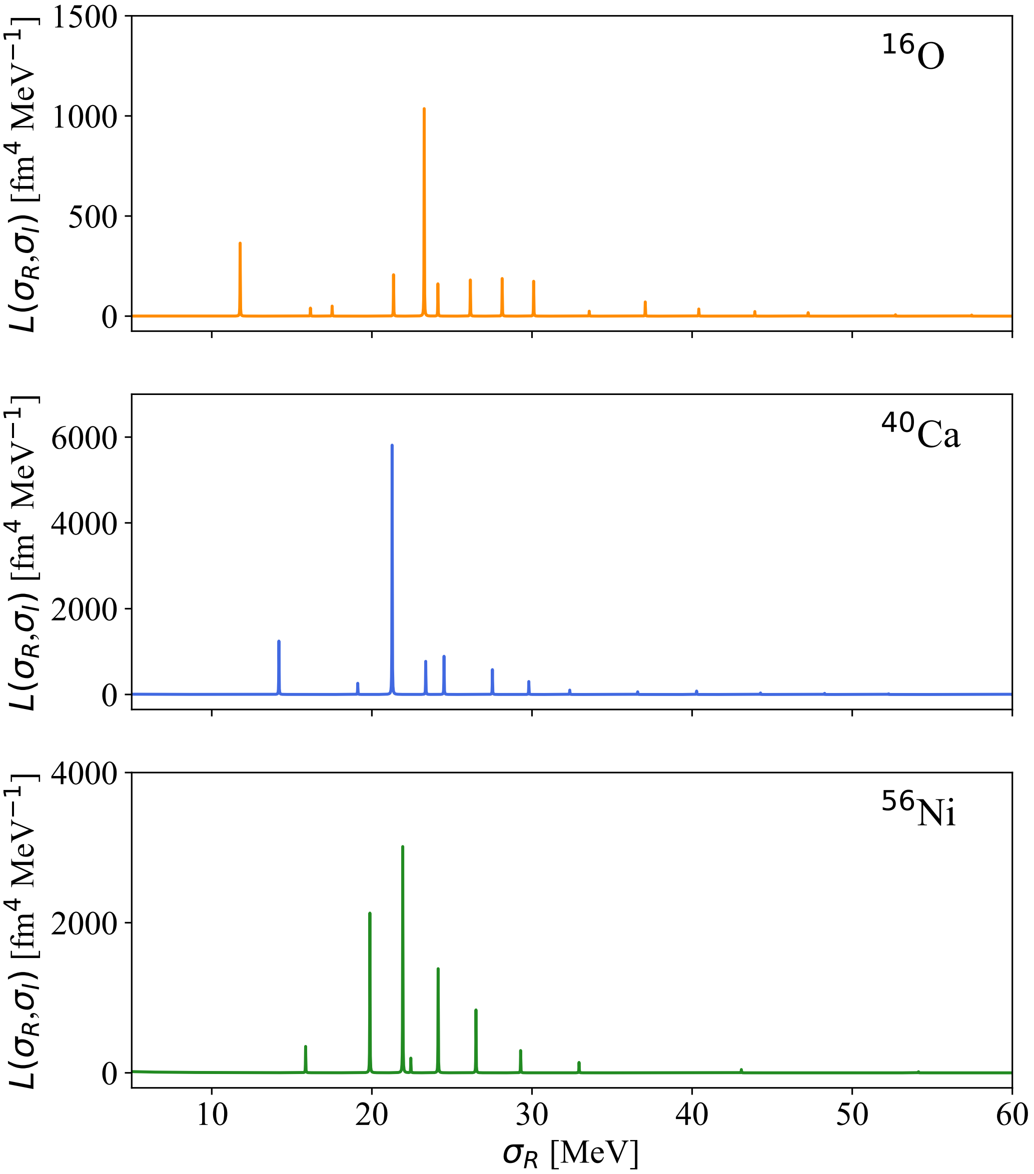

Figure 6.23: LIT of ^{16}O, ^{40}Ca and ^{56}Ni with $\sigma_I = 0.01$ MeV in the D/D framework for the chiral EFT interaction ΔNNLO$_{\text{GO}}$(394). These curves have been obtained with $N_{max} = 14$ and $\hbar\Omega = 12$ MeV.

the centroid energy E_{ISGMR} is systematically larger than experiment. This discrepancy could be attributed to the combination of two factors. First, the isoscalar monopole response has been measured only up to 40 MeV in ^{16}O, and up to 30 MeV in ^{40}Ca and ^{56}Ni, while on the theory side we can verify the convergence of the integral considering excitation energies higher than 100 MeV. Since the energy-weighted sum rule m_1 entering E_{ISGMR} is particularly sensitive to the high-energy part of the spectrum, neglecting the states above $30-40$ MeV could lead to a smaller experimental determination of the centroid. As an example, let us consider the case of ^{56}Ni. Integrating the discretized response only up to 30 MeV, we obtain $E_{\text{ISGMR}} = 20.5(1.2)$ MeV, which agrees with the experimental value. Moreover, as for the moment only one interaction has been considered, the theoretical uncertainties reported in Table 6.9 only account for the method error σ_{method}.

In Ref. [109], the SA-NCSM was employed to estimate E_{ISGMR} and K_A for ^{16}O and ^{40}Ca with the NNLO$_{\text{opt}}$ [248] interaction. Our results are in good accordance with the SA-NCSM values of $E_{\text{ISGMR}} = 24(1)$ MeV and $K_A = 75(7)$ MeV for ^{16}O. For ^{40}Ca, SA-NCSM calculations lead to a larger centroid energy (27(1) MeV) with respect to CC. This is most likely due to the fact that the NNLO$_{\text{opt}}$ interaction does not include 3N forces. The corresponding K_A, amounting to $170(10)$ MeV, is anyway compatible with CC within error bars.

The value of the incompressibility is determined by the interplay between the matter radius, increasing with mass number, and E_{ISGMR}. The latter contracts when going from ^{16}O to ^{40}Ca, and grows again when considering ^{56}Ni. Overall, CC estimates for the centroid energy vary less than 10% for the nuclei under study.

Using the values of K_A presented in Table 6.9, we can analyse the behaviour of the incompressibility as a function of A by carrying out a fit to Eq. (2.23). As explained in Chapter 2, the latter is a leptodermous expansion characterized by the volume, surface, isospin and Coulomb coefficients K_{vol}, K_{surf}, K_τ and K_{Coul}. As explained in Section 2.5, if one assumes that K_{vol} coincides with the incompressibility K_0 of symmetric nuclear matter, introduced in Eq. (2.6), a fit to Eq. (2.23) provides important information on the nuclear EOS. We can also compare the fit results to nuclear matter calculations performed in CC theory [103,249,250], establishing an internally consistent connection between finite and infinite nuclear systems.

For the nuclei considered in this Section, characterized by $N = Z$, the isospin term vanishes. Moreover, macroscopic models have shown that the Coulomb term is significantly smaller than the others, with K_{Coul} amounting to -5 MeV [35, 251]. Due to the limited dataset available, we adopt this approximation for K_{Coul}. As a consequence, our fit reduces to

$$K_{A,\text{modified}} = K_{vol} + K_{surf} A^{-1/3}, \tag{6.13}$$

where

$$K_{A,\text{modified}} = K_A + 5\, Z^2 A^{-4/3}. \tag{6.14}$$

The best fit for the CC estimates of K_A is shown in black in Figure 6.24, with a blue band encompassing the corresponding 1σ deviation. On the basis of our CC calculations with the ΔNNLO$_{\text{GO}}$(394) interaction, we get

$$K_{vol} = 300(20)\text{ MeV}, \quad K_{surf} = -530(60)\text{ MeV}. \tag{6.15}$$

Let us first focus on K_{vol}, which is connected to the incompressibility K_0 of SNM. Using a limited dataset of only 3 nuclei, we are able to estimate K_{vol} with an error bar of less than 10%. Our result is in remarkable agreement with the CC nuclear matter result of $K_0 = 294(4)$ MeV [103]. This demonstrates the internal consistency of finite and infinite nuclear matter calculations in CC theory. CC nuclear matter calculations were also performed with a set of non-implausible chiral interactions in Hu et al. [30]. Their range of values, $242 \leq$

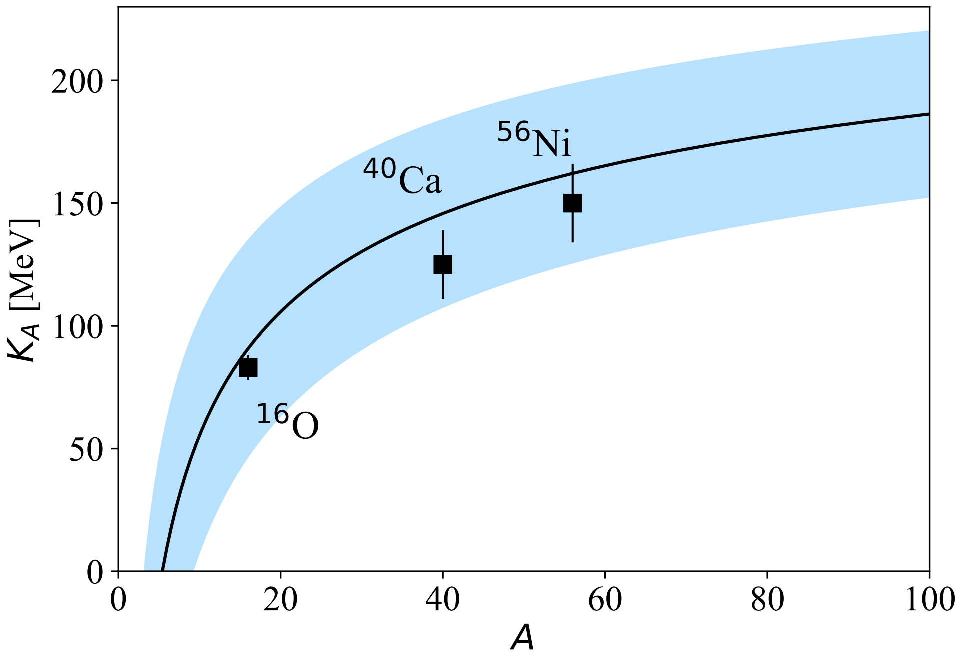

Figure 6.24: Incompressibility of an A-body system K_A as a function of A, calculated in CC theory with the ΔNNLO$_{\text{GO}}$(394) interaction. The best fit of the theoretical estimates of K_A to Eq. (6.13) is shown in black, with a blue band illustrating the 1σ deviation of the fit.

$K_0 \leq 331$ MeV, emcompasses our calculation. Moreover, our result is consistent with the range $250 < K_0 < 315$ MeV, obtained by Stone et al. [107], while lying above the estimate $K_0 = 240(20)$ MeV of Shlomo et al. [108].

In Table 6.10, we compare our result for K_0 with the SA-NCSM results of Ref. [109], starting from the NNLO$_{\text{opt}}$ and NNLO$_{\text{sat}}$ interaction[4]. Very recently, K_0 was also estimated with the PGCM [110] and the chiral NN+3N interaction of Ref. [252], on the basis of K_A values for ^{24}Mg, ^{28}Si and ^{46}Ti. We also report their result for comparison.

We find good accordance with the PGCM result, and with the SA-NCSM estimate based on the NNLO$_{\text{sat}}$ interaction. The NNLO$_{\text{opt}}$ result, instead, leads to a too small incompressibility with respect to the other calculations and to the analysis of Refs. [107, 108]. This comparison highlights the crucial role of 3N forces in achieving an accurate description of this quantity.

As for the surface parameter K_{surf}, the result of our fit is compatible with the range $-756 < K_{surf} < -400$ MeV, obtained combining the K_{vol} and $c = K_{surf}/K_{vol}$ ranges of Ref. [107], while lying above the PGCM outcome of $-632(9)$ MeV.

On the basis of these preliminary results, estimating the incompressibility of symmetric nuclear matter from the analysis of isoscalar monopole resonances appears to provide a

---

[4] In SA-NCSM calculations, 3N forces in the NNLO$_{\text{sat}}$ interaction are included as averages.

Table 6.10: Incompressibility of infinite nuclear matter in MeV based on CC, SA-NCSM calculations from Ref. [109] and PGCM calculations from Ref. [110]. CC computations employ the ΔNNLO$_{\mathrm{GO}}$(394) interaction, SA-NCSM results are based on the NNLO$_{\mathrm{opt}}$ and NNLO$_{\mathrm{sat}}$ interactions and PGCM result on the chiral NN+3N interaction of Ref. [252].

Method and interaction	K_{vol}
CC, ΔNNLO$_{\mathrm{GO}}$(394)	300(20)
SA-NCSM, NNLO$_{\mathrm{opt}}$	213(10)
SA-NCSM, NNLO$_{\mathrm{sat}}$	297(37)
PGCM, chiral NN+3N interaction [252]	284(3)

viable strategy to reduce uncertainties on this EOS parameter, independently from infinite nuclear matter calculations or experimental data. It is in our intention to further refine the results presented here for a future publication [8], adding more nuclei to the fit, including triples in the many-body expansion and examining the model uncertainty.

7 Conclusions and Outlook

In this thesis, the connection between electromagnetic observables, as electric dipole polarizabilities and isoscalar monopole resonances, and parameters of the nuclear matter equation of state has motivated us to extend the reach of ab initio calculations of such quantities across the nuclear chart.

We established a link between nuclear physics and astrophysics, illustrating how studies of the structure, dynamics and composition of neutron stars require the nuclear matter equation of state as a fundamental ingredient. In particular, we focused on modeling the equation of state at densities at and around saturation density, where nuclear physics plays a major role. We showed the strong correlation arising in different theoretical approaches, energy density functional theory and ab initio frameworks, between the EOS symmetry energy parameters, neutron skins and electric dipole polarizabilities, reviewing the progress that has been achieved up to now. We also elucidated the connection between the incompressibility of nuclear matter and systematic studies of isoscalar monopole resonances.

Next, we set the foundations for computing electric dipole polarizabilities and isoscalar monopole resonances in an ab initio fashion, combining modern nuclear forces rooted in Quantum Chromodynamics via chiral effective field theory and the coupled-cluster method, a systematically improvable many-body solver, scaling polynomially with increasing mass number. To ensure a proper treatment of the continuum excited states involved in the calculation of electromagnetic observables, we merged coupled-cluster theory with the Lorentz integral transform technique in the LIT-CC method, that has made possible calculations of electromagnetic break-up observables in medium-mass nuclei so far closed-shell. Most importantly, we presented a derivation of the main technical novelty of this thesis, which concerns the extension of the LIT-CC approach to open-shell nuclei obtained attaching two particles to a closed-shell core. This development is motivated by ongoing experimental campaigns tackling such nuclei [50].

Combining all these elements, we finally presented our results, constituting the original product of the research conducted during the body work of this thesis [1, 2, 5, 7, 8]. We first focused on the analysis of the electric dipole polarizability. We present a comparison between our LIT-CC predictions, experimental data, and energy density functional theory results for the dipole polarizability of the closed-shell nucleus ^{40}Ca [5]. Good agreement is found between the different approaches and the experimental determination. This analysis, in conjunction with earlier findings concerning ^{48}Ca [48], serves as a test of the closed-shell LIT-CC approach, and supports the constraints on the symmetry energy parameters suggested by the chiral effective field theory interactions utilized in this study.

We then arrived at the analysis of the first ab initio calculations of the electric dipole polarizability in open-shell nuclei, based on the newly developed 2PA-LIT-CC method [7]. We validate this new approach by considering the non-energy-weighted dipole sum rule and dipole polarizability of ^{16}O and ^{24}O, where both the closed-shell LIT-CC and 2PA-LIT-CC methods can be applied. The two frameworks yield compatible results within uncertainties, giving us confidence in the implementation of the 2PA-LIT-CC method. At the same time, such comparison suggested the need of higher-order excitations in the 2PA expansion to capture more accurately the contribution of the giant dipole resonance region to the polarizability. Performing calculations with both the closed-shell LIT-CC and 2PA-LIT-CC approaches, we considered the evolution of the dipole polarizability along the oxygen and calcium isotopic chains. In the case of oxygen isotopes, we compared predictions from coupled-cluster and other theoretical approaches for ^{14,16,18,22,24}O with available experimental data. This comparison shows an excellent understanding of the physics of the dipole polarizability for the closed-shell ^{16,22}O and the open-shell ^{18}O. We observed that theoretical predictions of the polarizability of ^{24}O, employing different interactions, span a large set of values, from 1 to 1.4 fm^3, calling for an experimental benchmark on this nucleus. As for calcium isotopes, we presented results for ^{36,38,40,42,48,50,52,54,56}Ca. In this case, although our predictions for open-shell nuclei are lower than the closed-shell ones, the tendency of the dipole polarizability to grow with the number of neutrons clearly emerges, except when going from ^{54}Ca to ^{56}Ca, making it an exciting region to investigate in future experiments. Soon experimental data on the polarizability of ^{42}Ca [50] will provide an experimental benchamark for our 2PA predictions. To improve the accuracy of our calculations, we plan to analyse the effect of adding triples in the coupled-cluster reference for 2PA-LIT-CC calculations.

Next, we pushed our calculations at the dripline, with an analysis of the most exotic nucleus on Earth, ^{8}He [1, 2, 6]. Using different chiral forces, we computed its ground-state properties, as the charge and point-neutron radius, finding consistency with available experimental data, and we employed the closed-shell LIT-CC approach to address its dipole polarizability. Comparing our theoretical predictions with high-statistics experimental data obtained at RIKEN, Japan, by the SAMURAI collaboration [94], we found a large discrepancy: at the maximum excitation energy reached by experiment, theory covers around 50% of the experimental value. We present a detailed analysis of the possible sources of such disagreement, dwelling on missing higher-order correlations, deficiencies in the nuclear Hamiltonian, possible deformation effects and the interpretation of experimental data.

In the end, we considered isoscalar monopole resonances. We presented preliminary constraints on the incompressibility of nuclear matter starting from LIT-CC calculations of the mean energy of isoscalar monopole resonances in ^{16}O, ^{40}Ca and ^{56}Ni. Our range for the incompressibility is in agreement with the corresponding value obtained from coupled-cluster nuclear matter calculations, highlighting the internal consistency between finite and infinite matter computations. It also overlaps with a global analysis of available experimental data on isoscalar monopole resonances [107], and with very recent calculations employing different ab initio approaches. We plan to complete these results adding more nuclei and performing a more sophisticated uncertainty quantification [8].

The new developments contained in this thesis open up numerous potential research avenues. For example, the derivation of the LIT-CC method for 2PA nuclei suggests a straightforward way to extend the capabilities of this approach also to open-shell nuclei obtained removing two nucleons from a closed (sub)shell (two-particle-removed, or 2PR). Work in this direction is underway [253]. The same reasoning could be applied also to one-particle-attached (1PA) and one-particle-removed (1PR) nuclei. With these methods at our disposal, we could explore electromagnetic observables in most of the nuclei of the medium-mass region. In parallel to this efforts, a more sophisticated estimate of the theoretical uncertainty within a Bayesian framework would be also desirable. Moreover, developing emulators (see, e.g., Ref. [254] for a recent review) for electromagnetic observables, we would be able to get an insight on the typically large Hamiltonian dependence that characterizes them, by evaluating their sensitivity to specific low-energy constants in the nuclear force. With a unified approach to the treatment of structure and electromagnetic observables, as the LIT-CC method, now available also for selected open-shell nuclei, we envision a variety of applications impacting our knowledge of the nuclear matter equation of state.

For instance, up to now, the correlation between neutron skins and dipole polarizabilities has been investigated in stable neutron-rich nuclei as ^{48}Ca and ^{208}Pb. However, cutting-edge radioactive ion beam facilities, as RIKEN, Japan and FRIB, USA, and advancements in their infrastructure, as the FRIB400 upgrade [51], are opening exciting opportunities to explore these observables also in extremely neutron-rich systems. Mapping the relation between neutron skins and polarizabilities in these nuclei from an ab initio perspective would be key to extract unique constraints on the symmetry energy. In this regard, interesting case studies could be neutron-rich nickel isotopes in the $A \approx 80-90$ region, around the closed-shell ^{86}Ni, which is predicted to have a large neutron skin [51, 255].

It would also be useful to understand if the polarizability can be used to constrain the symmetry energy parameters away from saturation. In the framework of energy density functional theory, two studies [256, 257] focused on investigating correlations between α_D and the symmetry energy at subsaturation density. These works found a strong correlation between $1/\alpha_D$ and the symmetry energy at densities around $1/3$ saturation density in ^{208}Pb. Using this relation, they obtained stringent constraints on the symmetry energy and the equation of state of pure neutron matter in this density regime, in agreement with previous works. It would be interesting to see a similar relation emerging also from ab initio calculations.

In the end, we would like to point out that the LIT-CC framework for closed-shell and 2PA nuclei, on which this thesis is built, could be used to compute also more general electroweak transitions. In this regard, possible future studies could focus on Gamow-Teller strengths of neutron-rich nuclei, which are of particular importance for nucleosynthesis simulations [258] and have been the object of recent experimental activity [259, 260].

Appendices

1 Rules for coupled-cluster diagrams

In this Section, we present the rules that allow us to derive the algebraic expression associated to a CC diagram. We take this list from Ref. [153], where they are derived in detail. To illustrate the procedure, we consider as an example one of the diagrams of the right Lanczos pivot $\mathbf{S}_R^{2PA}$

$$\langle ab|\overline{\Theta}R^{A+2}|0\rangle = \qquad (1)$$

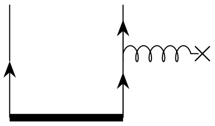

which contributes to the pivot at the 2p-0h level. The curly line ended by a cross represents the action of $\overline{\Theta}$, while the solid line corresponds to the EOM excitation operator R^{A+2}. To deduce the corresponding algebraic expression, we apply the following steps:

1. Associate hole and particle indices corresponding to the ones of the matrix element in the bra and ket of Eq. (1) with external, open lines. Associate different particle and hole indices to internal lines, as

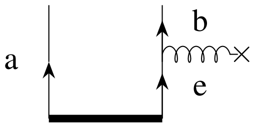

$$. \qquad (2)$$

2. Attach a factor $\langle \mathrm{out}|\overline{\Theta}|\mathrm{in}\rangle$ to any one-body operator vertex, as in this case $\overline{\Theta}$. With a two-body operator, the corresponding factor becomes $\langle \mathrm{out_{left}}\ \mathrm{out_{right}}|\overline{\Theta}|\mathrm{in_{left}}\ \mathrm{in_{right}}\rangle$, where “out” and “in” identify outward and inward lines linked to the vertex considered. In our example we get

$$\langle b|\overline{\Theta}|e\rangle\,. \qquad (3)$$

3. Associate to a EOM excitation operator R^{A+2} contributing at the 2p-0h level the corresponding amplitude

$$\langle b|\overline{\Theta}|e\rangle\,\langle ab|R^{A+2}|0\rangle\,. \qquad (4)$$

   In the case of the de-excitation operator L^{A+2}, a left amplitude $\langle 0|L^{A+2}|ab\rangle$ is included. If the diagram contributes at the 3p-1h level, the right (left) EOM amplitude $\langle abc|R^{A+2}|i\rangle$ $\big(\langle i|L^{A+2}|abc\rangle\big)$ is to be included. In the presence of T or Λ vertices, associate the corresponding amplitude.

4. Include a sum over all internal lines

$$\sum_e \langle b|\overline{\Theta}|e\rangle\,\langle ab|R^{A+2}|0\rangle\,. \qquad (5)$$

5. Include a factor $1/2$ for each pair of equivalent internal lines. Equivalent internal lines

connect the same two vertices, going in the same direction. In our example, no pairs of equivalent lines appear.

6. Each diagram has to be multiplied by an overall phase factor $(-1)^{h-l}$, where h is the number of hole lines and l is the number of loops. In counting loops we consider also virtual particle-hole loops, which can be generated by linking external open lines. Coming back to our example, we have $h=0$ and $l=0$. Therefore, we obtain an overall positive phase, and nothing changes in our expression at this stage.

7. Associate to each pair of inequivalent external hole or particle lines a permutation operator, $P(pq)=\mathbb{1}-P_{p,q}$, to ensure antisymmetry of the final expression. External lines are considered inequivalent if they are connected to different operator lines. This is the case of the a and b particle lines of our example. We get

$$P(ab)\sum_{e}\langle b|\overline{\Theta}|e\rangle\,\langle ae|R^{A+2}|0\rangle\,. \tag{6}$$

We have therefore obtained the expression reported in Eq. (5.89)

$$\langle ab|\overline{\Theta}R^{A+2}|0\rangle = P(ab)\sum_{e}\langle b|\overline{\Theta}|e\rangle\,\langle ae|R^{A+2}|0\rangle\,. \tag{7}$$

2 Spherical coupled-cluster theory for 2PA nuclei

As explained in Section 4.4, the benefit of employing EOM-based methods to address nuclei in the vicinity of closed shells lies in the possibility to operate within a j-scheme framework. This approach significantly reduces memory demands compared to the m-scheme approach, eliminating at the same time the need of symmetry restoration. In this Section, we briefly summarize the formalism and notation of spherical coupled-cluster theory, employed in the implementation of the 2PA-LIT-CC method. To this aim, we follow Refs. [86, 181]. As an example, we also show how the diagram in Eq. (1), entering the 2PA-LIT-CC Lanczos pivots, can be translated from m-scheme to j-scheme.

2.1 Formalism

Two- and three-body states

In Section 5.4, the diagrams contributing to the 2PA-LIT-CC method have been presented together with their algebraic expression in m-scheme. The matrix elements appearing in such expressions involve single-particle states

$$|p\rangle = |n_p,(l_p,s_p)j_pm_p\rangle\otimes|\tau_p,\tau_p^z\rangle = |\alpha_p,j_pm_p\rangle\,, \tag{8}$$

where $\alpha_p=\{n_p,(l_p,s_p),\tau_p,\tau_p^z\}$ is a cumulative index, enclosing all the quantum numbers except for the angular momentum j_p and its projection m_p. Relevant matrix elements include also two- and three-body states

$$|pq\rangle = |\alpha_p, j_p m_p; \alpha_q, j_q m_q\rangle\,, \quad |pqr\rangle = |\alpha_p, j_p m_p; \alpha_q, j_q m_q; \alpha_r, j_r m_r\rangle\,. \tag{9}$$

When working in j-scheme formulation, we start from the single-particle states

$$|p\rangle = |n_p, (l_p, s_p) j_p\rangle \otimes |\tau_p, \tau_p^z\rangle = |\alpha_p, j_p\rangle\,, \tag{10}$$

where the dependence on the projection m_p is suppressed.

We now consider the j-scheme equivalent of the two- and three-body states of Eq. (9). Starting from two-body states we obtain

$$|pq\rangle_C = \{|p\rangle \otimes |q\rangle\}^{J_{pq}}_{M_{pq}} = |\alpha_p, \alpha_q; j_p j_q; J_{pq}, M_{pq}\rangle\,, \tag{11}$$

where the subscript C indicates the coupling of j_p and j_q to total angular momentum J_{pq} with projection M_{pq}. Employing the completeness of the $|pq\rangle_C$ states

$$\hat{1} = \sum_{J_{pq} M_{pq}} |\alpha_p, \alpha_q; j_p j_q; J_{pq} M_{pq}\rangle \langle \alpha_p, \alpha_q; j_p j_q; J_{pq} M_{pq}|, \tag{12}$$

we get a relation between the m-scheme and j-scheme two-body states

$$\begin{aligned} |pq\rangle = |\alpha_p, j_p m_p; \alpha_q, j_q m_q\rangle &= \sum_{J_{pq} M_{pq}} \langle \alpha_p, \alpha_q; j_p j_q; J_{pq} M_{pq} | \alpha_p, j_p m_p; \alpha_q, j_q m_q\rangle \times \\ &\quad \times |\alpha_p, \alpha_q; j_p j_q; J_{pq} M_{pq}\rangle \\ &= \sum_{J_{pq} M_{pq}} C^{J_{pq} M_{pq}}_{j_p m_p j_q m_q} |pq\rangle_C\,. \end{aligned} \tag{13}$$

In the above equation, we introduced the Clebsch-Gordan coefficients, defined as

$$\langle \alpha_p, \alpha_q; j_p j_q; J_{pq} M_{pq} | \alpha_p, j_p m_p; \alpha_q, j_q m_q\rangle \equiv C^{J_{pq} M_{pq}}_{j_p m_p j_q m_q}\,. \tag{14}$$

We observe that in Eq. (13), the uncoupled state is determined by two separate contributions, with one of them being independent from single-particle angular momentum projections m.

We can follow a similar procedure also for three-body states. However, given a state $|pqr\rangle$, an additional complication arises, as different options for the coupling order can be applied. Here, we choose to adopt a two-step procedure, coupling first p and q and then the resulting two-body state (pq) with r. This leads to the following expression

$$\left\{ \{|p\rangle \otimes |q\rangle\}^{J_{pq}}_{M_{pq}} \otimes |r\rangle \right\}^{J_{pqr}}_{M_{pqr}} = |\alpha_p, \alpha_q, \alpha_r; j_p j_q; J_{pq} j_r; J_{pqr} M_{pqr}\rangle \equiv |pqr\rangle_C\,. \tag{15}$$

At this point we can find the three-body equivalent of Eq. (13), making repeated use of

Eqs. (13) and (14)

$$|pqr\rangle = \sum_{\substack{J_{pqr}M_{pqr}\\ J_{pq}M_{pq}}} C^{J_{pq}M_{pq}}_{j_p m_p j_q m_q} C^{J_{pqr}M_{pqr}}_{J_{pq}M_{pq} j_r m_r} |pqr\rangle_C \,. \tag{16}$$

Matrix elements of 2PA operators

Eqs. (13) and (16) allow us to derive coupled two- and three-body states starting from the corresponding uncoupled expression, eliminating the dependence on single-particle angular momentum projections. The calculation of matrix elements of operators, however, requires an additional step. As an example, let us consider a two-body spherical tensor operator $\mathscr{O}^J_M$ of rank J and projection M. This could correspond, for instance, to the two-body part of the similarity-transformed operator $\overline{\Theta}$ of Eq. (5.14). Employing Eq. (13), we can transform its matrix elements from m-scheme to j-scheme

$$\langle pq|\mathscr{O}^J_M|rs\rangle = \sum_{\substack{J_{pq}M_{pq}\\ J_{rs}M_{rs}}} C^{J_{pq}M_{pq}}_{j_p m_p j_q m_q} C^{J_{rs}M_{rs}}_{j_r m_r j_s m_s} \langle pq|\mathscr{O}^J_M|rs\rangle_C \,. \tag{17}$$

Although the dependence on the quantum number m is suppressed in the two-body states entering the coupled matrix element, the latter still carries a dependence on the projection M characterizing the tensor operator, as well as on the projections of the total angular momenta of the many-body state. This is where the Wigner-Eckart theorem comes into play, providing a way to connect the matrix elements of a spherical tensor operator $\mathscr{O}^J_M$ to its reduced matrix elements

$$\langle pq|\mathscr{O}^J_M|rs\rangle_C = C^{J_{pq}M_{pq}}_{JMJ_{rs}M_{rs}} \langle pq||\mathscr{O}^J||rs\rangle \,, \tag{18}$$

where we dropped the subscript C on the right-hand side of the equation, as the use of coupled states is implicit when considering reduced matrix elements. Eq. (18) corresponds to the convention adopted in Ref. [181], and it is the one we employ in the derivation of the 2PA-LIT-CC diagrams. Other choices are possible (see, e.g., Ref. [39, 193]). Applying the Wigner-Eckart theorem to Eq. (17), we get a direct link between m-scheme and reduced matrix elements of $\mathscr{O}$

$$\langle pq|\mathscr{O}^J_M|rs\rangle = \sum_{\substack{J_{pq}M_{pq}\\ J_{rs}M_{rs}}} C^{J_{pq}M_{pq}}_{j_p m_p j_q m_q} C^{J_{rs}M_{rs}}_{j_r m_r j_s m_s} C^{J_{pq}M_{pq}}_{JMJ_{rs}M_{rs}} \langle pq||\mathscr{O}^J||rs\rangle \,. \tag{19}$$

As shown in Section 5.4, the implementation of the 2PA-LIT-CC method in the 3p-1h approximation requires the calculation of matrix elements of right and left spherical tensor operators of rank K and projection M_K on the 2PA basis of Eq. (5.38). We denote the latter with $\mathscr{R}$ and $\mathscr{L}$, respectively. In m-scheme, the matrix elements of such operators at the

2p-0h and 3p-1h level can be written as

$$\langle ab|\mathscr{R}^{K}_{M_K}|0\rangle\,, \tag{20}$$
$$\langle abc|\mathscr{R}^{K}_{M_K}|i\rangle\,, \tag{21}$$

on the right side, and

$$\langle 0|\mathscr{L}^{K}_{M_K}|ab\rangle\,, \tag{22}$$
$$\langle i|\mathscr{L}^{K}_{M_K}|abc\rangle\,, \tag{23}$$

on the left side. Let us now construct the coupled two-body and three-body states entering 2p-0h and 3p-1h matrix elements, respectively. Using Eqs. (13) and (16), we obtain

$$\langle ab|\mathscr{R}^{K}_{M_K}|0\rangle = \sum_{J_{ab}M_{ab}} C^{J_{ab}M_{ab}}_{j_am_aj_bm_b}\,\langle ab|\mathscr{R}^{K}_{M_K}|0\rangle_C\,, \tag{24}$$
$$\langle abc|\mathscr{R}^{K}_{M_K}|i\rangle = \sum_{\substack{J_{abc}M_{abc}\\ J_{ab}M_{ab}}} C^{J_{ab}M_{ab}}_{j_am_aj_bm_b}\,C^{J_{abc}M_{abc}}_{J_{ab}M_{ab}j_cm_c}\,\langle abc|\mathscr{R}^{K}_{M_K}|i\rangle_C\,, \tag{25}$$

and similarly on the left side

$$\langle 0|\mathscr{L}^{K}_{M_K}|ab\rangle = \sum_{J_{ab}M_{ab}} C^{J_{ab}M_{ab}}_{j_am_aj_bm_b}\,\langle 0|\mathscr{L}^{K}_{M_K}|ab\rangle_C\,, \tag{26}$$
$$\langle i|\mathscr{L}^{K}_{M_K}|abc\rangle = \sum_{\substack{J_{abc}M_{abc}\\ J_{ab}M_{ab}}} C^{J_{ab}M_{ab}}_{j_am_aj_bm_b}\,C^{J_{abc}M_{abc}}_{J_{ab}M_{ab}j_cm_c}\,\langle i|\mathscr{L}^{K}_{M_K}|abc\rangle_C\,. \tag{27}$$

At this point, we can apply the Wigner Eckart theorem to suppress the residual dependence on angular momentum projections. We use the convention of Eq. (18) for the matrix elements of the excitation operator $\mathscr{R}$

$$\langle ab|\mathscr{R}^{K}_{M_K}|0\rangle_C = C^{J_{ab}M_{ab}}_{KM_K00}\,\langle ab||\mathscr{R}^{K}||0\rangle\,, \tag{28}$$
$$\langle abc|\mathscr{R}^{K}_{M_K}|i\rangle_C = C^{J_{abc}M_{abc}}_{KM_Kj_im_i}\,\langle abc||\mathscr{R}^{K}||i\rangle\,. \tag{29}$$

The matrix elements of the de-excitation operator $\mathscr{L}$ require more attention. In this case, we choose to define the left and right operators in such a way to obtain identical j-scheme algebraic expressions for the left and right diagrams, except for the fact that in the left case the operator is transposed. Following this strategy, the numerical implementation of the left part of the calculation is greatly simplified. In fact, the same code can be used for both the left and right diagrammatic contributions, except for the fact the operator in input is transposed when computing left matrix elements. This is equivalent to consider the following Wigner-Eckart convention for matrix elements of $\mathscr{L}$

$$\langle 0|\mathscr{L}^{K}_{M_K}|ab\rangle_C = C^{J_{ab}M_{ab}}_{KM_K00}\,\langle 0||\mathscr{L}^{K}||ab\rangle\,, \tag{30}$$

$$\langle i|\mathscr{L}^{K}_{M_K}|abc\rangle_C = C^{J_{abc}M_{abc}}_{KM_Kj_im_i}\,\langle i||\mathscr{L}^{K}||abc\rangle\,. \tag{31}$$

Substituting Eqs. (28), (29) in Eqs. (24), (25), respectively, we obtain

$$\langle ab|\mathscr{R}^{K}_{M_K}|0\rangle = \sum_{J_{ab}M_{ab}} C^{J_{ab}M_{ab}}_{j_am_aj_bm_b}C^{J_{ab}M_{ab}}_{KM_K00}\,\langle ab||\mathscr{R}^{K}||0\rangle\,, \tag{32}$$

$$\langle abc|\mathscr{R}^{K}_{M_K}|i\rangle = \sum_{\substack{J_{abc}M_{abc}\\ J_{ab}M_{ab}}} C^{J_{ab}M_{ab}}_{j_am_aj_bm_b}C^{J_{abc}M_{abc}}_{J_{ab}M_{ab}j_cm_c}C^{J_{abc}M_{abc}}_{KM_Kj_im_i}\,\langle abc||\mathscr{R}^{K}||i\rangle\,, \tag{33}$$

and similarly inserting Eqs. (30), (31) in Eqs. (26), (27) on the left side

$$\langle 0|\mathscr{L}^{K}_{M_K}|ab\rangle = \sum_{J_{ab}M_{ab}} C^{J_{ab}M_{ab}}_{j_am_aj_bm_b}C^{J_{ab}M_{ab}}_{KM_K00}\,\langle 0|||\mathscr{L}^{K}||ab\rangle\,, \tag{34}$$

$$\langle i|\mathscr{L}^{K}_{M_K}|abc\rangle = \sum_{\substack{J_{abc}M_{abc}\\ J_{ab}M_{ab}}} C^{J_{ab}M_{ab}}_{j_am_aj_bm_b}C^{J_{abc}M_{abc}}_{J_{ab}M_{ab}j_cm_c}C^{J_{abc}M_{abc}}_{KM_Kj_im_i}\,\langle i||\mathscr{L}^{K}||abc\rangle\,. \tag{35}$$

The above equations clearly show the power of the Wigner-Eckart theorem: matrix elements can be factorized in such a way that the dependence on angular momentum projections is isolated in Clebsch-Gordan coefficients only. Formulating the 2PA-LIT-CC method in j-scheme allow us to store only the reduced matrix elements of the relevant operators, significantly reducing the memory requirements of the calculations.

Up to now we have not specified the form of the 2PA operators $\mathscr{R}$ and $\mathscr{L}$, which differ on the basis of which part of a 2PA-LIT-CC computation is considered. Let us first focus on the calculation of the Lanczos pivots $\mathbf{S}^{2\text{PA}}_{R}$ and $\mathbf{S}^{2\text{PA}}_{L}$, defined in Eqs. (5.40) and (5.41), respectively. In this case, $\mathscr{R}$ and $\mathscr{L}$ assume the following form

$$\mathscr{R}^{K}_{M_K} = \left[\overline{\Theta}^{K'}_{M'_K}\otimes R^{A+2,J}_{M}\right]^{K}_{M_K}\,,\quad \mathscr{L}^{K}_{M_K} = \left[L^{A+2,J}_{M}\otimes\overline{\Theta^{\dagger}}^{K'}_{M'_K}\right]^{K}_{M_K}\,. \tag{36}$$

Therefore $\mathscr{R}^{K}_{M_K}$ ($\mathscr{L}^{K}_{M_K}$) corresponds to a tensor product between the similarity-transformed transition operator $\overline{\Theta}^{K'}_{M'_K}$ ($\overline{\Theta^{\dagger}}^{K'}_{M'_K}$), with rank K' and projection M'_K, and the 2PA (de-)excitation operators $R^{A+2,J}_{M}$ ($L^{A+2,J}_{M}$) related to the ground state of the 2PA nucleus, with rank J and projection M. From now on, we drop the superscript "$A+2$" in the left and right 2PA de-excitation operators for convenience. As most 2PA systems are characterized by total angular momentum 0 in their ground state, we restrict ourselves to scalar R and L operators. This implies $J=M=0$, and as a consequence $K'=K$, $M'_K=M_K$. When we consider instead the 2PA-LIT-CC matrix-vector product, $\mathscr{R}$ and $\mathscr{L}$ become

$$\mathscr{R}^{K}_{M_K} = \left[\overline{H}^{0}_{0}\otimes R^{K}_{M_K}\right]^{K}_{M_K}\,,\quad \mathscr{L}^{K}_{M_K} = \left[L^{K}_{M_K}\otimes\overline{H}^{0}_{0}\right]^{K}_{M_K}\,. \tag{37}$$

In this case, the similarity-transformed Hamiltonian, which is a scalar operator, is multiplied with a 2PA Lanczos vector, having the same quantum numbers as the Lanczos pivots described above.

Permutation operators

In the diagrams presented in Section 5.4, two-body and three-body permutation operators are used to obtain antisymmetrized amplitudes. In m-scheme representation, they are defined as

$$P(ab) = \mathbb{1} - P_{a,b}, \tag{38}$$

$$P(ab,c) = \mathbb{1} - P_{a,c} - P_{b,c}. \tag{39}$$

The action of such operators on reduced matrix elements leads to a different coupling order of the permuted indices with respect to the original one. To restore the correct coupling order, the expression of the permutation operator needs to be modified when working in j-scheme representation. A complete derivation of the j-scheme expression of $P(ab)$ and $P(ab,c)$ can be found in Ref. [181]. The final result is given by

$$P(ab) = \mathbb{1} - (-1)^{j_a+j_b-J} P_{a,b}, \tag{40}$$

$$P(ab,c) = \mathbb{1} + \sum_{J_{cb}} \hat{J}_{cb}\hat{J}_{ab} \begin{Bmatrix} j_c & j_b & J_{cb} \\ j_a & J_{abc} & J_{ab} \end{Bmatrix} P_{a,c} - \tag{41}$$

$$\sum_{J_{ac}} (-1)^{j_b+j_c-J_{ab}+J_{ac}} \hat{J}_{ab}\hat{J}_{ac} \begin{Bmatrix} j_c & j_a & J_{ac} \\ j_b & J_{abc} & J_{ab} \end{Bmatrix} P_{b,c}, \tag{42}$$

where we use the notation $\hat{J} = \sqrt{2J+1}$. As the antisymmetrization is among the most expensive parts of the calculations, the numerical implementation of the diagrams is performed in such a way that the permutation operators $P(ab)$ and $P(ab,c)$ are applied only once to the sum of all the 2p-0h and 3p-1h diagrammatic contributions, respectively. This is achieved by including an additional $1/2$ $(1/3)$ factor in the 2p-0h (3p-1h) diagrams which do not include permutation operators.

2.2 2PA-LIT-CC diagrams in j-scheme: an example

With the formalism developed in Section 2.1, we can compute all the diagrammatic contributions relevant for the 2PA-LIT-CC method in j-scheme. As an example, in this Section we illustrate how the diagram of Eq. (1) can be translated to j-scheme. Let us start from its m-scheme expression

$$\langle ab|[\overline{\Theta}^{K}_{M_K} \otimes R^0_0]^K_{M_K}|0\rangle = P(ab) \sum_{\alpha_e, j_e, m_e} \langle b|\overline{\Theta}^{K}_{M_K}|e\rangle \langle ae|R^0_0|0\rangle\,. \tag{43}$$

The sum over the index e is intended to run over all the quantum numbers of a single-particle m-scheme state, given by Eq. (8). In the above sum, we have explicitly specified the angular momentum indices, and denoted collectively the remaining quantum numbers with the index α_e. Let us start from the left-hand side of the above equation and rewrite it using Eq. (32)

$$\begin{aligned} \langle ab|[\overline{\Theta}^K_{M_K} \otimes R^0_0]^K_{M_K}|0\rangle &= \sum_{J_{ab}M_{ab}} C^{J_{ab}M_{ab}}_{j_a m_a j_b m_b} C^{J_{ab}M_{ab}}_{KM_K 00} \langle ab||[\overline{\Theta}^K \otimes R^0]^K||0\rangle \\ &= C^{KM_K}_{j_a m_a j_b m_b} \langle ab||[\overline{\Theta}^K \otimes R^0]^K||0\rangle\,, \end{aligned} \tag{44}$$

where in the last step we used

$$C^{J_{ab}M_{ab}}_{KM_K 00} = \delta_{K,J_{ab}}\delta_{M_K,M_{ab}}. \tag{45}$$

Considering now the right-hand side of Eq. (43), the one-body matrix element of $\overline{\Theta}$ appears. The corresponding reduced matrix element can be obtained by applying the Wigner-Eckart theorem

$$\langle b|\overline{\Theta}^K_{M_K}|e\rangle = C^{j_b m_b}_{KM_K j_e m_e} \langle b||\overline{\Theta}^K||e\rangle \tag{46}$$

Ignoring for the moment the presence of the permutation operator and the sum over α_e, we use Eq. (46) and apply Eq. (32) to the matrix element of the 2PA excitation operator R. We get

$$\begin{aligned} \sum_{j_e m_e} \langle b|\overline{\Theta}^K_{M_K}|e\rangle \langle ae|R^0_0|0\rangle &= \sum_{j_e m_e} \sum_{J_{ae}M_{ae}} C^{j_b m_b}_{KM_K j_e m_e} C^{J_{ae}M_{ae}}_{j_a m_a j_e m_e} C^{J_{ae}M_{ae}}_{0000} \langle b||\overline{\Theta}^K||e\rangle \langle ae||R^0||0\rangle \\ &= \sum_{j_e m_e} C^{j_b m_b}_{KM_K j_e m_e} C^{00}_{j_a m_a j_e m_e} \langle b||\overline{\Theta}^K||e\rangle \langle ae; J_{ae}=0||R^0||0\rangle\,, \end{aligned} \tag{47}$$

where in analogy to Eq. (45) we used $C^{J_{ae}M_{ae}}_{0000} = \delta_{J_{ae},0}\delta_{M_{ae},0}$, implying $J_{ae} = 0$. We can remove the $C^{00}_{j_a m_a j_e m_e}$ coefficient in the above equation by employing the relation[1]

$$C^{00}_{a\alpha b\beta} = \frac{(-1)^{a-\alpha}}{\hat{a}}\delta_{a,b}\delta_{\alpha,-\beta}, \tag{48}$$

obtaining

$$\sum_{j_e m_e} \langle b|\overline{\Theta}^K_{M_K}|e\rangle \langle ae|R^0_0|0\rangle = \sum_{j_e} C^{j_b m_b}_{KM_K j_a -m_a} \frac{(-1)^{j_a - m_a}}{\hat{j}_a} \langle b||\overline{\Theta}^K||e\rangle \langle ae; J_{ae}=0||R^0||0\rangle\, \delta_{j_a,j_e}. \tag{49}$$

The order of the indices in the remaining Clebsch-Gordan coefficient can be reshuffled to match the one of Eq. (44). Using the equality[2]

$$C^{c\gamma}_{a\alpha b\beta} = (-1)^{b+\beta}\frac{\hat{c}}{\hat{a}}C^{a\alpha}_{b-\beta c\gamma}, \tag{50}$$

---

[1] This equality corresponds to Eq. (1) page 248 of Ref. [193].

[2] This equality corresponds to Eq. (10) page 245 of Ref. [193]

we get

$$\sum_{j_e m_e} \langle b|\overline{\Theta}^K_{M_K}|e\rangle \, \langle ae|R^0_0|0\rangle = \sum_{j_e} C^{KM_K}_{j_a m_a j_b m_b} \frac{\hat{j}_b}{\hat{j}_a \hat{K}} \langle b||\overline{\Theta}^K||e\rangle \, \langle ae; J_{ae}=0||R^0||0\rangle \, \delta_{j_a, j_e}. \tag{51}$$

At this point we can write an expression for the diagram only in terms of reduced matrix elements, comparing Eqs. (44) and (51). We have

$$C^{KM_K}_{j_a m_a j_b m_b} \langle ab||[\overline{\Theta}^K \otimes R^0]^K||0\rangle = \sum_{j_e} C^{KM_K}_{j_a m_a j_b m_b} \frac{\hat{j}_b}{\hat{j}_a \hat{K}} \langle b||\overline{\Theta}^K||e\rangle \, \langle ae; J_{ae}=0||R^0||0\rangle \, \delta_{j_a, j_e} \tag{52}$$

By simplifying the last remaining Clebsch-Gordan coefficient we obtain the final *j*-scheme expression for this diagram

$$\langle ab||[\overline{\Theta}^K \otimes R^0]^K||0\rangle = \sum_{e} P(ab) \frac{\hat{j}_b}{\hat{j}_a \hat{K}} \langle b||\overline{\Theta}^K||e\rangle \, \langle ae; J_{ae}=0||R^0||0\rangle \, \delta_{j_a, j_e}. \tag{53}$$

It is worth pointing out that the sum over *e* appearing in the *j*-scheme expression is different from the sum over *e* found in the *m*-scheme expression. The latter has to be understood as a sum over "spherical *e*", where the projections are not included. The complexity of the spherical sum is sometimes reduced by the presence of a Kronecker delta on the values of the total angular momentum, as we see in this case.

3 2PA-LIT-CC Lanczos pivots: *j*-scheme diagrams

In this Section, we show the *j*-scheme expressions for the diagrams contributing to the right and left Lanczos pivots in the 2PA-LIT-CC method. For each diagram we report first the *m*-scheme expression and then the *j*-scheme one. In the diagrams, the curly line ended by a cross represents the action of the similarity-transformed operator $\overline{\Theta}$. The derivation of the *j*-scheme expressions for these diagrams is part of the original work of this thesis [7]. The diagrams contributing to the 2PA matrix-vector product can be found in Ref. [181].

3.1 Right pivot

Diagram 1

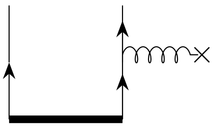

$$\langle ab|[\overline{\Theta}^K_{M_K} \otimes R^0_0]^K_{M_K}|0\rangle = \sum_{e} P(ab) \, \langle b|\overline{\Theta}^K_{M_K}|e\rangle \, \langle ae|R^0_0|0\rangle \,, \tag{54}$$

$$\langle ab||[\overline{\Theta}^K \otimes R^0]^K||0\rangle = \sum_{e} P(ab) \frac{\hat{j}_b}{\hat{j}_a \hat{K}} \langle b||\overline{\Theta}^K||e\rangle \, \langle ae; J_{ae}=0||R^0||0\rangle \, \delta_{j_a, j_e}. \tag{55}$$

Diagram 2

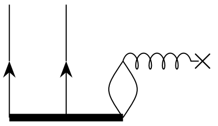

$$\langle ab|[\overline{\Theta}^K_{M_K}\otimes R^0_0]^K_{M_K}|0\rangle = \sum_{ne}\langle n|\overline{\Theta}^K_{M_K}|e\rangle\,\langle abe|R^0_0|n\rangle\,, \tag{56}$$

$$\begin{aligned}\langle ab||[\overline{\Theta}^K\otimes R^0]^K||0\rangle =&\sum_{ne}\frac{\hat{j}_n^2}{\hat{K}^2}\,\langle n||\overline{\Theta}^K||e\rangle \\ &\times\langle abe;J_{ab}=K;J_{abe}=j_n||R^0||n\rangle\,.\end{aligned} \tag{57}$$

Diagram 3

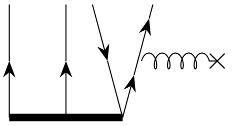

$$\langle abc|[\overline{\Theta}^K_{M_K}\otimes R^0_0]^K_{M_K}|i\rangle = P(ab,c)\sum_{e}\langle c|\overline{\Theta}^K_{M_K}|e\rangle\,\langle abe|R^0_0|i\rangle\,, \tag{58}$$

$$\begin{aligned}\langle abc;J_{ab};J_{abc}||[\overline{\Theta}^K\otimes R^0]^K||i\rangle =&\sum_{e}P(ab,c)(-1)^{j_c+J_{ab}+K+j_i}\,\hat{j}_i\hat{j}_c \\ &\times\left\{\begin{array}{ccc} j_e & J_{ab} & j_i \\ J_{abc} & K & j_c\end{array}\right\} \\ &\times\langle c||\overline{\Theta}^K||e\rangle\,\langle abe;J_{ab};J_{abe}=j_i||R^0||i\rangle\,.\end{aligned} \tag{59}$$

Diagram 4

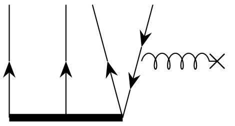

$$\langle abc|[\overline{\Theta}^K_{M_K}\otimes R^0_0]^K_{M_K}|i\rangle = -\sum_{n}\langle n|\overline{\Theta}^K_{M_K}|i\rangle\,\langle abc|R^0_0|n\rangle\,, \tag{60}$$

$$\begin{aligned}\langle abc;J_{ab};J_{abc}||[\overline{\Theta}^K\otimes R^0]^K||i\rangle =&-\sum_{n}\langle n||\overline{\Theta}^K||i\rangle \\ &\times\langle abc;J_{ab};J_{abc}=j_n||R^0||n\rangle\,\delta_{j_n,J_{abc}}\,.\end{aligned} \tag{61}$$

Diagram 5

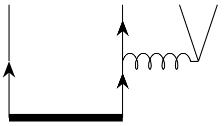

$$\langle abc|[\overline{\Theta}^K_{M_K} \otimes R^0_0]^K_{M_K}|i\rangle = P(a,bc)\sum_e \langle bc|\overline{\Theta}^K_{M_K}|ei\rangle \, \langle ae|R^0_0|0\rangle \,, \tag{62}$$

$$\begin{aligned}\langle abc;J_{ab};J_{abc}||[\overline{\Theta}^K \otimes R^0]^K||i\rangle =& \sum_e \sum_{J_{bc},J_{ei}} P(a,bc)(-1)^{j_b+J_{bc}+J_{ei}+J_{abc}+K} \frac{\hat{J}^3_{bc}\hat{J}_{ei}}{\hat{j_c}^3} \\ &\times \left\{ \begin{array}{ccc} j_i & K & J_{abc} \\ J_{bc} & j_c & J_{ei} \end{array} \right\} \\ &\times \langle bc;J_{bc}||\overline{\Theta}^K||ei;J_{ei}\rangle \, \langle ae;J_{ae}=0||R^0||0\rangle \, \delta_{j_a,j_e} \,.\end{aligned} \tag{63}$$

This diagram can be coupled in a more efficient way if we use the permutation operator in order to obtain the same coupling (e.g., in this case the coupling between *a* and *b*) on both sides. Starting from Eq. (62), we obtain

$$\begin{aligned}\langle abc|[\overline{\Theta}^K_{M_K} \otimes R^0_0]^K_{M_K}|i\rangle &= P(a,bc)\sum_e \langle bc|\overline{\Theta}^K_{M_K}|ei\rangle \, \langle ae|R^0_0|0\rangle \\ &= -P(c,ba)\sum_e \langle ba|\overline{\Theta}^K_{M_K}|ei\rangle \, \langle ce|R^0_0|0\rangle \\ &= -P(ab,c)\sum_e \langle ab|\overline{\Theta}^K_{M_K}|ei\rangle \, \langle ec|R^0_0|0\rangle \,.\end{aligned} \tag{64}$$

The j-scheme expression corresponding to the final result of Eq. (64) turns out to be:

$$\begin{aligned}\langle abc;J_{ab};J_{abc}|||[\overline{\Theta}^K \otimes R^0]^K||i\rangle =& P(ab,c)\sum_e \sum_{J_{ei}} (-1)^{1+K+J_{ei}+J_{abc}+j_c} \frac{\hat{J}_{ei}\hat{J}_{ab}}{\hat{j_c}} \\ &\times \left\{ \begin{array}{ccc} j_i & K & J_{abc} \\ J_{ab} & j_c & J_{ei} \end{array} \right\} \langle ab;J_{ab}||\overline{\Theta}^K||ei;J_{ei}\rangle \\ &\langle ec;J_{ec}=0||R^0||0\rangle \, \delta_{j_c,j_e} ,\end{aligned} \tag{65}$$

where we observe that this equation contain one less sum with respect to Eq. (63).

Diagram 6

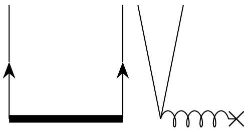

$$\langle abc|[\overline{\Theta}^K_{M_K} \otimes R^0_0]^K_{M_K}|i\rangle = P(ab,c) \, \langle c|\overline{\Theta}^K_{M_K}|i\rangle \, \langle ab|R^0_0|0\rangle \,, \tag{66}$$

$$\begin{aligned}\langle abc;J_{ab};J_{abc}||[\overline{\Theta}^K \otimes R^0]^K||i\rangle =& P(ab,c) \, \langle c||\overline{\Theta}^K||i\rangle \\ &\times \langle ab;J_{ab}=0||R^0||0\rangle \, \delta_{j_c,J_{abc}} \,.\end{aligned} \tag{67}$$

3.2 Left pivot

Diagram 1

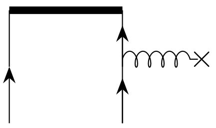

$$\langle 0|[L_0^0 \otimes \overline{\Theta^\dagger}^K_{M_K}]^K_{M_K}|ab\rangle = \sum_e P(ab)\,\langle e|\overline{\Theta^\dagger}^K_{M_K}|b\rangle\,\langle 0|L_0^0|ae\rangle\,, \tag{68}$$

$$\langle 0||[L^0 \otimes \overline{\Theta^\dagger}^K]^K||ab\rangle = \sum_e P(ab)\frac{\hat{j}_b}{\hat{j}_a\hat{K}}\,\langle e||\overline{\Theta^\dagger}^K||b\rangle\,\langle 0||L^0||ae; J_{ae}=0\rangle\,\delta_{j_a,j_e}. \tag{69}$$

Diagram 2

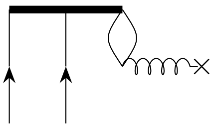

$$\langle 0|[L_0^0 \otimes \overline{\Theta^\dagger}^K_{M_K}]^K_{M_K}|ab\rangle = \sum_{ne}\langle e|\overline{\Theta^\dagger}^K_{M_K}|n\rangle\,\langle n|L_0^0|abe\rangle\,, \tag{70}$$

$$\begin{aligned}\langle 0||[L^0 \otimes \overline{\Theta^\dagger}^K]^K||ab\rangle = &\sum_{ne}\frac{\hat{j}_n^2}{\hat{K}^2}\,\langle e||\overline{\Theta^\dagger}^K||n\rangle \\ &\times\langle n||L^0||abe; J_{ab}=K; J_{abe}=j_n\rangle\,.\end{aligned} \tag{71}$$

Diagram 3

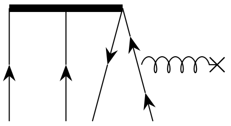

$$\langle i|[L_0^0 \otimes \overline{\Theta^\dagger}^K_{M_K}]^K_{M_K}|abc\rangle = \sum_e P(ab,c)\,\langle i|L_0^0|abe\rangle\,\langle e|\overline{\Theta^\dagger}^K_{M_K}|c\rangle\,, \tag{72}$$

$$\begin{aligned}\langle i||[L^0 \otimes \overline{\Theta^\dagger}^K]^K||abc\rangle = &\sum_e P(ab,c)(-1)^{j_i+j_c+K+J_{ab}}\,\hat{j}_i\hat{j}_c \\ &\times\left\{\begin{matrix} j_e & K & j_c \\ J_{abc} & J_{ab} & j_i\end{matrix}\right\} \\ &\times\langle i||L^0||abe; J_{ab}; J_{abe}=j_i\rangle\,\langle e||\overline{\Theta^\dagger}^K||c\rangle\,.\end{aligned} \tag{73}$$

Diagram 4

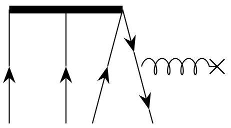

$$\langle i|[L^0_0 \otimes \overline{\Theta^\dagger}^K_{M_K}]^K_{M_K}|abc\rangle = -\sum_n \langle n|L^0_0|abc\rangle\,\langle i|\overline{\Theta^\dagger}^K_{M_K}|n\rangle\,, \tag{74}$$

$$\begin{aligned}\langle i||[L^0 \otimes \overline{\Theta^\dagger}^K]^K||abc\rangle = -\sum_n &\langle n||L^0||abc;J_{ab};J_{abc}=j_n\rangle \\ &\times \langle i||\overline{\Theta^\dagger}^K||n\rangle\,\delta_{j_n,J_{abc}}\,.\end{aligned} \tag{75}$$

Diagram 5

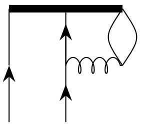

$$\langle 0|[L^0_0 \otimes \overline{\Theta^\dagger}^K_{M_K}]^K_{M_K}|ab\rangle = \frac{1}{2}\sum_{efn} P(ab)\,\langle n|L^0_0|aef\rangle\,\langle ef|\overline{\Theta^\dagger}^K_{M_K}|bn\rangle\,, \tag{76}$$

$$\begin{aligned}\langle 0||[L^0 \otimes \overline{\Theta^\dagger}^K]^K||ab\rangle = \frac{1}{2}\sum_{efn}\sum_{J_{ae},J_{ef},J_{bn}} &P(ab)(-1)^{K+j_a+j_e+j_f+j_n+J_{ef}+J_{bn}} \\ &\times \frac{\hat{J}_{ef}\hat{J}_{ae}\hat{j}_n\hat{J}^2_{bn}}{\hat{K}} \begin{Bmatrix} j_e & j_f & J_{ef} \\ j_n & j_a & J_{ae} \end{Bmatrix} \begin{Bmatrix} j_n & J_{ef} & j_a \\ K & j_b & J_{bn} \end{Bmatrix} \\ &\times \langle n||L^0||aef;J_{ae};J_{aef}=j_n\rangle\,\langle ef;J_{ef}||\overline{\Theta^\dagger}^K||bn;J_{bn}\rangle\,.\end{aligned} \tag{77}$$

As in the case of Diagram 5 for the right pivot, we can make this diagram more efficient using the permutation trick. We get

$$\begin{aligned}\langle 0|[L^0_0 \otimes \overline{\Theta^\dagger}^K_{M_K}]^K_{M_K}|ab\rangle &= \frac{1}{2}P(ab)\sum_{efn}\langle n|L^0_0|aef\rangle\,\langle ef|\overline{\Theta^\dagger}^K_{M_K}|bn\rangle \\ &= \frac{1}{2}P(ab)\sum_{efn}\langle n|L^0_0|efa\rangle\,\langle ef|\overline{\Theta^\dagger}^K_{M_K}|bn\rangle \\ &= -\frac{1}{2}P(ab)\sum_{efn}\langle n|L^0_0|efb\rangle\,\langle ef|\overline{\Theta^\dagger}^K_{M_K}|an\rangle\,.\end{aligned} \tag{78}$$

The *j*-scheme expression corresponding to the final result of Eq. (78) turns out to be

$$\begin{aligned}\langle 0||[L^0 \otimes \overline{\Theta^\dagger}^K]^K||ab\rangle = \frac{1}{2}P(ab)\sum_{efn}\sum_{J_{ef},J_{an}} &(-1)^{1+j_a+j_n+J_{an}} \\ &\times \frac{\hat{J}^2_{an}\hat{j}_n}{\hat{K}} \begin{Bmatrix} j_n & J_{ef} & j_b \\ K & j_a & J_{an} \end{Bmatrix} \\ &\times \langle n||L^0||efb;J_{ef};J_{efb}=j_n\rangle\,\langle ef;J_{ef}||\overline{\Theta^\dagger}^K||an;J_{an}\rangle\,.\end{aligned} \tag{79}$$

Diagram 6

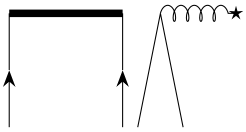

$$\langle i|[L_0^0 \otimes \overline{\Theta^\dagger}^K_{M_K}]^K_{M_K}|abc\rangle = P(ab,c)\,\langle 0|L_0^0|ab\rangle\,\langle i|\overline{\Theta^\dagger}^K_{M_K}|c\rangle\,, \tag{80}$$

$$\begin{aligned}\langle i||[L^0 \otimes \overline{\Theta^\dagger}^K]^K||abc\rangle =& P(ab,c)\,\langle 0||L^0||ab;J_{ab}=0\rangle \\ &\times \langle i||\overline{\Theta^\dagger}^K||c\rangle\,\delta_{j_c,J_{abc}}.\end{aligned} \tag{81}$$

Bibliography

[1] F. Bonaiti, S. Bacca, and G. Hagen, "Ab initio coupled-cluster calculations of ground and dipole excited states in ^{8}He," Phys. Rev. C, vol. 105, p. 034313, Mar 2022.

[2] B. Acharya, S. Bacca, F. Bonaiti, S. S. Li Muli, and J. E. Sobczyk, "Uncertainty quantification in electromagnetic observables of nuclei," Frontiers in Physics, vol. 10, 2023.

[3] D. Bazin, K. Becker, F. Bonaiti, C. Elster, K. Fossez, T. Frederico, A. Gnech, C. Hebborn, M. Higgins, L. Hlophe, B. Kay, S. König, K. Kravvaris, J. Lubian, A. Macchiavelli, F. Nunes, L. Platter, G. Potel, and X. Zhang, "Perspectives on Few-Body Cluster Structures in Exotic Nuclei," Few-Body Systems, vol. 64, p. 25, May 2023.

[4] P. Capel, D. R. Phillips, A. Andis, M. Bagnarol, B. Behzadmoghaddam, F. Bonaiti, R. Bubna, Y. Capitani, P.-Y. Duerinck, V. Durant, N. Döpper, A. El Boustani, R. Farrell, M. Geiger, M. Gennari, N. Goldberg, J. Herko, T. Kirchner, L.-P. Kubushishi, Z. Li, S. S. L. Muli, A. Long, B. Martin, K. Mohseni, I. Moumene, N. Paracone, E. Parnes, B. Romeo, V. Springer, I. Svensson, O. Thim, and N. Yapa, "Effective field theory analysis of the coulomb breakup of the one-neutron halo nucleus ^{19}C," The European Physical Journal A, vol. 59, p. 273, Nov. 2023.

[5] R. W. Fearick, P. von Neumann-Cosel, S. Bacca, J. Birkhan, F. Bonaiti, I. Brandherm, G. Hagen, H. Matsubara, W. Nazarewicz, N. Pietralla, V. Y. Ponomarev, P.-G. Reinhard, X. Roca-Maza, A. Richter, A. Schwenk, J. Simonis, and A. Tamii, "Electric dipole polarizability of ^{40}Ca," Phys. Rev. Res., vol. 5, p. L022044, May 2023.

[6] F. Bonaiti and S. Bacca, "Low-Energy Dipole Strength in ^{8}He," Few-Body Systems, vol. 65, p. 54, May 2024.

[7] F. Bonaiti, S. Bacca, G. Hagen, and G. R. Jansen, "Electromagnetic observables of open-shell nuclei from coupled-cluster theory," arXiv:2405.05608 [nucl-th]. Submitted to Physical Review C.

[8] F. Bonaiti, S. Bacca, and W. Jiang, "Nuclear incompressibility from isoscalar monopole resonances." , in preparation.

[9] "A New Era of Discovery - The Long Range Plan for Nuclear Science." https://doi.org/10.2172/2280968. Accessed: 2024-04-25.

[10] J. M. Lattimer and M. Prakash, “The physics of neutron stars,” Science, vol. 304, no. 5670, pp. 536–542, 2004.

[11] D. G. Yakovlev, P. Haensel, G. Baym, and C. Pethick, “Lev Landau and the concept of neutron stars,” Physics-Uspekhi, vol. 56, p. 289, Mar 2013.

[12] W. Baade and F. Zwicky, “Supernovae and cosmic rays,” Phys. Rev., vol. 45, p. 138, Jan 1934.

[13] R. C. Tolman, “Static Solutions of Einstein’s Field Equations for Spheres of Fluid,” Phys. Rev., vol. 55, pp. 364–373, Feb 1939.

[14] J. R. Oppenheimer and G. M. Volkoff, “On massive neutron cores,” Phys. Rev., vol. 55, pp. 374–381, Feb 1939.

[15] A. Hewish, S. J. Bell, J. D. H. Pilkington, P. F. Scott, and R. A. Collins, “Observation of a rapidly pulsating radio source,” Nature, vol. 217, pp. 709–713, Feb. 1968.

[16] R. W. Romani, D. Kandel, A. V. Filippenko, T. G. Brink, and W. Zheng, “PSR J0952-0607: The Fastest and Heaviest Known Galactic Neutron Star,” The Astrophysical Journal Letters, vol. 934, p. L17, Jul 2022.

[17] J. Piekarewicz, “The Nuclear Physics of Neutron Stars,” arXiv:2209.14877 [nucl-th].

[18] The LIGO Scientific Collaboration and Virgo Collaboration, “GW170817: Observation of Gravitational Waves from a Binary Neutron Star Inspiral,” Phys. Rev. Lett., vol. 119, p. 161101, Oct 2017.

[19] The LIGO Scientific Collaboration and the Virgo Collaboration, “Multi-messenger observations of a binary neutron star merger,” The Astrophysical Journal Letters, vol. 848, p. L12, oct 2017.

[20] The LIGO Scientific Collaboration and the Virgo Collaboration, “GW170817: Measurements of Neutron Star Radii and Equation of State,” Phys. Rev. Lett., vol. 121, p. 161101, Oct 2018.

[21] M. Centelles, X. Roca-Maza, X. Viñas, and M. Warda, “Origin of the neutron skin thickness of ^{208}Pb in nuclear mean-field models,” Phys. Rev. C, vol. 82, p. 054314, Nov 2010.

[22] M. Thiel, C. Sfienti, J. Piekarewicz, C. J. Horowitz, and M. Vanderhaeghen, “Neutron skins of atomic nuclei: per aspera ad astra,” Journal of Physics G: Nuclear and Particle Physics, vol. 46, p. 093003, Aug 2019.

[23] T. Donnelly, J. Dubach, and I. Sick, “Isospin dependences in parity-violating electron scattering,” Nuclear Physics A, vol. 503, no. 3, pp. 589–631, 1989.

[24] D. Adhikari, H. Albataineh, D. Androic, K. A. Aniol, D. S. Armstrong, T. Averett, C. Ayerbe Gayoso, S. K. Barcus, V. Bellini, R. S. Beminiwattha, J. F. Benesch, H. Bhatt, D. Bhatta Pathak, D. Bhetuwal, B. Blaikie, J. Boyd, Q. Campagna, A. Camsonne, G. D. Cates, Y. Chen, C. Clarke, J. C. Cornejo, S. Covrig Dusa, M. M. Dalton, P. Datta, A. Deshpande, D. Dutta, C. Feldman, E. Fuchey, C. Gal, D. Gaskell, T. Gautam, M. Gericke, C. Ghosh, I. Halilovic, J.-O. Hansen, O. Hassan, F. Hauenstein, W. Henry, C. J. Horowitz, C. Jantzi, S. Jian, S. Johnston, D. C. Jones, S. Kakkar, S. Katugampola, C. Keppel, P. M. King, D. E. King, K. S. Kumar, T. Kutz, N. Lashley-Colthirst, G. Leverick, H. Liu, N. Liyanage, J. Mammei, R. Mammei, M. McCaughan, D. McNulty, D. Meekins, C. Metts, R. Michaels, M. Mihovilovic, M. M. Mondal, J. Napolitano, A. Narayan, D. Nikolaev, V. Owen, C. Palatchi, J. Pan, B. Pandey, S. Park, K. D. Paschke, M. Petrusky, M. L. Pitt, S. Premathilake, B. Quinn, R. Radloff, S. Rahman, M. N. H. Rashad, A. Rathnayake, B. T. Reed, P. E. Reimer, R. Richards, S. Riordan, Y. R. Roblin, S. Seeds, A. Shahinyan, P. Souder, M. Thiel, Y. Tian, G. M. Urciuoli, E. W. Wertz, B. Wojtsekhowski, B. Yale, T. Ye, A. Yoon, W. Xiong, A. Zec, W. Zhang, J. Zhang, and X. Zheng, "Precision determination of the neutral weak form factor of ^{48}Ca," Phys. Rev. Lett., vol. 129, p. 042501, Jul 2022.

[25] S. Abrahamyan, Z. Ahmed, H. Albataineh, K. Aniol, D. S. Armstrong, W. Armstrong, T. Averett, B. Babineau, A. Barbieri, V. Bellini, R. Beminiwattha, J. Benesch, F. Benmokhtar, T. Bielarski, W. Boeglin, A. Camsonne, M. Canan, P. Carter, G. D. Cates, C. Chen, J.-P. Chen, O. Hen, F. Cusanno, M. M. Dalton, R. De Leo, K. de Jager, W. Deconinck, P. Decowski, X. Deng, A. Deur, D. Dutta, A. Etile, D. Flay, G. B. Franklin, M. Friend, S. Frullani, E. Fuchey, F. Garibaldi, E. Gasser, R. Gilman, A. Giusa, A. Glamazdin, J. Gomez, J. Grames, C. Gu, O. Hansen, J. Hansknecht, D. W. Higinbotham, R. S. Holmes, T. Holmstrom, C. J. Horowitz, J. Hoskins, J. Huang, C. E. Hyde, F. Itard, C.-M. Jen, E. Jensen, G. Jin, S. Johnston, A. Kelleher, K. Kliakhandler, P. M. King, S. Kowalski, K. S. Kumar, J. Leacock, J. Leckey, J. H. Lee, J. J. LeRose, R. Lindgren, N. Liyanage, N. Lubinsky, J. Mammei, F. Mammoliti, D. J. Margaziotis, P. Markowitz, A. McCreary, D. McNulty, L. Mercado, Z.-E. Meziani, R. W. Michaels, M. Mihovilovic, N. Muangma, C. Muñoz Camacho, S. Nanda, V. Nelyubin, N. Nuruzzaman, Y. Oh, A. Palmer, D. Parno, K. D. Paschke, S. K. Phillips, B. Poelker, R. Pomatsalyuk, M. Posik, A. J. R. Puckett, B. Quinn, A. Rakhman, P. E. Reimer, S. Riordan, P. Rogan, G. Ron, G. Russo, K. Saenboonruang, A. Saha, B. Sawatzky, A. Shahinyan, R. Silwal, S. Sirca, K. Slifer, P. Solvignon, P. A. Souder, M. L. Sperduto, R. Subedi, R. Suleiman, V. Sulkosky, C. M. Sutera, W. A. Tobias, W. Troth, G. M. Urciuoli, B. Waidyawansa, D. Wang, J. Wexler, R. Wilson, B. Wojtsekhowski, X. Yan, H. Yao, Y. Ye, Z. Ye, V. Yim, L. Zana, X. Zhan, J. Zhang, Y. Zhang, X. Zheng, and P. Zhu, "Measurement of the neutron radius of ^{208}Pb through parity violation in electron scattering," Phys. Rev. Lett., vol. 108, p. 112502, Mar 2012.

[26] D. Adhikari, H. Albataineh, D. Androic, K. Aniol, D. S. Armstrong, T. Averett, C. Ayerbe Gayoso, S. Barcus, V. Bellini, R. S. Beminiwattha, J. F. Benesch, H. Bhatt, D. Bhatta Pathak, D. Bhetuwal, B. Blaikie, Q. Campagna, A. Camsonne, G. D. Cates, Y. Chen, C. Clarke, J. C. Cornejo, S. Covrig Dusa, P. Datta, A. Deshpande, D. Dutta, C. Feldman, E. Fuchey, C. Gal, D. Gaskell, T. Gautam, M. Gericke, C. Ghosh, I. Halilovic, J.-O. Hansen, F. Hauenstein, W. Henry, C. J. Horowitz, C. Jantzi, S. Jian, S. Johnston, D. C. Jones, B. Karki, S. Katugampola, C. Keppel, P. M. King, D. E. King, M. Knauss, K. S. Kumar, T. Kutz, N. Lashley-Colthirst, G. Leverick, H. Liu, N. Liyange, S. Malace, R. Mammei, J. Mammei, M. McCaughan, D. McNulty, D. Meekins, C. Metts, R. Michaels, M. M. Mondal, J. Napolitano, A. Narayan, D. Nikolaev, M. N. H. Rashad, V. Owen, C. Palatchi, J. Pan, B. Pandey, S. Park, K. D. Paschke, M. Petrusky, M. L. Pitt, S. Premathilake, A. J. R. Puckett, B. Quinn, R. Radloff, S. Rahman, A. Rathnayake, B. T. Reed, P. E. Reimer, R. Richards, S. Riordan, Y. Roblin, S. Seeds, A. Shahinyan, P. Souder, L. Tang, M. Thiel, Y. Tian, G. M. Urciuoli, E. W. Wertz, B. Wojtsekhowski, B. Yale, T. Ye, A. Yoon, A. Zec, W. Zhang, J. Zhang, and X. Zheng, "Accurate determination of the neutron skin thickness of ^{208}Pb through parity-violation in electron scattering," Phys. Rev. Lett., vol. 126, p. 172502, Apr 2021.

[27] B. T. Reed, F. J. Fattoyev, C. J. Horowitz, and J. Piekarewicz, "Implications of PREX-2 on the Equation of State of Neutron-Rich Matter," Phys. Rev. Lett., vol. 126, p. 172503, Apr 2021.

[28] R. Essick, I. Tews, P. Landry, and A. Schwenk, "Astrophysical Constraints on the Symmetry Energy and the Neutron Skin of ^{208}Pb with Minimal Modeling Assumptions," Phys. Rev. Lett., vol. 127, p. 192701, Nov 2021.

[29] P.-G. Reinhard, X. Roca-Maza, and W. Nazarewicz, "Combined theoretical analysis of the parity-violating asymmetry for ^{48}Ca and ^{208}Pb," Phys. Rev. Lett., vol. 129, p. 232501, Dec 2022.

[30] B. Hu, W. Jiang, T. Miyagi, Z. Sun, A. Ekström, C. Forssén, G. Hagen, J. D. Holt, T. Papenbrock, S. R. Stroberg, and I. Vernon, "Ab initio predictions link the neutron skin of ^{208}Pb to nuclear forces," Nature Physics, vol. 18, pp. 1196–1200, Oct. 2022.

[31] B. T. Reed, F. J. Fattoyev, C. J. Horowitz, and J. Piekarewicz, "Density dependence of the symmetry energy in the post–PREX-CREX era," Phys. Rev. C, vol. 109, p. 035803, Mar 2024.

[32] X. Roca-Maza, M. Centelles, X. Viñas, M. Brenna, G. Colò, B. K. Agrawal, N. Paar, J. Piekarewicz, and D. Vretenar, "Electric dipole polarizability in ^{208}Pb: Insights from the droplet model," Phys. Rev. C, vol. 88, no. 2, p. 024316, 2013.

[33] J. Blaizot, "Nuclear compressibilities," Physics Reports, vol. 64, no. 4, pp. 171–248, 1980.

[34] N. Paar, D. Vretenar, E. Khan, and G. Colò, “Exotic modes of excitation in atomic nuclei far from stability,” Reports on Progress in Physics, vol. 70, p. R02, May 2007.

[35] X. Roca-Maza and N. Paar, “Nuclear equation of state from ground and collective excited state properties of nuclei,” Progress in Particle and Nuclear Physics, vol. 101, pp. 96–176, 2018.

[36] G. Colo’, “Theoretical Methods for Giant Resonances,” arXiv:2201.04578 [nucl-th].

[37] A. Ekström, C. Forssén, G. Hagen, G. R. Jansen, W. Jiang, and T. Papenbrock, “What is ab initio in nuclear theory?,” Frontiers in Physics, vol. 11, 2023.

[38] “TOP500 Statistics. TOP500.org.” https://www.top500.org/statistics/perfdevel/. Accessed: 2024-04-26.

[39] G. Hagen, T. Papenbrock, M. Hjorth-Jensen, and D. J. Dean, “Coupled-cluster computations of atomic nuclei,” Reports on Progress in Physics, vol. 77, p. 096302, sep 2014.

[40] H. Hergert, S. Bogner, T. Morris, A. Schwenk, and K. Tsukiyama, “The in-medium similarity renormalization group: A novel ab initio method for nuclei,” Physics Reports, vol. 621, pp. 165–222, 2016.

[41] C. Barbieri, F. Raimondi, and C. McIlroy, “Recent Applications of Self-Consistent Green’s Function Theory to Nuclei,” Journal of Physics: Conference Series, vol. 966, p. 012015, feb 2018.

[42] H. Hergert, “A Guided Tour of ab initio Nuclear Many-Body Theory,” Frontiers in Physics, vol. 8, 2020.

[43] V. D. Efros, W. Leidemann, G. Orlandini, and N. Barnea, “The Lorentz integral transform (LIT) method and its applications to perturbation-induced reactions,” Journal of Physics G: Nuclear and Particle Physics, vol. 34, p. R459, oct 2007.

[44] S. Bacca, N. Barnea, G. Hagen, G. Orlandini, and T. Papenbrock, “First-principles description of the giant dipole resonance in ^{16}O,” Phys. Rev. Lett., vol. 111, p. 122502, Sep 2013.

[45] S. Bacca, N. Barnea, G. Hagen, M. Miorelli, G. Orlandini, and T. Papenbrock, “Giant and pigmy dipole resonances in ^{4}He, ^{16,22}O, and ^{40}Ca from chiral nucleon-nucleon interactions,” Phys. Rev. C, vol. 90, p. 064619, Dec 2014.

[46] M. Miorelli, S. Bacca, N. Barnea, G. Hagen, G. R. Jansen, G. Orlandini, and T. Papenbrock, “Electric dipole polarizability from first principles calculations,” Phys. Rev. C, vol. 94, p. 034317, Sep 2016.

[47] G. Hagen, A. Ekström, C. Forssén, G. R. Jansen, W. Nazarewicz, T. Papenbrock, K. A. Wendt, S. Bacca, N. Barnea, B. Carlsson, C. Drischler, K. Hebeler, M. Hjorth-Jensen, M. Miorelli, G. Orlandini, A. Schwenk, and J. Simonis, "Neutron and weak-charge distributions of the ^{48}Ca nucleus," Nature Physics, vol. 12, pp. 186–190, 2016.

[48] J. Birkhan, M. Miorelli, S. Bacca, S. Bassauer, C. A. Bertulani, G. Hagen, H. Matsubara, P. von Neumann-Cosel, T. Papenbrock, N. Pietralla, V. Y. Ponomarev, A. Richter, A. Schwenk, and A. Tamii, "Electric dipole polarizability of ^{48}Ca and implications for the neutron skin," Phys. Rev. Lett., vol. 118, p. 252501, Jun 2017.

[49] S. Kaufmann, J. Simonis, S. Bacca, J. Billowes, M. L. Bissell, K. Blaum, B. Cheal, R. F. G. Ruiz, W. Gins, C. Gorges, G. Hagen, H. Heylen, A. Kanellakopoulos, S. Malbrunot-Ettenauer, M. Miorelli, R. Neugart, G. Neyens, W. Nörtershäuser, R. Sánchez, S. Sailer, A. Schwenk, T. Ratajczyk, L. V. Rodríguez, L. Wehner, C. Wraith, L. Xie, Z. Y. Xu, X. F. Yang, and D. T. Yordanov, "Charge radius of the short-lived ^{68}Ni and correlation with the dipole polarizability," Phys. Rev. Lett., vol. 124, p. 132502, Apr 2020.

[50] P. Von Neumann-Cosel. Private communication, March 2021.

[51] FRIB Science Community, "FRIB400 - The Scientific Case for the 400 MeV/u Energy Upgrade of FRIB." `https://frib.msu.edu/_files/pdfs/frib400_final.pdf`. Accessed: 2023-09-26.

[52] S. Huth, Equation of state of hot and dense matter in astrophysics and in the laboratory. PhD thesis, Technische Universität Darmstadt, Darmstadt, 2023.

[53] G. Raaijmakers, S. K. Greif, T. E. Riley, T. Hinderer, K. Hebeler, A. Schwenk, A. L. Watts, S. Nissanke, S. Guillot, J. M. Lattimer, and R. M. Ludlam, "Constraining the Dense Matter Equation of State with Joint Analysis of NICER and LIGO/Virgo Measurements," The Astrophysical Journal Letters, vol. 893, p. L21, apr 2020.

[54] T. E. Riley, A. L. Watts, S. Bogdanov, P. S. Ray, R. M. Ludlam, S. Guillot, Z. Arzoumanian, C. L. Baker, A. V. Bilous, D. Chakrabarty, K. C. Gendreau, A. K. Harding, W. C. G. Ho, J. M. Lattimer, S. M. Morsink, and T. E. Strohmayer, "A NICER View of PSR J0030+0451: Millisecond Pulsar Parameter Estimation," The Astrophysical Journal Letters, vol. 887, p. L21, dec 2019.

[55] M. C. Miller, C. Chirenti, and F. K. Lamb, "Constraining the equation of state of high-density cold matter using nuclear and astronomical measurements," The Astrophysical Journal, vol. 888, p. 12, dec 2019.

[56] L. Lindblom, "Determining the Nuclear Equation of State from Neutron-Star Masses and Radii," Astrophysical Journal, vol. 398, p. 569, Oct. 1992.

[57] G. Raaijmakers, T. E. Riley, A. L. Watts, S. K. Greif, S. M. Morsink, K. Hebeler, A. Schwenk, T. Hinderer, S. Nissanke, S. Guillot, Z. Arzoumanian, S. Bogdanov, D. Chakrabarty, K. C. Gendreau, W. C. G. Ho, J. M. Lattimer, R. M. Ludlam, and M. T. Wolff, "A NICER View of PSR J0030+0451: Implications for the Dense Matter Equation of State," The Astrophysical Journal Letters, vol. 887, p. L22, dec 2019.

[58] S. Huth, C. Wellenhofer, and A. Schwenk, "New equations of state constrained by nuclear physics, observations, and QCD calculations of high-density nuclear matter," Phys. Rev. C, vol. 103, p. 025803, Feb 2021.

[59] S. Huth, P. T. H. Pang, I. Tews, T. Dietrich, A. Le Fèvre, A. Schwenk, W. Trautmann, K. Agarwal, M. Bulla, M. W. Coughlin, and C. Van Den Broeck, "Constraining neutron-star matter with microscopic and macroscopic collisions," Nature, vol. 606, pp. 276–280, June 2022.

[60] C. Y. Tsang, M. B. Tsang, W. G. Lynch, R. Kumar, and C. J. Horowitz, "Determination of the equation of state from nuclear experiments and neutron star observations," Nature Astronomy, vol. 8, pp. 328–336, Mar 2024.

[61] Y. Lim and A. Schwenk, "Symmetry energy and neutron star properties constrained by chiral effective field theory calculations," Phys. Rev. C, vol. 109, p. 035801, Mar 2024.

[62] A. L. Watts, W. Yu, J. Poutanen, S. Zhang, S. Bhattacharyya, S. Bogdanov, L. Ji, A. Patruno, T. E. Riley, P. Bakala, A. Baykal, F. Bernardini, I. Bombaci, E. Brown, Y. Cavecchi, D. Chakrabarty, J. Chenevez, N. Degenaar, M. Del Santo, T. Di Salvo, V. Doroshenko, M. Falanga, R. D. Ferdman, M. Feroci, A. F. Gambino, M. Ge, S. K. Greif, S. Guillot, C. Gungor, D. H. Hartmann, K. Hebeler, A. Heger, J. Homan, R. Iaria, J. I. Zand, O. Kargaltsev, A. Kurkela, X. Lai, A. Li, X. Li, Z. Li, M. Linares, F. Lu, S. Mahmoodifar, M. Méndez, M. Coleman Miller, S. Morsink, J. Nättilä, A. Possenti, C. Prescod-Weinstein, J. Qu, A. Riggio, T. Salmi, A. Sanna, A. Santangelo, H. Schatz, A. Schwenk, L. Song, E. Šrámková, B. Stappers, H. Stiele, T. Strohmayer, I. Tews, L. Tolos, G. Török, D. Tsang, M. Urbanec, A. Vacchi, R. Xu, Y. Xu, S. Zane, G. Zhang, S. Zhang, W. Zhang, S. Zheng, and X. Zhou, "Dense matter with eXTP," Science China Physics, Mechanics & Astronomy, vol. 62, p. 29503, Aug. 2018.

[63] G. Baym, C. Pethick, and P. Sutherland, "The ground state of matter at high densities: Equation of state and stellar models," Astrophysical Journal, vol. 170, p. 299, Dec. 1971.

[64] D. G. Ravenhall, C. J. Pethick, and J. R. Wilson, "Structure of matter below nuclear saturation density," Phys. Rev. Lett., vol. 50, pp. 2066–2069, Jun 1983.

[65] D. Page and S. Reddy, “Dense matter in compact stars: Theoretical developments and observational constraints,” Annual Review of Nuclear and Particle Science, vol. 56, no. 1, pp. 327–374, 2006.

[66] R. Somasundaram, C. Drischler, I. Tews, and J. Margueron, “Constraints on the nuclear symmetry energy from asymmetric-matter calculations with chiral nn and $3n$ interactions,” Phys. Rev. C, vol. 103, p. 045803, Apr 2021.

[67] C. Drischler, K. Hebeler, and A. Schwenk, “Chiral interactions up to next-to-next-to-next-to-leading order and nuclear saturation,” Phys. Rev. Lett., vol. 122, p. 042501, Jan 2019.

[68] K. Hebeler, S. K. Bogner, R. J. Furnstahl, A. Nogga, and A. Schwenk, “Improved nuclear matter calculations from chiral low-momentum interactions,” Phys. Rev. C, vol. 83, p. 031301, Mar 2011.

[69] C. Drischler, K. Hebeler, and A. Schwenk, “Asymmetric nuclear matter based on chiral two- and three-nucleon interactions,” Phys. Rev. C, vol. 93, p. 054314, May 2016.

[70] C. Drischler, P. G. Giuliani, S. Bezoui, J. Piekarewicz, and F. Viens, “A Bayesian mixture model approach to quantifying the empirical nuclear saturation point,”

[71] G. W. Hoffmann, L. Ray, M. Barlett, J. McGill, G. S. Adams, G. J. Igo, F. Irom, A. T. M. Wang, C. A. Whitten, R. L. Boudrie, J. F. Amann, C. Glashausser, N. M. Hintz, G. S. Kyle, and G. S. Blanpied, “0.8 GeV p+^{208}Pb elastic scattering and the quantity Δr_{np},” Phys. Rev. C, vol. 21, pp. 1488–1494, Apr 1980.

[72] J. Zenihiro, H. Sakaguchi, T. Murakami, M. Yosoi, Y. Yasuda, S. Terashima, Y. Iwao, H. Takeda, M. Itoh, H. P. Yoshida, and M. Uchida, “Neutron density distributions of ^{204,206,208}Pb deduced via proton elastic scattering at $E_p = 295$ MeV,” Phys. Rev. C, vol. 82, p. 044611, Oct 2010.

[73] T. Aumann, C. A. Bertulani, F. Schindler, and S. Typel, “Peeling off neutron skins from neutron-rich nuclei: Constraints on the symmetry energy from neutron-removal cross sections,” Phys. Rev. Lett., vol. 119, p. 262501, Dec 2017.

[74] B. Kłos, A. Trzcińska, J. Jastrzebski, T. Czosnyka, M. Kisieliński, P. Lubiński, P. Napiorkowski, L. Pieńkowski, F. J. Hartmann, B. Ketzer, P. Ring, R. Schmidt, T. v. Egidy, R. Smolańczuk, S. Wycech, K. Gulda, W. Kurcewicz, E. Widmann, and B. A. Brown, “Neutron density distributions from antiprotonic ^{208}Pb and ^{209}Bi atoms,” Phys. Rev. C, vol. 76, p. 014311, Jul 2007.

[75] J. M. Mammei, C. J. Horowitz, J. Piekarewicz, B. Reed, and C. Sfienti, “Neutron Skins: Weak Elastic Scattering and Neutron Stars,” arXiv:2311.06146 [nucl-th].

[76] J. Piekarewicz, B. K. Agrawal, G. Colò, W. Nazarewicz, N. Paar, P.-G. Reinhard, X. Roca-Maza, and D. Vretenar, “Electric dipole polarizability and the neutron skin,” Phys. Rev. C, vol. 85, p. 041302, Apr 2012.

[77] J. Simonis, S. Bacca, and G. Hagen, “First principles electromagnetic responses in medium-mass nuclei,” The European Physical Journal A, vol. 55, p. 241, Dec. 2019.

[78] M. H. Mahzoon, M. C. Atkinson, R. J. Charity, and W. H. Dickhoff, “Neutron skin thickness of ^{48}Ca from a nonlocal dispersive optical-model analysis,” Phys. Rev. Lett., vol. 119, p. 222503, Nov 2017.

[79] M. C. Atkinson, M. H. Mahzoon, M. A. Keim, B. A. Bordelon, C. D. Pruitt, R. J. Charity, and W. H. Dickhoff, “Dispersive optical model analysis of ^{208}Pb generating a neutron-skin prediction beyond the mean field,” Phys. Rev. C, vol. 101, p. 044303, Apr 2020.

[80] F. J. Fattoyev, J. Piekarewicz, and C. J. Horowitz, “Neutron skins and neutron stars in the multimessenger era,” Phys. Rev. Lett., vol. 120, p. 172702, Apr 2018.

[81] J. M. Lattimer, “Constraints on nuclear symmetry energy parameters,” Particles, vol. 6, no. 1, pp. 30–56, 2023.

[82] C. M. Tarbert, D. P. Watts, D. I. Glazier, P. Aguar, J. Ahrens, J. R. M. Annand, H. J. Arends, R. Beck, V. Bekrenev, B. Boillat, A. Braghieri, D. Branford, W. J. Briscoe, J. Brudvik, S. Cherepnya, R. Codling, E. J. Downie, K. Foehl, P. Grabmayr, R. Gregor, E. Heid, D. Hornidge, O. Jahn, V. L. Kashevarov, A. Knezevic, R. Kondratiev, M. Korolija, M. Kotulla, D. Krambrich, B. Krusche, M. Lang, V. Lisin, K. Livingston, S. Lugert, I. J. D. MacGregor, D. M. Manley, M. Martinez, J. C. McGeorge, D. Mekterovic, V. Metag, B. M. K. Nefkens, A. Nikolaev, R. Novotny, R. O. Owens, P. Pedroni, A. Polonski, S. N. Prakhov, J. W. Price, G. Rosner, M. Rost, T. Rostomyan, S. Schadmand, S. Schumann, D. Sober, A. Starostin, I. Supek, A. Thomas, M. Unverzagt, T. Walcher, L. Zana, and F. Zehr, “Neutron skin of ^{208}Pb from coherent pion photoproduction,” Phys. Rev. Lett., vol. 112, p. 242502, Jun 2014.

[83] F. Colomer, P. Capel, M. Ferretti, J. Piekarewicz, C. Sfienti, M. Thiel, V. Tsaran, and M. Vanderhaeghen, “Theoretical analysis of the extraction of neutron skin thickness from coherent π^0 photoproduction off nuclei,” Phys. Rev. C, vol. 106, p. 044318, Oct 2022.

[84] C. Drischler, R. J. Furnstahl, J. A. Melendez, and D. R. Phillips, “How Well Do We Know the Neutron-Matter Equation of State at the Densities Inside Neutron Stars? A Bayesian Approach with Correlated Uncertainties,” Phys. Rev. Lett., vol. 125, p. 202702, Nov 2020.

[85] P.-G. Reinhard, X. Roca-Maza, and W. Nazarewicz, "Information content of the parity-violating asymmetry in ^{208}Pb," Phys. Rev. Lett., vol. 127, p. 232501, Nov 2021.

[86] M. Miorelli, Electromagnetic properties of medium-mass nuclei from coupled-cluster theory. PhD thesis, University of British Columbia, 2017.

[87] J. Eisenberg and W. Greiner, Nuclear Theory: Excitation mechanisms of the nucleus. North-Holland Publishing Company, 1975.

[88] J. Ahrens, H. Borchert, K. Czock, H. Eppler, H. Gimm, H. Gundrum, M. Kröning, P. Riehn, G. Sita Ram, A. Zieger, and B. Ziegler, "Total nuclear photon absorption cross sections for some light elements," Nuclear Physics A, vol. 251, no. 3, pp. 479–492, 1975.

[89] P. von Neumann-Cosel and A. Tamii, "Electric and magnetic dipole modes in high-resolution inelastic proton scattering at 0°," The European Physical Journal A, vol. 55, p. 110, July 2019.

[90] A. Tamii, I. Poltoratska, P. von Neumann-Cosel, Y. Fujita, T. Adachi, C. A. Bertulani, J. Carter, M. Dozono, H. Fujita, K. Fujita, K. Hatanaka, D. Ishikawa, M. Itoh, T. Kawabata, Y. Kalmykov, A. M. Krumbholz, E. Litvinova, H. Matsubara, K. Nakanishi, R. Neveling, H. Okamura, H. J. Ong, B. Özel-Tashenov, V. Y. Ponomarev, A. Richter, B. Rubio, H. Sakaguchi, Y. Sakemi, Y. Sasamoto, Y. Shimbara, Y. Shimizu, F. D. Smit, T. Suzuki, Y. Tameshige, J. Wambach, R. Yamada, M. Yosoi, and J. Zenihiro, "Complete electric dipole response and the neutron skin in ^{208}Pb," Phys. Rev. Lett., vol. 107, p. 062502, Aug 2011.

[91] T. Hashimoto, A. M. Krumbholz, P.-G. Reinhard, A. Tamii, P. von Neumann-Cosel, T. Adachi, N. Aoi, C. A. Bertulani, H. Fujita, Y. Fujita, E. Ganioğlu, K. Hatanaka, E. Ideguchi, C. Iwamoto, T. Kawabata, N. T. Khai, A. Krugmann, D. Martin, H. Matsubara, K. Miki, R. Neveling, H. Okamura, H. J. Ong, I. Poltoratska, V. Y. Ponomarev, A. Richter, H. Sakaguchi, Y. Shimbara, Y. Shimizu, J. Simonis, F. D. Smit, G. Süsoy, T. Suzuki, J. H. Thies, M. Yosoi, and J. Zenihiro, "Dipole polarizability of ^{120}Sn and nuclear energy density functionals," Phys. Rev. C, vol. 92, p. 031305, Sep 2015.

[92] D. M. Rossi, P. Adrich, F. Aksouh, H. Alvarez-Pol, T. Aumann, J. Benlliure, M. Böhmer, K. Boretzky, E. Casarejos, M. Chartier, A. Chatillon, D. Cortina-Gil, U. Datta Pramanik, H. Emling, O. Ershova, B. Fernandez-Dominguez, H. Geissel, M. Gorska, M. Heil, H. T. Johansson, A. Junghans, A. Kelic-Heil, O. Kiselev, A. Klimkiewicz, J. V. Kratz, R. Krücken, N. Kurz, M. Labiche, T. Le Bleis, R. Lemmon, Y. A. Litvinov, K. Mahata, P. Maierbeck, A. Movsesyan, T. Nilsson, C. Nociforo, R. Palit, S. Paschalis, R. Plag, R. Reifarth, D. Savran, H. Scheit, H. Simon, K. Sümmerer, A. Wagner, W. Waluś, H. Weick, and M. Winkler, "Measurement of

the dipole polarizability of the unstable neutron-rich nucleus ^{68}Ni," Phys. Rev. Lett., vol. 111, p. 242503, Dec 2013.

[93] T. Aumann, D. Aleksandrov, L. Axelsson, T. Baumann, M. J. G. Borge, L. V. Chulkov, J. Cub, W. Dostal, B. Eberlein, T. W. Elze, H. Emling, H. Geissel, V. Z. Goldberg, M. Golovkov, A. Grünschloß, M. Hellström, K. Hencken, J. Holeczek, R. Holzmann, B. Jonson, A. A. Korshenninikov, J. V. Kratz, G. Kraus, R. Kulessa, Y. Leifels, A. Leistenschneider, T. Leth, I. Mukha, G. Münzenberg, F. Nickel, T. Nilsson, G. Nyman, B. Petersen, M. Pfützner, A. Richter, K. Riisager, C. Scheidenberger, G. Schrieder, W. Schwab, H. Simon, M. H. Smedberg, M. Steiner, J. Stroth, A. Surowiec, T. Suzuki, O. Tengblad, and M. V. Zhukov, "Continuum excitations in ^{6}He," Phys. Rev. C, vol. 59, pp. 1252–1262, Mar 1999.

[94] C. Lehr, Low-energy dipole response of the halo nuclei ^{6,8}He. PhD thesis, Technische Universität Darmstadt, Germany, 2022.

[95] P.-G. Reinhard and W. Nazarewicz, "Information content of a new observable: The case of the nuclear neutron skin," Phys. Rev. C, vol. 81, p. 051303, May 2010.

[96] W. Myers and W. Swiatecki, "The nuclear droplet model for arbitrary shapes," Annals of Physics, vol. 84, no. 1, pp. 186–210, 1974.

[97] J. Meyer, P. Quentin, and B. Jennings, "The isovector dipole mode: A simple sum rule approach," Nuclear Physics A, vol. 385, no. 2, pp. 269–284, 1982.

[98] J. M. Lattimer and Y. Lim, "Constraining the symmetry parameters of the nuclear interaction," The Astrophysical Journal, vol. 771, p. 51, Jun 2013.

[99] X. Roca-Maza, X. Viñas, M. Centelles, B. K. Agrawal, G. Colò, N. Paar, J. Piekarewicz, and D. Vretenar, "Neutron skin thickness from the measured electric dipole polarizability in ^{68}Ni, ^{120}Sn, and ^{208}Pb," Phys. Rev. C, vol. 92, p. 064304, Dec 2015.

[100] J. Piekarewicz, "Implications of PREX-2 on the electric dipole polarizability of neutron-rich nuclei," Phys. Rev. C, vol. 104, p. 024329, Aug 2021.

[101] M. Miorelli, S. Bacca, G. Hagen, and T. Papenbrock, "Computing the dipole polarizability of ^{48}Ca with increased precision," Phys. Rev. C, vol. 98, p. 014324, Jul 2018.

[102] A. Ekström, G. R. Jansen, K. A. Wendt, G. Hagen, T. Papenbrock, B. D. Carlsson, C. Forssén, M. Hjorth-Jensen, P. Navrátil, and W. Nazarewicz, "Accurate nuclear radii and binding energies from a chiral interaction," Phys. Rev. C, vol. 91, p. 051301, May 2015.

[103] W. Jiang. Private communication, November 2023.

[104] D. H. Youngblood, C. M. Rozsa, J. M. Moss, D. R. Brown, and J. D. Bronson, "Isoscalar breathing-mode state in ^{144}Sm and ^{208}Pb," Phys. Rev. Lett., vol. 39, pp. 1188–1191, Nov 1977.

[105] Y. Gupta, U. Garg, K. Howard, J. Matta, M. Şenyiğit, M. Itoh, S. Ando, T. Aoki, A. Uchiyama, S. Adachi, M. Fujiwara, C. Iwamoto, A. Tamii, H. Akimune, C. Kadono, Y. Matsuda, T. Nakahara, T. Furuno, T. Kawabata, M. Tsumura, M. Harakeh, and N. Kalantar-Nayestanaki, "Are there nuclear structure effects on the isoscalar giant monopole resonance and nuclear incompressibility near A=90?," Physics Letters B, vol. 760, pp. 482–485, 2016.

[106] U. Garg and G. Colò, "The compression-mode giant resonances and nuclear incompressibility," Progress in Particle and Nuclear Physics, vol. 101, pp. 55–95, 2018.

[107] J. R. Stone, N. J. Stone, and S. A. Moszkowski, "Incompressibility in finite nuclei and nuclear matter," Phys. Rev. C, vol. 89, p. 044316, Apr 2014.

[108] S. Shlomo, V. M. Kolomietz, and G. Colò, "Deducing the nuclear-matter incompressibility coefficient from data on isoscalar compression modes," The European Physical Journal A - Hadrons and Nuclei, vol. 30, pp. 23–30, Oct. 2006.

[109] M. Burrows, R. B. Baker, S. Bacca, K. D. Launey, T. Dytrych, and D. Langr, "Response functions and giant monopole resonances for light to medium-mass nuclei from the \textitab initio symmetry-adapted no-core shell model," arXiv:2312.09782 [nucl-th], 2023.

[110] A. Porro, T. Duguet, J.-P. Ebran, M. Frosini, R. Roth, and V. Somà, "Ab initio description of monopole resonances in light- and medium-mass nuclei: Iii. moments evaluation in ab initio pgcm calculations."

[111] F. Gross, E. Klempt, S. J. Brodsky, A. J. Buras, V. D. Burkert, G. Heinrich, K. Jakobs, C. A. Meyer, K. Orginos, M. Strickland, J. Stachel, G. Zanderighi, N. Brambilla, P. Braun-Munzinger, D. Britzger, S. Capstick, T. Cohen, V. Crede, M. Constantinou, C. Davies, L. Del Debbio, A. Denig, C. DeTar, A. Deur, Y. Dokshitzer, H. G. Dosch, J. Dudek, M. Dunford, E. Epelbaum, M. A. Escobedo, H. Fritzsch, K. Fukushima, P. Gambino, D. Gillberg, S. Gottlieb, P. Grafstrom, M. Grazzini, B. Grube, A. Guskov, T. Iijima, X. Ji, F. Karsch, S. Kluth, J. B. Kogut, F. Krauss, S. Kumano, D. Leinweber, H. Leutwyler, H.-B. Li, Y. Li, B. Malaescu, C. Mariotti, P. Maris, S. Marzani, W. Melnitchouk, J. Messchendorp, H. Meyer, R. E. Mitchell, C. Mondal, F. Nerling, S. Neubert, M. Pappagallo, S. Pastore, J. R. Peláez, A. Puckett, J. Qiu, K. Rabbertz, A. Ramos, P. Rossi, A. Rustamov, A. Schäfer, S. Scherer, M. Schindler, S. Schramm, M. Shifman, E. Shuryak, T. Sjöstrand, G. Sterman, I. W. Stewart, J. Stroth, E. Swanson, G. F. de Téramond, U. Thoma, A. Vairo, D. van Dyk, J. Vary, J. Virto, M. Vos, C. Weiss, M. Wobisch, S. L. Wu, C. Young, F. Yuan,

X. Zhao, and X. Zhou, “50 years of quantum chromodynamics,” The European Physical Journal C, vol. 83, p. 1125, Dec. 2023.

[112] D. J. Gross and F. Wilczek, “Ultraviolet behavior of non-abelian gauge theories,” Phys. Rev. Lett., vol. 30, pp. 1343–1346, Jun 1973.

[113] H. D. Politzer, “Reliable perturbative results for strong interactions?,” Phys. Rev. Lett., vol. 30, pp. 1346–1349, Jun 1973.

[114] J. Greensite, An Introduction to the Confinement Problem. Lecture Notes in Physics, Springer Berlin Heidelberg, 2011.

[115] H. Wittig, QCD on the Lattice, pp. 137–262. Cham: Springer International Publishing, 2020.

[116] Y. Aoki, T. Blum, G. Colangelo, S. Collins, M. D. Morte, P. Dimopoulos, S. Dürr, X. Feng, H. Fukaya, M. Golterman, S. Gottlieb, R. Gupta, S. Hashimoto, U. M. Heller, G. Herdoiza, P. Hernandez, R. Horsley, A. Jüttner, T. Kaneko, E. Lunghi, S. Meinel, C. Monahan, A. Nicholson, T. Onogi, C. Pena, P. Petreczky, A. Portelli, A. Ramos, S. R. Sharpe, J. N. Simone, S. Simula, S. Sint, R. Sommer, N. Tantalo, R. Van de Water, U. Wenger, H. Wittig, and Flavour Lattice Averaging Group (FLAG), “FLAG review 2021,” The European Physical Journal C, vol. 82, p. 869, Oct. 2022.

[117] P. Achenbach, D. Adhikari, A. Afanasev, F. Afzal, C. Aidala, A. Al-bataineh, D. Almaalol, M. Amaryan, D. Androić, W. Armstrong, M. Arratia, J. Arrington, A. Asaturyan, E. Aschenauer, H. Atac, H. Avakian, T. Averett, C. Ayerbe Gayoso, X. Bai, K. Barish, N. Barnea, G. Basar, M. Battaglieri, A. Baty, I. Bautista, A. Bazilevsky, C. Beattie, S. Behera, V. Bellini, R. Bellwied, J. Benesch, F. Benmokhtar, C. Bernardes, J. Bernauer, H. Bhatt, S. Bhatta, M. Boer, T. Boettcher, S. Bogacz, H. Bossi, J. Brandenburg, E. Brash, R. Briceño, W. Briscoe, S. Brodsky, D. Brown, V. Burkert, H. Caines, I. Cali, A. Camsonne, D. Carman, J. Caylor, D. Cerci, S. Cerci, M. Chamizo Llatas, S. Chatterjee, J. Chen, Y. Chen, Y.-C. Chen, Y.-T. Chien, P.-C. Chou, X. Chu, E. Chudakov, E. Cline, I. Cloët, P. Cole, M. Connors, M. Constantinou, W. Cosyn, S. Covrig Dusa, R. Cruz-Torres, U. D’Alesio, C. da Silva, Z. Davoudi, C. Dean, D. Dean, M. Demarteau, A. Deshpande, W. Detmold, A. Deur, B. Devkota, S. Dhital, M. Diefenthaler, S. Dobbs, M. Döring, X. Dong, R. Dotel, K. Dow, E. Downie, J. Drachenberg, A. Dumitru, J. Dunlop, R. Dupre, J. Durham, D. Dutta, R. Edwards, R. Ehlers, L. El Fassi, M. Elaasar, L. Elouadrhiri, M. Engelhardt, R. Ent, S. Esumi, O. Evdokimov, O. Eyser, C. Fanelli, R. Fatemi, I. Fernando, F. Flor, N. Fomin, A. Frawley, T. Frederico, R. Fries, C. Gal, B. Gamage, L. Gamberg, H. Gao, D. Gaskell, F. Geurts, Y. Ghandilyan, N. Ghimire, R. Gilman, C. Gleason, K. Gnanvo, R. Gothe, S. Greene, H. Grießhammer, S. Grossberndt, B. Grube, D. Hackett, T. Hague, H. Hakobyan, J.-O. Hansen, Y. Hatta, M. Hattawy,

L. Havener, O. Hen, W. Henry, D. Higinbotham, T. Hobbs, A. Hodges, T. Holmstrom, B. Hong, T. Horn, C. Howell, H. Huang, M. Huang, S. Huang, G. Huber, C. Hyde, E. Isupov, P. Jacobs, J. Jalilian-Marian, A. Jentsch, H. Jheng, C.-R. Ji, X. Ji, J. Jia, D. Jones, M. Jones, S. Joosten, N. Kalantarians, G. Kalicy, Z. Kang, J. Karthein, D. Keller, C. Keppel, V. Khachatryan, D. Kharzeev, H. Kim, M. Kim, Y. Kim, P. King, E. Kinney, S. Klein, H. Ko, V. Koch, M. Kohl, Y. Kovchegov, G. Krintiras, V. Kubarovsky, S. Kuhn, K. Kumar, T. Kutz, J. Lajoie, J. Lauret, I. Lavrukhin, D. Lawrence, J. Lee, K. Lee, S. Lee, Y.-J. Lee, S. Li, W. Li, X. Li, X. Li, J. Liao, H.-W. Lin, M. Lisa, K.-F. Liu, M. Liu, T. Liu, S. Liuti, N. Liyanage, W. Llope, C. Loizides, R. Longo, W. Lorenzon, S. Lunkenheimer, X. Luo, R. Ma, B. McKinnon, D. Meekins, Y. Mehtar-Tani, W. Melnitchouk, A. Metz, C. Meyer, Z.-E. Meziani, R. Michaels, J. Michel, R. Milner, H. Mkrtchyan, P. Mohanmurthy, B. Mohanty, V. Mokeev, D. Moon, I. Mooney, C. Morningstar, D. Morrison, B. Müller, S. Mukherjee, J. Mulligan, C. Munoz Camacho, J. Murillo Quijada, M. Murray, S. Nadeeshani, P. Nadel-Turonski, J. Nam, C. Nattrass, G. Nijs, J. Noronha, J. Noronha-Hostler, N. Novitzky, M. Nycz, F. Olness, J. Osborn, R. Pak, B. Pandey, M. Paolone, Z. Papandreou, J.-F. Paquet, S. Park, K. Paschke, B. Pasquini, E. Pasyuk, T. Patel, A. Patton, C. Paudel, C. Peng, J. Peng, H. Pereira Da Costa, D. Perepelitsa, M. Peters, P. Petreczky, R. Pisarski, D. Pitonyak, M. Ploskon, M. Posik, J. Poudel, R. Pradhan, A. Prokudin, C. Pruneau, A. Puckett, P. Pujahari, J. Putschke, J. Pybus, J.-W. Qiu, K. Rajagopal, C. Ratti, K. Read, R. Reed, D. Richards, C. Riedl, F. Ringer, T. Rinn, J. Rittenhouse West, J. Roche, A. Rodas, G. Roland, F. Romero-López, P. Rossi, T. Rostomyan, L. Ruan, O. Ruimi, N. Saha, N. Sahoo, T. Sakaguchi, F. Salazar, C. Salgado, G. Salmè, S. Salur, S. Santiesteban, M. Sargsian, M. Sarsour, N. Sato, T. Satogata, S. Sawada, T. Schäfer, B. Scheihing-Hitschfeld, B. Schenke, S. Schindler, A. Schmidt, R. Seidl, M. Shabestari, P. Shanahan, C. Shen, T.-A. Sheng, M. Shepherd, A. Sickles, M. Sievert, K. Smith, Y. Song, A. Sorensen, P. Souder, N. Sparveris, S. Srednyak, A. Stahl Leiton, A. Stasto, P. Steinberg, S. Stepanyan, M. Stephanov, J. Stevens, D. Stewart, I. Stewart, M. Stojanovic, I. Strakovsky, S. Strauch, M. Strickland, D. Sunar Cerci, M. Suresh, B. Surrow, S. Syritsyn, A. Szczepaniak, A. Tadepalli, A. Tang, J. Tapia Takaki, T. Tarnowsky, A. Tawfik, M. Taylor, C. Tennant, A. Thiel, D. Thomas, Y. Tian, A. Timmins, P. Tribedy, Z. Tu, S. Tuo, T. Ullrich, E. Umaka, D. Upton, J. Vary, J. Velkovska, R. Venugopalan, A. Vijayakumar, I. Vitev, W. Vogelsang, R. Vogt, A. Vossen, E. Voutier, V. Vovchenko, A. Walker-Loud, F. Wang, J. Wang, X. Wang, X.-N. Wang, L. Weinstein, T. Wenaus, S. Weyhmiller, S. Wissink, B. Wojtsekhowski, C. Wong, M. Wood, Y. Wunderlich, B. Wyslouch, B. Xiao, W. Xie, W. Xiong, N. Xu, Q. Xu, Z. Xu, D. Yaari, X. Yao, Z. Ye, Z. Ye, C. Yero, F. Yuan, W. Zajc, C. Zhang, J. Zhang, F. Zhao, Y. Zhao, Z. Zhao, X. Zheng, J. Zhou, and M. Zurek, “The present and future of qcd,” Nuclear Physics A, vol. 1047, p. 122874, 2024.

[118] S. Weinberg, “Nuclear forces from chiral lagrangians,” Physics Letters B, vol. 251,

no. 2, pp. 288–292, 1990.

[119] S. Weinberg, “Effective chiral lagrangians for nucleon-pion interactions and nuclear forces,” Nuclear Physics B, vol. 363, no. 1, pp. 3–18, 1991.

[120] S. Weinberg, “Three-body interactions among nucleons and pions,” Physics Letters B, vol. 295, no. 1, pp. 114–121, 1992.

[121] R. Machleidt and D. Entem, “Chiral effective field theory and nuclear forces,” Physics Reports, vol. 503, no. 1, pp. 1–75, 2011.

[122] E. Epelbaum, H.-W. Hammer, and U.-G. Meißner, “Modern theory of nuclear forces,” Rev. Mod. Phys., vol. 81, pp. 1773–1825, Dec 2009.

[123] H.-W. Hammer, S. König, and U. van Kolck, “Nuclear effective field theory: Status and perspectives,” Rev. Mod. Phys., vol. 92, p. 025004, Jun 2020.

[124] K. Hebeler, “Three-nucleon forces: Implementation and applications to atomic nuclei and dense matter,” Physics Reports, vol. 890, pp. 1–116, 2021.

[125] E. Epelbaum, “Nuclear forces from chiral effective field theory: a primer,” arXiv:1001.3229 [nucl-th].

[126] Particle Data Group, “Review of Particle Physics,” Progress of Theoretical and Experimental Physics, vol. 2022, p. 083C01, 08 2022.

[127] S. Scherer, “Introduction to chiral perturbation theory,” arXiv:hep-ph/0210398.

[128] S. Coleman, J. Wess, and B. Zumino, “Structure of Phenomenological Lagrangians. I,” Phys. Rev., vol. 177, pp. 2239–2247, Jan 1969.

[129] C. G. Callan, S. Coleman, J. Wess, and B. Zumino, “Structure of Phenomenological Lagrangians. II,” Phys. Rev., vol. 177, pp. 2247–2250, Jan 1969.

[130] O. Thim, E. May, A. Ekström, and C. Forssén, “Bayesian analysis of chiral effective field theory at leading order in a modified Weinberg power counting approach,” Phys. Rev. C, vol. 108, p. 054002, Nov 2023.

[131] D. R. Entem, R. Machleidt, and Y. Nosyk, “High-quality two-nucleon potentials up to fifth order of the chiral expansion,” Phys. Rev. C, vol. 96, p. 024004, Aug 2017.

[132] D. R. Entem, R. Machleidt, and Y. Nosyk, “Nucleon-Nucleon Scattering Up to N5LO in Chiral Effective Field Theory,” Frontiers in Physics, vol. 8, 2020.

[133] I. Tews, Z. Davoudi, A. Ekström, J. D. Holt, and J. E. Lynn, “New ideas in constraining nuclear forces,” Journal of Physics G: Nuclear and Particle Physics, vol. 47, p. 103001, Aug 2020.

[134] H. Krebs, E. Epelbaum, and U.-G. Meißner, "Nuclear forces with Δ excitations up to next-to-next-to-leading order, part I: Peripheral nucleon-nucleon waves," The European Physical Journal A, vol. 32, pp. 127–137, May 2007.

[135] A. Ekström, G. Hagen, T. D. Morris, T. Papenbrock, and P. D. Schwartz, "Δ isobars and nuclear saturation," Phys. Rev. C, vol. 97, p. 024332, Feb 2018.

[136] H. Krebs, A. M. Gasparyan, and E. Epelbaum, "Three-nucleon force in chiral effective field theory with explicit $\Delta(1232)$ degrees of freedom: Longest-range contributions at fourth order," Phys. Rev. C, vol. 98, p. 014003, Jul 2018.

[137] M. Piarulli and I. Tews, "Local nucleon-nucleon and three-nucleon interactions within chiral effective field theory," Frontiers in Physics, vol. 7, 2020.

[138] W. G. Jiang, A. Ekström, C. Forssén, G. Hagen, G. R. Jansen, and T. Papenbrock, "Accurate bulk properties of nuclei from $a = 2$ to ∞ from potentials with Δ isobars," Phys. Rev. C, vol. 102, p. 054301, Nov 2020.

[139] D. O. Riska and R. Schiavilla, "Chiral electroweak currents in nuclei," International Journal of Modern Physics E, vol. 26, no. 01n02, p. 1740022, 2017.

[140] H. Krebs, "Nuclear currents in chiral effective field theory," The European Physical Journal A, vol. 56, p. 234, Sep 2020.

[141] D. Rozpedzik, J. Golak, R. Skibinski, H. Witala, W. Gloeckle, E. Epelbaum, A. Nogga, and H. Kamada, "A first estimation of chiral four-nucleon force effects in 4he," 2006.

[142] S. Schulz, Four-Nucleon Forces in Ab Initio Nuclear Structure. PhD thesis, Technische Universität Darmstadt, February 2018.

[143] A. Dyhdalo, R. J. Furnstahl, K. Hebeler, and I. Tews, "Regulator artifacts in uniform matter for chiral interactions," Phys. Rev. C, vol. 94, p. 034001, Sep 2016.

[144] D. R. Entem and R. Machleidt, "Accurate charge-dependent nucleon-nucleon potential at fourth order of chiral perturbation theory," Phys. Rev. C, vol. 68, p. 041001, Oct 2003.

[145] E. Epelbaum, A. Nogga, W. Glöckle, H. Kamada, U.-G. Meißner, and H. Witała, "Three-nucleon forces from chiral effective field theory," Phys. Rev. C, vol. 66, p. 064001, Dec 2002.

[146] S. K. Bogner, R. J. Furnstahl, and R. J. Perry, "Similarity renormalization group for nucleon-nucleon interactions," Phys. Rev. C, vol. 75, p. 061001, Jun 2007.

[147] J. Simonis, K. Hebeler, J. D. Holt, J. Menéndez, and A. Schwenk, "Exploring *sd*-shell nuclei from two- and three-nucleon interactions with realistic saturation properties," Phys. Rev. C, vol. 93, p. 011302, Jan 2016.

[148] T. D. Morris, J. Simonis, S. R. Stroberg, C. Stumpf, G. Hagen, J. D. Holt, G. R. Jansen, T. Papenbrock, R. Roth, and A. Schwenk, "Structure of the lightest tin isotopes," Phys. Rev. Lett., vol. 120, p. 152503, Apr 2018.

[149] M. C. M. Rentmeester, R. G. E. Timmermans, and J. J. de Swart, "Determination of the chiral coupling constants c_3 and c_4 in new pp and np partial-wave analyses," Phys. Rev. C, vol. 67, p. 044001, Apr 2003.

[150] F. Coester, "Bound states of a many-particle system," Nuclear Physics, vol. 7, pp. 421–424, 1958.

[151] F. Coester and H. Kümmel, "Short-range correlations in nuclear wave functions," Nuclear Physics, vol. 17, pp. 477–485, 1960.

[152] R. J. Bartlett and M. Musiał, "Coupled-cluster theory in quantum chemistry," Rev. Mod. Phys., vol. 79, pp. 291–352, Feb 2007.

[153] I. Shavitt and R. J. Bartlett, Many-Body Methods in Chemistry and Physics: MBPT and Coupled-Cluster Theory. Cambridge Molecular Science, Cambridge University Press, 2009.

[154] R. F. Bishop, "An overview of coupled cluster theory and its applications in physics," Theoretica chimica acta, vol. 80, pp. 95–148, Mar. 1991.

[155] J. H. Heisenberg and B. Mihaila, "Ground state correlations and mean field in ^{16}O," Phys. Rev. C, vol. 59, pp. 1440–1448, Mar 1999.

[156] P. Gysbers, G. Hagen, J. D. Holt, G. R. Jansen, T. D. Morris, P. Navrátil, T. Papenbrock, S. Quaglioni, A. Schwenk, S. R. Stroberg, and K. A. Wendt, "Discrepancy between experimental and theoretical β-decay rates resolved from first principles," Nature Phys., vol. 15, no. 5, pp. 428–431, 2019.

[157] J. Žofka, "Application of the Hartree-Fock method in nuclear theory," Czechoslovak Journal of Physics B, vol. 20, pp. 926–938, Aug. 1970.

[158] D. Gogny and P. L. Lions, "Hartree-Fock theory in nuclear physics," ESAIM: Mathematical Modelling and Numerical Analysis - Modélisation Mathématique et Analyse Numérique, vol. 20, no. 4, pp. 571–637, 1986.

[159] G. Hagen, T. Papenbrock, D. J. Dean, A. Schwenk, A. Nogga, M. Włoch, and P. Piecuch, "Coupled-cluster theory for three-body hamiltonians," Phys. Rev. C, vol. 76, p. 034302, Sep 2007.

[160] R. Roth, S. Binder, K. Vobig, A. Calci, J. Langhammer, and P. Navrátil, "Medium-Mass Nuclei with Normal-Ordered Chiral $NN+3N$ Interactions," Phys. Rev. Lett., vol. 109, p. 052501, Jul 2012.

[161] C. David Sherrill and H. F. Schaefer, "The configuration interaction method: Advances in highly correlated approaches," vol. 34 of Advances in Quantum Chemistry, pp. 143–269, Academic Press, 1999.

[162] R. J. Bartlett and G. D. Purvis, "Many-body perturbation theory, coupled-pair many-electron theory, and the importance of quadruple excitations for the correlation problem," International Journal of Quantum Chemistry, vol. 14, no. 5, pp. 561–581, 1978.

[163] R. J. Bartlett, "Many-body perturbation theory and coupled cluster theory for electron correlation in molecules," Annual Review of Physical Chemistry, vol. 32, no. 1, pp. 359–401, 1981.

[164] K. R. S. Marcel Nooijen and D. Mukherjee, "Reflections on size-extensivity, size-consistency and generalized extensivity in many-body theory," Molecular Physics, vol. 103, no. 15-16, pp. 2277–2298, 2005.

[165] B. Hall, Lie Groups, Lie Algebras, and Representations: An Elementary Introduction. Graduate Texts in Mathematics, Springer New York, 2010.

[166] J. D. Watts, J. Gauss, and R. J. Bartlett, "Coupled-cluster methods with noniterative triple excitations for restricted open-shell Hartree–Fock and other general single determinant reference functions. Energies and analytical gradients," The Journal of Chemical Physics, vol. 98, pp. 8718–8733, 06 1993.

[167] Z. H. Sun, C. A. Bell, G. Hagen, and T. Papenbrock, "How to renormalize coupled cluster theory," Phys. Rev. C, vol. 106, p. L061302, Dec 2022.

[168] J. F. Stanton and R. J. Bartlett, "The equation of motion coupled-cluster method. a systematic biorthogonal approach to molecular excitation energies, transition probabilities, and excited state properties," The Journal of Chemical Physics, vol. 98, no. 9, pp. 7029–7039, 1993.

[169] J. D. Watts and R. J. Bartlett, "Economical triple excitation equation-of-motion coupled-cluster methods for excitation energies," Chemical Physics Letters, vol. 233, no. 1, pp. 81–87, 1995.

[170] S. Binder, J. Langhammer, A. Calci, and R. Roth, "Ab initio path to heavy nuclei," Physics Letters B, vol. 736, pp. 119–123, 2014.

[171] G. Hagen, G. R. Jansen, and T. Papenbrock, "Structure of ^{78}Ni from first-principles computations," Phys. Rev. Lett., vol. 117, p. 172501, Oct 2016.

[172] M. Bender, P.-H. Heenen, and P.-G. Reinhard, "Self-consistent mean-field models for nuclear structure," Rev. Mod. Phys., vol. 75, pp. 121–180, Jan 2003.

[173] J. A. Sheikh, J. Dobaczewski, P. Ring, L. M. Robledo, and C. Yannouleas, "Symmetry restoration in mean-field approaches," Journal of Physics G: Nuclear and Particle Physics, vol. 48, p. 123001, Nov 2021.

[174] S. J. Novario, G. Hagen, G. R. Jansen, and T. Papenbrock, "Charge radii of exotic neon and magnesium isotopes," Phys. Rev. C, vol. 102, p. 051303, Nov 2020.

[175] G. Hagen, S. J. Novario, Z. H. Sun, T. Papenbrock, G. R. Jansen, J. G. Lietz, T. Duguet, and A. Tichai, "Angular-momentum projection in coupled-cluster theory: Structure of ^{34}Mg," Phys. Rev. C, vol. 105, p. 064311, Jun 2022.

[176] A. Ekström, C. Forssén, G. Hagen, G. R. Jansen, T. Papenbrock, and Z. H. Sun, "How chiral forces shape neutron-rich Ne and Mg nuclei," arXiv:2305.06955 [nucl-th].

[177] M. Musiał and R. J. Bartlett, "Equation-of-motion coupled cluster method with full inclusion of connected triple excitations for electron-attached states: EA-EOM-CCSDT," The Journal of Chemical Physics, vol. 119, pp. 1901–1908, 07 2003.

[178] M. Musiał, S. A. Kucharski, and R. J. Bartlett, "Equation-of-motion coupled cluster method with full inclusion of the connected triple excitations for ionized states: IP-EOM-CCSDT," The Journal of Chemical Physics, vol. 118, pp. 1128–1136, 01 2003.

[179] G. Hagen, T. Papenbrock, and M. Hjorth-Jensen, "Ab Initio Computation of the ^{17}F Proton Halo State and Resonances in $A = 17$ Nuclei," Phys. Rev. Lett., vol. 104, p. 182501, May 2010.

[180] G. R. Jansen, M. Hjorth-Jensen, G. Hagen, and T. Papenbrock, "Toward open-shell nuclei with coupled-cluster theory," Phys. Rev. C, vol. 83, p. 054306, May 2011.

[181] G. R. Jansen, "Spherical coupled-cluster theory for open-shell nuclei," Phys. Rev. C, vol. 88, p. 024305, Aug 2013.

[182] J. Shen and P. Piecuch, "Double electron-attachment equation-of-motion coupled-cluster methods with up to 4-particle–2-hole excitations: improved implementation and application to singlet–triplet gaps in ortho-, meta-, and para-benzyne isomers," Molecular Physics, vol. 119, no. 21-22, p. e1966534, 2021.

[183] D. Andreasi, W. Leidemann, C. Reiß, and M. Schwamb, "New inversion methods for the Lorentz Integral Transform," The European Physical Journal A - Hadrons and Nuclei, vol. 24, pp. 361–372, June 2005.

[184] N. Barnea, V. D. Efros, W. Leidemann, and G. Orlandini, "The lorentz integral transform and its inversion," Few-Body Systems, vol. 47, pp. 201–206, May 2010.

[185] V. D. Efros, W. Leidemann, and G. Orlandini, “Response functions from integral transforms with a Lorentz kernel,” Physics Letters B, vol. 338, no. 2, pp. 130–133, 1994.

[186] V. D. Efros, W. Leidemann, and G. Orlandini, “Electromagnetic Few-Body Response Functions with the Lorentz Integral Transform Method,” Few-Body Systems, vol. 26, pp. 251–269, June 1999.

[187] J. Golak, R. Skibiński, W. Glöckle, H. Kamada, A. Nogga, H. Witała, V. Efros, W. Leidemann, G. Orlandini, and E. Tomusiak, “Benchmark calculation of the three-nucleon photodisintegration,” Nuclear Physics A, vol. 707, no. 3, pp. 365–378, 2002.

[188] V. D. Efros, W. Leidemann, G. Orlandini, and E. L. Tomusiak, “Longitudinal electron scattering response functions of ^{3}H and ^{3}He,” Phys. Rev. C, vol. 69, p. 044001, Apr 2004.

[189] S. Bacca and S. Pastore, “Electromagnetic reactions on light nuclei,” Journal of Physics G: Nuclear and Particle Physics, vol. 41, p. 123002, Nov 2014.

[190] J. E. Sobczyk, B. Acharya, S. Bacca, and G. Hagen, “Ab initio computation of the longitudinal response function in ^{40}Ca,” Phys. Rev. Lett., vol. 127, p. 072501, Aug 2021.

[191] J. E. Sobczyk, B. Acharya, S. Bacca, and G. Hagen, “^{40}Ca transverse response function from coupled-cluster theory,” Phys. Rev. C, vol. 109, p. 025502, Feb 2024.

[192] J. K. Cullum, “Arnoldi versus nonsymmetric lanczos algorithms for solving nonsymmetric matrix eigenvalue problems,” Technical Report TR-3576, University of Maryland, 1995.

[193] D. A. Varshalovich, A. N. Moskalev, and V. K. Khersonskiĭ, Quantum theory of angular momentum : irreducible tensors, spherical harmonics, vector coupling coefficients, 3nj symbols. Singapore: World Scientific Pub., 1988.

[194] “NTCL: The Nuclear Tensor Contraction Library.” `https://gitlab.com/ntcl/ntcl`.

[195] T. Miyagi, S. R. Stroberg, P. Navrátil, K. Hebeler, and J. D. Holt, “Converged ab initio calculations of heavy nuclei,” Phys. Rev. C, vol. 105, p. 014302, Jan 2022.

[196] R. J. Furnstahl, D. R. Phillips, and S. Wesolowski, “A recipe for EFT uncertainty quantification in nuclear physics,” Journal of Physics G: Nuclear and Particle Physics, vol. 42, p. 034028, Feb 2015.

[197] J. A. Melendez, S. Wesolowski, and R. J. Furnstahl, “Bayesian truncation errors in chiral effective field theory: Nucleon-nucleon observables,” Phys. Rev. C, vol. 96, p. 024003, Aug 2017.

[198] J. Ahrens, “The total absorption of photons by nuclei,” Nuclear Physics A, vol. 446, no. 1, pp. 229–239, 1985.

[199] B. S. Ishkhanov, I. M. Kapitonov, E. I. Lileeva, E. V. Shirokov, V. A. Erokhova, M. A. Elkin, and A. V. Izotova, “Cross sections of photon absorption by nuclei with nucleon numbers 12 - 65,” Tech. Rep. MSU-INP-2002-27/711 (Institute of Nuclear Physics, Moscow State University, 2002.

[200] A. Leistenschneider, T. Aumann, K. Boretzky, D. Cortina, J. Cub, U. D. Pramanik, W. Dostal, T. W. Elze, H. Emling, H. Geissel, A. Grünschloß, M. Hellstr, R. Holzmann, S. Ilievski, N. Iwasa, M. Kaspar, A. Kleinböhl, J. V. Kratz, R. Kulessa, Y. Leifels, E. Lubkiewicz, G. Münzenberg, P. Reiter, M. Rejmund, C. Scheidenberger, C. Schlegel, H. Simon, J. Stroth, K. Sümmerer, E. Wajda, W. Walús, and S. Wan, “Photoneutron cross sections for unstable neutron-rich oxygen isotopes,” Phys. Rev. Lett., vol. 86, pp. 5442–5445, Jun 2001.

[201] C. Stumpf, T. Wolfgruber, and R. Roth, “Electromagnetic Strength Distributions from the Ab Initio No-Core Shell Model,” arXiv:1709.06840 [nucl-th].

[202] C. Stumpf, Nuclear Spectra and Strength Distributions from Importance-Truncated Configuration-Interaction Methods. PhD thesis, Technische Universität Darmstadt, 2018.

[203] F. Raimondi and C. Barbieri, “Nuclear electromagnetic dipole response with the self-consistent Green’s function formalism,” Phys. Rev. C, vol. 99, p. 054327, May 2019.

[204] M. Duer, T. Aumann, R. Gernhäuser, V. Panin, S. Paschalis, D. M. Rossi, N. L. Achouri, D. Ahn, H. Baba, C. A. Bertulani, M. Böhmer, K. Boretzky, C. Caesar, N. Chiga, A. Corsi, D. Cortina-Gil, C. A. Douma, F. Dufter, Z. Elekes, J. Feng, B. Fernández-Domínguez, U. Forsberg, N. Fukuda, I. Gasparic, Z. Ge, J. M. Gheller, J. Gibelin, A. Gillibert, K. I. Hahn, Z. Halász, M. N. Harakeh, A. Hirayama, M. Holl, N. Inabe, T. Isobe, J. Kahlbow, N. Kalantar-Nayestanaki, D. Kim, S. Kim, T. Kobayashi, Y. Kondo, D. Körper, P. Koseoglou, Y. Kubota, I. Kuti, P. J. Li, C. Lehr, S. Lindberg, Y. Liu, F. M. Marqués, S. Masuoka, M. Matsumoto, J. Mayer, K. Miki, B. Monteagudo, T. Nakamura, T. Nilsson, A. Obertelli, N. A. Orr, H. Otsu, S. Y. Park, M. Parlog, P. M. Potlog, S. Reichert, A. Revel, A. T. Saito, M. Sasano, H. Scheit, F. Schindler, S. Shimoura, H. Simon, L. Stuhl, H. Suzuki, D. Symochko, H. Takeda, J. Tanaka, Y. Togano, T. Tomai, H. T. Törnqvist, J. Tscheuschner, T. Uesaka, V. Wagner, H. Yamada, B. Yang, L. Yang, Z. H. Yang, M. Yasuda, K. Yoneda, L. Zanetti, J. Zenihiro, and M. V. Zhukov, “Observation of a correlated free four-neutron system,” Nature, vol. 606, pp. 678–682, June 2022.

[205] F. M. Marqués and J. Carbonell, “The quest for light multineutron systems,” The European Physical Journal A, vol. 57, p. 105, Mar 2021.

[206] T. Faestermann, A. Bergmaier, R. Gernhäuser, D. Koll, and M. Mahgoub, "Indications for a bound tetraneutron," Physics Letters B, vol. 824, p. 136799, 2022.

[207] M. Duer. Private communication, October 2023.

[208] R. Lazauskas, E. Hiyama, and J. Carbonell, "Low energy structures in nuclear reactions with 4*n* in the final state," Phys. Rev. Lett., vol. 130, p. 102501, Mar 2023.

[209] Y. Yamaguchi, W. Horiuchi, T. Ichikawa, and N. Itagaki, "Dineutron-dineutron correlation in ^{8}He," Phys. Rev. C, vol. 108, p. L011304, Jul 2023.

[210] T. Kobayashi, S. Shimoura, I. Tanihata, K. Katori, K. Matsuta, T. Minamisono, K. Sugimoto, W. Müller, D. Olson, T. Symons, and H. Wieman, "Electromagnetic dissociation and soft giant dipole resonance of the neutron-dripline nucleus ^{11}Li," Physics Letters B, vol. 232, no. 1, pp. 51–55, 1989.

[211] T. Aumann and T. Nakamura, "The electric dipole response of exotic nuclei," Physica Scripta, vol. 2013, p. 014012, Jan 2013.

[212] M. Meister, K. Markenroth, D. Aleksandrov, T. Aumann, T. Baumann, M. Borge, L. Chulkov, D. Cortina-Gil, B. Eberlein, T. Elze, H. Emling, H. Geissel, M. Hellström, B. Jonson, J. Kratz, R. Kulessa, A. Leistenschneider, I. Mukha, G. Münzenberg, F. Nickel, T. Nilsson, G. Nyman, M. Pfützner, V. Pribora, A. Richter, K. Riisager, C. Scheidenberger, G. Schrieder, H. Simon, O. Tengblad, and M. Zhukov, "^{8}He–^{6}He: a comparative study of electromagnetic fragmentation reactions," Nuclear Physics A, vol. 700, no. 1, pp. 3–16, 2002.

[213] K. Markenroth, M. Meister, B. Eberlein, D. Aleksandrov, T. Aumann, L. Axelsson, T. Baumann, M. Borge, L. Chulkov, W. Dostal, T. Elze, H. Emling, H. Geissel, A. Grünschloß, M. Hellström, J. Holeczek, B. Jonson, J. Kratz, R. Kulessa, A. Leistenschneider, I. Mukha, G. Münzenberg, F. Nickel, T. Nilsson, G. Nyman, M. Pfützner, V. Pribora, A. Richter, K. Riisager, C. Scheidenberger, G. Schrieder, H. Simon, J. Stroth, O. Tengblad, and M. Zhukov, "^{8}He–^{6}He: a comparative study of nuclear fragmentation reactions," Nuclear Physics A, vol. 679, no. 3, pp. 462–480, 2001.

[214] M. Golovkov, L. Grigorenko, G. Ter-Akopian, A. Fomichev, Y. Oganessian, V. Gorshkov, S. Krupko, A. Rodin, S. Sidorchuk, R. Slepnev, S. Stepantsov, R. Wolski, D. Pang, V. Chudoba, A. Korsheninnikov, E. Kuzmin, E. Nikolskii, B. Novatskii, D. Stepanov, P. Roussel-Chomaz, W. Mittig, A. Ninane, F. Hanappe, L. Stuttgé, A. Yukhimchuk, V. Perevozchikov, Y. Vinogradov, S. Grishechkin, and S. Zlatoustovskiy, "The ^{8}He and ^{10}He spectra studied in the (t,p) reaction," Physics Letters B, vol. 672, no. 1, pp. 22–29, 2009.

[215] Y. Iwata, K. Ieki, A. Galonsky, J. J. Kruse, J. Wang, R. H. White-Stevens, E. Tryggestad, P. D. Zecher, F. Deák, A. Horváth, A. Kiss, Z. Seres, J. J. Kolata, J. von Schwarzenberg, R. E. Warner, and H. Schelin, "Dissociation of ^{8}He," Phys. Rev. C, vol. 62, p. 064311, Nov 2000.

[216] X. Jun et al., "New Measurements for ^{8}He Excited States," Chinese Physics Letters, vol. 29, p. 082501, aug 2012.

[217] M. Holl, R. Kanungo, Z. Sun, G. Hagen, J. Lay, A. Moro, P. Navrátil, T. Papenbrock, M. Alcorta, D. Connolly, B. Davids, A. Diaz Varela, M. Gennari, G. Hackman, J. Henderson, S. Ishimoto, A. Kilic, R. Krücken, A. Lennarz, J. Liang, J. Measures, W. Mittig, O. Paetkau, A. Psaltis, S. Quaglioni, J. Randhawa, J. Smallcombe, I. Thompson, M. Vorabbi, and M. Williams, "Proton inelastic scattering reveals deformation in ^{8}He," Physics Letters B, vol. 822, p. 136710, 2021.

[218] J. Piekarewicz, "Insights into the possible existence of a soft dipole mode in ^{8}He," Phys. Rev. C, vol. 105, p. 044310, Apr 2022.

[219] T. Myo and K. Katō, "Modeling the electric dipole strength of neutron-rich ^{8}He: Prediction of multineutron collective excitations," Phys. Rev. C, vol. 106, p. L021302, Aug 2022.

[220] T. Myo, M. Odsuren, and K. Katō, "Soft dipole resonance in neutron-rich ^{8}He," Progress of Theoretical and Experimental Physics, vol. 2022, p. 103D01, 09 2022.

[221] G. De Gregorio, F. Knapp, P. Veselý, and N. Lo Iudice, "Survey of the ^{8}He properties within a microscopic multiphonon approach," Phys. Rev. C, vol. 108, p. 024316, Aug 2023.

[222] E. Tiesinga, P. J. Mohr, D. B. Newell, and B. N. Taylor, "CODATA recommended values of the fundamental physical constants: 2018," Rev. Mod. Phys., vol. 93, p. 025010, Jun 2021.

[223] A. A. Filin, V. Baru, E. Epelbaum, H. Krebs, D. Möller, and P. Reinert, "Extraction of the neutron charge radius from a precision calculation of the deuteron structure radius," Phys. Rev. Lett., vol. 124, p. 082501, Feb 2020.

[224] J. L. Friar, J. Martorell, and D. W. L. Sprung, "Nuclear sizes and the isotope shift," Phys. Rev. A, vol. 56, pp. 4579–4586, Dec 1997.

[225] A. Ong, J. C. Berengut, and V. V. Flambaum, "Effect of spin-orbit nuclear charge density corrections due to the anomalous magnetic moment on halo nuclei," Phys. Rev. C, vol. 82, p. 014320, Jul 2010.

[226] G. Papadimitriou, A. T. Kruppa, N. Michel, W. Nazarewicz, M. Płoszajczak, and J. Rotureau, "Charge radii and neutron correlations in helium halo nuclei," Phys. Rev. C, vol. 84, p. 051304, Nov 2011.

[227] P. Mueller, I. A. Sulai, A. C. C. Villari, J. A. Alcántara-Núñez, R. Alves-Condé, K. Bailey, G. W. F. Drake, M. Dubois, C. Eléon, G. Gaubert, R. J. Holt, R. V. F. Janssens, N. Lecesne, Z.-T. Lu, T. P. O'Connor, M.-G. Saint-Laurent, J.-C. Thomas, and L.-B. Wang, "Nuclear charge radius of ^{8}He," Phys. Rev. Lett., vol. 99, p. 252501, Dec 2007.

[228] M. Brodeur, T. Brunner, C. Champagne, S. Ettenauer, M. J. Smith, A. Lapierre, R. Ringle, V. L. Ryjkov, S. Bacca, P. Delheij, G. W. F. Drake, D. Lunney, A. Schwenk, and J. Dilling, "First direct mass measurement of the two-neutron halo nucleus ^{6}He and improved mass for the four-neutron halo ^{8}He," Phys. Rev. Lett., vol. 108, p. 052504, Jan 2012.

[229] J. J. Krauth, K. Schuhmann, M. A. Ahmed, F. D. Amaro, P. Amaro, F. Biraben, T.-L. Chen, D. S. Covita, A. J. Dax, M. Diepold, L. M. P. Fernandes, B. Franke, S. Galtier, A. L. G., J. Götzfried, T. Graf, T. W. Hänsch, J. Hartmann, M. Hildebrandt, P. Indelicato, L. Julien, K. Kirch, A. Knecht, Y.-W. Liu, J. Machado, C. M. B. Monteiro, F. Mulhauser, B. Naar, T. Nebel, F. Nez, J. M. F. dos Santos, J. P. Santos, C. I. Szabo, D. Taqqu, J. F. C. A. Veloso, J. Vogelsang, A. Voss, B. Weichelt, R. Pohl, A. Antognini, and F. Kottmann, "Measuring the α-particle charge radius with muonic helium-4 ions," Nature, vol. 589, pp. 527–531, 2021.

[230] Y. M. Arkatov, P. I. Vatset, V. I. Voloshuchuk, V. A. Zolenko, I. M. Prokhorets, and V. I. Chimil Sov. J. Nucl. Phys., vol. 19, p. 598, 1974.

[231] Y. M. Arkatov, P. I. Vatset, V. I. Voloshuchuk, V. A. Zolenko, and I. M. Prokhorets Sov. J. Nucl. Phys., vol. 31, p. 726, 1980.

[232] K. Pachucki and A. M. Moro, "Nuclear polarizability of helium isotopes in atomic transitions," Phys. Rev. A, vol. 75, p. 032521, Mar 2007.

[233] I. Tanihata, D. Hirata, T. Kobayashi, S. Shimoura, K. Sugimoto, and H. Toki, "Revelation of thick neutron skins in nuclei," Physics Letters B, vol. 289, no. 3, pp. 261–266, 1992.

[234] G. Alkhazov, A. Dobrovolsky, P. Egelhof, H. Geissel, H. Irnich, A. Khanzadeev, G. Korolev, A. Lobodenko, G. Münzenberg, M. Mutterer, S. Neumaier, W. Schwab, D. Seliverstov, T. Suzuki, and A. Vorobyov, "Nuclear matter distributions in the ^{6}He and ^{8}He nuclei from differential cross sections for small-angle proton elastic scattering at intermediate energy," Nuclear Physics A, vol. 712, no. 3, pp. 269–299, 2002.

[235] X. Liu, P. Egelhof, O. Kiselev, and M. Mutterer, "Nuclear matter density distributions of the neutron-rich ^{6,8}He isotopes from a sum-of-gaussian analysis of elastic proton scattering data at intermediate energies," Phys. Rev. C, vol. 104, p. 034315, Sep 2021.

[236] J. Noga, R. J. Bartlett, and M. Urban, “Towards a full CCSDT model for electron correlation. CCSDT-n models,” Chemical Physics Letters, vol. 134, no. 2, pp. 126–132, 1987.

[237] W. C. Haxton and C. Johnson, “Weak-interaction rates in ^{16}O,” Phys. Rev. Lett., vol. 65, pp. 1325–1328, Sep 1990.

[238] A. Ekström and G. Hagen, “Global sensitivity analysis of bulk properties of an atomic nucleus,” Phys. Rev. Lett., vol. 123, p. 252501, Dec 2019.

[239] K. D. Launey, T. Dytrych, G. H. Sargsyan, R. B. Baker, and J. P. Draayer, “Emergent symplectic symmetry in atomic nuclei,” The European Physical Journal Special Topics, vol. 229, pp. 2429–2441, Oct. 2020.

[240] S. Typel and G. Baur, “Higher order effects in electromagnetic dissociation of neutron halo nuclei,” Phys. Rev. C, vol. 64, p. 024601, Jun 2001.

[241] J. Bradt, D. Bazin, F. Abu-Nimeh, T. Ahn, Y. Ayyad, S. Beceiro Novo, L. Carpenter, M. Cortesi, M. Kuchera, W. Lynch, W. Mittig, S. Rost, N. Watwood, and J. Yurkon, “Commissioning of the active-target time projection chamber,” Nuclear Instruments and Methods in Physics Research Section A: Accelerators, Spectrometers, Detectors and Associated Equipment, vol. 875, pp. 65–79, 2017.

[242] Y. Huang, J. T. Zhang, Y. Kuang, J. Geng, X. L. Tu, K. Yue, W. H. Long, and Z. P. Li, “Matter radius determination of ^{16}O via small-angle differential cross sections,” The European Physical Journal A, vol. 59, p. 4, Jan. 2023.

[243] C. N. Papanicolas, W. Q. Summer, J. S. Blair, and A. M. Bernstein, “Variation of the matter densities of nuclei from ^{40}Ca to ^{68}Zn,” Phys. Rev. C, vol. 25, pp. 1296–1303, Mar 1982.

[244] M. von Schmid, T. Aumann, S. Bagchi, S. Bönig, M. Csatlós, I. Dillmann, C. Dimopoulou, P. Egelhof, V. Eremin, T. Furuno, H. Geissel, R. Gernhäuser, M. N. Harakeh, A.-L. Hartig, S. Ilieva, N. Kalantar-Nayestanaki, O. Kiselev, H. Kollmus, C. Kozhuharov, A. Krasznahorkay, T. Kröll, M. Kuilman, S. Litvinov, Y. A. Litvinov, M. Mahjour-Shafiei, M. Mutterer, D. Nagae, M. A. Najafi, C. Nociforo, F. Nolden, U. Popp, C. Rigollet, R. Roth, S. Roy, C. Scheidenberger, M. Steck, B. Streicher, L. Stuhl, M. Thürauf, T. Uesaka, H. Weick, J. S. Winfield, D. Winters, P. J. Woods, T. Yamaguchi, K. Yue, J. C. Zamora Cardona, J. Zenihiro, and EXL Collaboration, “Matter radius of the doubly-magic ^{56}Ni measured in a storage ring,” The European Physical Journal A, vol. 59, p. 83, Apr. 2023.

[245] Y.-W. Lui, H. L. Clark, and D. H. Youngblood, “Giant resonances in ^{16}O,” Phys. Rev. C, vol. 64, p. 064308, Nov 2001.

[246] D. H. Youngblood, Y.-W. Lui, and H. L. Clark, “Giant monopole resonance strength in ^{40}Ca,” Phys. Rev. C, vol. 55, pp. 2811–2818, Jun 1997.

[247] C. Monrozeau, E. Khan, Y. Blumenfeld, C. E. Demonchy, W. Mittig, P. Roussel-Chomaz, D. Beaumel, M. Caamaño, D. Cortina-Gil, J. P. Ebran, N. Frascaria, U. Garg, M. Gelin, A. Gillibert, D. Gupta, N. Keeley, F. Maréchal, A. Obertelli, and J.-A. Scarpaci, “First measurement of the giant monopole and quadrupole resonances in a short-lived nucleus: ^{56}Ni,” Phys. Rev. Lett., vol. 100, p. 042501, Jan 2008.

[248] A. Ekström, G. Baardsen, C. Forssén, G. Hagen, M. Hjorth-Jensen, G. R. Jansen, R. Machleidt, W. Nazarewicz, T. Papenbrock, J. Sarich, and S. M. Wild, “Optimized chiral nucleon-nucleon interaction at next-to-next-to-leading order,” Phys. Rev. Lett., vol. 110, p. 192502, May 2013.

[249] G. Baardsen, A. Ekström, G. Hagen, and M. Hjorth-Jensen, “Coupled-cluster studies of infinite nuclear matter,” Phys. Rev. C, vol. 88, p. 054312, Nov 2013.

[250] G. Hagen, T. Papenbrock, A. Ekström, K. A. Wendt, G. Baardsen, S. Gandolfi, M. Hjorth-Jensen, and C. J. Horowitz, “Coupled-cluster calculations of nucleonic matter,” Phys. Rev. C, vol. 89, p. 014319, Jan 2014.

[251] H. Sagawa, S. Yoshida, G.-M. Zeng, J.-Z. Gu, and X.-Z. Zhang, “Isospin dependence of incompressibility in relativistic and nonrelativistic mean field calculations,” Phys. Rev. C, vol. 76, p. 034327, Sep 2007.

[252] T. Hüther, K. Vobig, K. Hebeler, R. Machleidt, and R. Roth, “Family of chiral two-plus three-nucleon interactions for accurate nuclear structure studies,” Physics Letters B, vol. 808, p. 135651, 2020.

[253] F. Marino, F. Bonaiti, S. Bacca, et al. , in preparation.

[254] T. Duguet, A. Ekström, R. J. Furnstahl, S. König, and D. Lee, “Eigenvector continuation and projection-based emulators,” arXiv:2310.19419 [nucl-th].

[255] P. Arthuis, K. Hebeler, and A. Schwenk, “Neutron-rich nuclei and neutron skins from chiral low-resolution interactions,” arXiv: 2401.06675 [nucl-th].

[256] Z. Zhang and L.-W. Chen, “Constraining the density slope of nuclear symmetry energy at subsaturation densities using electric dipole polarizability in ^{208}Pb,” Phys. Rev. C, vol. 90, p. 064317, Dec 2014.

[257] Z. Zhang and L.-W. Chen, “Electric dipole polarizability in ^{208}pb as a probe of the symmetry energy and neutron matter around $\rho_0/3$,” Phys. Rev. C, vol. 92, p. 031301, Sep 2015.

[258] B. Côté, C. L. Fryer, K. Belczynski, O. Korobkin, M. Chruślińska, N. Vassh, M. R. Mumpower, J. Lippuner, T. M. Sprouse, R. Surman, and R. Wollaeger, "The Origin of r-process Elements in the Milky Way," The Astrophysical Journal, vol. 855, p. 99, mar 2018.

[259] A. Spyrou, S. N. Liddick, F. Naqvi, B. P. Crider, A. C. Dombos, D. L. Bleuel, B. A. Brown, A. Couture, L. Crespo Campo, M. Guttormsen, A. C. Larsen, R. Lewis, P. Möller, S. Mosby, M. R. Mumpower, G. Perdikakis, C. J. Prokop, T. Renstrøm, S. Siem, S. J. Quinn, and S. Valenta, "Strong neutron-γ competition above the neutron threshold in the decay of ^{70}Co," Phys. Rev. Lett., vol. 117, p. 142701, Sep 2016.

[260] S. Lyons, A. Spyrou, S. N. Liddick, F. Naqvi, B. P. Crider, A. C. Dombos, D. L. Bleuel, B. A. Brown, A. Couture, L. C. Campo, J. Engel, M. Guttormsen, A. C. Larsen, R. Lewis, P. Möller, S. Mosby, M. R. Mumpower, E. M. Ney, A. Palmisano, G. Perdikakis, C. J. Prokop, T. Renstrøm, S. Siem, M. K. Smith, and S. J. Quinn, "^{69,71}Coβ-decay strength distributions from total absorption spectroscopy," Phys. Rev. C, vol. 100, p. 025806, Aug 2019.